DOE/NASA/0167-9
NASA CR-174886
GARRETT NO. 31-3725(9)

ADVANCED GAS TURBINE (AGT) TECHNOLOGY DEVELOPMENT

NINTH SEMIANNUAL PROGRESS REPORT
(JANUARY 1984 — JUNE 1984)

Engineering Staff of
Garrett Turbine Engine Company
A Division of The Garrett Corporation

DECEMBER 1984

Prepared for
NATIONAL AERONAUTICS AND SPACE ADMINISTRATION
Lewis Research Center
Cleveland, Ohio 44135
Under Contract DEN3-167

(NASA-CR-174886) ADVANCED GAS TURBINE (AGT) POWERTRAIN SYSTEM DEVELOPMENT FOR AUTOMOTIVE APPLICATIONS REPORT Semiannual Progress Report, Jan. - Jun. 1984 (Garrett Mfg. Ltd.) 112 p HC A06/MF A01 CSCL 13F G3/85
N86-11087
Unclas 27560

for

U.S. DEPARTMENT OF ENERGY
Office of Vehicle and Engine Research and Development
Technology Development and Analysis Division
Washington D.C. 20585

DOE/NASA/0167-9
NASA CR-174886
GARRETT NO. 31-3725(9)

ADVANCED GAS TURBINE (AGT) TECHNOLOGY DEVELOPMENT

NINTH SEMIANNUAL PROGRESS REPORT
(JANUARY 1984 — JUNE 1984)

Engineering Staff of
Garrett Turbine Engine Company
A Division of The Garrett Corporation

DECEMBER 1984

Prepared for
NATIONAL AERONAUTICS AND SPACE ADMINISTRATION
Lewis Research Center
Cleveland, Ohio 44135
Under Contract DEN3-167

for
U.S. DEPARTMENT OF ENERGY
Office of Vehicle and Engine Research and Development
Technology Development and Analysis Division
Washington D.C. 20585

PRECEDING PAGE BLANK NOT FILMED

TABLE OF CONTENTS

		Page
1.0	SUMMARY	1
1.1	Power Section Development	1
1.2	Combustor Development	1
1.3	Regenerator	2
1.4	Ceramic Development	2
2.0	INTRODUCTION	3
3.0	POWER SECTION DEVELOPMENT	5
3.1	Engine S/N 001	5
3.1.1	Hydrodynamic Thrust Bearing	5
3.2	Engine S/N 002C	12
3.3	Engine S/N 003	19
3.3.1	Foil Bearing Environment/Thermal Test	19
3.3.2	Compressor Backface Smoothing	20
3.3.3	Increased Foil Bearing Stiffness	20
3.3.4	Ball Bearing Area Configuration Changes	21
3.3.5	Initial Engine Motoring Tests	21
3.3.6	Compensated Engine Motoring Test	22
3.3.7	Ceramic Turbine Wheel Motoring Test	26
4.0	COMPONENT/SUBSYSTEM DEVELOPMENT	29
4.1	Compressor Development	29
4.2	Turbine Development	29
4.3	Combustion	29
4.3.1	Diffusion Flame (DF) Combustor	29
4.3.1.1	Combustor Rig Performance Check	29
4.3.2	Fuel Nozzle Development	31
4.3.3	Torch Ignitor	34
4.4	Regenerator	36
4.4.1	Ford Regenerator Development	36
4.4.2	Garrett Regenerator Development	41
4.4.2.1	Regenerator Rig Testing	41

TABLE OF CONTENTS (Contd)

		Page
4.5	Ceramic	41
	4.5.1 Materials and Component Development	41
	4.5.1.1 Ceramic Material Testing Summary	42
	4.5.1.2 Kyocera SC201 Silicon Carbide Testing	42
	4.5.1.3 RBSN Turbine Shroud Cut-Up Properties	42
	4.5.1.4 Alumina - LAS Sticking Study	43
	4.5.1.5 Carborundum SASC and Kyocera SC201 Sticking	43
	4.5.1.6 Insulation System	43
	4.5.1.7 Slip Casting Rheology Studies	49
	4.5.2 Screening Rigs	49
	4.5.2.1 Ceramic Component Thermal Screen Tests	49
	4.5.3 Ceramic Rotor Material Development	63
4.6	Rotor Dynamics/Foil Bearing	66
	4.6.1 Rotor Dynamics/Foil Bearing Rig	66
	4.6.2 Single Foil Bearing Rig Testing	68
APPENDICES		
APPENDIX A	FORD MOTOR COMPANY ADVANCED GAS TURBINE (AGT) POWERTRAIN SYSTEM DEVELOPMENT PROGRAM NINTH AGT101 SEMI-ANNUAL TECHNICAL PROGRESS REPORT	73
APPENDIX B	AIRESEARCH CASTING COMPANY (ACC) ADVANCED GAS TURBINE (AGT) POWERTRAIN SYSTEM DEVELOPMENT PROGRAM NINTH AGT101 SEMI-ANNUAL TECHNICAL PROGRESS REPORT	77
APPENDIX C	THE CARBORUNDUM COMPANY (UNIQUE WORK) ADVANCED GAS TURBINE (AGT) POWERTRAIN SYSTEM DEVELOPMENT PROGRAM NINTH AGT101 SEMI- ANNUAL TECHNICAL PROGRESS REPORT	83
APPENDIX D	DISPERSION OF SILICON POWDER	87
APPENDIX E	DEVELOPMENT OF HOMOGENEITY IN Si_3N_4 CERAMICS BY COLLOIDAL FILTRATION	135
APPENDIX F	LIST OF SYMBOLS, ABBREVIATIONS AND ACRONYMS	201
REFERENCES		203
NASA-C-168 FORM		204

LIST OF FIGURES

Figure	Title	Page
1	AGT101 Program Schedule	4
2	Foil Bearing Assembly/Structure Thermocouple Location	6
3	AGT101 Foil Bearing Finite Element Model Primary Leakage Path	6
4	Predicted Foil Bearing Sway Space Change for Different Steady-State Operting Points. (Bore and Carrier Cooling)	7
5	Predicted Foil Bearing Sway Space Change for Different Steady-State Operating Points. (Carrier Cooling Only)	7
6	Predicted Foil Bearing Sway Space Change for Different Steady-State Operating Points. (No Bore and Carrier Cooling)	8
7	Predicted Foil Bearing Sway Space Change for a Typical Cold Engine Lightoff and Acceleration	8
9	Hydrodynamic Thrust Bearing Design Improvements	9
10	Engine S/N 001, Build 20 Rotor Vibration	9
11	Engine S/N 001, Build 20 Speed Limiting Shaft Excursions	10
12	Engine S/N 001, Build 21 Rotor Vibration	11
13	Engine S/N 001, Build 21 Rotor Subsynchronous Frequency	11
14	Engine S/N 001, Build 22 Rotor Vibration	11
15	Engine S/N 001, Build 22 Rotor Subsynchronous Frequency	11
16	S/N 001 Build 23 Rotor Vibration	12
17	S/N 001 Build 23 Rotor Susbynchronous Frequency	12
18	Ceramic Rotor in Metal Engine, Build 24	13
19	Engine S/N 001, Build 25 Rotor Vibration	13
20	Engine S/N 001, Build 25 Subsynchronous Frequency	13
21	Revised Start Transient Cycle for First Ceramic Engine	14
22	Ceramic Engine Assembly in Process	15
23	Ceramic Turbine Shroud Module Assembled	15
24	Module Installed in Compressor Housing	15
25	Back Shroud Installed	15
26	Combustor Baffle Installed	16
27	Transition Duct Installed	16
28	Flow Separator Housing and Regenerator Shield Installed	16
29	S/N 002C - T4 Schedule Tested on February 16, 1984	17
30	Turbine Rotor/Backshroud Rub	18
31	Turbine Rotor Backface Metal Shavings Deposited on Turbine Backshroud	18
32	Turbine Shroud Shows Radial Rub from Turbine Rotor	18
33	Chipped Ceramic Combustor Baffle Support Leg	18
34	Comparison of Old and New Foil Bearing Housing Design	20
35	Compressor Backface Configurations	20
36	Motoring Test Configurations	21
37	Motoring Set Up in Foil Bearing Lab of Engine S/N 003	23
38	S/N 003 Motoring Test - Subsynchronous Motion	24
39	Breakaway Torque Versus Sway Space for Different Foil Bearings	24
40	S/N 003 Motoring Tests - Subsynchronous Motion	25
41	Alternative Bearings Tested	25
42	S/N 008 Motoring Tests - Subsynchronous Whirl Amplitude	26
43	Ceramic Turbine Wheel Compared to Baseline - Motoring Test	27
44	Performance Rating Stations	29
45	AGT101 (2100F) Nonregenerative Cycle Lean Blow Out Versus Percent of Load	30

LIST OF FIGURES (Contd)

Figure	Title	Page
46	DF Combustor, Water/Air Cooled Nozzle	30
47	AGT101 (2100F) Effect of Air Assisted Pressure on Fuel Air Ratio-Lean Blow Out at Idle Nonregenerated Condition ($T_{3.5}$ = 200F)	30
48	Combustor Test Rig Simulation of Engine Start Ramp	31
49	Simplex Mod II Fuel Nozzle	31
50	Simplex Mod I - FC Fuel Nozzle	32
51	SIMCAB Fuel Nozzle	32
52	Variation of Carbon Monoxide Emissions Relative to NO_x Emissions	33
53	Combustor Radial Concentration of NO_x Emission Species	34
54	Combustor Radial Concentration of CO Emission Species	34
55	Torch Ignitor	35
56	Multi-Fuel Torch Ignitor	35
57	Torch Test Data Using JP-4 Fuel	35
58	Regenerator Diaphragm System	36
59	Diaphragm Finite Element Model	36
60	Middle (Support) Diaphragm Temperature Distribution for Minimum Cooling Flow.	38
61	Middle (Support) Diaphragm Temperature Distribution for Maximum Cooling Flow	39
62	AGT101 Regenerator Seal Leakage	40
63	AGT101 Regenerator Core Torque	40
64	Diagonal Bond Configuration	40
65	Ford Ceramic Structures Rig	41
66	Phase V Regenerator Seal Drive Torque Versus Seal Pressure	42
67	Phase V Regenerator Seals Hot Seal Leakage Test	42
68	Comparison of Phase III with Phase V Regenerator Seals, Hot Seal Leakage Test	43
69	Kyocera SC201 Fracture Surface (A) and Polished Section (B)	46
70	Turbine Shroud Test Bar Area	47
71	AGT101 Insulation Test Rig	47
72	Maximum Power and Idle Condition of Lockheed HTP-16 Insulation	48
73	Lockheed HTP-16 Cylinders After Cyclical Flow Testing	48
74	Turbine Shroud Screening Rig With New Insulation Configuration (Babcock & Wilcox "Kaowool")	50
75	Turbine Shroud Screening Rig With "Old" Insulation Configuration (Fiberglass "wet blanket"	50
76	Turbine Shroud Screening Rig With "Donut" Added to Former Insulation Configuration	50
77	Shroud Thermal Screen Cycle	51
78	Turbine Shroud Second Seal Land Area	51
79	Baseline Turbine Shroud Screening Rig	52
80	Modified Turbine Shroud Screening Rig	52
81	Modified Turbine Shroud Screening Rig	54
82	Reconfigured Turbine Shroud Screening Rig	54
83	Rig Configuration for First Successful 2500F Run	56
84	Turbine Shroud Thermal Screening Rig Rapid Transient Test	58
85	Rig Configuration to the Engine Loading Configuration	59
86	Turbine Shroud Thermal Test Rig Charts	60

LIST OF FIGURES (Contd)

Figure	Title	Page
87	First- and Second-Generation Load Spacers	62
88	First- and Second-Generation Rocker/Eccentric Design Comparison	62
89	Microstructures of ACC Cast Rotors Densified by Ford and ASEA	67
90	ASEA and Ford Processed Rotors X-Ray Diffraction Results	68
91	Location of Foil and Carrier Thermocouples for Rotor Dynamics Rig Thermal Testing	70
92	Foils and Backing Spring Thermocouple Installation	71
93	Sway Space as a Function Speed	71

LIST OF TABLES

Table	Title	Page
1	Engine S/N 003 Test Comparison	9
2	Performance Analysis Leakage	12
3	1982 NGK Core Data	13
4	Engine Testing Through June 1983	14
5	Fuel Distributor Ring Surface Temperatures for Simplex Mod I Fuel Nozzle	23
6	Regenerator Core Performance	25
7	Summary of AGT Regenerator Performance	29
8	Summary of AET Components and Materials	33
9	Summary of AGT Ceramic Material Characterization at Garrett	34
10	Summary of Heat-Treated RBN 104 Flexure Strength Data	35
11	Ceramic Structures Rig, Build 6	36
12	Structures Rig Build 6 Teardown Summary	39
13	Fracture Analysis Summary, Structures Rig Build 6	39
14	RM-3 4-Point MOR Fast Fracture Strength	47
15	RM-3 4-Point MOR Strength After 300 Hour Oxidation	49
16	RM-3 Stress Rupture Results	49
17	Stress Rupture Results	50
18	Summary of Hardware Delivery	54

1.0 SUMMARY

This report describes progress and work performed by the Garrett Turbine Engine Company/Ford Motor Company Team during January through June 1984 to develop technology for an Advanced Gas Turbine (AGT) engine for automotive applications. This work was performed for the Department of Energy under NASA Contract DEN3-167. This is the ninth in a series of semiannual reports. Work performed during the first eight periods (References 1 through 8) initiated design and analysis, ceramic development, component testing, and test bed evaluation.

Project effort conducted under this contract is part of the DOE* Gas Turbine Highway Vehicle System Program. This program is oriented at providing the United States automotive industry the high-risk long-range technology necessary to produce gas turbine engines for automobiles with reduced fuel consumption and reduced environmental impact. Technology resulting from this program is intended to reach the marketplace by the early 1990s.

The advanced automobile gas turbine, when installed in a Ford vehicle (3000 pounds inertia weight), will provide:

- A combined federal driving cycle (CFDC) fuel economy of 42.8 miles per gallon based on Environmental Protection Agency (EPA) test procedures and Diesel No. 2 fuel (DF-2). The AGT-powered vehicle will substantially give the same overall vehicle driveability and performance as a comparable production vehicle powered by a conventional spark-ignition powertrain system
- Emissions less than federal standards
- Ability to use a variety of fuels

*A list of abbreviations and acronyms is presented in Appendix F, herein.

The major accomplishments for this period are summarized in the following paragraphs.

1.1 Power Section Development

Rotor dynamic instability was successfully reduced with the incorporation of an oil film thrust bearing. Operation to 100,000 rpm was achieved repeatedly and with stability. The instability forces were isolated during cold motoring of the engine and found to be the bladed components.

The first ceramic structures engine was successful to 2100F. All components passed the initial tests without distress.

1.2 Combustor Development

A stable diffusion flame combustor system was developed for engine use at 2100F. Testing continued on the lean burn concept with effort on the film-cooled Simplex nozzle. Corrected test conditions for 2500F operation were established as before at 1600F to determine nozzle emission data and integrity. As in previous tests, the nozzle performed quite well. Effort was initiated on this torch ignitor used to light the main burner during startup. Excellent lightoff characteristics were demonstrated.

1.3 Regenerator

Initial Phase V seals were delivered and tested in the ceramic structures rig at 2000F and in the engine at 2100F. In general, the seals performed quite well in the diaphragm area. However, the I-85 coating showed signs of overtemperature and will be replaced with I-151, a higher heat capacity coating. An initial lot of I-151 seals was delivered to Garrett for testing.

Regenerator rig testing of Phase V seals showed better leakage and core torque values than the Phase IV or III seals.

1.4 Ceramic Development

Ceramic component screening tests were continued on the transition duct/baffle, inner/outer diffuser housings, and turbine shroud. The inner/outer diffusers and transition duct/baffle were successfully screened for normal start conditions and thus are qualified for AGT101 (2500F) operation. The turbine shroud screening rig was designed to better simulate the flowpath. Following several mechanical problems, the rig was successfully ramped to 2500F and held for six minutes. All components were inspected following test with no distress noted.

Fabrication continued on rotors at AiResearch Casting Company and Ford. Several rotors were used for cut-up specimen testing with encouraging results. In both the axial and radial orientation, rotor density and strength were essentially identical.

2.0 INTRODUCTION

This report is the ninth in a series of Semiannual Technical Summary Reports for the Advanced Gas Turbine (AGT) Technology Development Project, authorized under NASA Contract DEN3-167 and sponsored by the DOE. This report has been prepared by The Garrett Turbine Engine Company (hereinafter referred to as Garrett), a Division of The Garrett Corporation, and includes information provided by the Ford Motor Company (hereinafter referred to as Ford), The Carborundum Company, and AiResearch Casting Company (ACC). The project was administered by Mr. Roger Palmer, Project Manager, NASA-Lewis Research Center, Cleveland, Ohio. This report presents plans and progress from January through June 1984.

Project effort conducted under this contract is part of the DOE Gas Turbine Highway Vehicle System Program. This program is oriented at providing the United States automotive industry the high-risk, long-range technology necessary to produce gas turbine engines for automobiles that will have reduced fuel consumption and reduced environmental impact. The intent is that technology resulting from this program be capable of reaching the marketplace by the early 1990s.

The advanced gas turbine, when installed in a Ford vehicle (3000 pounds inertia weight) would provide:

- A CFDC fuel economy of 42.8 miles per gallon based on EPA test procedures and DF-2. The AGT-powered vehicle shall give substantially the same overall vehicle driveability and performance as a comparable production vehicle powered by a conventional spark-ignition powertrain system.
- Emissions less than federal standards
- Ability to use a variety of fuels

The Garrett/Ford advanced gas turbine has been designated the AGT101.

The program is oriented toward developing advanced gas turbine long-range high-risk technology such that the automotive industry can carry forward to production in the 1990s. Emphasis on ceramics, gas bearings, low emission combustion, and improved component performance shall continue. The AGT101 is being used as a test bed in which to develop these technologies.

The program schedule is depicted in Figure 1. The program continues technology work through FY86, culminating in demonstration of the original goals of engine specific fuel consumption, power output, and emissions. In addition, the viability of ceramics will have been demonstrated in the AGT101 test beds, and the potential of economically producing the ceramic parts in automotive production quantities will have been assessed. When these goals are achieved, Ford will be in a position to proceed, without Government support, through the typical preproduction tasks that then could lead to production in the 1990s.

The primary technology challenge in the program continues to be the development of ceramic components and related high performance gas turbine aerothermodynamic components development for the AGT101. The AGT101 nominally is a 100 shp engine, capable of speeds to 100,000 rpm and operating at turbine inlet temperatures (TIT) to 2500F with a specific fuel consumption level of 0.3 pounds/horsepower/hour over much of the operating range.

This report reviews the power section (metal and ceramic) effort conducted to date, followed by a review of the component/ceramic technology development. Appendices include reports of progress from Ford, ACC and The Carborundum Company. Additionally, study reports prepared by Garrett subcontracted professionals on materials and processes are contained in Appendices D and E.

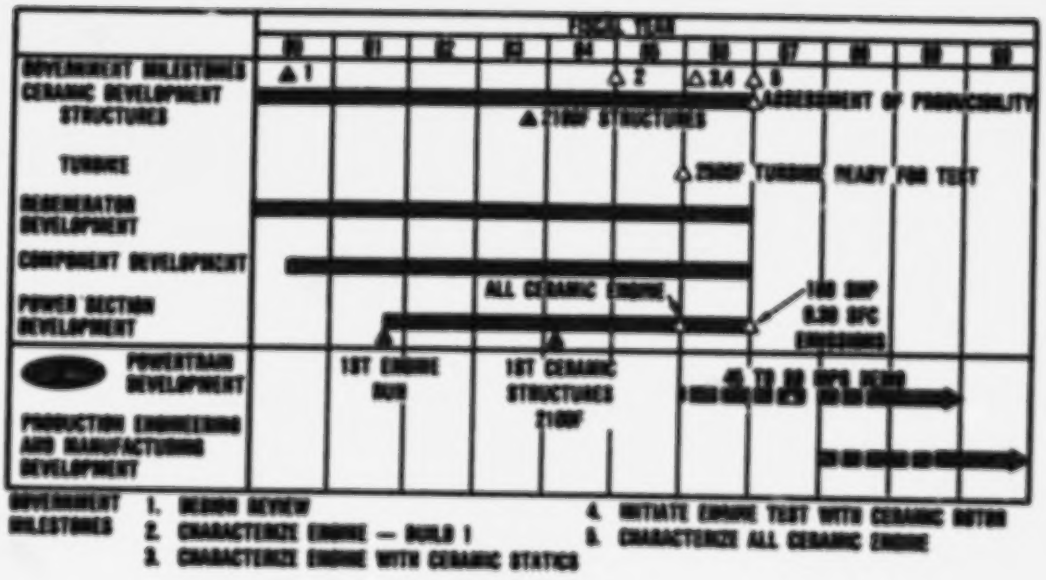

Figure 1. AGT101 Program Schedule.

3.0 POWER SECTION DEVELOPMENT

Testing of all three development engines continued during this reporting period. S/N 001 and S/N 003 were dedicated to resolving rotor dynamic instability problems, while S/N 002 was tested with ceramic structures to 2100F. The incorporation of an oil film thrust bearing forward of the compressor impeller and aft of the ball bearing has added moment stiffness and damping to the system. Operation to 100,000 rpm was achieved repeatedly with stability. Cold motoring of S/N 003 provided a means of identifying instability sources. Back-to-back testing showed the driving forces of instability to be the bladed components. S/N 002 was successfully tested through one and later ten thermal cycles to 2100F. Teardown inspection showed all ceramic components to be in good shape.

3.1 Engine S/N 001

Engine S/N 001 was used as part of an intensive effort to resolve the rotor dynamic instability. This activity, directed by the AGT101 Rotor Dynamics Task Force, included thermal mapping of the engine foil bearing structure and initial testing of an oil film thrust bearing.

From Build 17 through Build 19, S/N 001 engine was used to evaluate thermal conditions in the foil bearing and surrounding structure. This information was correlated with 2-D and 3-D computer models to determine how foil bearing sway space (diametrial clearance between journal and foils) dimensionally varied with engine operating condition.

Steady state information was collected at 50-, 60-, 70-, 80- and 90,000 rpm and transient data was collected as the engine was accelerated to 100-percent speed. Turbine bore cooling and foil bearing housing cooling were also varied to determine their effect on foil bearing structure temperatures and on rotor behavior.

Rotor dynamic characteristics, which were similar on each of the engine builds, are summarized in Table 1.

On Builds 17 and 19, foil bearing failures occurred while dwelling at speeds greater than 96,000 rpm due to excessive rotor vibration.

Thermal data was collected using thermocouples mounted on the compressor backshroud, foil bearing housing, and foil bearing carrier, as shown on Figure 2. This data was used to establish boundary conditions for 2-D analytical modeling as shown in Figure 3. Agreement between the resulting model and the engine test data was very good.

The analysis evaluated three conditions with respect to non-engine supplied external cooling of the foil bearing assembly. The first condition used both turbine bore cooling air and external foil bearing carrier cooling air, the second condition turned off the bore cooling, and the third condition turned off bore cooling and carrier cooling. The results of this analysis for steady state engine operating conditions are shown in Figures 4 through 7. In each case the foil bearing sway space decreased from cold build to idle operating conditions. Additionally, the sway space decreased as the engine speed increased. Reductions in external cooling air further decreased sway space. The transient response for a typical cold engine lightoff and acceleration is illustrated in Figure 8, which shows sway space quickly responding to speed changes.

Based on the result of the analysis, rotor dynamic instability does not appear to be explained by changing thermal environments.

3.1.1 Hydrodynamic Thrust Bearing

S/N 001 engine Builds 20 through 25 were devoted to the evaluation of a hydrodynamic thrust bearing (Figure 9). The oil film thrust

Table 1. Engine S/N 001 Rotor Dynamic Summary

Build No.	17	18	19
Maximum speed obtained (rpm)	99,600	95,400	98,000
Maximum steady state speed (rpm)	91,000	85,200	88,000
Limiting subsynchronous vibration (mils)	0.82 at 124 Hz Turbine	1.16 at 110 Hz Turbine	0.92 at 105 Hz Turbine

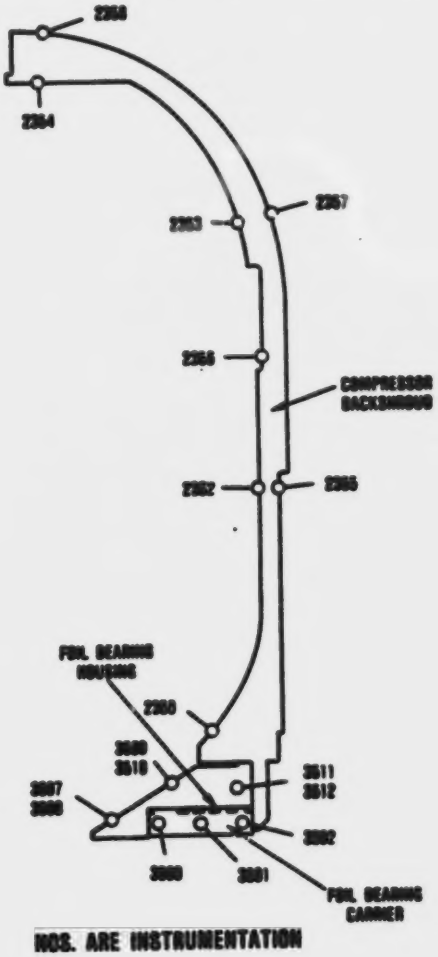

Figure 2. Foil Bearing Assembly/Structure Thermocouple Location.

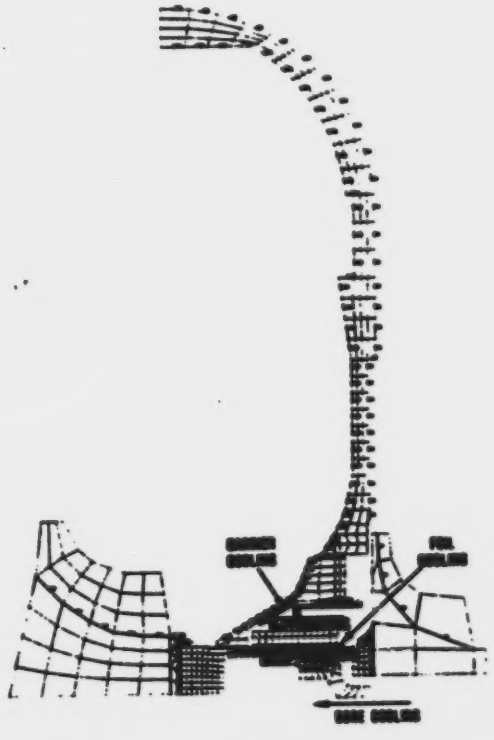

Figure 3. AGT101 Foil Bearing Finite Element Model.

bearing is designed to work in concert with the hydraulically mounted ball bearing such that the thrust bearing will carry a major portion of the aerodynamic thrust, allowing the hydraulic mount on the ball bearing to more

ORIGINAL PAGE IS
OF POOR QUALITY

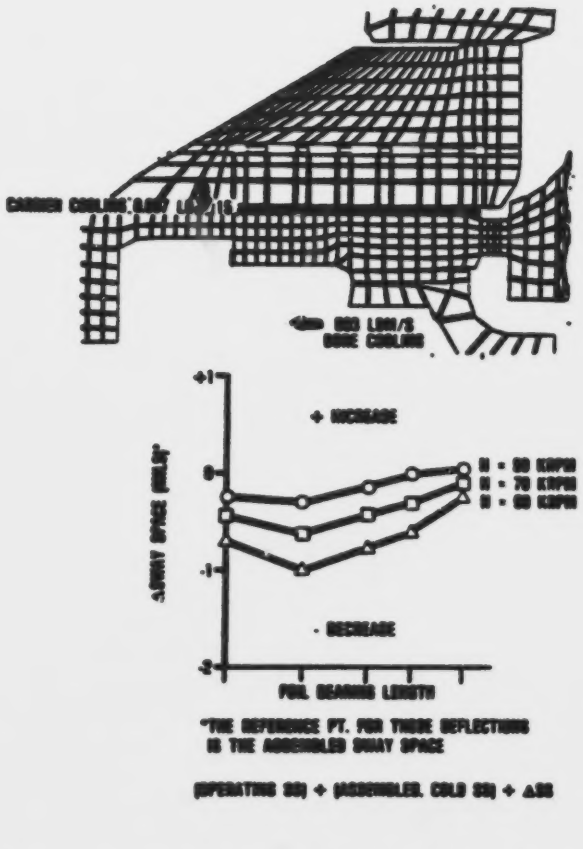

Figure 4. Predicted Foil Bearing Sway Space Change for Different Steady-State Operating Points. (Bore and Carrier Cooling).

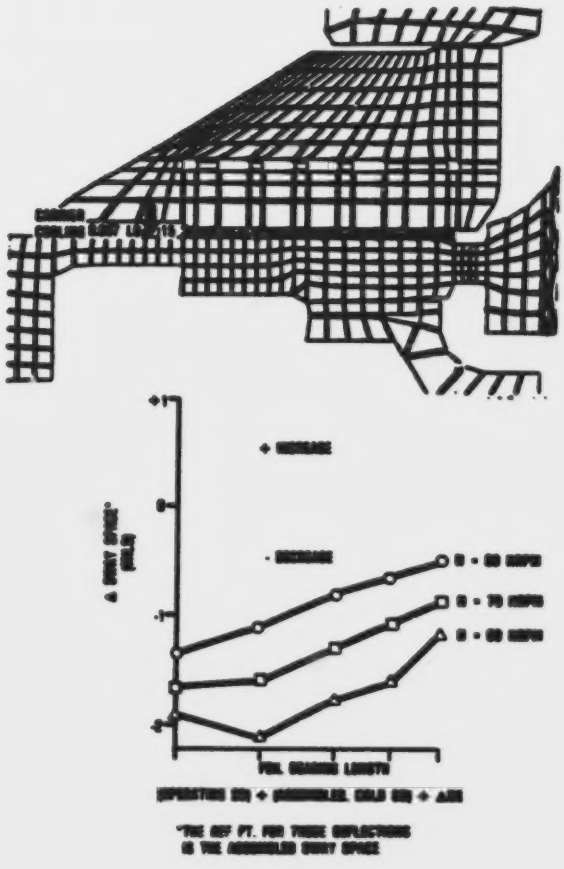

Figure 5. Predicted Foil Bearing Sway Space Change for Different Steady-State Operating Points. (Carrier Cooling Only).

efficiently dampen rotor motion. Additionally, the thrust bearing itself contributes to damping and rotor angular stiffness. Table 2 summarizes the salient build configurations. Test results are described below:

Build 20: The engine was operated to a maximum speed of 80,000 rpm. Speed was limited by rapidly increasing turbine synchronous vibration amplitudes, as shown in Figure 10. As this maximum speed was approached, quill shaft motion, shown in Figure 11. was erratic.

Build 21: Two significant modifications were made in this build. First, a foil bearing with a thicker foil substrate was used, because this configuration demonstrated improved performance on the rotor dynamic rigs (see Section 4.6 herein). Second, in an attempt to stabilize quill shaft motion versus Build 20, 0.003 inch of copper plate was added to the splined spacer major diameter, inducing a diametral interference fit of 0.0025 to 0.003 inch (Figure 9).

Rotor dynamic performance for this engine is shown in Figures 12 and 13, revealing excellent synchronous and subsynchronous vibration trends. The only item of note is a mild

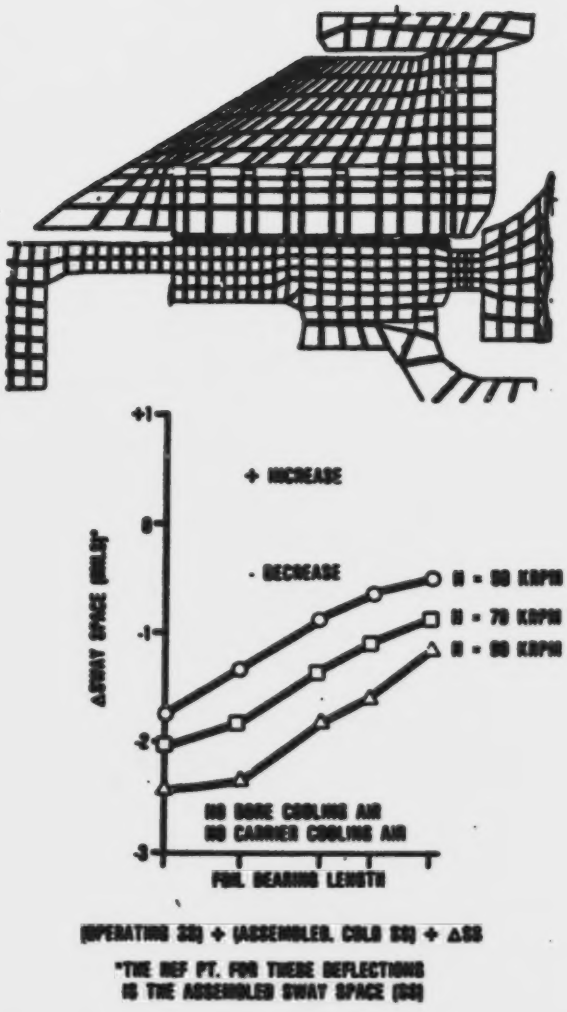
+ INCREASE
- DECREASE
N = 50 KRPM
N = 70 KRPM
N = 90 KRPM
NO BORE COOLING AIR
NO CARRIER COOLING AIR
FOIL BEARING LENGTH
(OPERATING SS) + (ASSEMBLED, COLD SS) + ΔSS
*THE REF PT. FOR THESE DEFLECTIONS
IS THE ASSEMBLED SWAY SPACE (SS)

Figure 6. Predicted Foil Bearing Sway Space Change for Different Steady-State Operating Points. (No Bore and Carrier Cooling).

synchronous peak between 85,000 and 95,000 rpm.

Build 22: The thrust bearing was structurally modified to facilitate assembly. The same splined spacer and quill shaft from Build 21 were used. During testing, the engine exhibited poor rotor dynamic characteristics with large synchronous turbine motion as engine

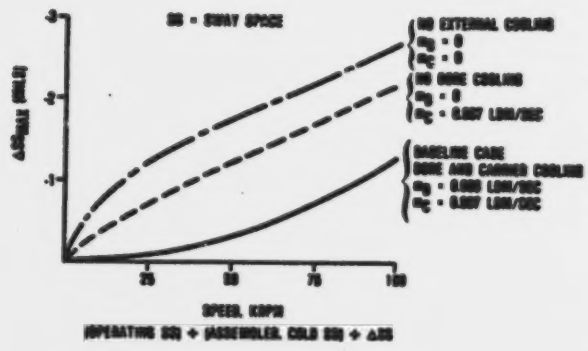

Figure 7. Predicted Maximum Sway Space Change During Steady-State Operation.

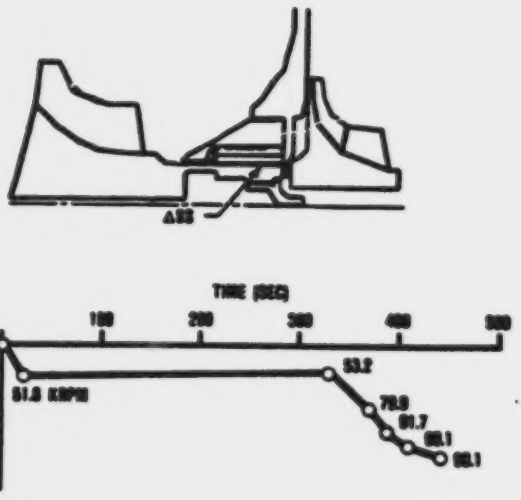

TIME (SEC)	N (KRPM)	ΔSS* (MIL)
0	0	0
20	51.800	-0.000032
330	53.170	-0.000022
370	79.870	-0.000092
380	91.710	-0.000098
410	98.110	-0.000104
440	98.110	-0.000108

*REFERENCED TO ASSEMBLED STATE (SS = SWAY SPACE)

Figure 8. Predicted Foil Bearing Sway Space Change for a Typical Cold Engine Lightoff and Acceleration.

ORIGINAL PAGE IS
OF POOR QUALITY

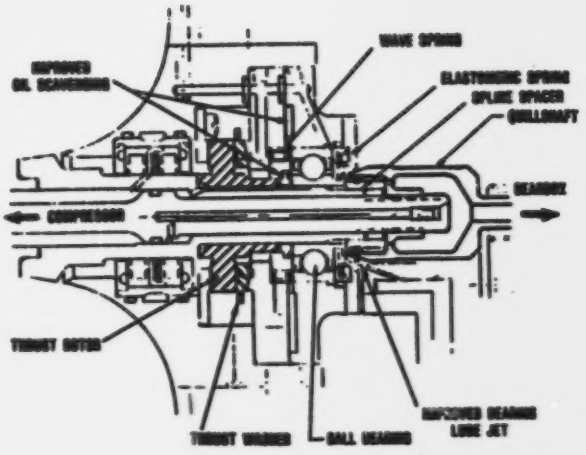

Figure 9. Hydrodynamic Thrust Bearing Design Improvements.

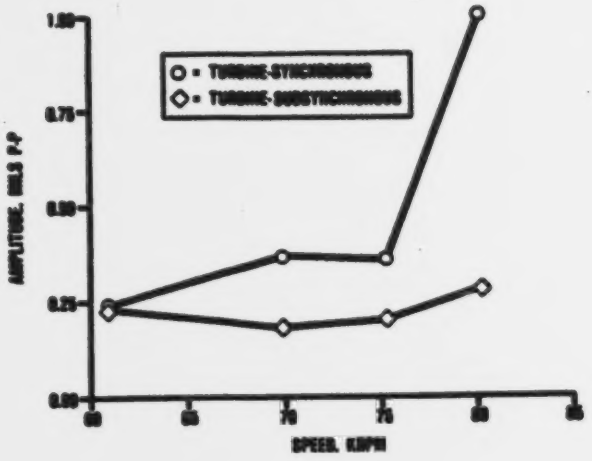

Figure 10. Engine S/N 001, Build 20 Rotor Vibration.

Table 2. S/N 001 Hydrodynamic Thrust Bearing Builds
Rotor Configuration

Build	20	21	22	23	24	25
Hydraulic mount clearance (inch)	0.0046	0.0046	0.0046	0.0046	0.0046	0.0046
Thrust bearing build clearance (inch)	0.004	0.004 to 0.007	0.002 to 0.001	0.004 to 0.007	0.004	0.004
Foil bearing sway space(1) (inch)	0.0062	0.0063	0.0063	0.0083	0.0083	0.0050
Foil bearing substrate thickness (inch)	0.005	0.006	0.006	0.006	0.006	0.006
Foil bearing spring rate (lb/in)	1737	3225	3225	3738	3738	1700
Turbine rotor	Astroloy	Astroloy	Astroloy	Dual Alloy	Ceramic	Ceramic
Quill shaft/ splined spacer	Set No 3 Unplated	Set No 3 New plating	Set No 3 Worn plating	Set No 3 New plating 0.0025 to 0.003 inch diametral interference fit	Set No 184 New plating 0.0025 to 0.003 inch diametral interference fit	Set No 3 New plating 0.0025 to 0.003 inch diametral interference fit

(1) Calculated

ORIGINAL PAGE IS
OF POOR QUALITY

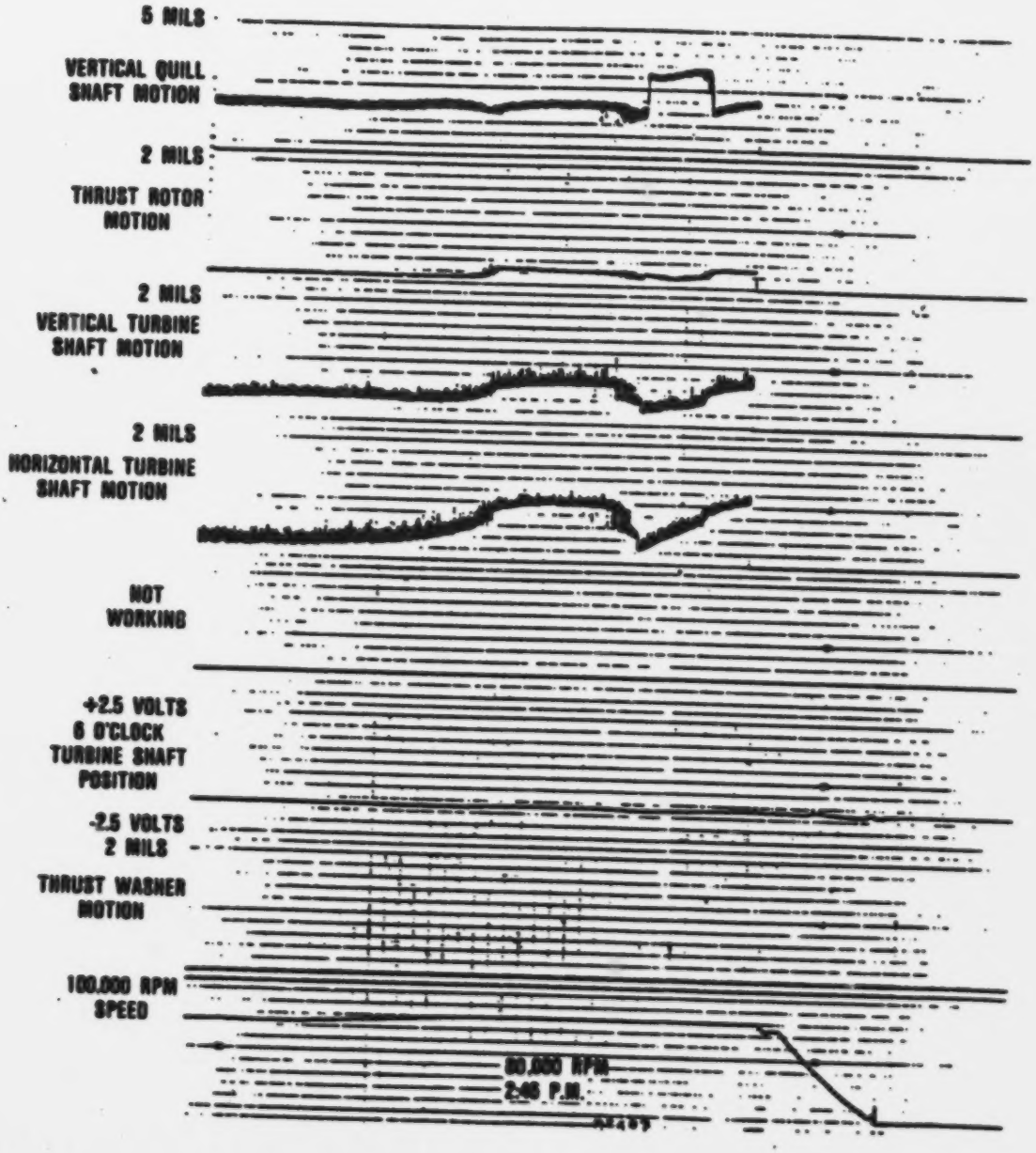

Figure 11. Engine S/N 001, Build 2B Speed Limiting Shaft Excursions.

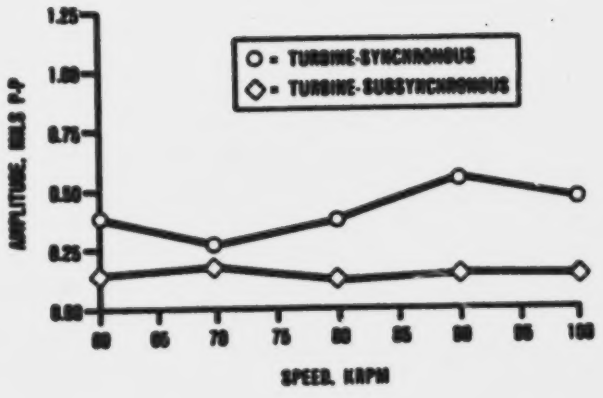

Figure 12. Engine S/N 001 Build 21 Rotor Vibration.

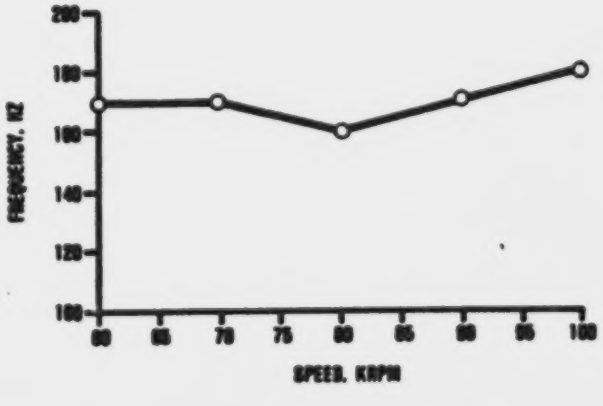

Figure 13. Engine S/N 001 Build 21 Rotor Subsynchronous Frequency.

speed approached 80,000 rpm. Figures 14 and 15 show turbine synchronous and subsynchronous vibration characteristics versus speed. A minor build error that produced a much smaller ball bearing preload was discovered. This situation was corrected but the engine ran with no change from earlier testing. Based on Build 22 results, the decision was made to repeat the Build 21 configuration.

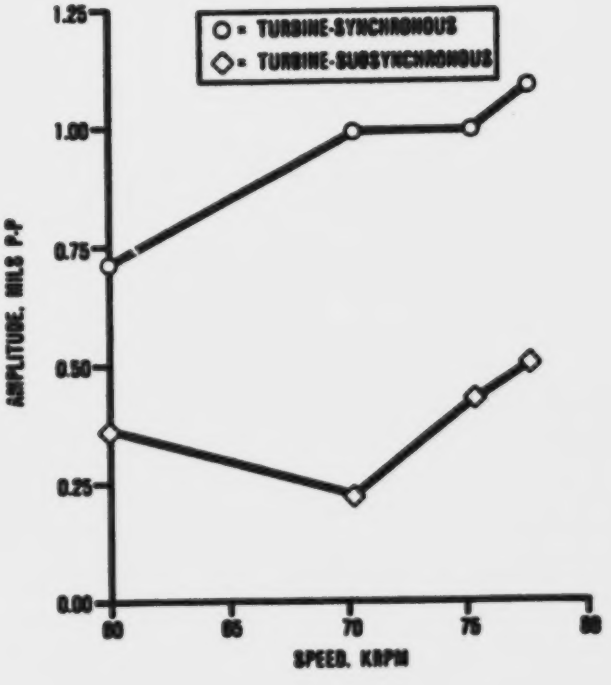

Figure 14. Engine S/N 001 Build 22 Rotor Vibration.

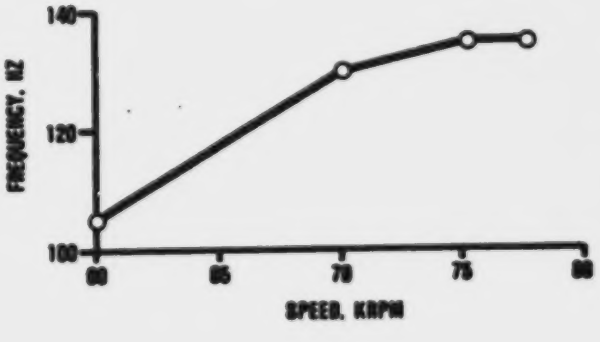

Figure 15. Engine S/N 001 Build 22 Rotor Subsynchronous Frequency.

Build 23: The thrust bearing configuration was modified to match, as closely as practical, that of Build 21. The original Build 21 thrust bearing configuration was used, the spline

spacer was replated with copper to the same thickness as Build 21, and all the Build 21 clearance dimensions were used. Rotor dynamic behavior was very similar to that observed on the Build 21 tests, showing significant improvement over Build 22. The engine was operated to 100-percent speed with acceptable synchronous vibration and insignificant subsynchronous vibration, as shown in Figures 16 and 17. Ball bearing preload was reduced from 20 pounds to less than 5 pounds to determine its effect on engine rotor dynamics. No change was evident.

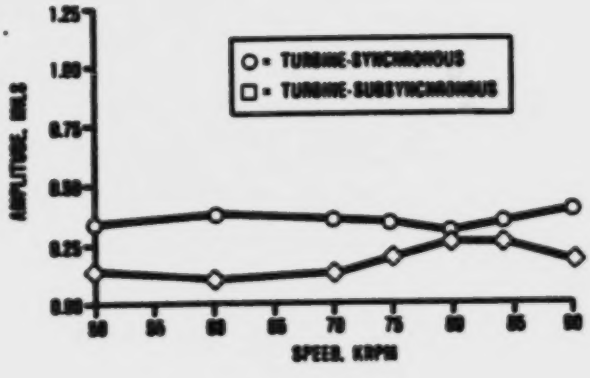

Figure 16. S/N 001 Build 23 Rotor Vibration.

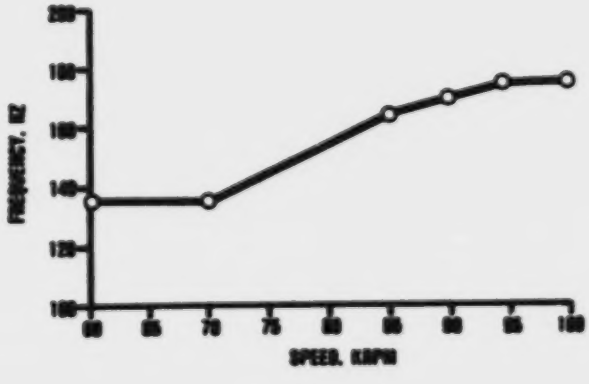

Figure 17. S/N 001 Build 23 Rotor Subsynchronous Frequency.

Build 24: A ceramic turbine rotor was built into this engine to determine the effects on rotor dyanamics behavior (Figure 18). The engine was assembled in the Build 23 configuration. The old quill shaft/splined spacer set was replaced with a new set, the splined spacer being appropriately copper plated. The engine was motored to 16,000 rpm before being shut down due to high synchronous vibration. The problem was traced to the quill shaft and the interference fit with the splined spacer. During assembly, the quill shaft rigidly cocked relative to the splined spacer, causing large driven response in the rotor as the engine was motored.

Build 25: The large excursions from Build 24 damaged the foil bearing, making replacement necessary. The quill shaft/splined spacer set was replaced with the newly plated set from Build 23. The engine ran with rotor dynamic characteristics similar to those of Builds 21 and 23 up to 97,300 rpm. At that speed the ceramic rotor failed. Figures 19 and 20 describe the synchronous and subsynchronous rotor excursions for this run. Investigations are underway to determine the failure mode.

3.2 Engine S/N 002C

Build 1: Preparations continued for Build 1 of the 2100F ceramic structures engine. Changes in the test plan were made to incorporate additional supporting instrumentation and visual readout to aid the test engineer. Various engine safety parameters, such as maximum speed and automatic overspeed shutdown by the electronic control unit (ECU), were modified to better suit the test activities.

Figure 21 depicts a revised start transient cycle selected after re-evaluation of the ceramic component stress levels during start. The revised schedule accommodates a 20-percent stress margin below the level of exposure seen in the ceramic structures rig (Reference 8). The ECU was modified to implement the thermal ramp cycle.

The assembly of engine S/N 002C is depicted in Figures 22 through 28. Assembly of the

ORIGINAL PAGE IS
OF POOR QUALITY

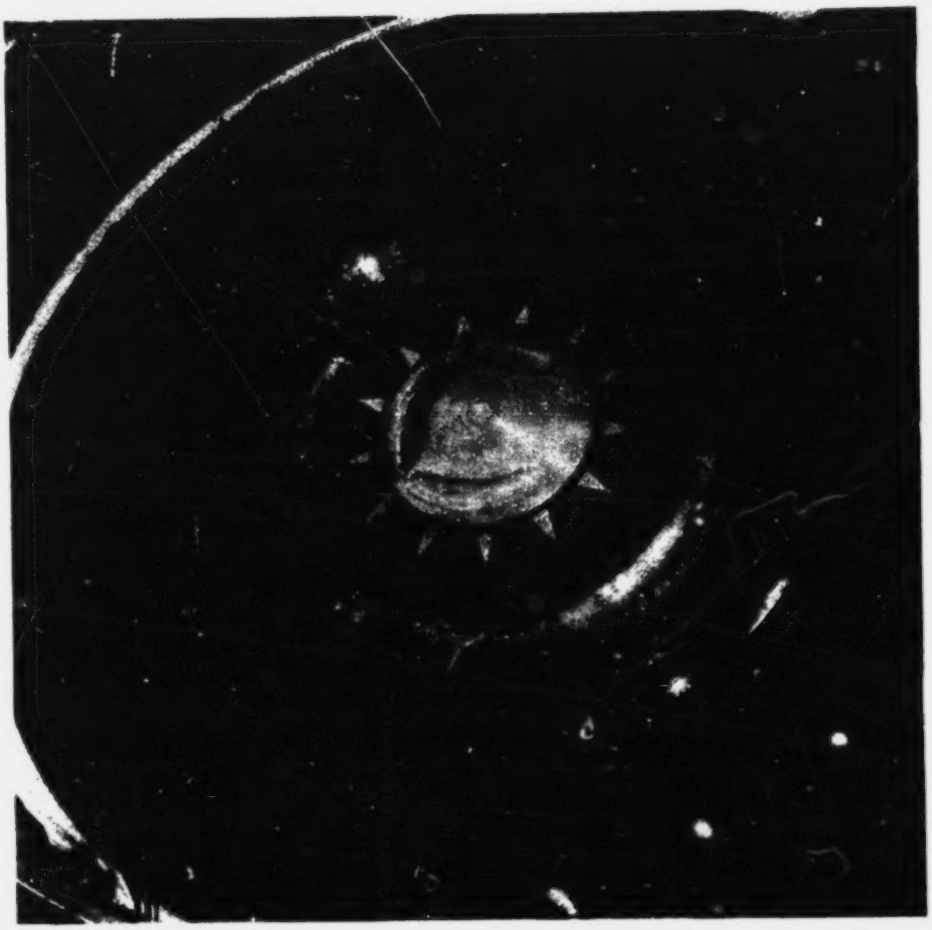

Figure 18. Ceramic Rotor in Metal Engine, Build 24.

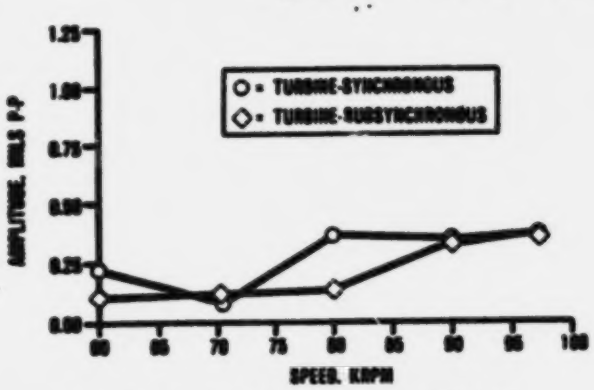

Figure 19. Engine S/N 001, Build 25 Rotor Vibration.

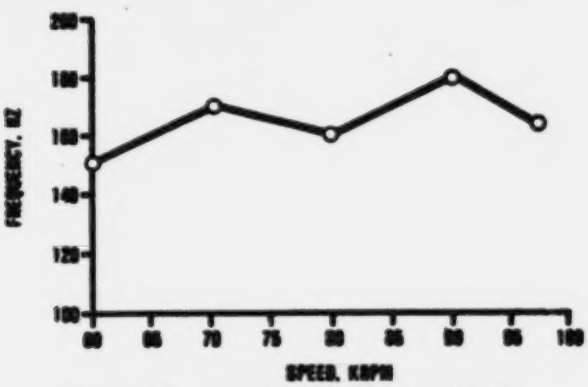

Figure 20. Engine S/N 001, Build 25 Subsynchronous Frequency.

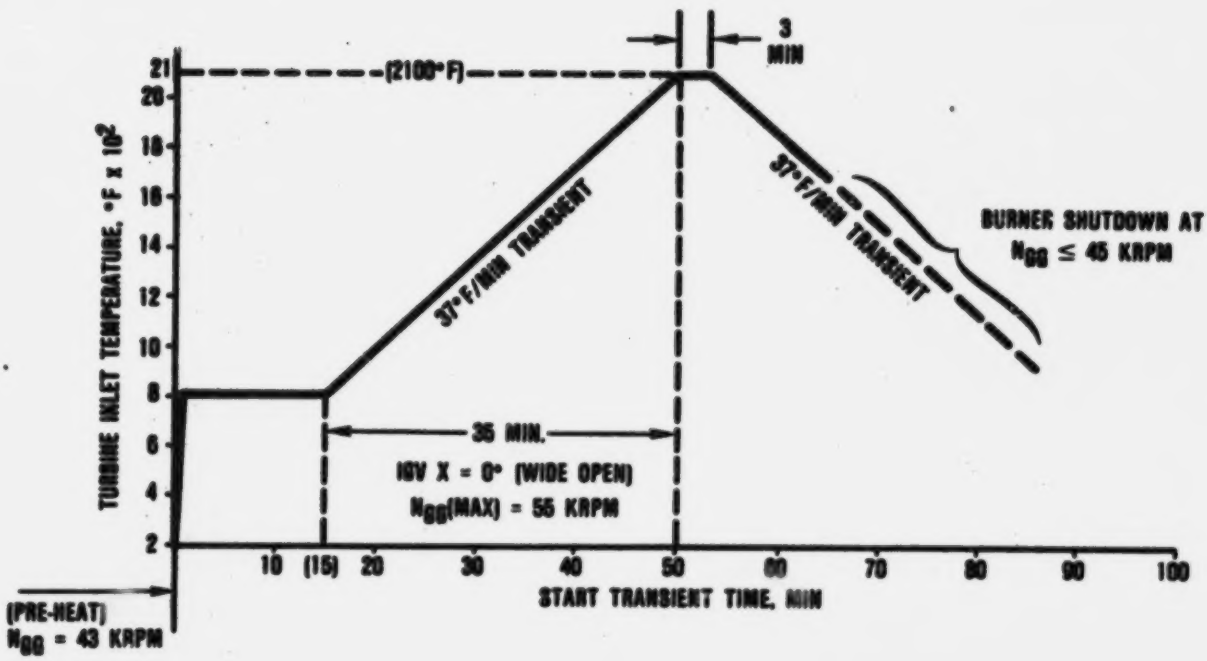

Figure 21. Revised Start Transient Cycle for First Ceramic Engine.

ceramic turbine shroud module starts with the compressor backshroud followed by ceramic insulation (Figure 22), then the spacer assembly, inner diffuser housing, rocker assembly, outer diffuser housing, turbine shroud, and ceramic bolt assembly are installed, completing the shroud module subassembly (Figure 23). The module is then installed in the engine outer case (compressor housing) and the dual alloy turbine rotor is installed (Figure 24). Figures 25 through 28 depict the remainder of the assembly. Following assembly the engine was installed in the test cell.

After several motoring runs and aborted starts, a partial teardown was conducted to inspect the ceramic hardware. No evidence of deterioration was noted. The engine was reassembled and testing continued.

Engine S/N 002C was successfully tested on February 16, 1984, through one thermal cycle to a TIT of 2100F and an engine speed of 55,000 rpm. Figure 29 depicts the actual cycle, showing a peak temperature of 2100F for approximately 5 minutes.

During the initial test, the starter was engaged throughout the run to assist in loading the engine as temperature was ramped to 2100F. At approximately 1700F, appearances were given that the engine would self-sustain. However, no attempt was made to drop the starter out during this initial cycle.

Engine disassembly and inspection revealed no ceramic component damage. Subsequent nondestructive evaluation (NDE) further substantiated the successful run with no indications of cracking or interface damage. The components were returned to the assembly area for further testing.

Build 3. Build 3 of S/N 002C was completed using the same hardware. The engine was installed in the test cell and several modifica-

ORIGINAL PAGE IS
OF POOR QUALITY

Figure 22. Ceramic Engine Assembly in Process.

Figure 23. Ceramic Turbine Shroud Module Assembled.

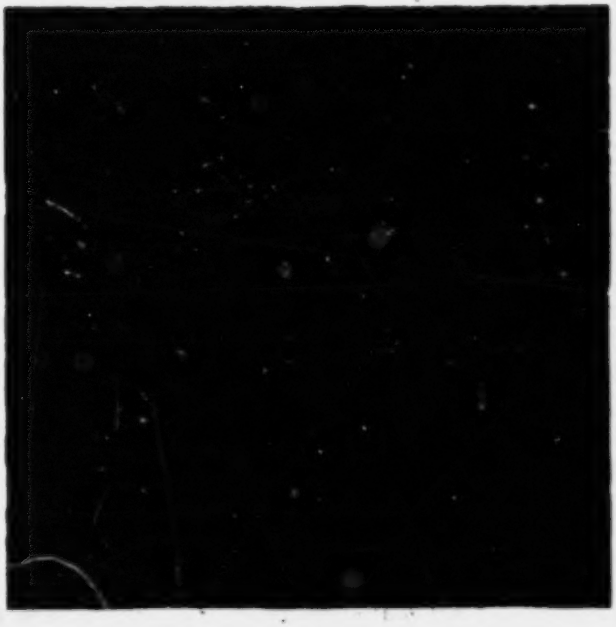

Figure 24. Module Installed in Compressor Housing.

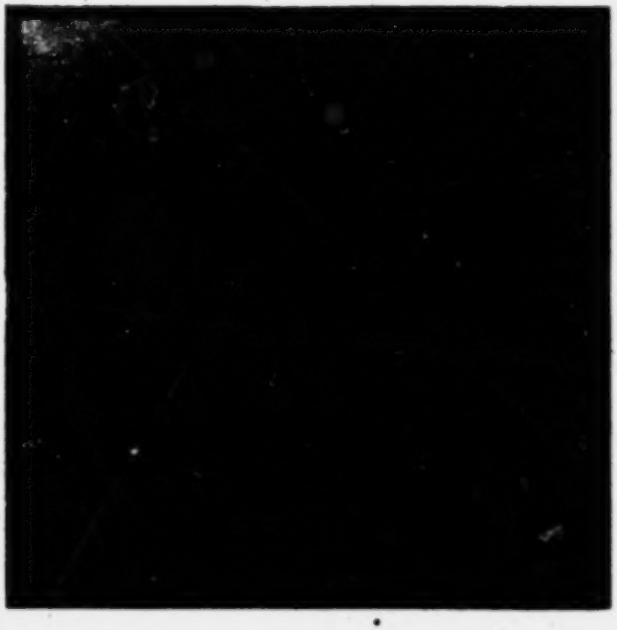

Figure 25. Back Shroud Installed.

ORIGINAL PAGE IS
OF POOR QUALITY

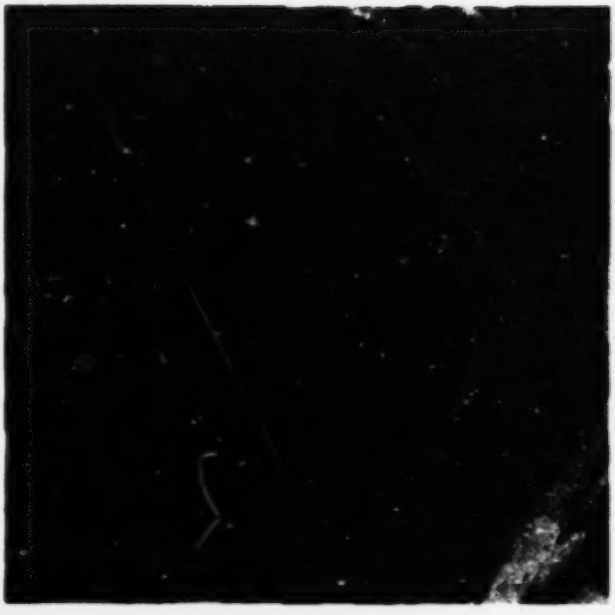

Figure 26. Combustor Baffle Installed.

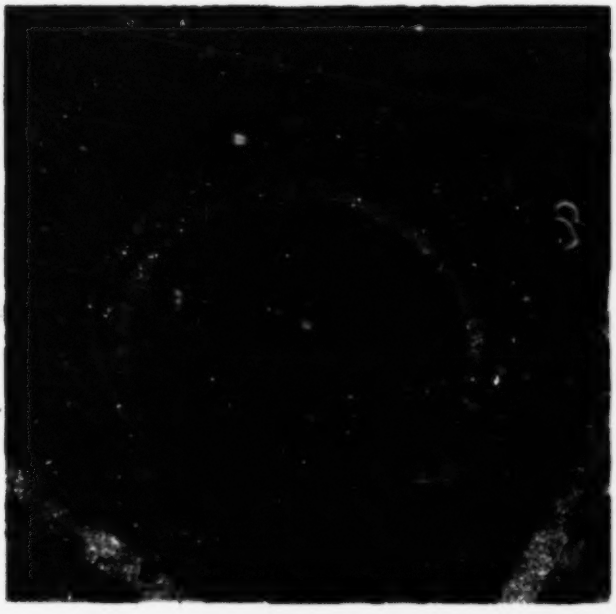

Figure 27. Transition Duct Installed.

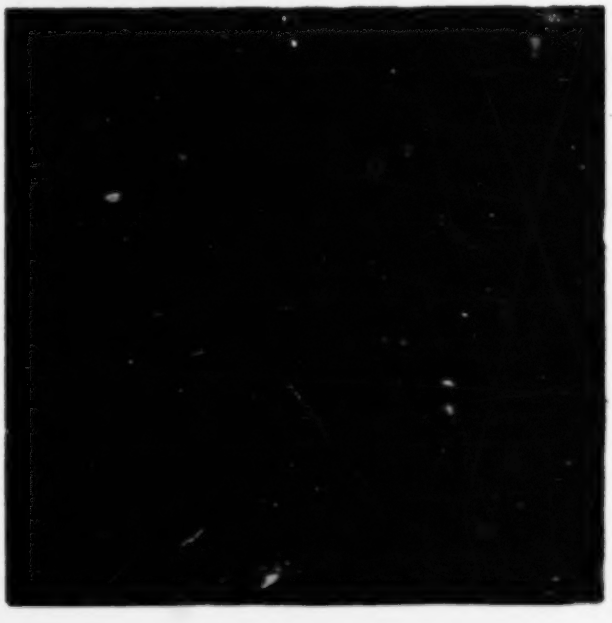

Figure 28. Flow Separator Housing and Regenerator Shield Installed.

tions were made to the ECU and supporting equipment based on Cycle 1 data. The objective of this second test was to complete 10 thermal cycles similar to Cycle 1. During the first of the 10 cycles, starter assist was dropped out of the system at an indicated self-sustaining temperature of approximately 1700F; the unit oversped to 80,000 rpm and shut down. This indicated that indeed a self-sustaining engine condition had been reached. Several additional attempts to maintain speed control without starter drag were made, but the engine was very sensitive to small increases or decreases in load. It was decided to maintain starter engagement throughout the cycles. Testing was completed with no acoustic events noted throughout the 10 cycles.

Engine teardown was completed on April 13, 1984. All major ceramic components survived 10 thermal cycles with only minor damage. The following observations were made:

- The flow separator housing was chipped in an area of a previously repaired chip

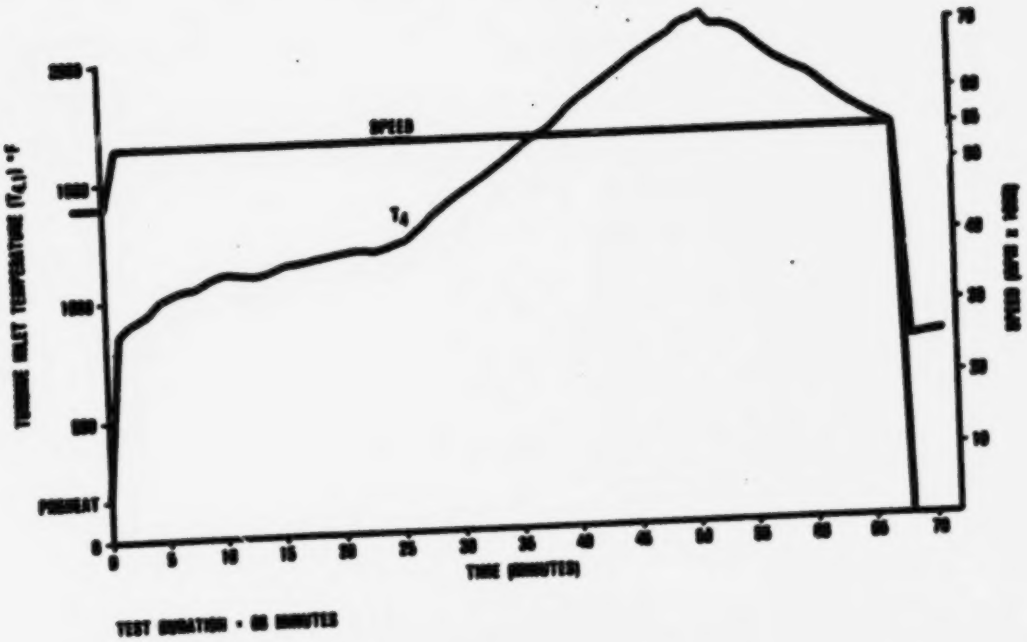

Figure 29. S/N 002C - T4 Schedule Tested on February 16, 1984.

- Four stators were chipped at contact stress locations
- All ceramic bolts were loading in the fillet against the radius on the crowned spacers—(not design intent)—no resultant damage was observed
- The foil bearing assembly was in good condition with no abnormal wear pattern
- No evidence of turbine rotor rubs was noted on the turbine shroud or backshroud

Engine S/N 002C has accumulated 14.7 hours with 25 starts. These hours represent 11 start transient thermal cycles on the same set of ceramic structures.

Build 4. Build 4 was completed utilizing a second set of ceramic structures (Build 10, Structures Rig, Reference 8). The engine was installed in test cell C-102 on May 1, 1984.

During the first thermal cycle of a projected 10-cycle test series, a turbine rub was encountered at approximately 1600F TIT, 55,000 rpm, and 38 minutes into the test. Testing was aborted and the engine was removed for disassembly. At the time of rub, the major events recorded by the acoustic emissions equipment monitoring the test did not indicate a response signature detrimental to the ceramic structure.

Engine teardown was completed on May 2, 1984, and inspection revealed the following:

- A heavy turbine wheel rub with the ceramic turbine backshroud was incurred (See Figure 30).
- Metal "shavings" from the turbine rotor backface were deposited on the ceramic turbine backshroud (Figure 31)
- The ceramic turbine shroud was radially rubbed by the metallic turbine rotor; no significant damage was evident (Figure 32)
- A ceramic combustor baffle support leg was the only ceramic part found chipped (Figure 33)

ORIGINAL PAGE IS
OF POOR QUALITY

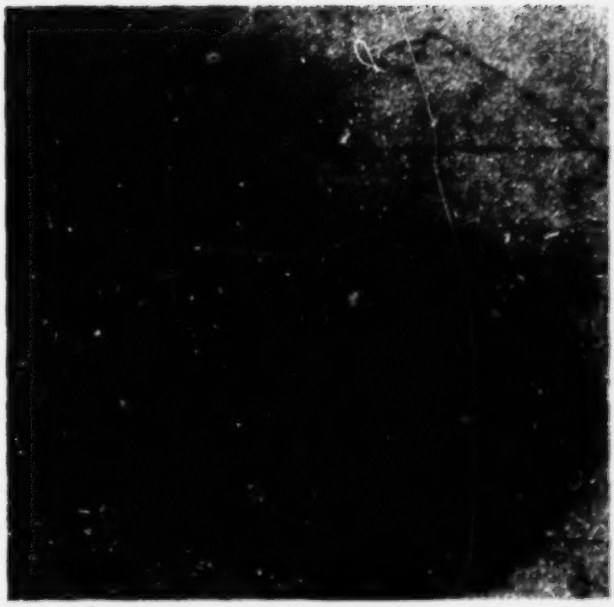

Figure 30. Turbine Rotor/Backshroud Rub.

Figure 31. Turbine Rotor Backface Metal Shavings Deposited on Turbine Backshroud.

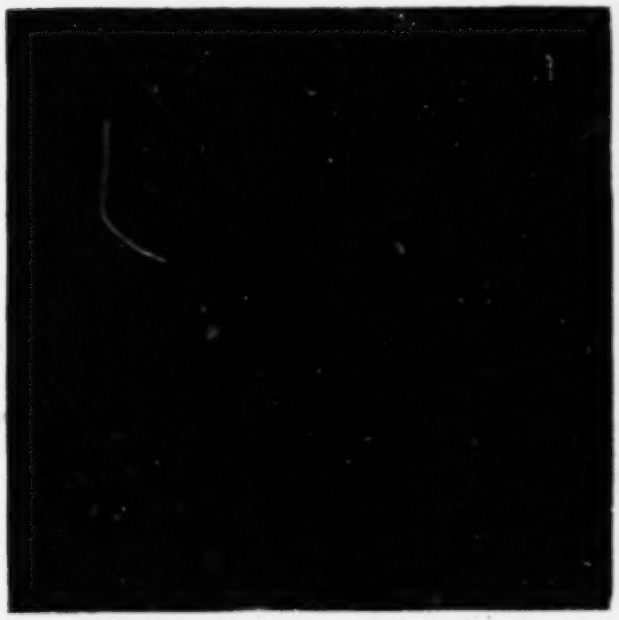

Figure 32. Turbine Shroud Shows Radial Rub from Turbine Rotor.

Figure 33. Chipped Ceramic Combustor Baffle Support Leg.

- The turbine rotor can be reused after resurfacing the foil bearing journal area, hand finishing the rub area, and rebalancing

- The turbine backshroud and turbine shroud can be recontoured, heat treated, and reused

The primary cause of failure was insufficient turbine backface rotor-to-turbine backshroud clearance. Dimensions on the turbine backshroud were rechecked against the Build 3 backshroud, and a local contour discrepancy was found.

Total engine run time to date is 15.5 hours, 27 starts.

Build 5: The engine was reconfigured with the new oil film thrust bearing and an updated foil bearing assembly for achieving stable rotor dynamics throughout the operating speed range. (See Sections 3.1 and 3.3) The test plan was revised to include a full-speed run to 2100F for 5 minutes. Following assembly and installation, testing was initiated on Build 5.

The engine proceeded routinely through the first thermal cycle at 1840F on an increasing temperature ramp until an electrical problem caused a premature shutdown. Subsequently, a motoring run was initiated to cool the engine down to enable a restart, but the foil bearing failed while accelerating to idle speed.

A complete foil bearing failure, with a light turbine rub on the ceramic turbine shroud, was evident at teardown. No ceramic hardware was damaged as a result of the test. The surface of the turbine journal in the foil bearing area was highly distressed and requires resurfacing prior to use in subsequent builds. The Wayne-Kerr probes were damaged by the rotor journal and also require resurfacing or replacement. No foil bearing carrier damage or compressor rub was evident in the teardown.

Total engine run time to date is 16.25 hours, 28 starts.

3.3 Engine S/N 003

Using engine S/N 003 as a rotor dynamic test bed, a great deal of progress was made to isolate the source of instability and develop solutions to this recurring problem. A unique test setup allowing cold motoring of the rotor in the engine made it possible to isolate aerodynamic effects. These effects, emanating from the bladed components, are the primary cause of the subsynchronous motion described in References 5-8.

Another dramatic effect was made on instability with the regenerator drive mechanism. Full speed operation of S/N 003 was achieved several times by manipulating the regenerator core speed to suppress subsynchronous amplitude.

By incorporating the hydrodynamic thrust bearing in engine S/N 001, subsynchronous whirl was completely suppressed (Section 3.1). Engine S/N 003 was used to develop alternative solutions. Damper mechanisms at the foil bearing were tried but did not develop into viable solutions. High preload foil bearings showed significant improvements and will continue to be developed to stabilize the rotor system. The following sections describe engine S/N 003 activities during this reporting period.

3.3.1 Foil Bearing Environment/Thermal Test

A new foil bearing thermal isolation support structure has been incorporated into the engine (Figure 34). Similar to S/N 001, the environment and structures around the foil bearing were extensively instrumented to monitor possible distortions in the foil bearing that may correlate with rotor dynamic problems. Once the engine reached thermal equilibrium, testing showed that foil bearing distortion was minimal.

Additional testing included varying engine conditions such as inlet guide vane (IGV) position (open to full closed), engine load on the output shaft (0 to 200 in-lb), foil bearing and shaft bore cooling flows (on and off), and the

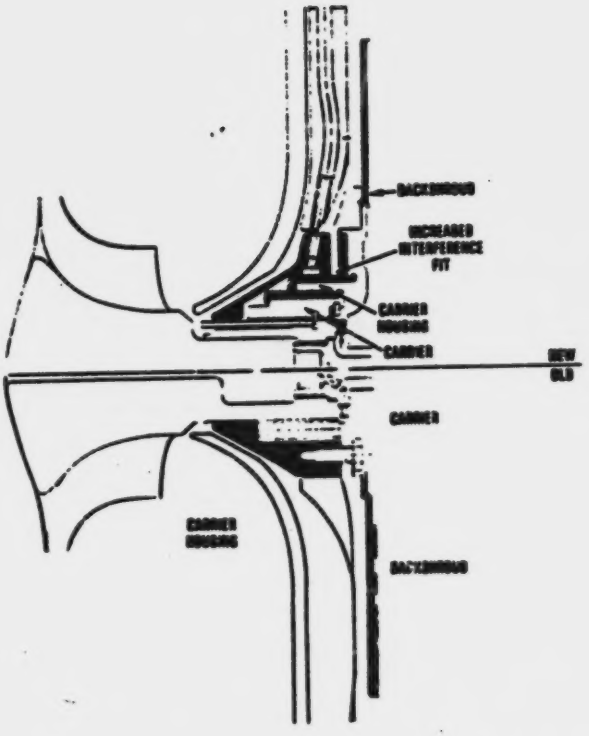

Figure 34. Comparison of Old and New Foil Bearing Housing Design.

fuel control (changed from pulse-width-modulated to a gear pump type). The effects of these parameters on rotor dynamics were negligible.

3.3.2 Compressor Backface Smoothing

The new foil bearing housing and mounting bolts (Figure 35) increased flow disturbances on the compressor backface (foil bearing cooling flow). In an effort to smooth this area, the bolts were changed to countersunk screws with a bolt shroud to submerse the screw heads and fill in the pockets around the local flange taps on the new foil bearing housing. These changes, implemented on Builds 40 and 41 (see Figure 35) did suppress the subsynchronous whirl to some extent as the engine achieved 10,000 rpm higher speed.

3.3.3 Increased Foil Bearing Stiffness

The foil and spring thicknesses were increased to increase foil bearing stiffness. The "6+1" (0.006-inch thick foil substrate-plus-0.001-inch thick coating) foil bearing increased the spring rate of the "5+1" foil bearing from 1800 to 2800 lb-in. This configuration achieved nearly 89,000 rpm before a

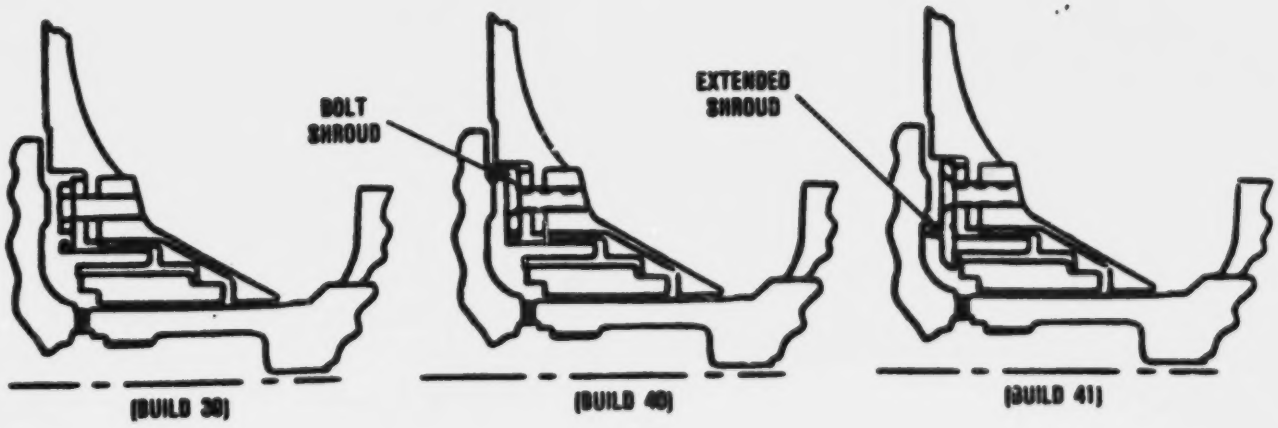

Figure 35. Compressor Backface Configurations.

ORIGINAL PAGE IS
OF POOR QUALITY

sudden increase in synchronous motion caused an engine shutdown. This synchronous motion increase was thought to be caused by a shift in quill shaft eccentricity due to the loose fit in the splined shaft.

3.3.4 Ball Bearing Area Configuration Changes

This test was conducted to determine the effects on rotor dynamics resulting from of changes made in the ball bearing area. These changes included replacing the aluminum inlet housing with steel, copper plating the splined spacer, decreasing the oil mount diametral clearance, and replacing the ball bearing (Build 45).

Testing was initiated without the engine loader installed and bore cooling flow on. After 10 minutes at idle the bore cooling flow was turned off. The engine was accelerated to 87,000 rpm at which time the synchronous and subsynchronous motion exceeded the 1-mil limit. Regenerator speed was set at 18 rpm. Speed was varied from 12 to 22.5 rpm and the subsynchronous amplitude changed dramatically. Another engine acceleration was made to 95,700 rpm, where the synchronous motion reached 1.29 mils p-p, and the engine decelerated. With the engine operating at 75,700 rpm the effect of regenerator speed was investigated; subsynchronous amplitude decreased from 1.32 to 0.49 mils as regenerator speed was changed from 14 to 13 rpm.

Later, the engine was accelerated five times from 85,000 to 100,000 rpm, the first four times for a 10-second duration and the last time for a 10-minute duration. In this speed range, the optimum regenerator speed was 14.5 rpm. The engine was loaded (IGVs set at 12-percent and bore cooling off) with no detrimental effect on rotor dynamics.

3.3.5 Initial Engine Motoring Tests

A series of motoring tests was completed during this reporting period. The objective of these tests was to isolate the sources of destabilizing energy causing unstable rotor motion. The configurations tested are shown in Figure 36. The baseline configuration is the

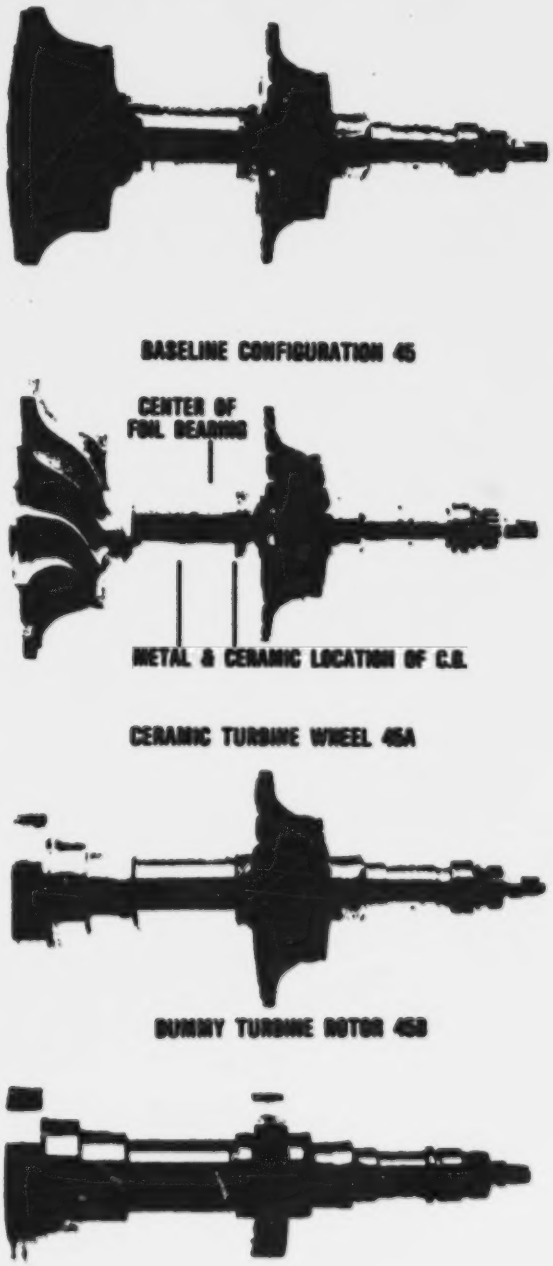
BASELINE CONFIGURATION 45
CENTER OF FOIL BEARING
METAL & CERAMIC LOCATION OF C.G.
CERAMIC TURBINE WHEEL 45A
DUMMY TURBINE ROTOR 45B
DYNAMIC RIG ROTOR 45C

Figure 36. Motoring Test Configurations.

configuration that was tested to full speed (100,000 rpm) in the engine as discussed in Section 3.3.4 (Build 45). The engine was transferred to the Foil Bearing Laboratory and an air turbine starter (ATS) was coupled to the output shaft. This essentially completed the motoring setup shown in Figure 37. The only additional setup was a lubrication system for the ATS and engine gearbox.

To isolate aerodynamic energy, the bladed components were replaced with nonbladed rotating discs like those used for the rotor dynamic rig. The turbine wheel was replaced with the dummy turbine rotor in Build 45B, and the impeller was replaced with the dummy compressor in Build 45C.

An acceleration was accomplished to the maximum speed within the vibration limits with these rotors installed in the engine. The results are summarized in Figure 38, with subsynchronous amplitude plotted versus rotor speed. The data also are tabulated in Table 3.

The results show that the baseline rotor could not be run at speeds greater than 80,000 rpm without exceeding the 1-mil vibration limit. Some of the reasons why this baseline run was worse than the hot engine run of identical configuration are:

- The operating sway space was somewhat larger in the motoring test than in the self-sustained engine run because the turbine wheel (including the journal on which the foil bearing runs) was significantly cooler
- The air densities and aerodynamic effects are affected by the addition of combustor heat
- The rotor is being driven through the gearbox instead of producing power to the output shaft

The subsynchronous amplitude was significantly reduced when the bladed rotor was replaced with the dummy turbine wheel (Figure 36, Build 45B). This test was terminated because of test equipment failure, not rotor dynamics. The amplitude became virtually insignificant when the bladed impeller also was replaced with a dummy (Figure 36, Build 45C).

This test and the resulting data show that the primary source of destabilizing energy is the aerodynamic effects induced by the bladed components.

As evidenced in engine S/N 001 (Build 21), additional damping can be added to the system to sufficiently suppress this energy. This approach is supported by a recent technical article (Reference 9).

3.3.6 Compensated Engine Motoring Test

The purpose of these tests was to determine what rotor dynamic improvements can be made by adding damping at the foil bearing. Both high preload foil bearings and additional damper mechanisms were tried to improve dynamics. The various bearing preloads (stated in terms of breakaway torque) are summarized in Figure 39 as a function of sway space. Bearing characteristics are summarized in Table 4. The sway space of the bearings tested was kept at 6 mils to provide consistent comparisons with the baseline bearing.

Bearing Preload - The changes to increase preload in the foil bearing proved more successful in increasing the damping (or decreasing the subsynchronous amplitude). The amplitude is plotted in Figure 40. The "7+1" design (increasing the foil substrate thickness by 1 mil) showed a minor improvement, and the improved "6+1" bearing (increasing the backing spring preform radius from 0.9 to 1.1 inches) showed a significant suppression of the subsynchronous whirl amplitude. The most effective improvement was the longer "6+1" axial bearing (incorporating the spring radius change), which achieved 87,000 rpm with excessive synchronous motion (the subsynchronous motion was still well within the 1-mil limit).

Teardown of this engine revealed a severely damaged bearing in the gearbox and a slightly pitted bearing on the rotor. These

ORIGINAL PAGE IS
OF POOR QUALITY

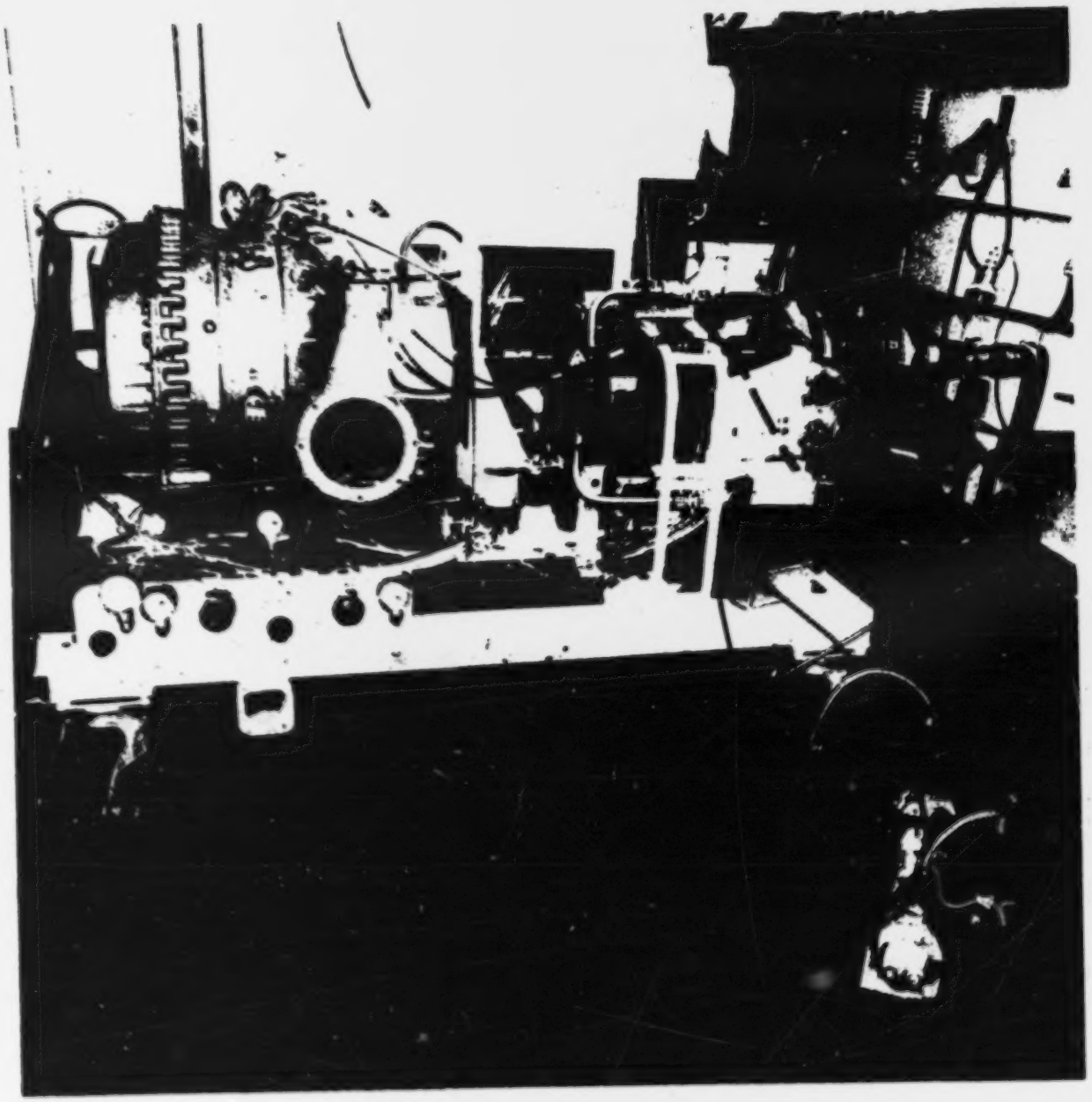

Figure 37. Motoring Set Up in Foil Bearing Lab of Engine S/N 003.

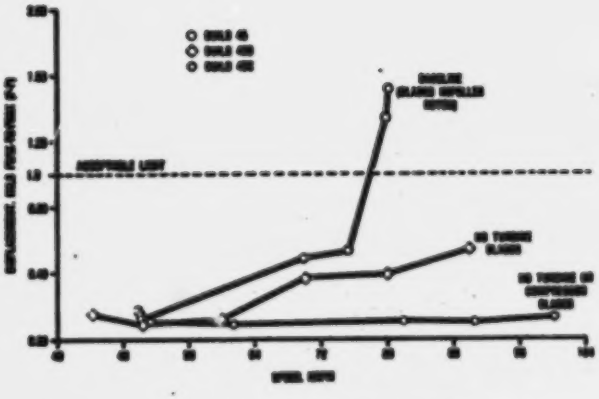

Figure 38. S/N 003 Motoring Test - Subsynchronous Motion.

parts will be replaced and the test repeated to see if this configuration can be run to full speed.

Dampers - The dampers tested were the metal mesh and coated foils. These two bearing-damper combinations are shown in Figure 41, along with the baseline and the longer axial foil bearing.

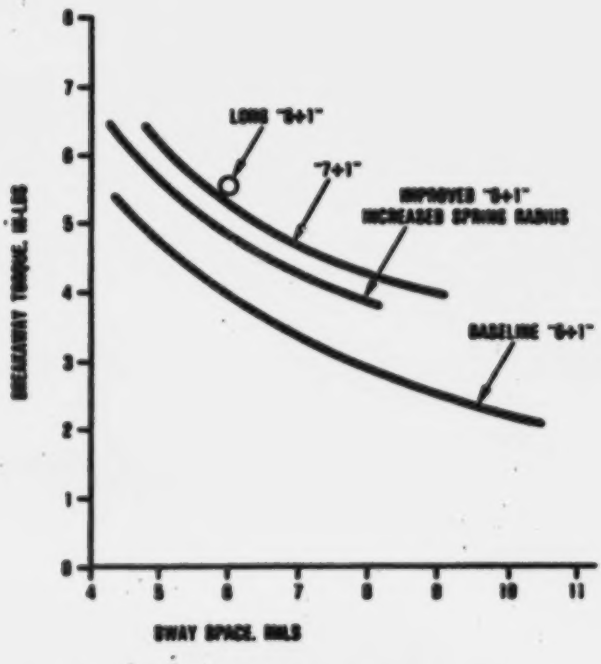

Figure 39. Breakaway Torque Versus Sway Space for Different Foil Bearings.

Table 2. S/N 003 Motoring Test Summary

Test Date	Build No.	Compressor	Turbine	Foil Bearing	Speed, rpm	Turbine Motion Frequency, Hz	Turbine Motion Amplitude, mils	Quill Shaft Motion Frequency, Hz	Quill Shaft Motion Amplitude, mils	Comments
5-3	45	Ti Wheel	Actroloy	6+1	80,000	100(A) 1235(H)	1.5 0.8	1235	1.7	Baseline
5-10	45A	Ti Wheel	Ceramic	6+1	90,000	170(A) 1500(H)	1.0 1.5	1500	1.5	0.9-mil runout on ceramic rotor sleeve
5-14	45B	Ti Wheel	Dummy Metal	6+1	90,000	105(A) 1500(H)	0.5 0.7	1500	1.5	ATB failed at 90,000 rpm
5-25	45C	Dummy	Dummy Metal	6+1	100,000	125(A) 1670(H)	0.1 0.8	1670	2.6	
5-31 and 6-6	45C	Dummy Metal	Dummy	6+1	100,000	110(A) 1005(H)	0.3 0.4	1005	0.7	Regenerator speed effect (response at 15-20 rpm)

(A) Subsynchronous
(H) Synchronous

ORIGINAL PAGE IS
OF POOR QUALITY

Table 4. AGT101 Foil Bearing Characteristics Summary

Nomenclature	Length, inch	Foil Radius, inch	Backing Spring Radius, inch	Foil Thickness
Baseline "8+1"	1.07	1.125	0.90	0.006 inch substrate (+) 0.001 inch coating
Improved "8+1"	1.07	1.125	1.10	0.006 inch substrate (+) 0.001 inch coating
Long "8+1"	1.40	1.125	0.90	0.006 inch substrate (+) 0.001 inch coating
"7+1"	1.07	1.125	0.90	0.007 inch substrate (+) 0.001 inch coating

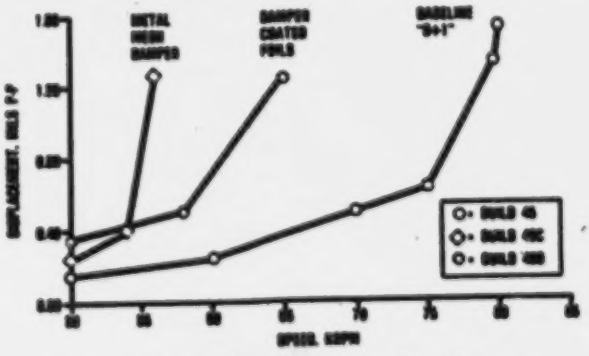

Figure 40. S/N 003 Motoring Tests – Subsynchronous Motion.

Figure 41. Alternative Bearings Tested.

Table 5 summarizes the results.

The rotor dynamic improvements can best be portrayed by plotting subsynchronous whirl amplitude versus engine speed. Figure 42 is a plot of this parameter. That the dynamics of the metal mesh and foil coating dampers are not as good as those of the baseline becomes obvious. The probable reasons for this deterioration in dynamic behavior are:

- Metal Mesh Damper – Since this concept adds a spring in series with the foil bearing, the net bearing stiffness decreases compared to the baseline. The static spring rate decreased 25 percent and the first critical frequency (an indicator of dynamic stiffness) decreased from 120 to 80 Hz. Since rotor amplitude is greatly affected over this frequency range, further development of this concept would require raising the dynamic stiffness. Based on the results, however, this development is not warranted at this time.

- Damper Coating Foils – The flame spray on the back (convex) surface of the foils significantly increases foil-to-foil friction. This increase in friction may have been excessive and prevented sufficient sliding

Table I. S/N 002 Motoring Test Summary

Test Date 1965	Build No.	Compressor	Turbine	Foil Bearing	Speed, rpm	Turbine Motion Frequency, Hz	Turbine Motion Amplitude, mils	Quill Shaft Motion Frequency, Hz	Quill Shaft Motion Amplitude, mils	Comments
8-7, 8-8	45	Ti Wheel (Spring Radius 1.1)	Astroloy	6+1	90,000	225(A) 1265(S)	1.8 1.8	1260	2.1	Negligible effect with symmetrical joint
8-12	45A	Ti Wheel	Astroloy	7+1	94,000	230(A) 1480(S)	1.1 0.9	1480	1.8	
8-13	45B	Ti Wheel	Astroloy	7+1	91,000	230(A) 1260(S)	1.1 1.8	1250	1.3	New quill notched not without copper plating
8-19	45C	Ti Wheel	Astroloy	6+1	88,000	85(A) 920(S)	1.2 0.4	920	0.5	Metal mesh damper and foil bearing
8-21	45D	Ti Wheel	Astroloy	6+1	85,000	115(A) 1265(S)	1.2 0.8	1265	0.6	With damper coating on foils
8-22	45E	Ti Wheel	Astroloy	6+1	89,000	180(A) 1235(S)	1.3 0.8	1235	2.1	Repeat of baseline Build 45, Tested 8-2-65
8-28	45F	Ti Wheel	Astroloy	Long 6+1	87,000	125(A) 1420(S)	0.6 1.5			

(A) Subsynchronous
(S) Synchronous

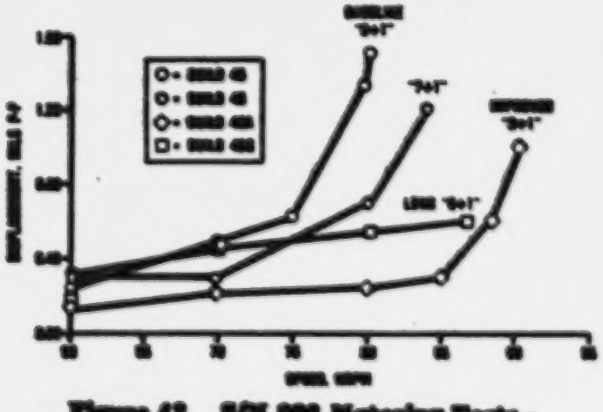

Figure 42. S/N 002 Motoring Tests - Subsynchronous Whirl Amplitude.

motion to allow the foils to follow the radial motion of the shaft.

3.3.7 Ceramic Turbine Wheel Motoring Test

The ceramic turbine wheel was installed in place of the metal (Astroloy) wheel and designated Build 45A (see Figure 36). This rotor configuration was run to 92,000 rpm before the subsynchronous amplitude reached 1 mil compared to 80,000 rpm for the baseline. With half the mass in this ceramic wheel (versus the Astroloy wheel), not only was the gravity load on the foil bearing reduced, but more importantly, the undesirable overhung mass was reduced. The center of gravity was moved from 0.78 inch on the turbine side (metal wheel) to 0.15 inch on the compressor side (ceramic wheel) relative to the foil bearing center.

This significant change was tested to determine the effect on rotor dynamics. The results are plotted in Figure 43 and show somewhat improved dynamics (lower amplitude of the subsynchronous motion). However, the change from the metal to the ceramic turbine wheel is not sufficient to eliminate all instabilities.

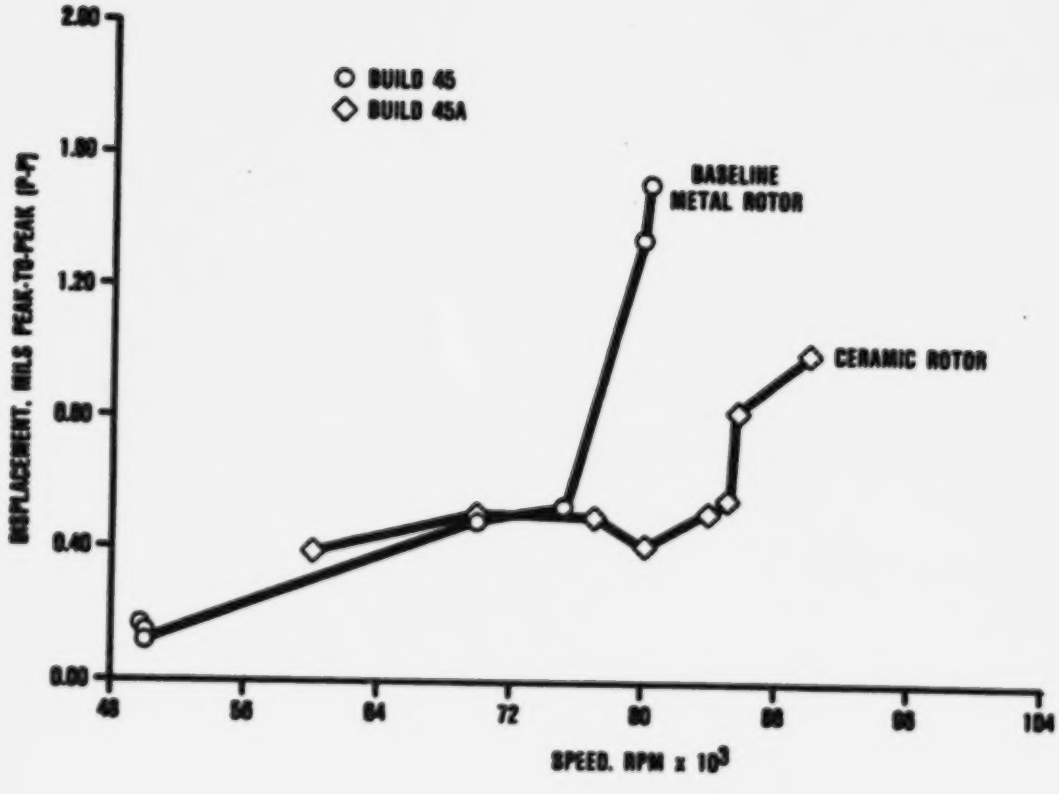

Figure 43. Ceramic Turbine Wheel Compared to Baseline - Motoring Test.

4.0 COMPONENT/SUBSYSTEM DEVELOPMENT

Component/subsystem development activities during this reporting period concentrated on supporting AGT101 1600F engine testing, ceramic development, combustion nozzle tests, and hot regenerator testing. Figure 44 shows the performance rating stations for the AGT101 engine and components.

The following sections discuss major efforts and accomplishments during the reporting period for each component subsystem.

4.1 Compressor Development

No activity during this reporting period.

4.2 Turbine Development

No activity during this reporting period.

4.3 Combustion

4.3.1 Diffusion Flame (DF) Combustor

4.3.1.1 Combustor Rig Performance Check

Test development continued on the DF metal for the 2100F rated engine. The lean blowout limits were established as a function of engine load. These data are shown in Figure 45, which depicts the lean blowout fuel/air ratio as a function of load. The fuel atomization air output pressure drop was maintained at 4 psid for these tests.

During testing, a problem area in the DF fuel nozzle design was noted. Due to the higher thermal environment, nozzle plugging was encountered. To overcome this problem,

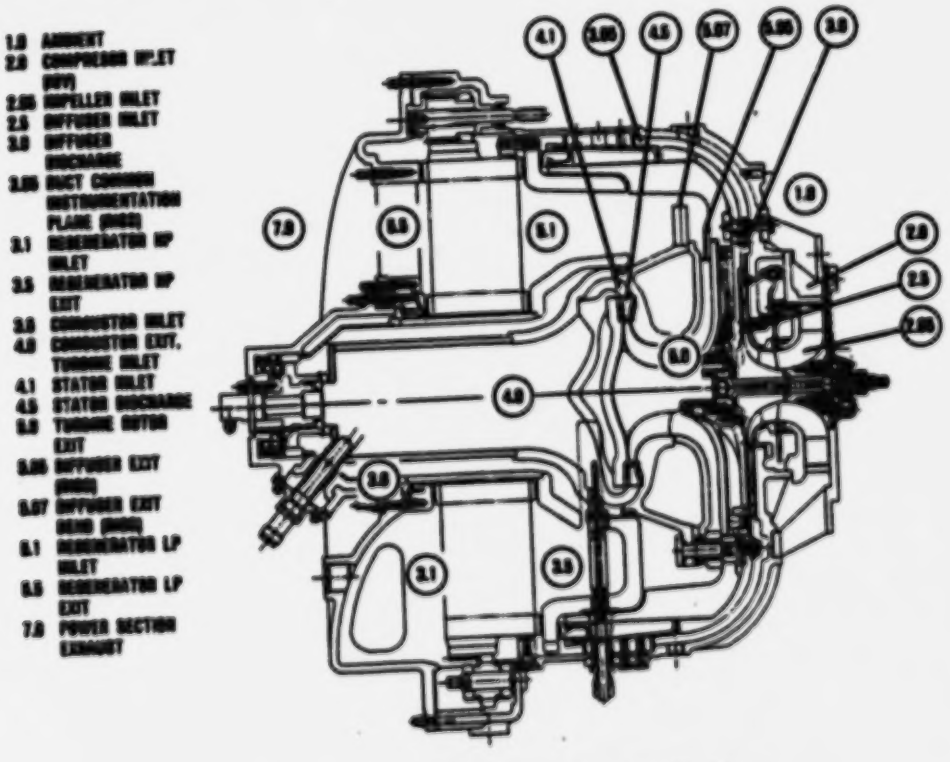

Figure 44. Performance Rating Stations.

PRECEDING PAGE BLANK NOT FILMED

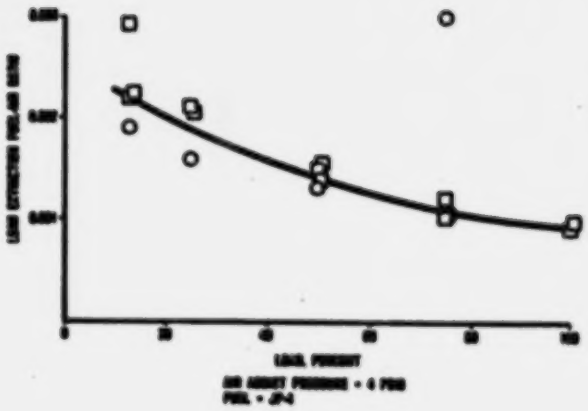

Figure 45. AGT101 (2100F) Nonregenerative Cycle Lean Blow Out Versus Percent of Load.

a water-cooled fuel nozzle was designed and fabricated (Figure 46.) However, as received, this nozzle leaked from the fuel to the coolant side, resulting in fuel being dumped overboard, and thus was unusable.

In another technique of nozzle cooling, air assist was also used as a nozzle coolant. Testing assessed the effect of increased air assist pressure on combustion performance to established the maximum level of air assist pressure that could be tolerated before significant degradation of combustion performance occurred. Figure 47 presents the results of these tests.

For an air assist pressure of 30 psid, the combustor temperature rise at blowout is 120F. This is substantially lower than the combustion temperature experienced in the engine thermal ramp schedule (Section 3.2), which varies between 200F at start and 880F at stabilized idle. An air assist pressure of 30 psid was therefore selected as a satisfactory pressure level that does not compromise combustion.

During cleaning of several plugged nozzles, the fact that fuel metering was accomplished internal to the nozzle, was noted, which might be contributing to the plugging problem. The internal orifice was enlarged from 0.016 to 0.050 inch and an external metering orifice was installed.

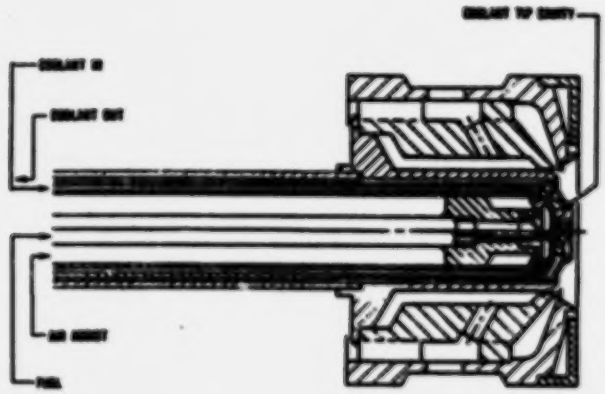

Figure 46. DF Combustor, Water/Air Cooled Nozzle.

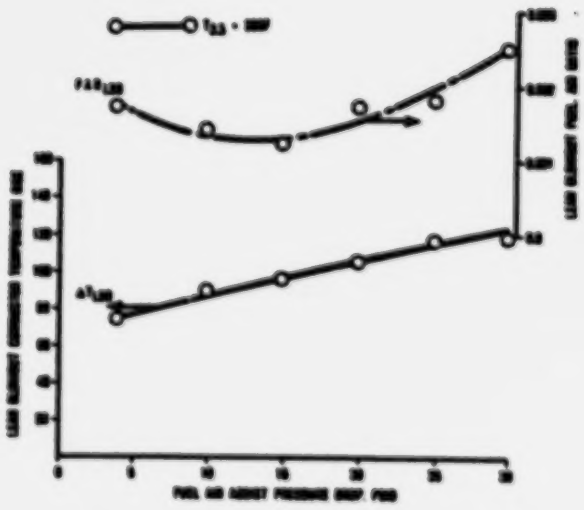

Figure 47. AGT101 (2100F) Effect of Air Assisted Pressure on Fuel Air Ratio-Lean Blow Out at Idle Nonregenerated Condition ($T_{3.5}$ = 200F).

A rig evaluation was made to verify that the ignition, lean blowout, and air assist performance data obtained for the DF combustor would satisfy the combustor operating conditions when thermally ramped according to the schedule determined for engine S/N 002 (Figure 21).

Figure 48 shows the engine thermal ramp superimposed on the test rig simulation results. This rig simulation was representative of that scheduled for the engine, and during this simulation no combustion instabilities were detected and no fuel nozzle plugging occurred. The combustor and nozzle were considered satisfactory for operation in engine S/N 002.

4.3.2 Fuel Nozzle Development

Rig testing of the Simplex fuel nozzle was restarted following facility modifications and repair (Reference 8). Three nozzle configurations were made ready for testing and two versions were evaluated. Figures 49 through 51 depict the nozzle geometries.

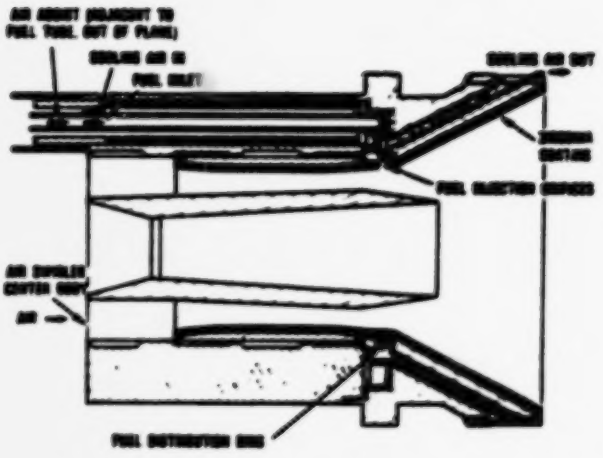

Figure 49. Simplex Mod II Fuel Nozzle.

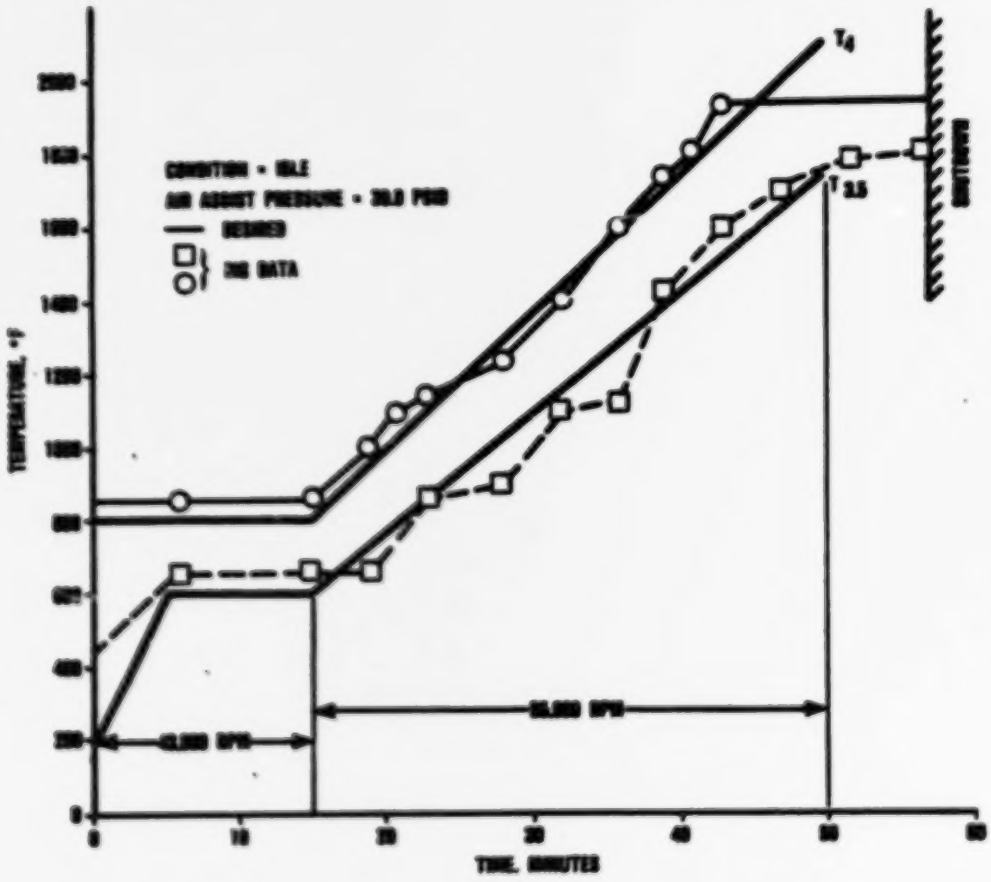

Figure 48. Combustor Test Rig Simulation of Engine Start Ramp.

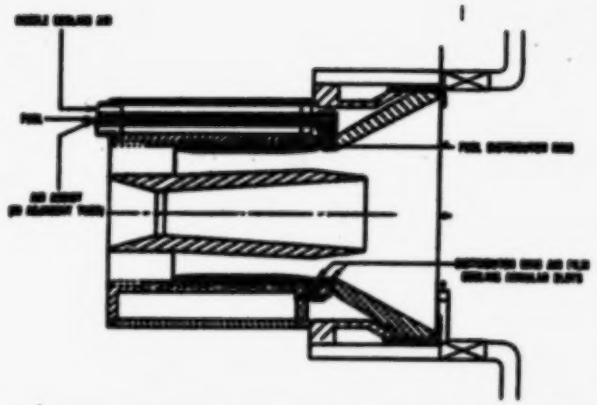

Figure 50. Simplex Mod I - FC Fuel Nozzle.

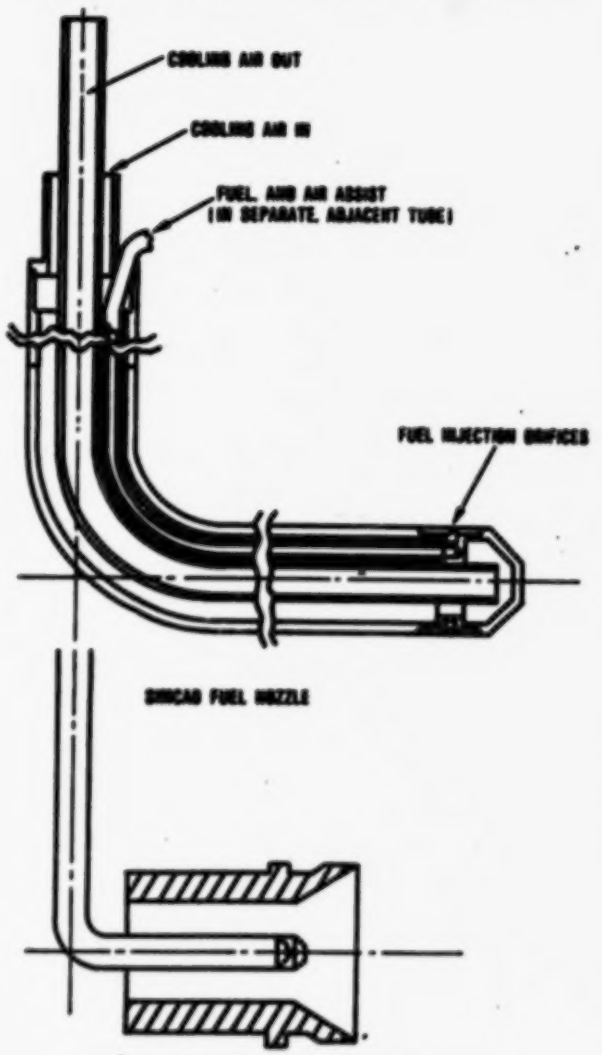

Figure 51. SIMCAB Fuel Nozzle.

The Simplex Mod II and Simplex Mod I-FC nozzles differ only in the cooling flow geometry internal to the nozzle, the discharge location of the cooling flow, and the thermal barrier coating (TBC) along the flowpath.

The Simplex Cone Air Blast (SIMCAB) fuel nozzle is an alternative fuel injection configuration in which fuel is injected into the combustion zone from a central location. This fuel nozzle fits inside the Simplex Mod II fuel nozzle envelope, which will preserve similar aerodynamic features. The cooling technique is a closed circuit arrangement in which the coolant is fed into the nozzle and returned.

Rig tests were conducted at simulated engine conditions to verify nozzle integrity at inlet conditions of 1600F.

The cooling air flow rate was varied between 0.055 and 0.015 lb/min, and the air assist flow rate was varied between 0.015 and 0.025 lb/min. Fuel flow was maintained between 1.4 and 1.6 lb/hr, below the idle value of 1.8 lb/hr. No nozzle plugging was observed.

Emission levels of the Simplex Mod I-FC fuel nozzle were obtained in rig tests at simulated conditions of maximum power, flat rated power (88,000 rpm), cruise (60,000 rpm), and idle.

At each of these simulated operating conditions a matrix of data points was run in which air cooling pressure and air assist pressure were varied to establish whether these parameters could be adjusted to affect fuel penetration and, ultimately, emission profiles.

Figure 52 shows the variation of carbon monoxide emissions relative to NO_x emissions for each engine condition. Carbon monoxide levels for maximum power, flat rated power, cruise, and idle are well within the 38-g/kg fuel target levels. NO_x emissions at maximum

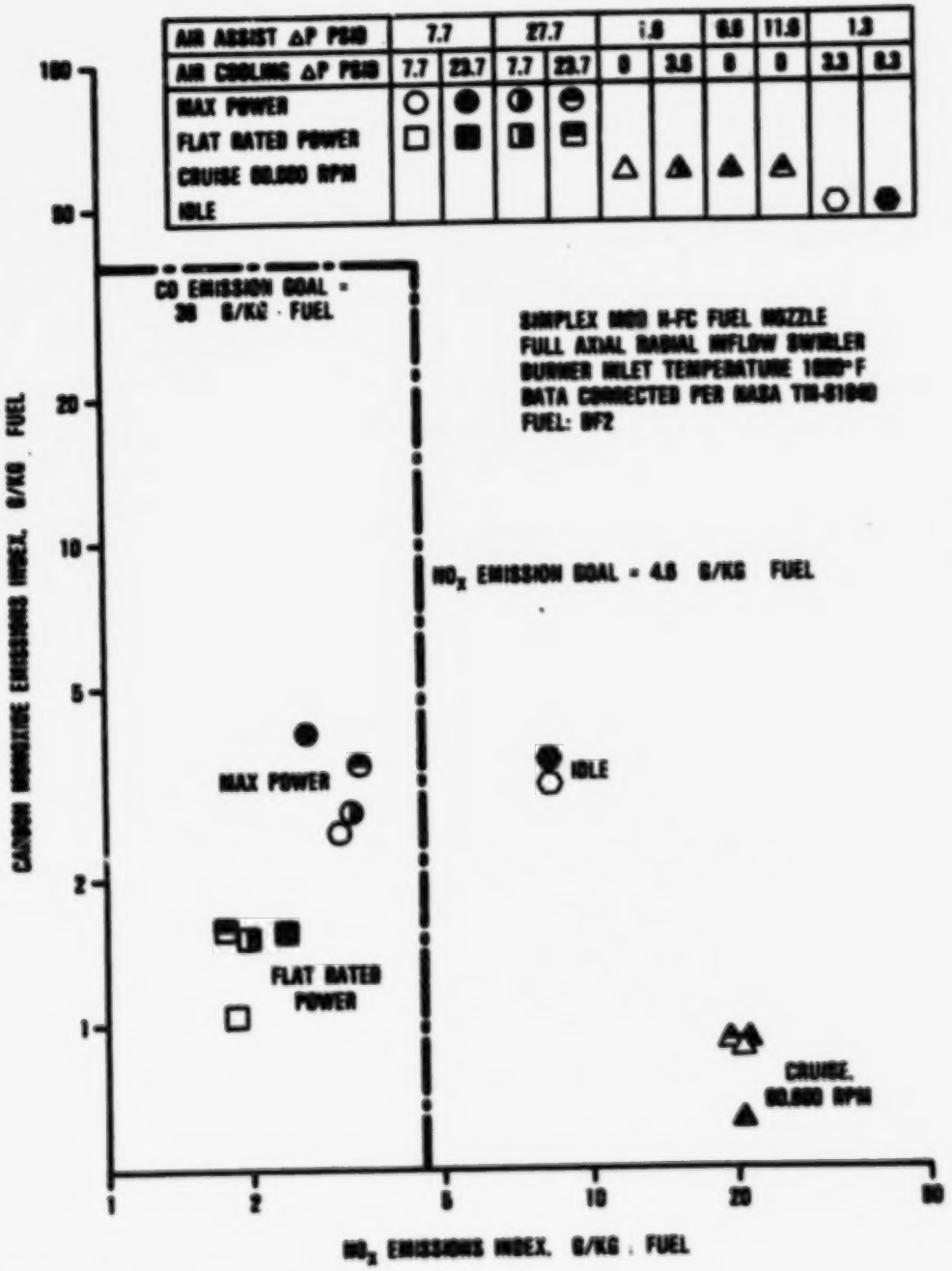

Figure 52. Variation of Carbon Monoxide Emissions Relative to NO_x Emissions.

power and flat rated power are within the target values. However, for the cruise and idle conditions, the target level is exceeded.

The radial profiles of NO_x emission species for the maximum power, cruise, and idle conditions are shown in Figure 53, as well as the corresponding carbon monoxide species profiles for test conditions are shown in Figure 54. The concentration of these components for the flat rated power condition are generally similar to those of the maximum power condition and have been omitted for the purposes of clarity. These curves indicate that within the range of engine pressures tested, neither the cooling air or air assist played a significant role in overall emission concentrations. Unburned hydrocarbon emissions were measured and were below target levels for all power conditions.

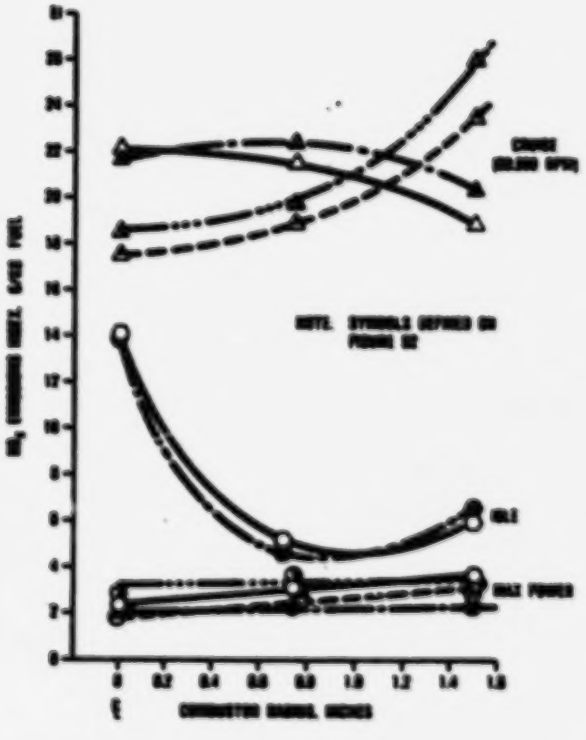

Figure 53. Combustor Radial Concentration of NO_x Emission Species.

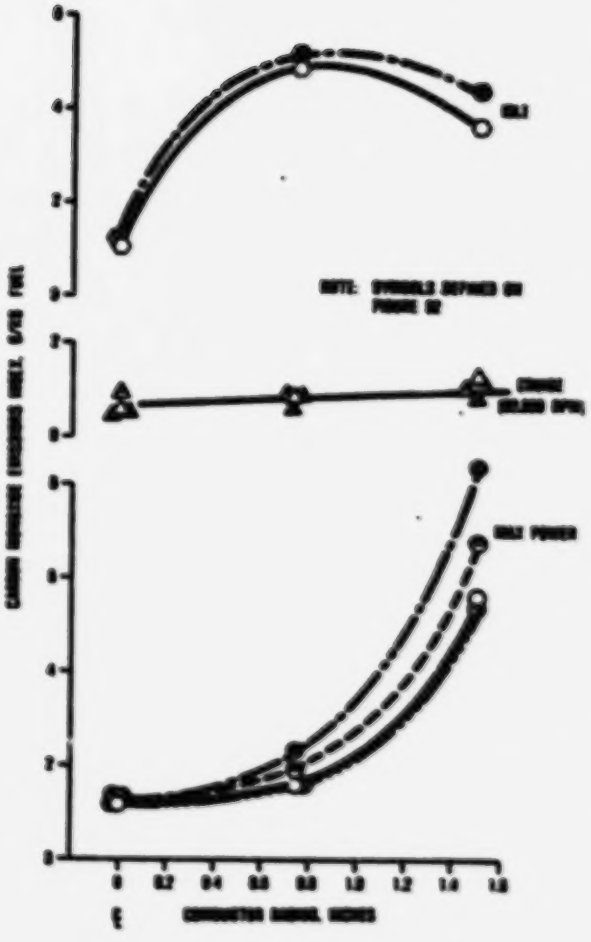

Figure 54. Combustor Radial Concentration of CO Emission Species.

4.3.3 Torch Ignitor

The design of the lean burn combustion system introduces all the airflow to the combustor in close proximity to the fuel injection location. Ignition initiation and the establishment of stable combustion is possible with this arrangement at the high combustor inlet air temperatures available during steady state operating conditions. However, "cold" light off is not feasible with an ignitor alone, so an extra source of heat addition is required to initiate combustion. This requirement is satisfied by a torch ignition system, where the torch is located at the combustor head.

Preliminary combustion tests with a torch ignitor (Figure 55), conducted early in the program, demonstrated light off capability on natural gas. This design was upgraded to operate on liquid fuels ranging from gasoline to DF-2 by increasing the size of the torch combustor (Figure 56). For this purpose, two diameters were selected, 2.75 and 1.875 inches. Exploratory tests on these torches were conducted with JP-4 (Figure 57). The minimum measured fuel flow at which combustion initiated was 0.5 lb/hr, which coincidentally is the minimum capability measurable by the flow meter. Lower ignition fuel flows than this are possible.

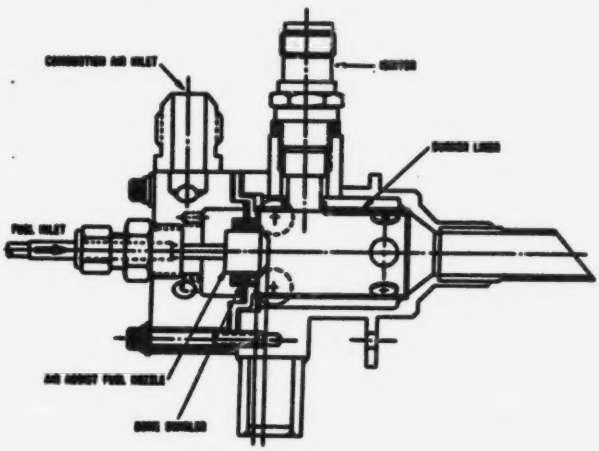

Figure 55. Torch Ignitor.

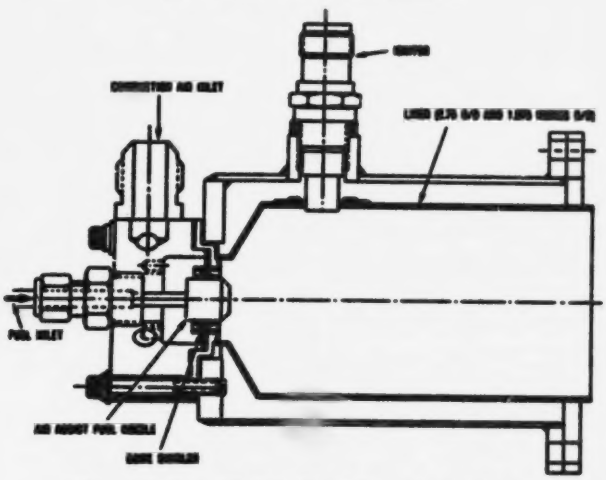

Figure 56. Multi-Fuel Torch Ignitor.

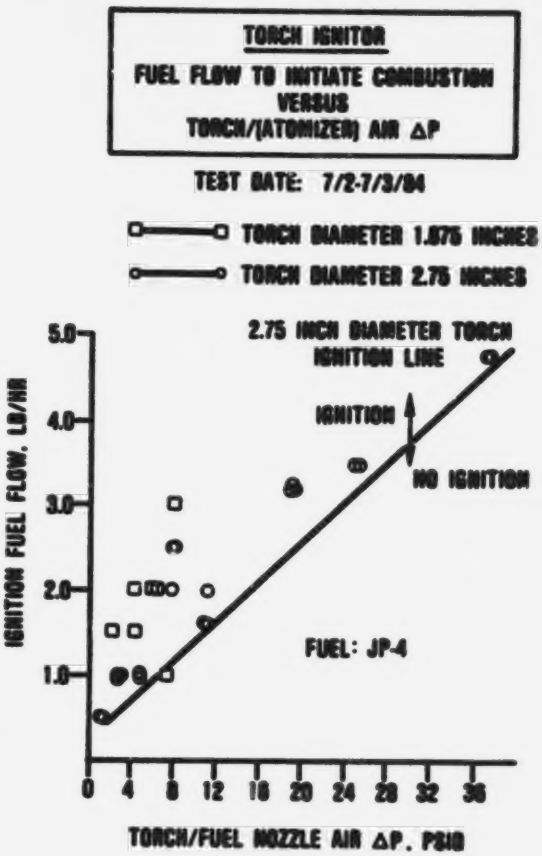

Figure 57. Torch Test Data Using JP-4 Fuel.

With the particular geometry tested, the upper limit to ignition for the 1.875-inch diameter torch combustor was found to be of the order of 3.0 lb/hr because of ignitor fuel saturation. This problem probably can be corrected by relocating the ignitor to a position in the dome, adjacent to the fuel nozzle. This location also would enhance the torch geometrical arrangement with respect to the combustor cap.

The effect of length on torch light-off and steady state combustion was explored by moving a blocking plate with a central orifice along the torch axis. The maximum distance obtainable was as far as the ignitor, and at this location no decrease in light-off performance occurred.

4.4 Regenerator

4.4.1 Ford Regenerator Development

To accommodate the higher operating temperatures associated with the AGT101 (2500F) engine, the regenerator inboard (hot) seal crossarm requires diaphragm cooling. The design objective is to keep the middle (support) diaphragm (Figure 58) below 1600F, which should provide adequate strength using Rene 41 or Waspalloy materials for the expected diaphragm stress levels.

A new finite element model (Figure 59), utilizing solid instead of shell elements, was incorporated into a three-dimensional heat transfer analysis program. The model consists of 231 nodes and 98 elements, and will be used as a design tool to support the prototype seal configurations being fabricated for evaluation in the hot structures rig at Garrett.

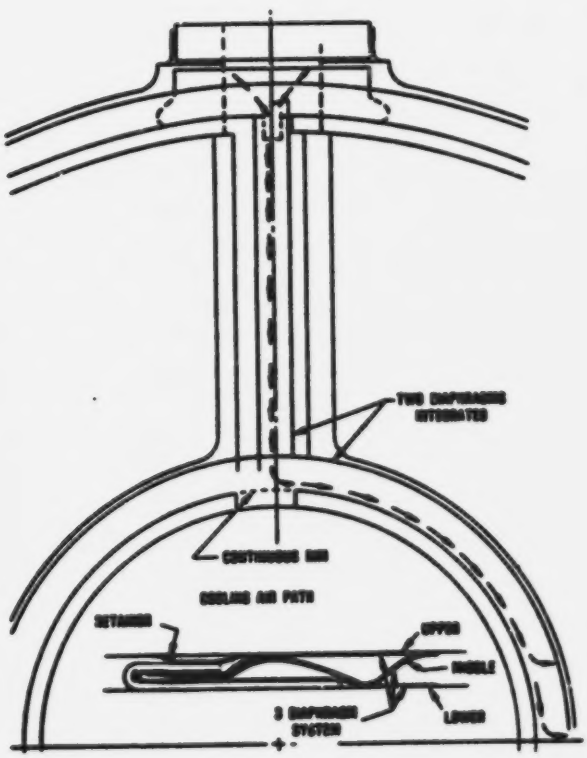

Figure 58. Regenerator Diaphragm System.

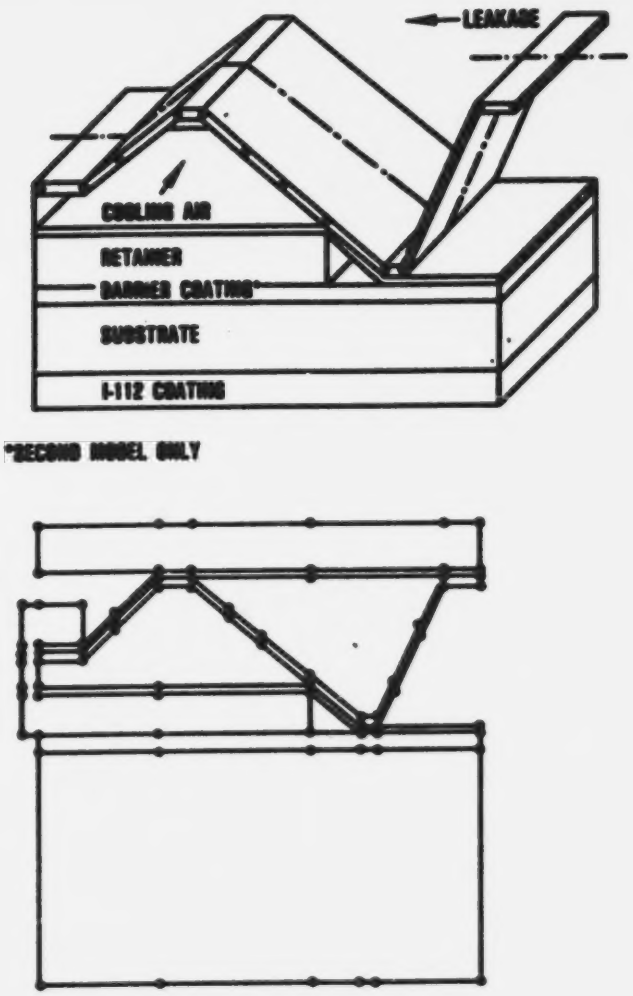

*SECOND MODEL ONLY

Figure 59. Diaphragm Finite Element Model.

The initial configuration evaluated in the hot structures rig (Section 4.5) contained thermocouples attached to both halves of the crossarm shoe and middle diaphragm. The results indicated excellent cooling at the crossarm outer extremities, but inadequate cooling at the center hole region. To establish a baseline for design iterations, a parametric study was conducted in an attempt to correlate with the test temperatures. The amount of cooling air flow is dependent on the pressure differential that exists in the channel. For discharge holes in the middle diaphragm at the center of the periphery, the

pressure differential (less than 0.25 psi) establishes the minimum rate of cooling air flow. For maximum cooling, holes in the retainer (Figure 58) allow the air to discharge into the center hole cavity, which is vented to the exhaust duct.

Convection coefficients were estimated based on cooling air flow and cross-sectional area of the channel. In addition, convection coefficients for leakage between the upper diaphragm and flow separator housing also were estimated.

Temperature distribution of the middle (support) diaphragm for minimum and maximum cooling flow are illustrated on Figures 60 and 61, respectively. The results indicate that, for these operating conditions, minimum cooling flow is sufficient for the enclosed portion of the middle diaphragm. The trailing edge portion of the middle diaphragm is not affected by either cooling air flow rate. The predicted temperatures in this region correlate with the thermocouple locations on the instrumented seal. In effect, this portion of the middle diaphragm represents a direct conduction path between the flow separator housing and the rubbing seal shoe.

To reduce temperatures in this region, a barrier coating must be applied to the back of the coated shoe. This effect was simulated by incorporating a 0.030-inch thick coating of zirconium oxide to the model. Minimum (Figure 60) and maximum (Figure 61) cooling conditions were repeated. The results indicate that, for these operating conditions, maximum cooling flow combined with barrier coating (Figure 61) will satisfy the diaphragm temperature requirement. AGT101 (2500F) operating conditions will be evaluated next to optimize the cooling air flow rate and barrier coating thickness.

The initial set of Phase V seals was evaluated in the hot regenerator rig. This design features an integrated crossarm and inner peripheral diaphragm, which eliminates secondary diaphragms in the inside corners. These seals exhibited the lowest leakage level (Figure 62) of any seal design tested at hot operating conditions, and correlates with the static seal leakage data. In addition, drive torque characteristics were significantly reduced at high seal ΔP compared to Phase IV seals (Figure 63).

The initial Phase V seals contained diaphragms that were fabricated by hand and heat treated in an oxidizing atmosphere. Based on tests conducted in the static seal leakage rig, additional improvements are expected after receiving new diaphragm dies, which have been ordered. In addition, heat treatment in an inert atmosphere will improve the assembly procedure.

Based on visual observations of hot flowpath components tested in the hot structures rig and ceramic engine at 2000 to 2100F TIT, the I-85 coating for the hot seal outer periphery shoes may be marginal. To raise the upper temperature limit, a replacement coating (I-151) will be evaluated. Based on wear rig tests at Ford, the I-151 (zinc-oxide base) has a temperature capability 200F higher than that of I-85 (copper base). Additionally, zinc has less tendency to form oxide deposits than copper. The initial set of seals coated with I-151 material was delivered to Garrett for evaluation near the end of the period covered in this report.

Wall porosity leakage of the new NGK core matrix (CO.9) with rectangular cell geometry (1100 cells/in^2) was evaluated in the static seal rig. This core contained GE-Cordierite coating on the inner and outer surfaces in addition to matrix-wall impregnation to compensate for the high (35 percent) wall porosity of the parent material. At 100-percent gas generator speed, the corrected thru-wall porosity leakage is 0.80 percent, which is approximately 0.5 percent higher than the thick-wall isosceles triangular matrix (CO.3). The cores fabricated with either matrix geometry offer acceptable performance levels on an interim basis until NGK can develop a denser material that is more suitable for the regenerator application.

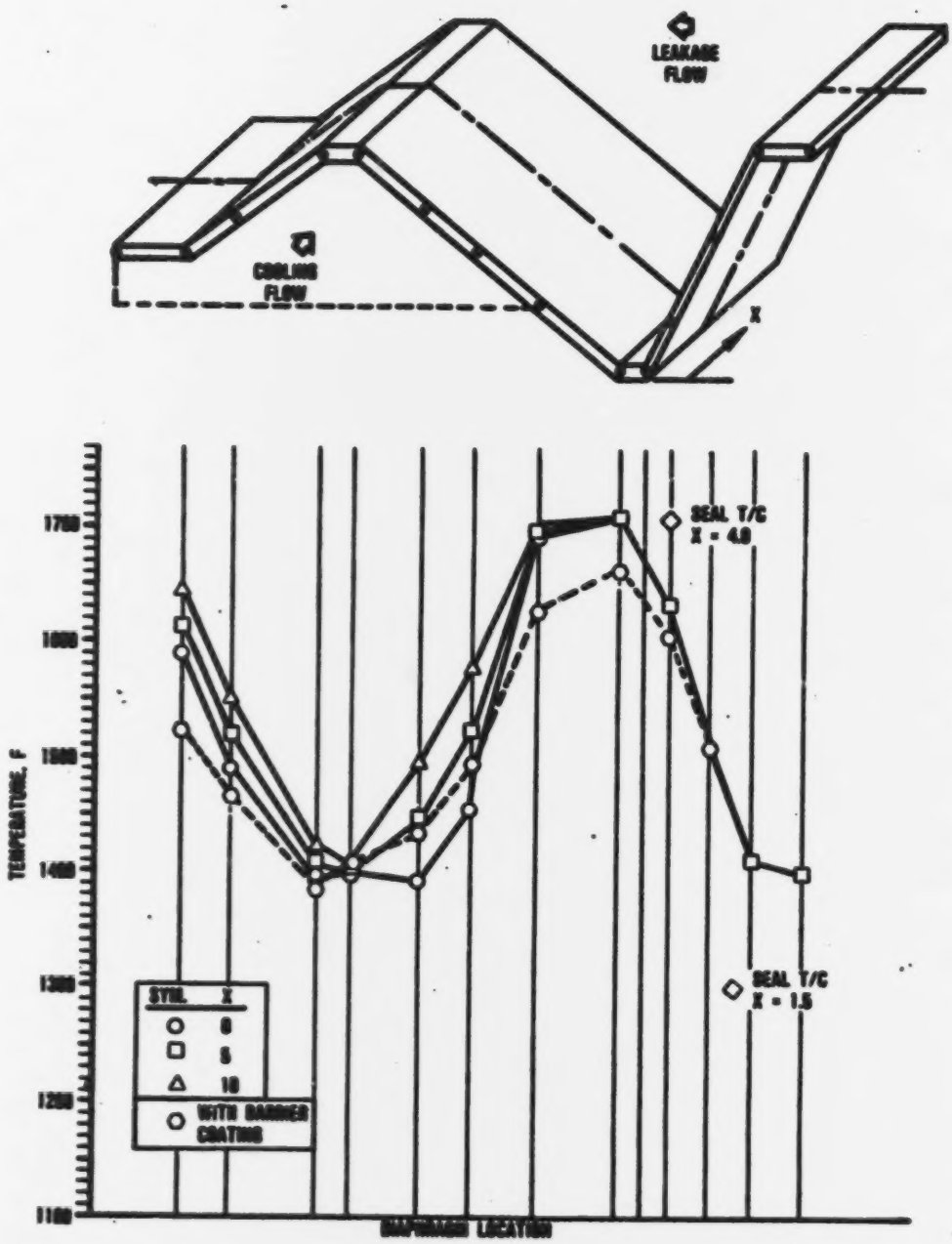

Figure 68. Middle (Support) Diaphragm Temperature Distribution for Minimum Cooling Flow.

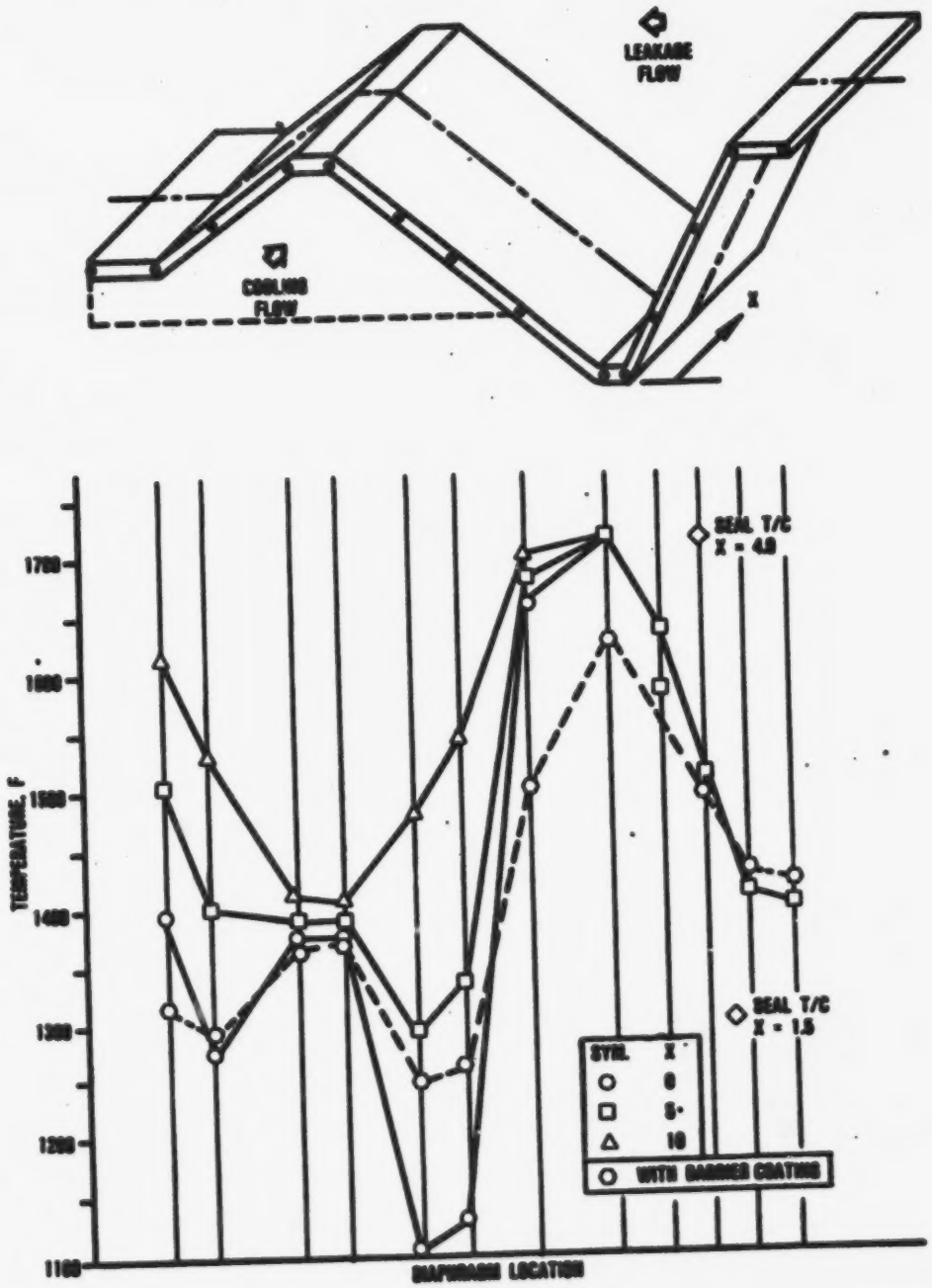

Figure 61. Middle (Support) Diaphragm Temperature Distribution for Maximum Cooling Flow.

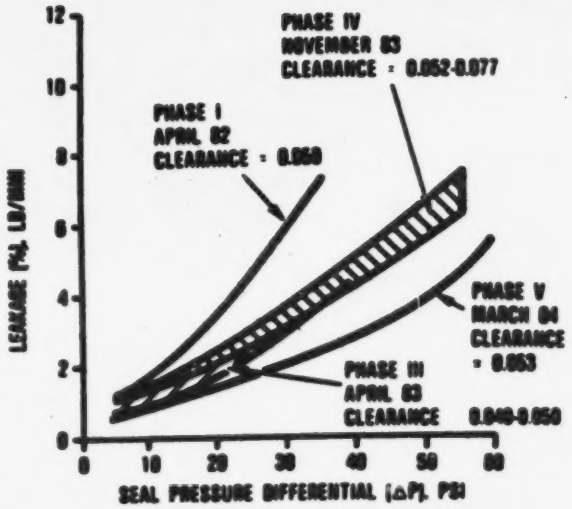

Figure 62. AGT101 Regenerator Seal Leakage.

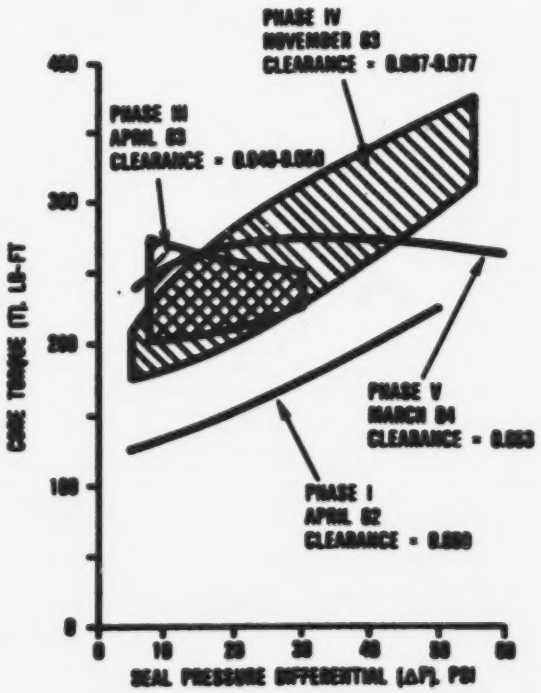

Figure 63. AGT101 Regenerator Core Torque.

High torque levels, generated by Phase IV seals running at tight clearances, cause ring gear separation from two NGK cores by shearing the elastomer. To improve elastomer shear strength the diagonal bond configuration cross section has been modified (Figure 64). Application of the GE-Cordierite coating to the outer peripheral core surface creates a very hard layer, that should withstand the additional radial force associated with the modified design. Two cores were bonded with this configuration near the end of this reporting period for evaluation at Garrett.

The Ford ceramic structures rig (Figure 65) was assembled during this reporting period. A series of check-out runs was completed. A system for injecting Fuller's earth into the rig prior to shutdown for evaluating seal leakage was adapted. To simulate the pressure drop of a rotating rotor at different operating conditions, a tapered disc was designed to replace the stationary rotor. A system for adjusting the disc axial location is being designed.

To measure seal system leakage, a design modification for the rig has been completed as illustrated in Figure 65. The modified rig will incorporate an exit orifice with the existing inlet orifice.

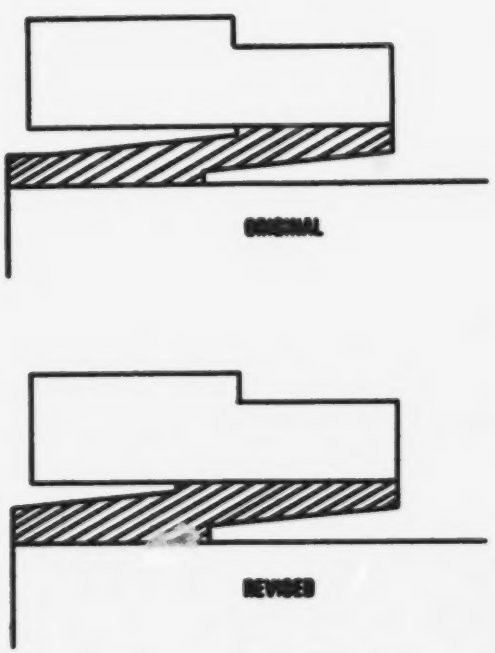

Figure 64. Diagonal Bond Configuration.

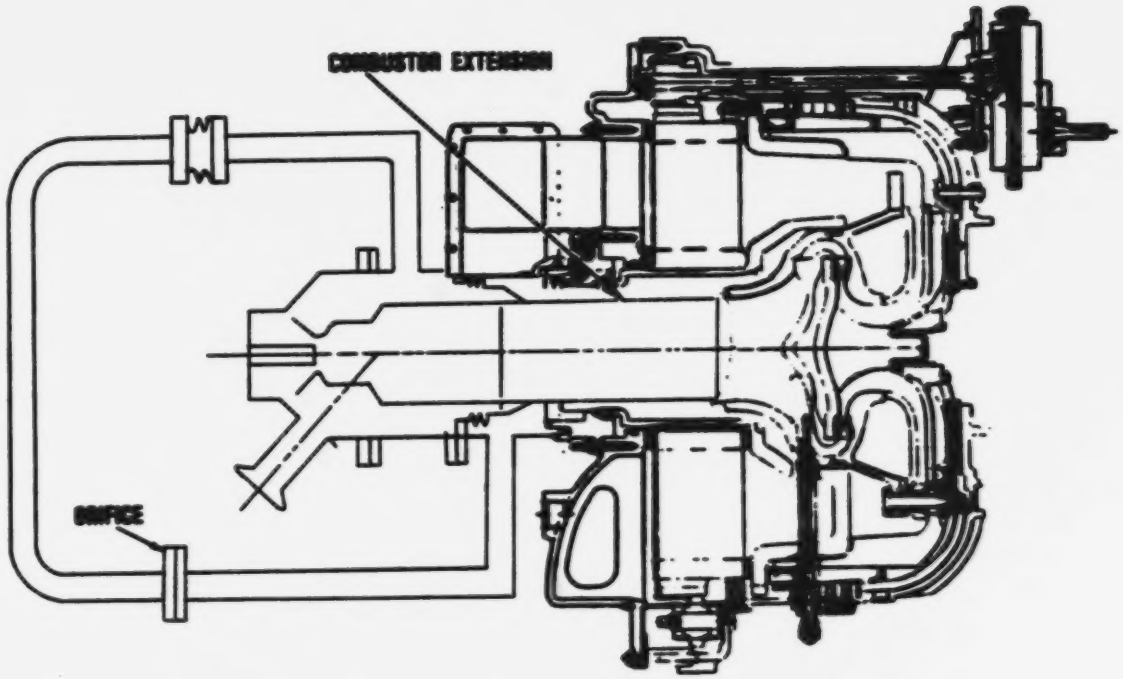

Figure 65. Ford Ceramic Structures Rig.

4.4.2 Garrett Regenerator Development

4.4.2.1 Regenerator Rig Testing

The hot regenerator rig was assembled and tested with the following objectives:

- Measure regenerator system leakage (core porosity, seals, carryover, and cooling, and drive torque with Phase V seals under (AGT101, 1600F) nominal conditions
- Gather additional data on the variations in regenerator inner peripheral seal clearance

Several tests were run and the cold build seal clearance was varied to determine optimum clearance with respect to seal leakage and drive torque. Figures 66 and 67 show seal leakage and regenerator drive torque plotted versus rig pressure for 0.053 inch seal clearance (optimum) and also for a 0.061 inch seal clearance. Leakage at low pressures proved insensitive to seal clearance while, at high pressures, sensitivity to leakage increased dramatically. Seal clearances smaller than 0.053 inch were tested, but excessive drive torques precluded gathering data at the higher pressures and the data that was obtained showed no improvement over the leakage with 0.053 inch seal clearance.

Unlike earlier generation seals, the drive torque at the optimum seal clearance is almost constant with respect to rig pressure.

Relative to the best of the earlier generation seals, the Phase V seals represent an improvement in leakage. A comparison is shown with Phase III leakage curves in Figure 68 (Reference 7). The seal leakage, measured at two values for total seal clearance, is shown plotted versus rig pressure. Analysis and reduction of the clearance probe data that was used to determine the inner peripheral seal clearance variations is in process and will be reported at a later date.

4.5 Ceramics

4.5.1 Materials and Component Development

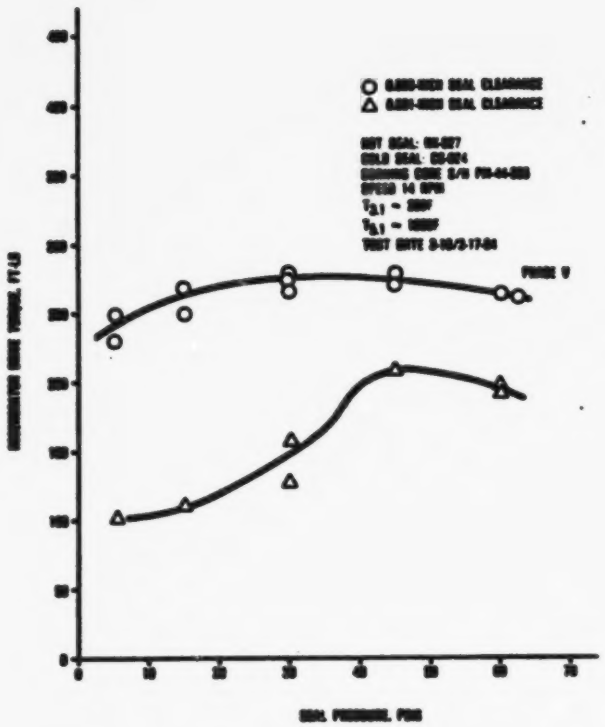

Figure 66. Phase V Regenerator Seal Drive Torque Versus Seal Pressure.

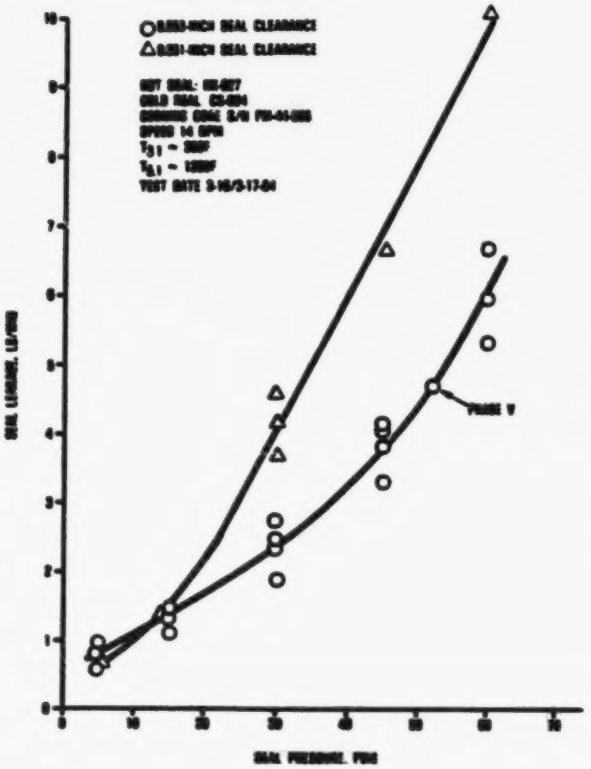

Figure 67. Phase V Regenerator Seals Hot Seal Leakage Test.

4.5.1.1 Ceramic Material Testing Summary

A summary of the material property results is presented in Table 6. Additionally, a material characterization reference chart is shown in Table 7.

4.5.1.2 Kyocera SC201 Silicon Carbide Testing

Twenty test bars of SC201 silicon carbide were received from Kyocera as certification specimens for turbine shrouds that also were received. All test bars were 0.250 x 0.125 inch in cross section and were received in the as-machined condition. Five test bars were flexure tested in the as-received condition and five were tested after receiving a 2200F/2-hour oxidizing heat treatment. This treatment currently is utilized for Carborundum SASC components. Results of this testing are summarized in Table 8.

These results show that SC201 responds significantly to thermal treatment and that the heat-treated SC201 test bars shown in Figure 69 has good material strength.

Analyses of both fracture surfaces and polished sections of the SC201 indicate a uniform fine grain size with almost no porosity.

4.5.1.3 RBSN Turbine Shroud Cut-Up Properties

RBSN (ACC RBN104) turbine shroud S/N 377 that was fractured in a 2100F thermal screening test, was cut up to provide test bars for flexural evaluation. Test bars were machined from the area indicated in Figure 70 heat treated at 2200F for 2 hours, and flexure tested at room temperature. Results are summarized in Table 9 and are compared to the flexure strength results for certification

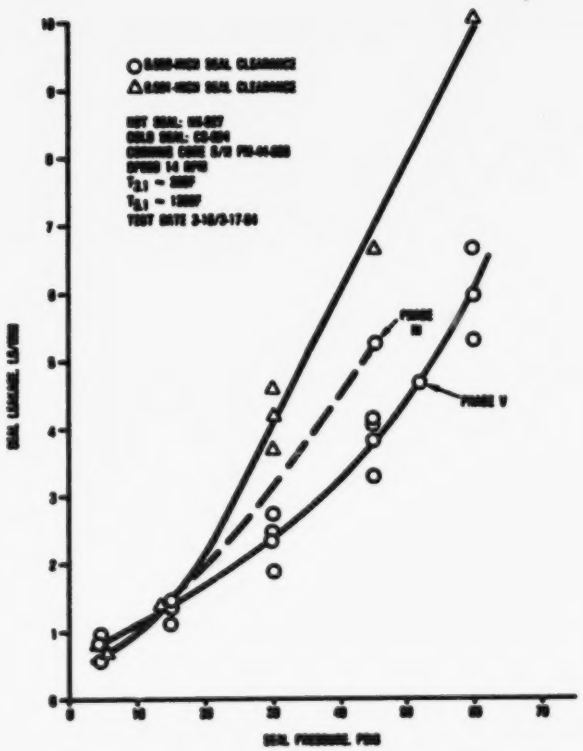

Figure 68. Comparison of Phase III with Phase V Regenerator Seals, Hot Seal Leakage Test.

test bars processed in parallel with the turbine shroud. Although the quantity of bars tested was insufficient to obtain an accurate indication of material strength and scatter, the results do indicate that certification and component strengths match or exceed baseline strength properties for RBN104.

4.5.1.4 Alumina - LAS Sticking Study

Alumina thermocouple spacers and seals have been fabricated for use on the T_4 thermocouple. These spacers and seals seat against the LAS flow separator housing and the SASC transition duct and are exposed to a peak temperature of approximately 2000F. To evaluate the potential of sticking at these interfaces, a stack of LAS, Al_2O_3, and SASC materials was exposed to 2000F for approximately 20 hours with a compressive 15-pound load simulating engine assembly. After completion of exposure and cool down, no sticking between the LAS and alumina or between the SASC and alumina was observed.

4.5.1.5 Carborundum SASC and Kyocera SC201 Sticking

Test bars of Carborundum SASC and Kyocera SC201 sintered SiC were stacked, loaded, and thermally soaked for 20 hours using methods similar to those described in Reference 5. The stack was assembled and arranged so that SASC to SASC, SASC to SC201, and SC201 to SC201 interface combinations could be evaluated. The material stack was loaded to 0.2 ksi and heated to 1970F. The load was held constant at 0.2 ksi during the 20-hour soak; furnace cooling was then performed under continued loading. This test condition was selected because sticking at SASC-to-SASC interfaces had occurred in previous evaluations. Under this repeat test, light sticking was observed at all interface combinations. Testing and evaluation will continue.

4.5.1.6 Insulation System

Insulation test results reported in Reference 8 demonstrated the durability of the Lockheed HTP insulation under short-term exposure to 75 ft/sec gas velocities at 2100F. Additional testing was directed toward evaluating insulation capabilities under representative turbine rotor discharge conditions, simulating gas velocities and temperatures rather than at the turbine diffuser dump location. Two test conditions were selected representative of engine maximum power (1770F, 1000 ft/sec) and idle (2000F, 350 ft/sec) flow conditions. To perform these tests, additional RCG-coated and uncoated test cylinders were obtained from Lockheed. The cylinders were 3-inches long with a 2.75-inch inner diameter (needed to attain the higher gas velocity conditions). The new cylinders were a higher density HTP-16 (16 lb/ft^3) than the previously HTP-12 material previously tested. The cylinders were tested in the test rig illustrated in Figure 71.

ORIGINAL PAGE IS
OF POOR QUALITY

Table 6. AGT101 Component and Material Summary

				Qualification Bar							Ceramic Component						
				Room Temperature			Elevated Temperature				Room Temperature			Elevated Temperature			
Supplier	Material	Process	Condition	σ_β (4)	$\dot{n}$	Population	σ_β (4)	$\dot{n}$	F	Population	σ_β (4)	$\dot{n}$	Population	σ_β (4)	$\dot{n}$	F	Population
ACC																	
Inner Diffuser	RBSN	Slip	As-Fired	48.7	4.5	30	52.1	10.1	2200	10	44.2(6)	8	31				
Outer Diffuser (RBN104)		Cast	Longitudinally Ground	53.2	5.5	10					48.3	5.3	27				
Turbine Shroud			Heat Treated	54.8	8.5	20					50.2(7)	7.6(7)	7				
ACC Stator	RBSN (RBN112)	Injection Molded	As-Fired(1)	48.1	4.8	19	44.5	8.4	2200	22							
ACC Rotor	Sintered Si_3N_4 (SNN 502)	Ford Rotor ASEA HIPped	Longitudinally(2) Ground								116(3)	14	30	91	10	2200	10
											100(3)	10	19	80	10	2200	21
	Sintered Si_3N_4 (SNN 522)	Injection Molded	As-Fired	88.2	8.9	30	80.9	7.8	1800	9							
							85.1	11.1	2000	30							
							87.5	10.8	2200	10							
							85.6	13.6	2300	12							
Carborundum																	
Turbine Shroud, Stator	Sintered -SiC	Injection Cast	As-Fired Ground	48.8	9.5	30	48.9	5.9	2500	10	55.6(5)	7.1	9				
Transition Duct, Regen Shield, Rotor-shroud	Sintered -SiC	Improved	Longitudinally Ground	57.7	7.7	30	56.2	11.9	2500	19							
Ford																	
Rotor	SRBSN (RBN-2)	Slip Cast	Longitudinally Ground	100.3	13.8	6	72.1	16.4	2200	6							
Stator	RBSN	Injection	As-Fired	43.1	8.3	30	45.8	7.7	2200	10							
NGK Rotor/shroud Transition Duct	Sintered Si_3N_4 (SN-60)	Improved	Longitudinally Ground	87.6	10.5	10	67.1	13.6	2000	7							
Corning Flow Separator Housing	LAS	Slip Cast	Longitudinally Ground	14.9	13.3	11	13.5	9.7	2000	13							
Kyocera Turbine Shroud	SC201	Improved	Longitudinally Ground	88.6(7)	11.1(7)	5											

All test bars 0.250 x 0.125-inch cross section unless noted. Bars tested in 4-point flexure, 1.50-inch outer span, and 0.75-inch inner span. Cross head speed, 0.05 inch/minute

(1) Test bar cross sec n 0.31 x 0.15 inch
(2) Test bar cross sec ion: 0.2 x 0.1 inch
(3) 95 percent dense
(4) Characteristic strength, ksi
(5) As machined, longitudinally ground
(6) Test bar cross section 0.236 x 0.1 inch
(7) Average strength and standard deviation

ORIGINAL PAGE IS
OF POOR QUALITY

Table 7. AGT101 Ceramic Material Characterization at Garrett

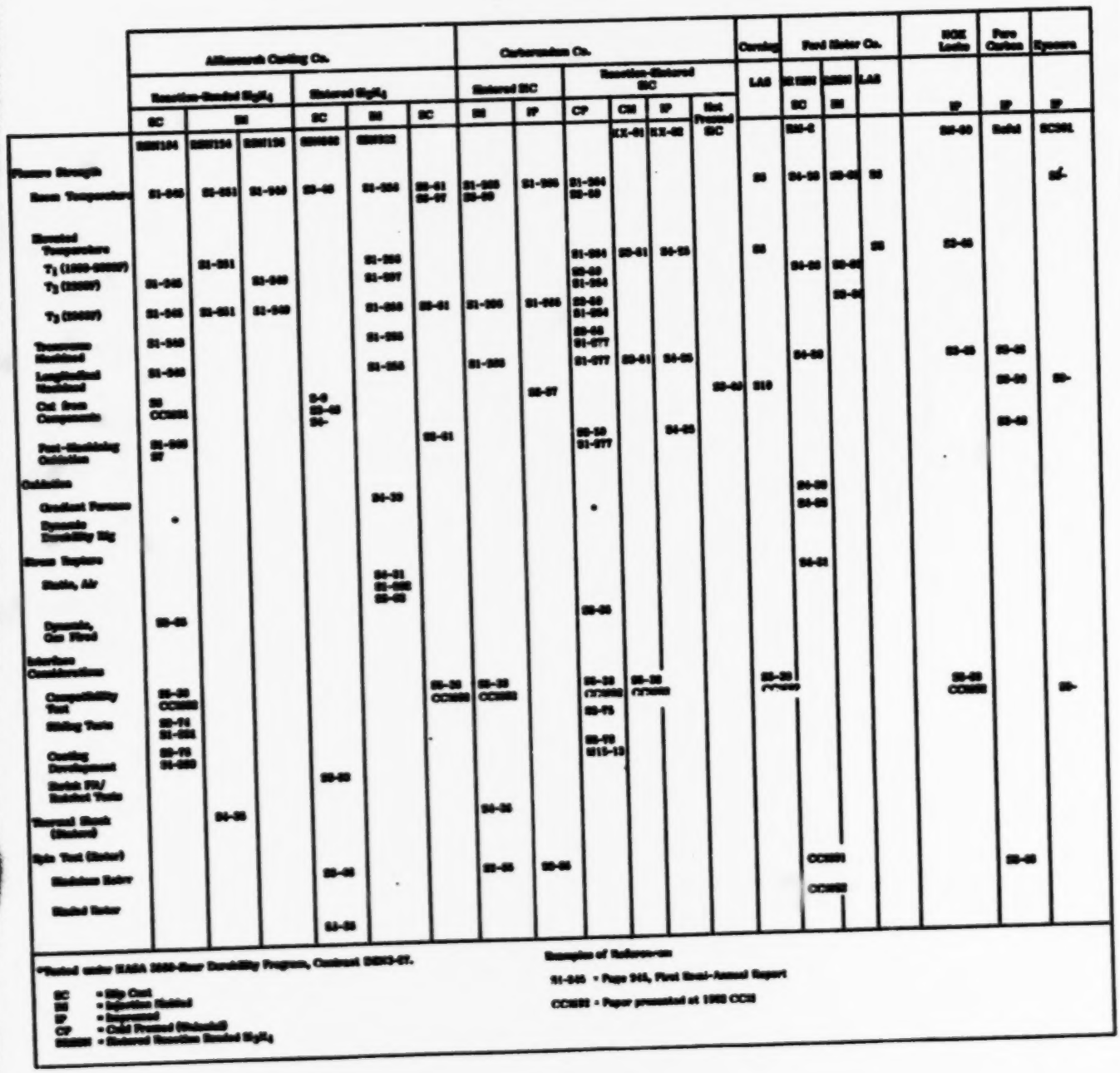

ORIGINAL PAGE IS
OF POOR QUALITY

Table 8. SC201 Flexure Strengths *

	Heat-Treated ksi	As-Received ksi
	70.8 66.0 79.2 85.2 74.9	51.3 52.1 67.1 54.7 76.6
Average:	75.2	60.4
Standard Deviation:	7.4	11.1

*Test bars tested in four-point flexure with a 1.5-inch outer and 0.75-inch inner span. A cross-head speed of 0.02-inch per minute was used.

Testing was performed for 7 cycles profiled in Figure 72. The test rig was disassembled for inspection after completion of Cycles 1, 3, and 7. At completion of Cycles 1 and 3, no material distress was observed. Following Cycle 7, however, disassembly revealed coated sample shrinkage, uncoated sample shrinkage, and melting (illustrated in Figure 73). Based on previous testing at both Garrett and Lockheed, these results did not correlate with 2000F exposures. Thus, the two samples were returned to Lockheed for post-test analysis. Meanwhile, the test conditions were reviewed at Garrett, including recalibration of the three control thermocouples located downstream of the test cylinder discharge. Three conditions were identified that may have contributed to the atypical results. These included the use of a gas discharge water quench downstream of the test cylinders for rig ducting protection. This discharge may have provided recirculated contamination or

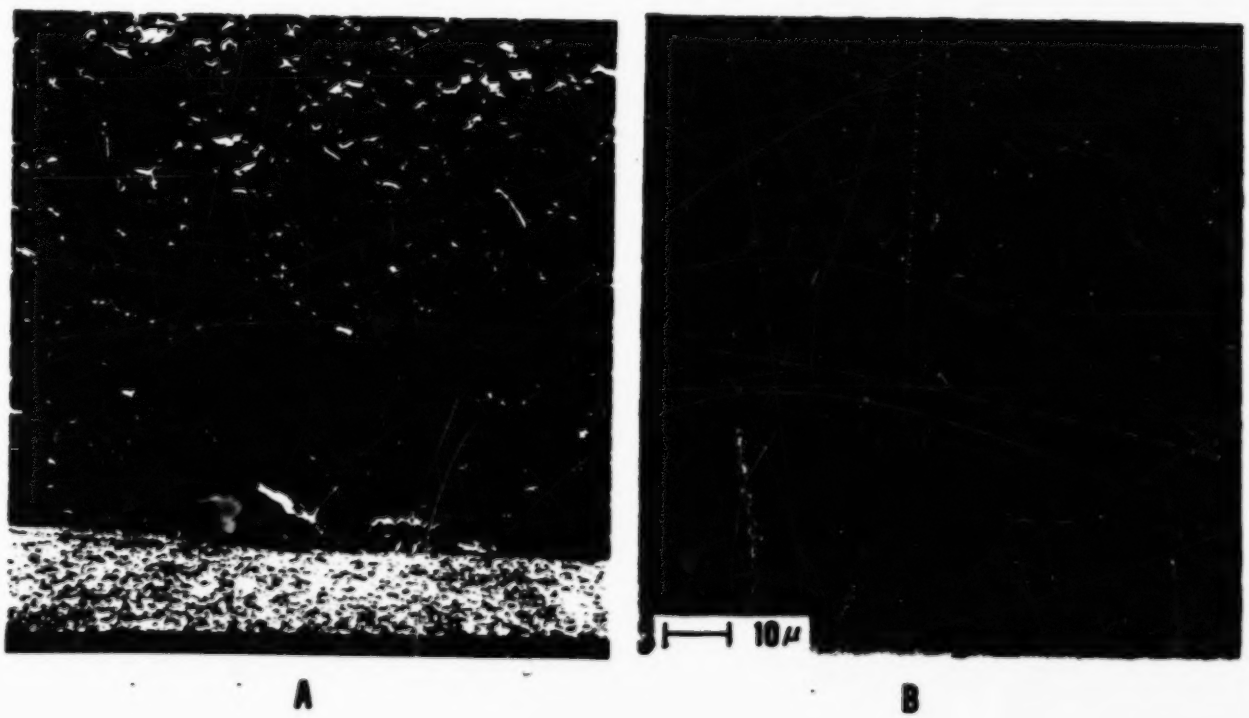

Figure 69. Kyocera SC201 Fracture Surface (A) and Polished Section (B).

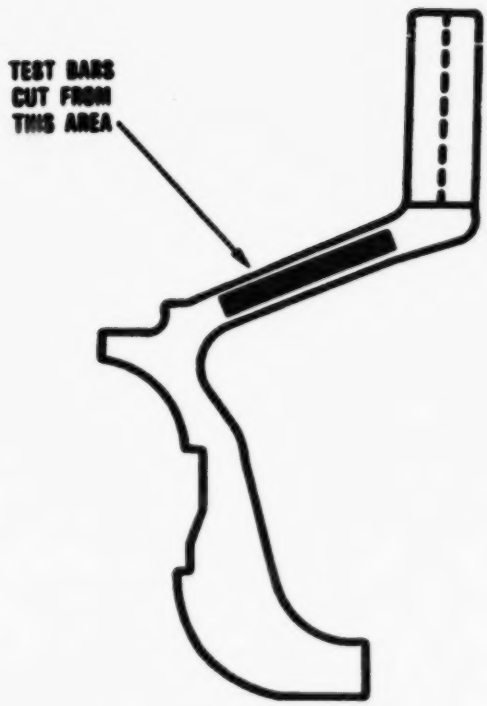

Figure 70. Turbine Shroud Test Bar Area.

Table 9. Cut-Up and Certification Test Bar Strength for ACC RBN184 Turbine Shroud S/N 377*

	Certification Bars, ksi	Cut-Up Bars, ksi
	44.6	54.1
	41.2	51.8
	51.8	52.7
	51.6	48.1
	51.8	60.5
		64.8
		55.3
Average:	48.2	55.3
Standard Deviation:	5.0	7.4

*All test bars 0.250 x 0.125 inch cross section, tested with 1.5-inch outer span, 0.75-inch inner span, using a cross-head speed of 0.02 inch/min. All bars heat treated at 2200F for 2 hours.

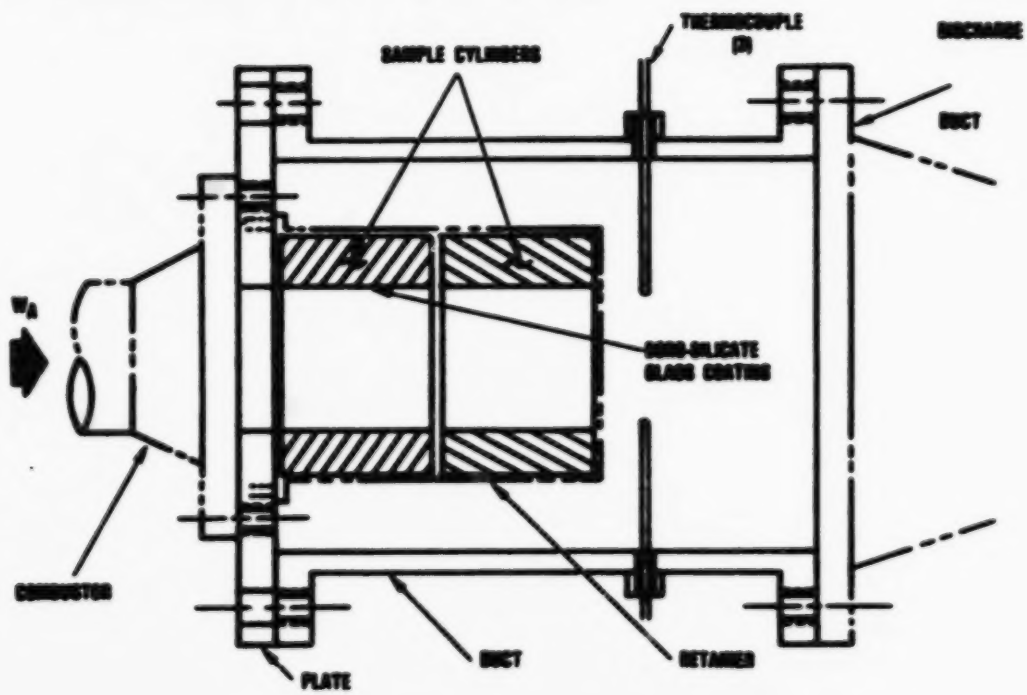

Figure 71. AGT101 Insulation Test Rig.

ORIGINAL PAGE IS
OF POOR QUALITY

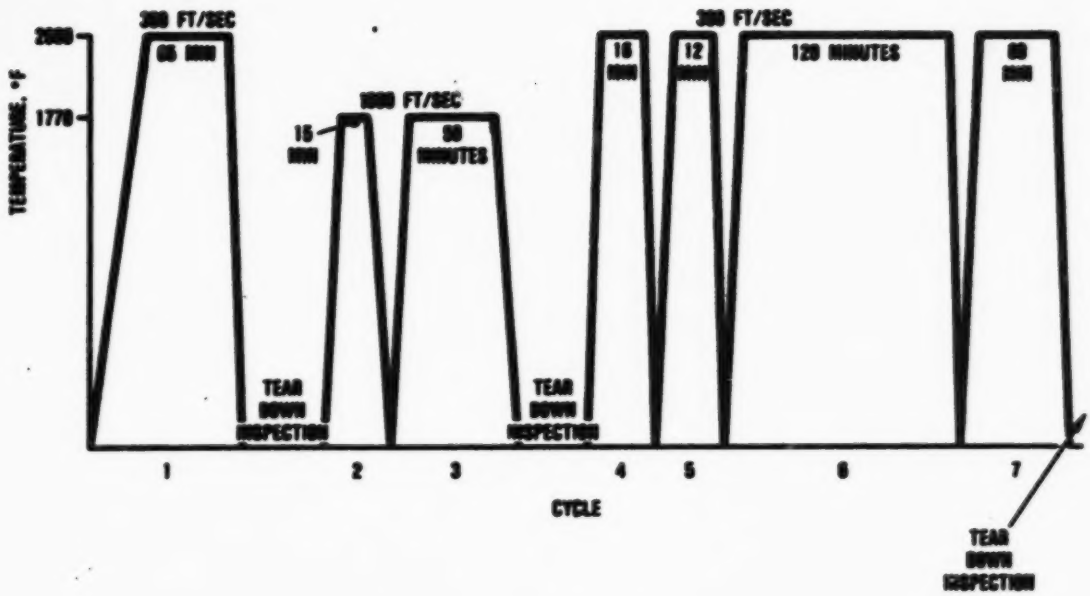

Figure 72. Maximum Power and Idle Condition of Lockheed HTP-16 Insulation.

Figure 73. Lockheed HTP-16 Cylinders After Cyclical Flow Testing.

vapor that could conceivably have reached the test articles. Contaminants may have contributed to a reduction in the melting temperature of the insulation materials. Water quenching was used only in test cycles subsequent to Cycle 3.

Another possible contributor was the occurrence of wet starts in which unburned fuel may have been sprayed onto, and by, the insulators. Subsequent operation would have produced local burning and hot spots, which would have contributed to insulation melting.

The most likely contribution to insulation damage probably occurred at overtemperature test conditions. Post-test calibration of the three Type S thermocouples indicated that one thermocouple was reading substantially lower microvolt output than the others. Due to the averaging of the output of these thermocouples by the control and recording systems, there is a strong possibility that temperatures 900F over the 2000F desired test condition occurred in the cycles subsequent to Cycle 3. Thermocouple deterioration is believed to have occurred during the final phases of testing (Cycles 6 and 7).

Continuing discussions with Lockheed regarding these results confirmed the typical occurrence of HTP material shrinkage at

2900F, supporting the indications of an over-temperature condition. Thus, a retest under maximum power and idle conditions will be performed. Nonetheless, encouragement is gained in that the test samples demonstrated short-term durability during the first 3 cycles, and that even under the excessive conditions of Cycles 4 through 7, only limited deterioration occurred.

4.5.1.7 Slip Casting Rheology Studies

Two subcontracts were initiated during the summer of 1983 to study the rheology of Si and Si_3N_4-Y_2O_3-Al_2O_3 particulate dispersions in water. The program objectives are briefly discussed in subsequent paragraphs and the results are presented in detail in Appendices D and E.

The Si slip program was subcontracted to Dr. M.D. Sacks of the University of Florida to support reaction-bonded Si_3N_4 processing at ACC.

Objectives/tasks included:

- o Baseline characterization of ACC-supplied Si powder
  - Particle size distribution
  - Powder surface area measurement
- o Electrophonetic mobility versus pH
- o Zeta potential versus pH
- o Shear stress versus shear rate as a function of solids content, pH, and ultrasonic agitation
- o Viscosity versus shear rate as a function of solids content, pH, and ultrasonic agitation
- o Total porosity and median pore radius of cast samples as a function of slip solids content, pH, and ultrasonic agitation
- o Screening study of potential dispersants

The study report, "Dispersion of Silicon Powder", covering June through September, 1983, is included as Appendix D. A technical paper was subsequently prepared by Dr. Sacks and submitted (after NASA approval) to the American Ceramic Society for publication.

The Si_3N_4-Y_2O_3-Al_2O_3 slip program was subcontracted to Dr. I.A. Aksay of UCLA and subsequently of the University of Washington to support sintered Si_3N_4 rotor processing technology.

Objectives/tasks included:

- o Baseline characterization of commercial Si_3N_4, Al_2O_3 powders
  - Agglomerate content and structure
  - Particle size distribution
  - Particle size control by ellutriation
- o Electrophonetic mobility for each powder in aqueous suspension
- o Zeta potential versus pH
- o Preparation of cast specimens for sintering and evaluation at Garrett

The study report, "Development of Homogeneity in Si_3N_4 Ceramics by Colloidal Filtration", was co-authored by I.A. Aksay and C.A. Ambarian of UCLA and covers June through September, 1983. The report is included as Appendix E.

Substantial progress was achieved in the two university subcontracts. Both contracts were extended through May 1984.

4.5.2 Screening Rigs

4.5.2.1 Ceramic Component Thermal Screen Tests

4.5.2.1.1 Turbine Shroud Screening Rig

In January 1984, the AGT101 turbine shroud screening rig was tested to determine the effect of various rig insulation configurations on the heat transfer rate into the turbine shroud. A metal turbine shroud, instrumented with thermocouples, was used to

model the heat transfer coefficients. The purposes of the test series were to evaluate the effect of the new insulation configuration that was in use when two shrouds fractured during screening, and to determine a suitable rig insulation configuration (and thermal transient cycle) for future ceramic shroud screening.

Tests were run using improved insulation both with and without stators. The rig then was reconfigured to the previous insulation arrangement. Again, tests were run with and without stators. Finally, the new insulation piece, which nests behind the turbine shroud, was installed with the remainder of the rig employing the former insulation. This configuration was run to provide data on any effects that this single change may have. The three different insulation configurations are illustrated in Figures 74, 75, and 76.

In February 1984, RBSN turbine shroud S/N 432 was thermal-screen tested to 2100F with a Ford (one-piece) RBSN stator S/N 206 and SASC backshroud S/N 104A. The thermal transient cycle used is shown in Figure 77. The rig insulation configuration and thermal cycle conform with those previously used with success in this rig. (Analysis of data regarding insulation effects was not available at this reporting period.)

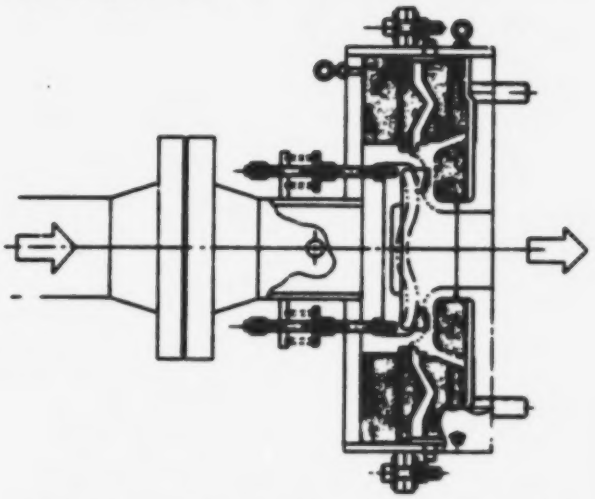

Figure 74. Turbine Shroud Screening Rig With New Insulation Configuration (Babcock & Wilcox "Kaowool").

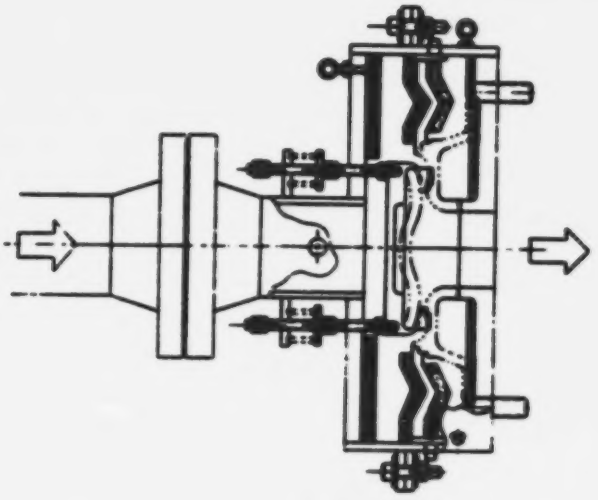

Figure 75. Turbine Shroud Screening Rig With "Old" Insulation Configuration (Fiberglass "wet blanket").

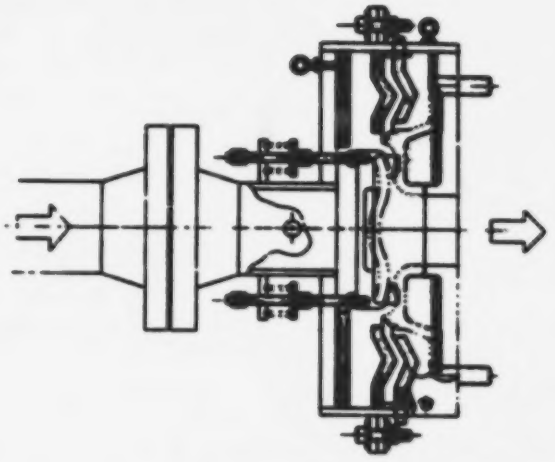

Figure 76. Turbine Shroud Screening Rig With "Donut" Added to Former Insulation Configuration.

While some acoustic events of high dB output were noted during the cycle, ringdown counts associated with these events were low, giving reason to believe that no ceramic fracture had occurred. However, disassembly at the finish of the test series revealed that the turbine shroud had suffered multiple fractures and that the stator was chipped at one corner.

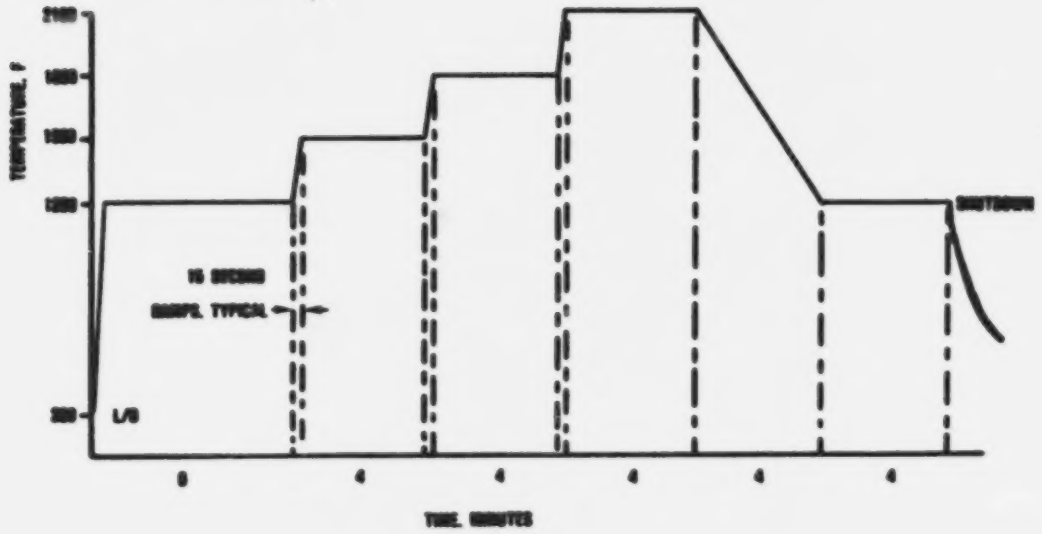

Figure 77. Shroud Thermal Screen Cycle.

The primary cause of fracture is thought to be excessive thermally induced stress at the fillet of a second seal land (Figure 78) that was introduced to accommodate a possible alternative seal design. This turbine shroud was the only one screened that incorporated this additional land. Calculations show the fillet of the second seal land to be even more highly stressed than the first seal land fillet, thus making it the area of highest stress in the part.

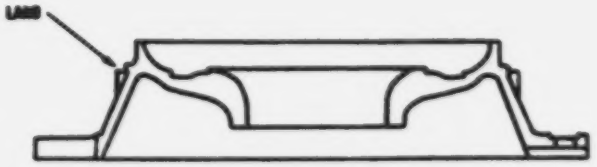

Figure 78. Turbine Shroud Second Seal Land Area.

In spite of the conclusions regarding thermal stress as the cause of initial fracture, concern remains over the possibility of mechanical interference that may induce excessive mechanical stress in the ceramic parts. Specifically, the all-thread rods used to transmit a spring load to the ceramic parts are known to relax and bend at test temperatures, allowing a mechanical bind to develop where the rods pass through the rig inlet housing. Ceramic fracture could result. To preclude this possibility, the rig was modified so that the ceramic test parts are loaded from the turbine shroud side rather than from the turbine backshroud side.

This redesign and fabrication activity was carried out during late February and early March 1984. Figure 79 shows the baseline rig configuration (as used for Turbine Shroud S/N 432). Figure 80 depicts the same rig after the modifications. Advantages of the modifications are as follows:

- o Removal of spring loading mechanism to a lower temperature area
- o Inclusion of a transition duct (as dedicated rig hardware) to better duplicate engine flowpath geometry

The revised rig was first used with turbine shroud S/N 379 in March 1984. Transition duct S/N 110 was incorporated in this rig to better simulate engine flowpath conditions (no other major ceramic components were employed).

A mechanical interference, due to inadequate allowance for thermal growth of the turbine shroud backing plate (a new part for

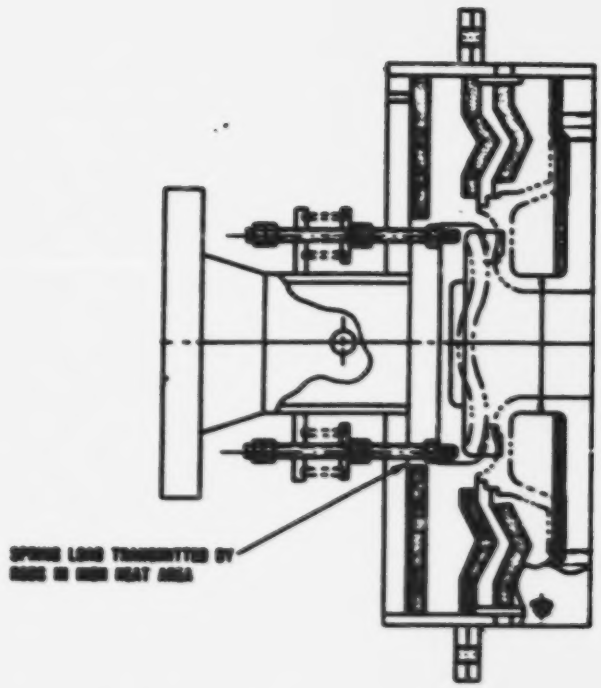

Figure 79. Baseline Turbine Shroud Screening Rig.

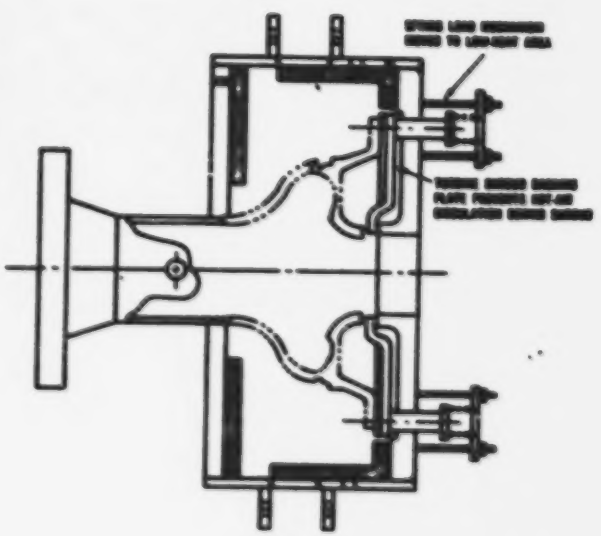

Figure 80. Modified Turbine Shroud Screening Rig.

this rig, Figure 80), resulted in fracture of the turbine shroud during this test. The transition duct was not damaged. Further rework of the rig was initiated following the test. Modifications included slotting the backplate and opening clearances at the plungers. In addition, the combustor baffle, turbine backshroud, and seal rings were added to better simulate the flow path. The next test was performed in early April 1984 and included the ceramic parts listed in Table 10:

The assembly was subjected to the thermal cycles described in Table 11. The test resulted in a mechanically induced fracture of the turbine shroud, initiating at the turbine shroud discharge section inner diameter. Interference, as shown in Figure 81, was the most likely cause of fracture; there was evidence of possible interference between plungers and shroud holes as well. Following this test, the rig was again reconfigured (Figure 82).

In mid-April 1984, testing was resumed with the ceramic parts listed in Table 12.

Following cycles to 2100F, similar to previous testing, the parts were observed with a boroscope to verify that no fracture had occurred. A decision then was made to attempt a cycle to 2300F according to the schedule in Table 13.

Lack of significant acoustic emissions was taken as a positive sign that no fractures occurred at the 2300F cycle. Again, a decision was made to increase the maximum temperature, this time to 2500F, according to the schedule in Table 14.

After 3.5 minutes at 2500F, a high dB event was noted. This event coincided with a minor adjustment to the discharge valve position (to control rig pressure) and with an approximate 50F drop in temperature. Also, a series of high dB events occurred at 29 minutes after shutdown.

Disassembly revealed fractures to the turbine shroud and the integral stator ring. The stator failure was secondary to the turbine

Table 10. Turbine Shroud Rig Ceramic Parts

S/N	Part Name	Material	Source
468	Turbine Shroud	RBSN	ACC
206A	Turbine Stator	RBSN	Ford
105A	Turbine Backshroud	SASC	CBO
111	Combustor Baffle	SASC	CBO
115	Transition Duct	SASC	CBO
P/N			
3689851	Seal Ring	RBSN	ACC
3689853	Wave Springs (2)	RBSN	ACC

Table 11. Turbine Shroud Thermal Test Cycles *

Time, min		Temperature, F
6		1200
4		1500
4		1800
4		2100
4	rampdown to	1200
4		1200
Shutdown		

*Light-off to 1200F in 15 seconds; 15 second ramps

shroud fracture. The most likely explanation of the fracture is that the pressure difference across the stators created a force sufficient to counteract the spring load holding the ceramic stack together. Thus, the assembly was sensitive to any fluctuations in pressure. Initiation of fracture was at the turbine shroud seal land outer diameter (OD) where contact was made with the transition duct. Pieces of RBSN (from the turbine shroud) were lodged in the pilot diameter fillet of the transition duct, indicating a contact problem in the area.

Also noteworthy is that, although a part of an assembly did suffer fracture, the turbine backshroud, combustor baffle, transition duct, ceramic seal, and ceramic wave springs all survived a thermal transient cycle to 2500F. Thus, thermal screening of these parts to 2500F has been successfully initiated.

Prior to further testing, the turbine shroud screening rig was modified as follows:

- The metal spring-loaded plungers were replaced with ceramic material (HPSN)
- The metal backing plate behind the turbine shroud was replaced with a modified ceramic outer diffuser housing
- Ceramic fiber woven cloth was installed at the interface of the turbine shroud and the transition duct
- Displacement transducers were mounted at the plungers to monitor spring height changes due to rig thermal growth and any sudden movement of the turbine shroud

The modifications are illustrated in Figure 83.

In mid-May 1984, the turbine shroud screening rig was assembled to the new configuration and tested to a maximum temperature of 2500F with the ceramic components listed in Table 15.

A description of the thermal transient cycles is given in Table 16. Rig inlet pressure

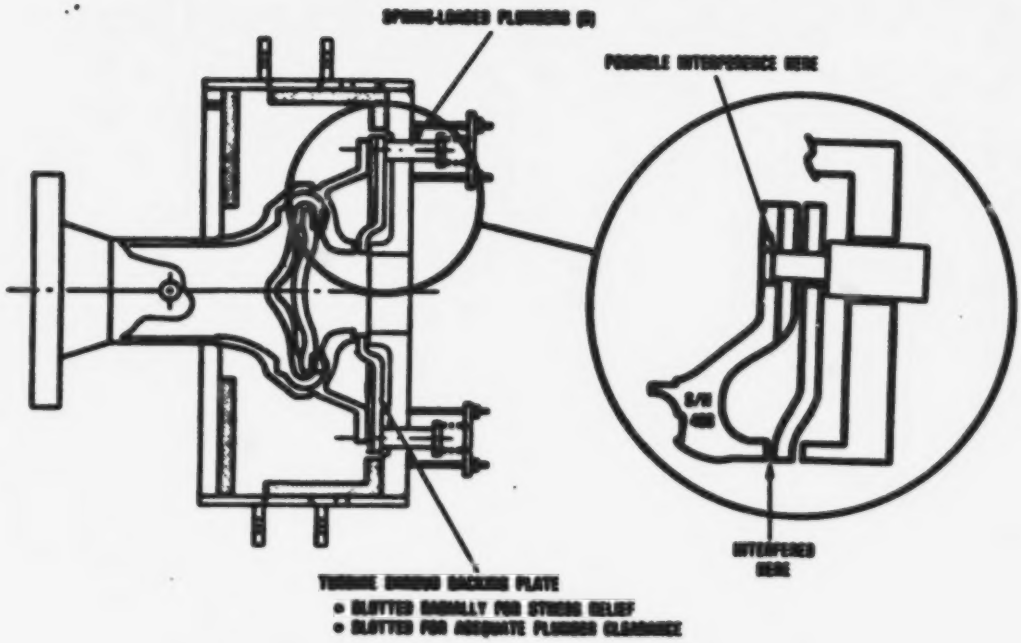

Figure 81. Modified Turbine Shroud Screening Rig.

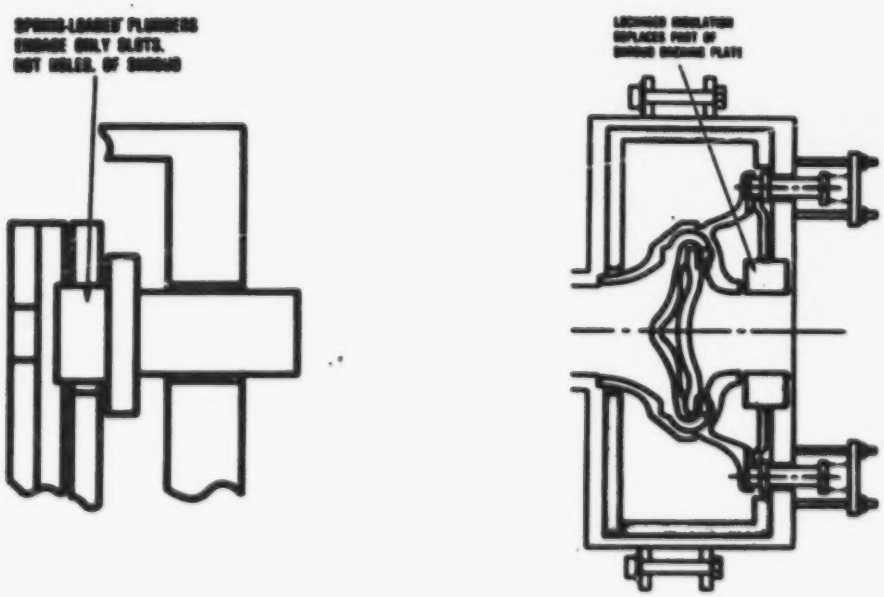

Figure 82. Reconfigured Turbine Shroud Screening Rig.

Table 12. Turbine Shroud Rig Ceramic Parts

S/N	Part Name	Material	Source
468	Turbine Shroud	RBSN	ACC
206	Turbine Stator	RBSN	Ford
105A	Turbine Backshroud	SASC	CBO
111	Combustor Baffle	SASC	CBO
115	Transition Duct	SASC	CBO
P/N			
3809851	Seal Ring	RBSN	ACC
3809853	Wave Springs (X)	RBSN	ACC

Table 13. Turbine Shroud Thermal Test Cycles *

Time, min		Temperature, F
6		1200
4		1500
4		1800
4		2100
10		2300
4	rampdown to	1200
4		1200
Shutdown		

*Light-off to 1200F in 15 seconds; 15 second ramps

Table 14. Turbine Shroud Thermal Test Cycles *

Time, min		Temperature, F
6		1200
4		1500
4		1800
4		2100
4		2300
4		2500
5	rampdown to	1200
4		1200
Shutdown		

*Light-off to 1200F in 15 seconds; 15 second ramps

was held from 5 to 7 psig during testing (as opposed to 10 psig) to limit rig differential pressure to under 6 psid. The lower pressures assure that the forces generated by the pressure differential are not sufficient to offset the spring forces that load the ceramic parts in the rig.

Although acoustic emissions indicated a high energy dissipation at 3 minutes after shutdown (2500F maximum temperature), rig teardown revealed all components intact, with the exception of a spalled wave spring. This discrepancy in acoustic indications could be explained by the wave guide wiping across the surface of the turbine shroud as the rig cooled. Wave spring spalling has been traced to the quality of the powder used in spring manufacture. This situation has since been rectified.

Successful completion of this test marks a significant milestone--survivability at 2500F of a ceramic subassembly. The same set of hardware will be used in the hot stator rig to demonstrate survivability over an extended period of time and under more severe thermal transients.

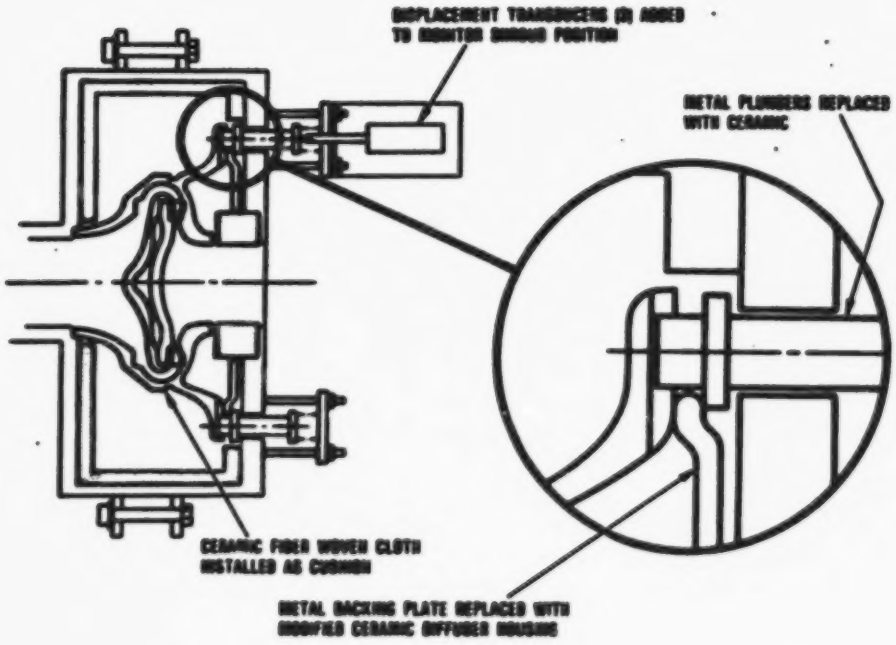

Figure 83. Rig Configuration for First Successful 2500F Run.

Table 15. Turbine Shroud Rig Ceramic Parts

S/N	Part Name	Material	Source
546	Turbine Shroud	RBSN	ACC
205	Stator	RBSN	Ford
122	Combustor Baffle	SASC	CBO
105A	Turbine Backshroud	SASC	CBO
112	Transition Duct	SASC	CBO
—	Spacer	LAS	
P/N			
3609653	Wave Spring	RBSN	ACC
3609651	Seal Ring	RBSN	ACC

Table 16. Turbine Shroud Screening Test

	Ramp, sec	Temperature, F	Hold Time, min	Acoustic Indications
Cycle 1 P_{rig} = 7 psig	15	1200	6	No significant events
	15	1500	4	
	15	1800	4	
	15	2100	4	
	240	1200	4	
	0	Shutdown	Boroscope	
Cycle 2 P_{rig} = 7 psig	15	1200	6	No significant events
	15	1500	4	
	15	1800	4	
	15	2100	4	
	15	2300	10	
	360	1200	6	
	0	Shutdown	Boroscope	
Cycle 3 P_{rig} = 5-7 psig	15	1200	6	
	15	1500	4	
	15	1800	4	
	15	2100	4	
	15	2300	4	
	15	2500	5	
	360	1200	6	
	0	Shutdown	Disassemble	Many events 90+ dB at 3 minutes after shutdown. No fracture.

Later in May 1984, the turbine shroud screening rig was reassembled and tested with the ceramic components listed in Table 17.

The test objective was to screen the turbine shroud subassembly to a more severe thermal start transient (Figure 84). The test was conducted in a stepwise manner to the desired transient. Transients to 1200, 1400, 1600, 1800, and 1900F were successfully run prior to the 2000F run.

Two ceramic waveguides were utilized in this test; one in direct contact with the turbine shroud mounting flange and the other in contact with the transition duct. The new AE

Table 17. Turbine Shroud Rig Ceramic Parts

S/N	Part Name	Material	Source
545	Turbine Shroud	RBSN	ACC
Set 4	Turbine Stator Assembly	SASC	CBO
101A	Turbine Backshroud	SASC	CBO
120	Combustor Baffle	SASC	CBO
110	Transition Duct	SASC	CBO

monitoring equipment was used in conjunction with the waveguides, with data storage in real time on floppy disk.

During the transient run to 2000F, both AE probes registered a high dB event that was coupled to within 20 μsec. The energy detected was approximately equal in magnitude on both waveguides, indicating a fracture had occurred within the subassembly.

Disassembly/inspection revealed a fractured turbine shroud and one chipped stator. (The stator was hand finished and used in a subsequent test).

Fractography revealed the fracture origin in the stator platform OD region and propagating into the seal land area.

Component stress analysis is in process to define the stress field in the region of the fracture origin. Prior to further turbine shroud screening, modifications were made to the rig to provide a closer duplication of the engine component loading configuration.

Figure 83 shows the turbine shroud spring loaded through the stators, backshroud, and baffle to the transition duct. The spring load in this case was reacted against the rig hous-

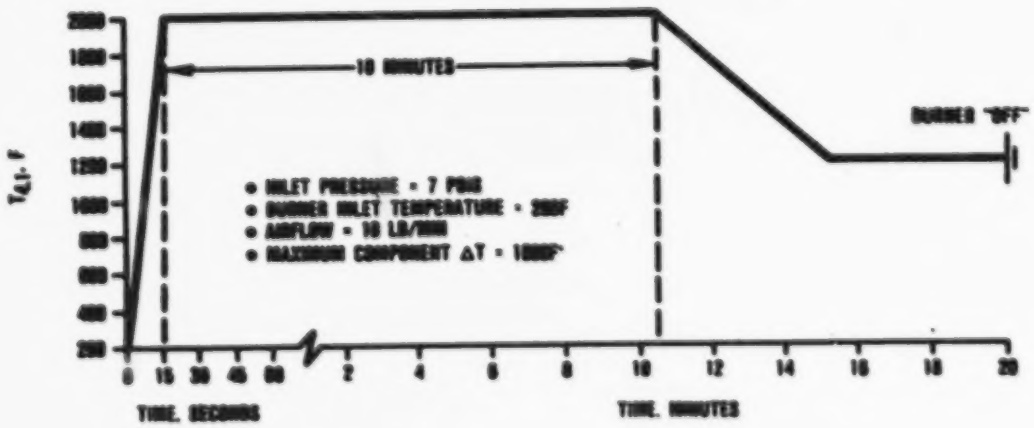

Figure 84. Turbine Shroud Thermal Screening Rig Rapid Transient Test.

ing. The engine loading has the spring load on the transition duct through the combustor liner and the turbine shroud is fixed against the rocker assembly. Since a question remains as to whether the fracture of turbine shroud S/N 545 was mechanically or thermally induced, rig reconfiguration to the engine loading configuration eliminated the possibility of excessive mechanical loading in future tests (Figure 85).

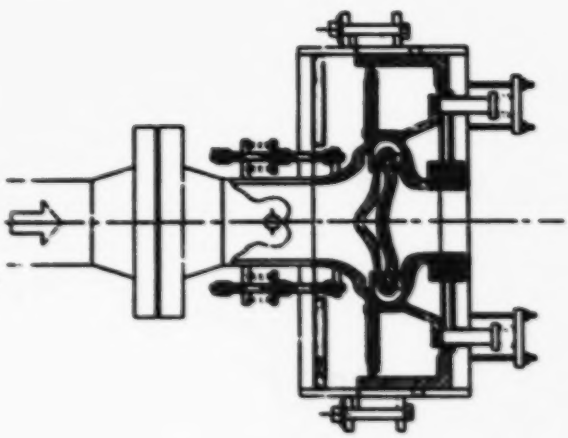

Figure 85. Rig Configuration to the Engine Loading Configuration.

A followup test was conducted in late May 1984, using the components listed in Table 18.

As in the previous screening test, acoustic emissions were monitored in real time on two waveguides, and rig inlet conditions at initial lightoff were the same. A rig checkout run to 1400F was programmed into the electronic control using Type "S" (Platinum-Platinum 10-percent) thermocouples in the temperature control loop.

As the test was initiated, a fluctuation in $T_{4.1}$ (turbine shroud subassembly inlet temperature) was recorded on a strip chart with an indicated reading of less than the desired 1400F set point. At this same time in the test, a fuel flow in excess of that required to achieve a 2500F rig inlet temperature was recorded. The recorded parameters are shown in Figure 86 and indicate that at 45 seconds into the test a high dB (coupled) acoustic event occurred, followed by a drop in rig differential pressure.

On disassembly and inspection, the turbine shroud and turbine backshroud were found to be fractured, with several stators exhibiting secondary damage. The rig showed evidence of overtemperature during the test in excess of 2500F, apparently caused by a failed temperature control loop thermocouple. Fractography of components is in process.

Table 18. Turbine Shroud Rig Ceramic Components

S/N	Part Name	Material	Source
102	Turbine Shroud	SASC	Kyocera
110	Transition Duct	SASC	CBO
120	Combustor Baffle	SASC	CBO
101A	Turbine Backshroud	SASC	CBO
Set 4	Turbine Stator	RBSN	ACC

ORIGINAL PAGE IS
OF POOR QUALITY

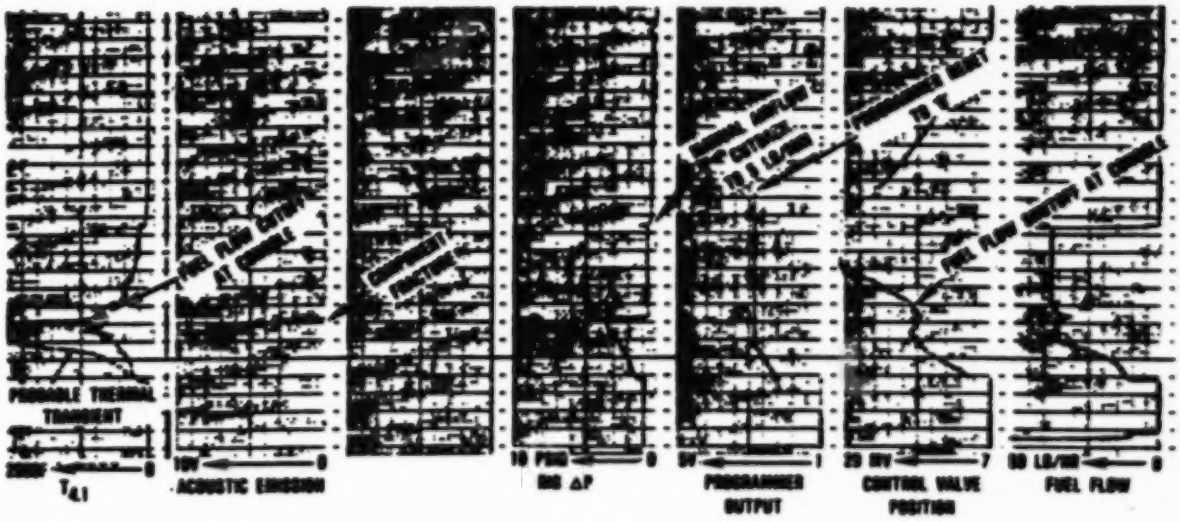

Figure 86. Turbine Shroud Thermal Test Rig Charts.

Inner Diffuser Housing and Outer Diffuser Housing Screening Rig

During late March 1984, three inner and outer diffuser subassemblies were successfully thermal screened to 2100F in a start transient of 15-seconds duration. Table 19 details the test conditions and the hardware that was screened.

In this series of tests, an off-the-shelf ceramic ball (Al_2O_3 aluminum) was substituted for the ceramic (LAS) load spacer. The LAS load spacer had a tendency to become cocked and wedged in the guide sleeve. A comparison of the two load spacer types is shown in Figure 87.

Additionally, this series of tests incorporated the second-generation rocker/eccentric design and a revised ceramic bolt design. Figure 88 illustrates the difference in first- and second-generation rocker/eccentric designs.

Transition Duct and Baffle Screening Rig

During early May 1984, four sets of ceramic transition ducts and combustor baffles were screened to a maximum temperature of 2250F. Several lightoffs were made to increasingly higher temperatures, with the limit being a lightoff to 2250F in 15 seconds. The specific parts screened are listed in Table 20.

During testing, transition duct S/N 113 fractured when the automatic control system malfunctioned because of a faulty adjustment. The malfunction exposed the parts to temperature excursions from well over 2500F to under 1500F at several points in the testing. Analysis indicated the fracture was due to thermal stresses in a cool-down mode, consistent with the excursions seen. During this series AE went to 85 dB at almost 300 ring-down counts.

All other pieces screened (including combustor baffle S/N 123, tested with duct S/N

Table 18. Inner and Outer Diffuser Housing Test Conditions and Hardware

Test Conditions	
Airflow	10 lb/min
Preheat temperature	150-200F
Maximum temperature	2100F
Transient time to T_{max}	15 seconds
Time at temperature	5 minutes
Downshock transient	30 seconds from T_{max} to 1300F (T_{min})
Hold time at T_{min}	4 minutes
Total cycles each set	5

Hardware*

S/N	P/N	Part Name	Material	Source
110-2	PA3609638	Inner Diffuser Housing	SNN	NGK
109-2	PA3609637	Outer Diffuser Housing	SNN	NGK
108-6	PA3609639	Spacer Ring	SNN	NGK
110-1	PA3609638	Inner Diffuser Housing	SNN	NGK
109-1	PA3609637	Outer Diffuser Housing	SNN	NGK
108-1	PA3609639	Spacer Ring	SNN	NGK
348	PA3609638	Inner Diffuser Housing	RBSN	ACC
339	PA3609675	Outer Diffuser Housing	RBSN	ACC

*All components were successfully screened through the five start transients.

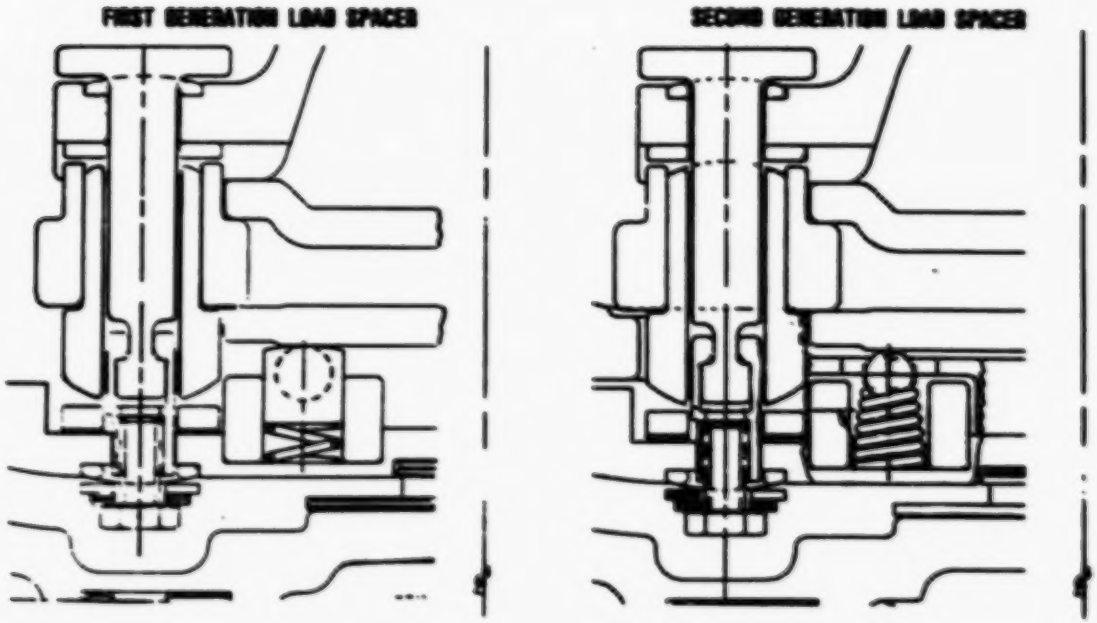

Figure 87. First- and Second-Generation Load Spacers.

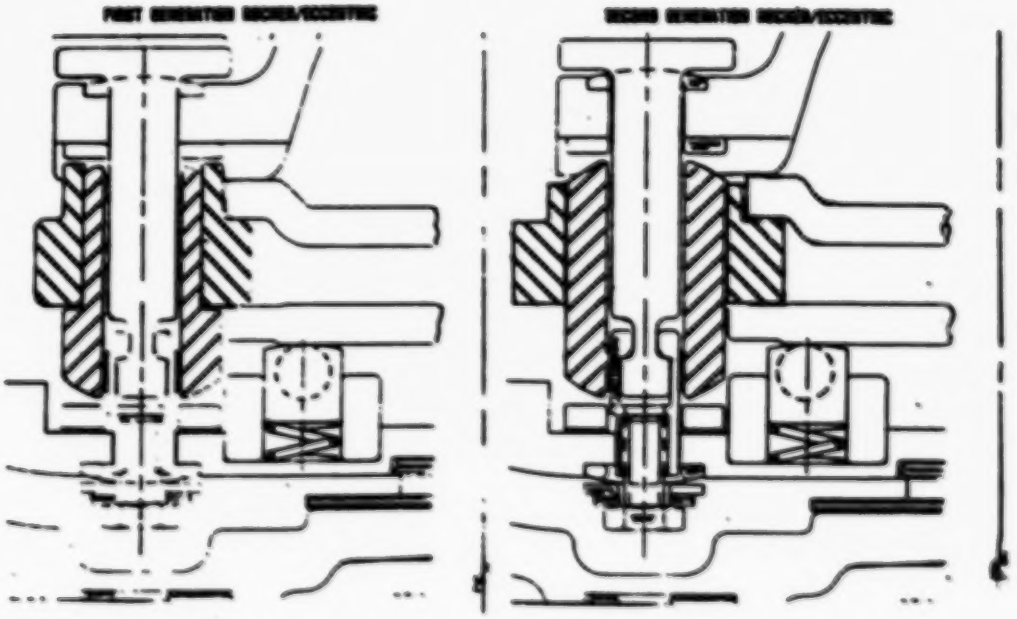

Figure 88. First- and Second-Generation Rocker/Eccentric Design Comparison.

Table 20. Transition Duct and Baffle Screening Components

Date	Baffle S/N	Transition Duct S/N
May 7, 1984	124	115
May 8, 1984	125	112
May 8, 1984	123	113
May 9, 1984	122	114

113) survived the screening without damage. This testifies to the high level of confidence that can be placed in these parts in simulated (or actual) engine lightoffs.

Hot Stator Rig

Building of the test rig was initiated following the successful screening tests of RBSN turbine shroud S/N 546 and associated components. The rig build will incorporate the components used in the 2500F screening tests, as well as a LAS flow separator housing and an SASC regenerator shield. The primary purpose of the initial moderate temperature runs will be to verify the rig setup and the identification of potential problem areas.

Build activity for this period included: cementing additional rig insulation into place, fabrication of a spacer ring to center the flow separator housing, modification to acoustic waveguide mounting locations, installation of the turbine shroud, bolts, alignment spacers and related hardware; and fabrication of a ceramic seal spacer (to accommodate the transition duct with short pilot).

A list of the ceramic parts being built into this rig is given in Table 21.

4.5.3 Ceramic Rotor Material Development

ACC continues to fabricate rotors of 8-percent Y_2O_3, 4-percent Al_2O_3 composition designated Code 1. Efforts also continue to develop a 6-percent Y_2O_3, 2-percent Al_2O_3 material (Code 2) and a sintered, reaction-bonded Si_3N_4 composition.

ASEA furnished Garrett with initial rotor hot isostatic pressing (HIP) study results (Table 22).

Rotor C/N 03093 was cut into test bars for density and modulus of rupture (MOR) measurements, microstructure, and X-ray evaluation. The average density of 41 specimens was 99 percent theoretical between a range of 98 to 100 percent theoretical. The density variation was random throughout the rotor. The room temperature flexure strength of 19 specimens was 105 ±11 ksi and the 2200F flexure strength of 21 specimens was 60 ±6 ksi. Table 23 summarizes flexure strength results and corresponding fracture origins. There does not appear to be a direct correlation between type of fracture origins and the low or high strength values.

A second rotor, slip cast by ACC (8-percent Y_2O_3, 4-percent Al_2O_3) and sintered at Ford, was cut into test bar specimens. Both the Ford sintered and ASEA HIP rotors were 99 percent of theoretical density. The strength of the Ford sintered material was measured at room temperature and 2200F. Table 24 shows a comparison of the room temperature and 2200F flexure strength of both the Ford sintered and ASEA HIPped rotors. There is little difference in the room temperature strength of the rotors. At 2200F, the Ford sintered rotor has a strength of 51 ±6 ksi, compared to 60 ±5 ksi for the ASEA HIPped rotor.

Future testing is required to verify the apparent improvement in high temperature strength of HIPped rotors.

During this reporting period, evaluation of the microstructure and phase composition of rotors S/N 316 (Ford sintered) and C/N 03093 (ASEA HIPped) was completed. Figure 89 compares the microstructure of the two rotors. The microstructure of C/N 03093 con-

Table 21. Hot Stator Rig Ceramic Parts

P/N	Description	Material	S/N
PA3689628	Bolt Assembly (3)	HPSN	013, 014, 015
PA3689619	Alignment Spacer (Rocker) (3)	HPSN	004, 005, 006
PS3689679	Turbine Shroud	RBSN	546
3946122	Stator (integral)	RBSN	295
PA3689616	Backshroud	SASC	105A
PA3689652	Seal, Flow Separator	RBSN	102
PA3689653	Wave Spring	RBSN	249
PA3689653	Seal, Piston Ring	RBSN	321
PA3689615	Combustor Baffle	SASC	122
PA3689649	Transition Duct	SASC	112
3946154	Regenerator Shield	SASC	101B
PA3689655	Flow Separator Housing	LAS	12
PA3689610	Plug Seal	Alumina	
PA3689620	Mounting Platform	Alumina	104, 105, 106
PA3689629	Inner Thermocouple Load Spacer	Alumina	
PA3689630	Male Seal	Alumina	
PA3689631	Female Seal	HPSN	284, 285, 286

Table 22. Rotor Hot Isostatic Pressing Results

	Rotor No.	HIP Temperature, F	Time, hours	Density, g/cm^3
Cast and Nitrided by Ford	R 140	3137	1	3.31
	R 146	3137	1	3.31
	R 149	3137	1	3.31
	10142	3002	1	3.26
Cast by ACC	03093	3002	1	3.27
	09212A	3002	2	3.23

Table 23. Summary of Flexure Strength and Fracture Origins Rotor C/N 03003 HIPped at ASEA, 3002F

Specimen Number	Room Temperature Strength	Fracture Origin (40X)
13743	119.3	—
13744	128.8	Tensile Face (TF)
13745	95.6	TF Metallic Inclusion
13746	106.9	—
13747	110.8	Internal Metallic Inclusion
13748	92.3	—
13749	115.9	Internal Metallic Inclusion
13750	102.4	—
13751	120.9	Chamfer Metallic Inclusion
13752	101.3	Subsurface Metallic Inclusion
13769	115.9	—
13770	104.6	TF
13771	96.2	Internal Metallic Inclusion
13772	91.1	TF
13773	108.6	TF
13774	88.3	Metallic Inclusion
13775	97.3	TF
13776	90.0	Porous Agglomerate
13777	106.9	Internal Metallic Inclusion
Specimen Number	**2200F Strength**	**Fracture Origin (40X)**
13753	58.5	—
13754	61.9	TF
13755	54.6	TF
13756	54.0	Chamfer
13757	58.5	TF
13778	57.4	TF
13779	66.4	TF
13780	54.6	Chamfer
13781	65.3	TF
13782	63.6	TF
13758	71.0	TF
13759	60.2	No chamfer/broke at sharp corner
13760	59.7	TF
13761	60.2	TF
13762	58.1	Chamfer
13763	60.1	Chamfer
13764	66.4	TF
13765	58.1	TF
13766	60.1	TF - White surface spot
13767	59.7	Chamfer
13768	58.6	TF

Table 24. Ford Sintered and ASEA HIP Rotor Flexure Strength Comparison

	Ford (S/N 316)		ASEA (C/N 03093)	
	Room Temperature	2200F	Room Temperature	2200F
Number of Test Bars	30	10	19	21
Average Flexure Strength, ksi	110 ±10	51 ±6	105 ±11	60 ±5
Characteristics Strength, ksi	114	54	110	62
Weibull Modulus	14	10	11	16

sists of very small equiaxed grains, while the microstructure of S/N 316 consists of large elongated grains in a fine grain matrix.

The microstructures are consistent with the densification temperatures and times employed. The ASEA HIP process consisted of a 1-hour hold at 3002F and the Ford sintering process is approximately a 3-hour hold at higher than 3362F.

Figure 90 presents X-ray diffraction results comparing the ASEA and Ford-processed rotors. Both rotors have Si_3N_4 as the major phase, with some evidence of a second phase ($Y_2Si_2O_7$) in the ASEA rotor. More detailed X-ray work is necessary to evaluate the presence of any minor phases.

ACC continues to fabricate rotors of the 8-percent Y_2O_3, 4-percent Al_2O_3 composition, with final densification accomplished at Ford, ASEA, and ACC. Preliminary data suggests that a minimum green density in cast rotors must be obtained to assure full densification during sintering. ACC now processes rotors that exhibit green densities above a defined minimum. Efforts continue on the development of the 6-percent Y_2O_3, 2-percent Al_2O_3 composition.

Also, work continues on developing a sintered reaction bonded Si_3N_4 composition.

Ceramic Rotors Received

Tables 25 and 26 present the status of ACC Code 1 and 2 rotors received during this period. Ford did not deliver any rotors during this period.

4.6 Rotor Dynamics/Foil Bearing

4.6.1 Rotor Dynamics/Foil Bearing Rig

As indicated in Reference 8, an aggressive effort to map the rotor dynamics rig thermal environment was undertaken including actual foil bearing temperatures. Figures 91 and 92 show the thermocouple locations and installation used for testing. Measured temperature levels were lower than previously predicted by approximately 8 to 10 percent. Using these values and associated structural temperature measurements, the changes in sway space were determined for the test rig (Figure 93) as a function of speed. Since rotor stability is improved with decreasing sway space within limits, an investigation of starting sway space build dimensions was initiated to define the geometry limits over which stability can be maintained. Tests were conducted from 0.020 to 0.006 inch diametral sway space. Stability was maintained throughout a range from 0.016 to 0.006 inch diametral sway space on the rig.

ORIGINAL PAGE IS
OF POOR QUALITY

(A) 500x (B) 1000x

(A) ROTOR C/N 03003
HIPped BY ASEA (P = 3.28 g/cm³)

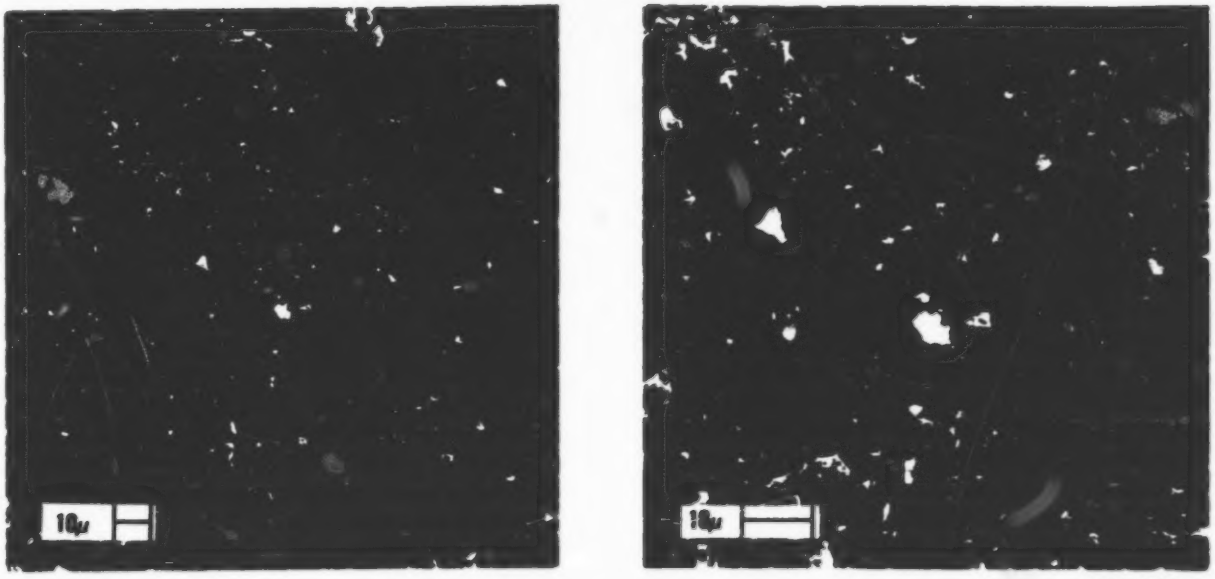

(A) 500x (B) 1000x

(B) ROTOR S/N 316
SINTERED BY FORD (P = 3.27 g/cm³)

Figure 89. Microstructures of ACC Cast Rotors Densified by Ford and ASEA.

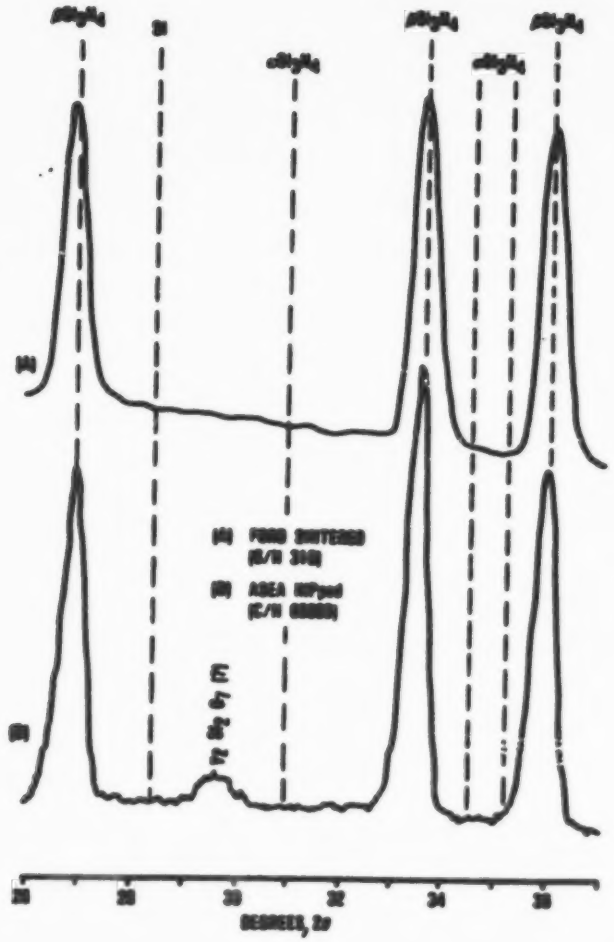

Figure 96. ASEA and Ford Processed Rotors X-Ray Diffraction Results.

Additional activities included screening bearings for engine operation, supporting rotor dynamic task force activities, and preparing for the planned rotating group imbalance tests.

4.8.2 Single Foil Bearing Rig Testing

Single foil bearing rig testing to determine the thermal test bearing and the sway space versus stability test bearing (Sequence 1 of this testing) was completed. The stated test objectives were:

- Map power consumption throughout a speed range corresponding to the engine operating speed range for the subject bearings
- Provide empirical data for use in further refinement of existing analytical foil bearing models

Test objectives were met. Table 27 shows a summary of results. The Sequence 1 sway space test bearing was run twice because oil from the loading device contaminated the bearing, causing erroneous power losses. Both

Table 25. ACC Code 1 Rotors Received

January 1 - June 30, 1994

Rotor Number	Process Status	Comments
S/N 572	Sintered at Ford/ failed NDE	Undergoing NDE study
S/N 573	Sintered at Ford/ passed NDE	
S/N 632	Sintered at Ford	
S/N 633	Sintered at Ford	
S/N 634	Sintered at Ford	
C/N 0319402	Presintered	At Ford for sintering
C/N 03154	Presintered	At Ford for sintering
C/N 0319401	Presintered	At ASEA for sintering
C/N 04124	Presintered	At ASEA for sintering
C/N 04184	Presintered	At ASEA for sintering
C/N 0424402	Presintered	At Ford for sintering
C/N 0416402	Presintered	At Ford for sintering
C/N 04254	Presintered	At Ford for sintering
C/N 05014	Presintered	At Ford for sintering

bearings were run with no load and a 1-g (6-pound) load to provide data for correlation with analytical bearing models.

Post-run inspection showed no damage or excessive wear on either bearing. Extremely low coating wear was indicated by post-run excessive wear on either bearing. Extremely low coating wear was indicated by post-run load-deflection tests showing almost no

Power consumption testing also was completed for 6.9 mil total thickness "P" type foil change in total bearing deflection.

bearing of the same type currently used in the engine with a 6-mil sway space. The two cases tested were no load and a 1-g load representative of the engine. The no-load case was run to provide empirical data for use in improving the analytical foil bearing model now in use. The 1-g case provides data for use in engine thermal analysis. Test results showed bearing power consumption as follows:

- o 1-g load (100,000 rpm) 219 watts
- o No load (100,000 rpm) 145.6 watts

Table 26. ACC Code 2 Rotor Received

January 1 - June 30, 1984

Rotor Number	Process Status	Comments
C/N 0502301	Presintered	At ASEA for sintering
C/N 0502302	Presintered	At ASEA for sintering
C/N 05093	Presintered	At ASEA for sintering
C/N 04303	Presintered	At ASEA for sintering

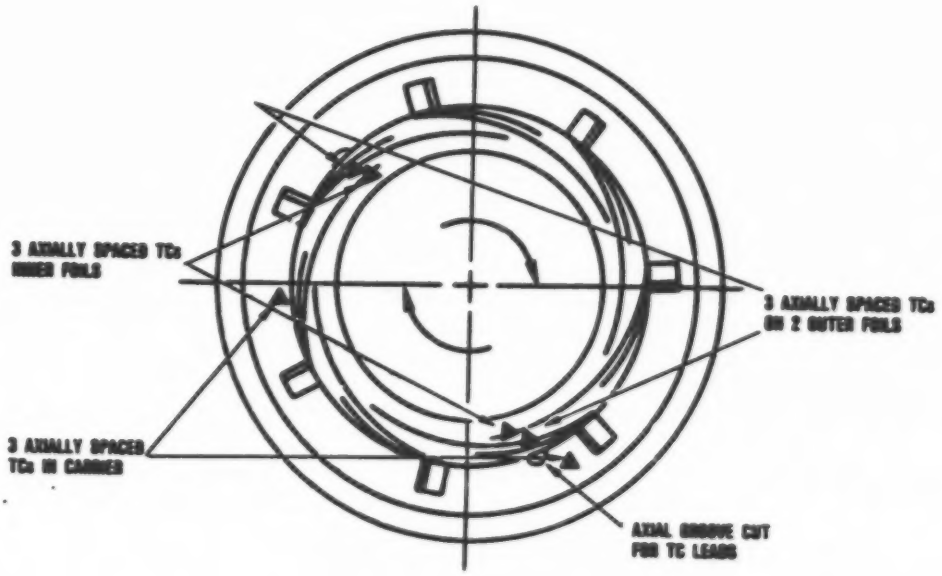

Figure 91. Location of Foil and Carrier Thermocouples for Rotor Dynamics Rig Thermal Testing.

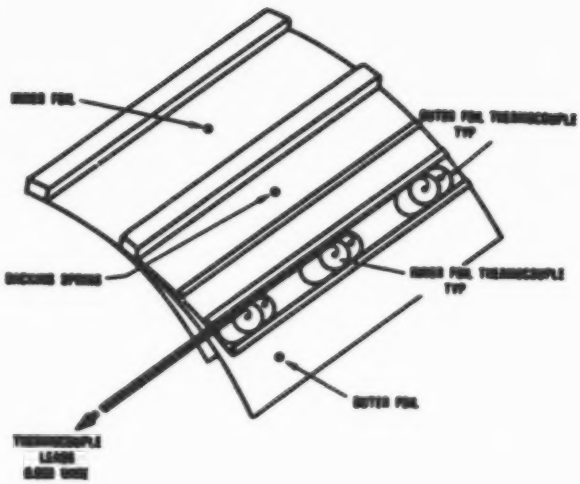

Figure 92. Foils and Backing Spring Thermocouple Installation.

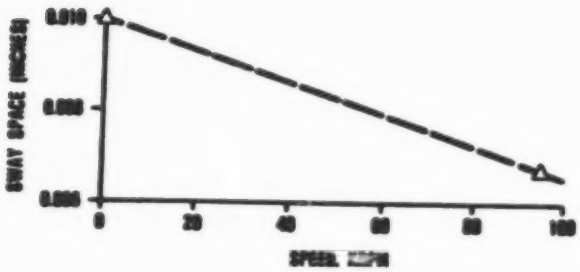

Figure 93. Sway Space as a Function Speed.

Table 27. Foil Bearing Power Consumption

Parameter	100,000 rpm		50,000 rpm	
	No Load Power Consumption, watts	1-g Load Power Consumption, watts	No Load Power Consumption, watts	1-g Load Power Consumption, watts
Thermal Test Bearing	100.6	155.1	32.0	60.1
Sequence 1 Sway Space Test Bearing	60.4	174.6	31.4	79.9

APPENDIX A
FORD MOTOR COMPANY
ADVANCED GAS TURBINE (AGT)
POWERTRAIN SYSTEM DEVELOPMENT PROGRAM
NINTH AGT SEMIANNUAL
TECHNICAL PROGRESS REPORT

1.0 TASK 2.3 - CERAMIC ROTOR

1.1 Material Development and Characterization

To provide for longer term material capability over that presently offered by SRBSN RM-3 material, sintering studies have been conducted to determine the sintering behavior of a number of SRBSN compositions. Composition ranges evaluated were 2 to 8 percent (by weight) Y_2O_3 and zero to 2 percent Al_2O_3. A number of compositions were found to be sinterable at one atmosphere nitrogen pressure to densities exceeding 99 percent. Some compositions were found to be sinterable to 99 percent with the addition of a second high pressure (100 atmospheres) stage to the sintering cycle. Billets have been submitted for machining into test bars to be used for property evaluation. The experimental data has been formulated into a model that can predict the sintering behavior of SRBSN materials. This model will be used for preliminary evaluation of further compositions.

As a result of recent reduction in program funding, the work in progress on material development described above will be completed, however, no further effort will be initiated in this area.

1.2 Bladed Rotor Fabrication

1.2.1 Slip Casting of RM-3 Material Rotors

Seventeen rotors, V-30 through V-47, were cast with the silicon slip casting process for RM-3 material during this report period. All were cast with slips containing the cationic polymer addition in combination with the 0.012-percent Keltex solution. Thirteen rotors were nitrided, and all except two were within the density range of 2.306 to 2.380 g/cm^3. Rotor V-30 had a density of 2.435 g/cm^3, and V-43 2.453 g/cm^3. Rotors V-31, V-32, V-33, and V-35 were not nitrided.

One rotor, V-26, was sintered to a density of 3.245 g/cm^3, slightly below the desired density of 3.27 g/cm^3. This rotor is scheduled for spin testing. Two rotors with no visible flaws, V-27 and V-41, are scheduled to be sintered.

Despite the progress made, cracking has not been fully resolved in development of the RM-3 silicon slip casting process. Considering recent budget restrictions, further development work on this process will cease and concentrate efforts on a modified, pre-reacted process (RM-20 Material). However, RM-3 rotors already cast will continue through nitriding, sintering, and spin testing, as appropriate.

1.2.2 Slip Casting of RM-20 Material Rotors

Eleven AGT rotor castings have been made using the fugitive wax mold system by the modified, pre-reacted process (RM-20 Material). Stable slips have been developed using Dispex as a deflocculant and a dispersator for establishing a castable slurry. The slip remains stable under casting conditions for over 48 hours. Casting times of 24 hours are required. Hub cracking has been eliminated with a sealed plaster mold system. The plaster is sized according to the moisture content of the slip; subsequently all surfaces are sealed to prevent water loss to the atmosphere. This technique eliminates green shrinkage during the casting period by precluding excessive water dissipation from the hub region. Piping and low density regions within

the hub have been eliminated by reducing the casting times to 24 hours and optimizing the centrifugal casting speed. Sintering cycles have been developed to yield final densities of 97 percent of theoretical density.

Problem areas that remain in casting include achievement of complete blade fill on a consistent basis, and improvement in water removal techniques. Wetting agents and centrifugal fill techniques are being investigated to improve blade fill, while improved drying processes are under investigation.

Rotor SC-8, of RM-20 material, was spin tested at room temperature in a vacuum to 102,400 rpm, at which point fragments from three blades separated from the rotor. Fracture surfaces were examined, but fracture initiation sites could not be identified. This rotor is being rebalanced and will be retested.

2.0 TASK 2.7 - STATOR

2.1 Molding Development

An outer insert sticking problem was encountered with the stator tooling near the end of the last report period. This problem has been corrected and molding development resumed.

Additional molding studies were conducted varying material temperature, tool temperature, and inner (trailing edge forming) insert retraction timing during the tool opening sequence. No significant improvement in leading or trailing edge cracks was obtained.

Tool temperature measurements have shown that trailing edge cracks are influenced by the inner insert temperature. However, hot water supplied to temperature control passages in the tooling cannot provide sufficient heat to the inner inserts without adversely affecting the temperature in other areas of the tool. An additional electrical heating element has been designed and procured to supplement tool heat in the inner insert area.

Fifteen stators were molded at conditions previously identified as optimum for best overall quality. These parts were made to increase the supply of "best effort" parts for further processing.

A group of 624 test bars (1/8 x 1/4 x 4 inches) were molded of the same material used for stator molding. The bars were x-rayed and will continue through the processing steps.

Because of budget restrictions, further molding development of stators was discontinued during this reporting period.

2.2 Stator Processing

Feasibility of machining two-piece stators using crack-free half sections was established. However, since preliminary hot screening tests at Garrett showed encouraging results on one-piece stators with small vane cracks, additional work on the two-piece configuration was discontinued.

Fifteen stators were processed through nitriding in three batches. The first nitriding run included six stators. Because of a facilities power failure, all six were poorly nitrided and not candidates for further processing.

Visual inspection of the five stators in the second nitriding showed many shroud cracks in three of the stators. Two appeared acceptable and were submitted for machining. One of these subsequently developed many shroud cracks. The other stator (S/N 1020308) was visually inspected, appeared acceptable, and is continuing through machining.

Four stators were processed in the third nitriding run. One was cracked after nitriding. Another power failure occurred very early in the run and is believed to have caused the failure. The three other stators (S/N's 0125408, 0221405 and 0207404) are in good condition and will be processed for delivery.

MOR bars were processed through nitriding in two batches. Many of the bars in the first batch had numerous surface cracks similar to

those found in the stators. The second batch of test bars were nitrided along with the third group of stators and appear to be acceptable for further processing and shipment.

Because of reduction in program funding during this reporting period, parts in process will be completed, after which, no further work will be performed this fiscal year in stator process development.

3.0 TASK 2.7 - FLOW SEPARATOR HOUSING

Corning Glass Company delivered two flow separator housing castings to Ford. These castings are being inspected against the flow separator housing specifications, and will be returned to Corning for final machining. Assuming component casting quality meets specification, delivery to Ford of the first machined component is expected in September 1984.

APPENDIX B
AIRESEARCH CASTING COMPANY (ACC)
ADVANCED GAS TURBINE (AGT)
POWERTRAIN SYSTEM DEVELOPMENT PROGRAM
NINTH AGT SEMIANNUAL
TECHNICAL PROGRESS REPORT

1.0 SUMMARY

A total of 60 rotors were cast at AiResearch Casting Company (ACC) during this reporting period. These rotors, after passing final inspection at Garrett, were processed by ACC, ASEA, and Ford by sintering, encapsulation plus HIP, and by sinter/HIP. Densities of the rotors using these techniques consistently fell within the 3.26 to 3.28 g/cm^3 range.

ACC continued development of sinter/HIP equipment, and anticipates the delivery of a 2000C, 1500 psi system in September 1984 that will have a furnace capacity of 15 inches in diameter by 28 inches in length. The 100 psi nitrogen sintering unit is being utilized for pre-sintering of rotors. The current sinter/HIP units are capable of operating up to 15,000 psi in nitrogen, and with combinations of nitrogen and argon, of operating up to 30,000 psi.

During this reporting period a total of 39 static components were slip cast. These components included: turbine shrouds, inner and outer diffuser housings, baffles, transition ducts, and seal ring components. Twenty-six of these components have been processed and forwarded to Garrett for testing. Nine are in processing and four were scrapped during processing. Eighty-four stator vanes were injection molded and 33 of these were fully processed and shipped.

Several SRN-rotors have been processed to evaluate the relationship between slip viscosity, casting density, and depth of nitriding. A facility has been established to support materials characterization and specifications for Si_3N_4 and Si feed materials. This facility is being utilized in support of both slip casting and injection molding efforts.

2.0 BCDA - ROTOR - MATERIALS AND FABRICATION DEVELOPMENT

2.1 Productivity of Rotors

As a result of a more systematic process control program conducted at ACC, the rate and yield of fabrication during this reporting period has significantly improved. This improved productivity is clearly demonstrated by the increased number of pre-sintered rotors that passed final inspection at Garrett and were shipped to Ford or ASEA for final densification. Table B-1 compares the rotor productivities in the last three reporting periods. The increased productivity was due to the improved yield at each processing step based on the inspection specifications established at ACC. Table B-2 lists the data for this reporting period.

Table B-1. Increase In Rotor Productivity

Period	No. of Pre-Sintered Rotors Qualified for Final Densification
January - June 1983	3
July - December 1983	5
January - June 1984	9

2.2 Quality Control Program

To illustrate the improved quality control procedures, the following paragraphs provide some examples.

2.2.1 Characterization of Slips

Some typical values of slips for particle size distribution tests performed at ACC using equivalent spherical diameters in microns are listed in Table B-3.

PRECEDING PAGE BLANK NOT FILMED

Table B-2. Yield of Rotor Fabrication

Month (1984)	*Total Castings	No. of Rotors Passing Inspection After		
		Casting	Drying	Pre-sintering
January	10	9	7	2
February	8	4	3	3
March	7	4	4	4
April	9	6	6	5
May	11	10	10	4 (6 remain to be pre-sintered)
June	8	6	6	(not pre-sintered)

*Experimental castings are not included.

Table B-3. Particle Size Distributions of Slips

Slip No.	Particle Size at Percentiles, μm		
	90th	50th	10th
05014	2.7	0.88	0.37
04164	2.7	0.86	0.36
04184	2.8	0.90	0.37
05104	2.7	0.86	0.37
06124	2.7	0.86	0.37
05234	2.7	0.86	0.37
04274	2.7	0.86	0.37

A series of slips was tested using the Haake viscometer at 25C, with CV100 measuring drive, and ZA30 measuring system. Yield points of the slips were then determined on the shear stress versus shear strain rate curves. Table B-4 seems to indicate a correlation between yield point and gelling. This investigation may lead to the use of the Haake viscometer to control the quality of the slip prior to casting.

Table B-4. Yield Point of Slip and Quality of Casting

Slip No.	Test Date	Yield Point, Pa	Remarks
06044	6-13-84	0.14	Good casting
06124	6-19-84	0.13	Good casting
05314	6-12-84	0.29	Slip gelled; rotor cracked
04274	5-14-84	0.22	Good casting
04184	5-10-84	0.24	Good casting
04164	4-26-84	0.24	Good Casting

2.2.2 Particle Size Distribution Within a Casting

Particle size distribution (PSD) measurements were made at different locations on several rotors to determine whether there is any variation in particle size distribution within dried green rotors. The results from one randomly selected rotor are given in Table B-5. No significant differences in PSD were found within the rotor.

Table B-5. Particle Size Variation Within A green Rotor

Location	Particle Size of Percentiles, μm		
	90th	50th	10th
Dome	2.61	0.90	0.36
Leading Edge	2.61	0.90	0.36
Blade	2.64	0.90	0.36
Trailing Edge	2.58	0.90	0.36
Shaft	2.60	0.89	0.36

2.2.3 Variation in Density Within a Rotor

Variation in density within rotor C/N 0507401 was measured. The segments taken from different locations were sintered at ACC.

The results indicated in Table B-6 show no significant variation in density within the rotor, also assuming that the sintering behavior of the segments represents the interior portion of the rotor.

Table B-6. Density Variation Within a Rotor

Location	Sintered Density, g/cm^3	Weight Loss, Percent
Shaft	3.25	0.56
Blade	3.26	0.44
Dome	3.27	0.78

2.3 Discoloration

The systematic discoloration near the upper edge of each blade of a rotor casting remains a concern. Several experiments were conducted trying to understand and eliminate the problem.

- A rubber-lined mill is presently used to mill the silicon nitride power with the appropriate additives. Milling in a plastic container with a silicon nitride grinding media was conducted to determine if discoloration is caused by the rubber lining.

  Results: Severe outgassing of the slip caused voids and negative lines on the cast rotors.

- Milling in an alumina mill jar with silicon nitride grinding media was tried.

  Results: Discoloration is still evident on the blades of the rotor.

- Bubbling slip, decanting the "clean" slip, discarding the slip surface which is full of "black discoloration".
- Results: This experiment is still on-going.

2.4 Sinter/HIP Experiments

Three experimental sinter/HIP runs were made on three presintered rotors which yielded final densities of 3.26, 3.25 and 3.23 g/cm^3.

2.5 Rotor Dimension Control

As an initial step to dimensionally control the densified rotors, some rotors have been measured after pre-sintering to evaluate dimensional stability. This data will be used to establish a precise shrinkage factor for future tooling design. The measurements were done at the following locations:

- From leading edge to leading edge
- From leading edge to trailing edge
- From trailing edge to trailing edge
- Shaft diameter

3.0 BCD - CERAMIC STRUCTURES

3.1 Turbine Shroud

Eight turbine shrouds were nitrided and delivered to Garrett for testing. Four additional shrouds are in processing. One turbine shroud was shipped to Garrett for green machining early in this reporting period. All green machining is now done at ACC.

The casting of turbine shrouds effort was reduced in March 1984 since an adequate number were available at Garrett for testing and an anticipated design change was being considered. Later in the reporting period, problems with a nitriding furnace caused further processing delays. One furnace has been rebuilt twice and now is in operation. One furnace is awaiting new components to replace defective components and will be in operation in early September 1984. A new furnace is to be delivered in early July 1984 and will be operational shortly thereafter.

3.2 Turbine Inner Diffuser

Six inner diffuser housings were cast, machined, nitrided, and delivered to Garrett for testing. Additional inner diffuser housings will be processed to meet Garrett requirements as needed. Machining and nitriding schedules are being evaluated for these.

3.3 Turbine Outer Diffuser

Six outer diffuser housings were cast, machined, nitrided, and delivered to Garrett for testing.

3.4 Stator Vanes

Eighty-four stator vanes were injection molded for processing at ACC during this reporting period. Thirty-three stator vanes were fully processed and shipped to Garrett for testing.

Twenty-seven of the injection molded stator vanes were rejected after dewaxing as a result of x-ray evaluations. Thirty-four blades have been dewaxed, tested, and are ready for nitriding. No additional stator vanes will be injection molded since an adequate number is available for Garrett testing schedules.

3.5 Combustor Baffle

Two combustor baffles were cast, nitrided, and forwarded to Garrett.

3.6 Transition Ducts

Five transition ducts have been cast and are being processed.

3.7 Ring Components

Six flow separator housing seal rings were cast, nitrided, and shipped to Garrett for testing. In addition, two 9.5 inch diameter cylinders were cast, prenitrided, and shipped to Garrett for machining into flow separator housing rings.

In addition to the delivery of hardware, ACC intends to develop improved process controls and more rapid delivery of hardware. All incoming materials and slip viscosities are fully characterized to be sure that the process controls produce consistent results. The flow properties of injection molding mixes are fully evaluated to determine if more rapid throughput can be accomplished.

4.0 SRN - ROTOR - MATERIAL AND PROCESS DEVELOPMENT

The serious outgassing problem often associated with a Y_2O_3 compound containing silicon has been solved by an improved slip preparation procedure.

Investigations were conducted to study ways to increase the depth and degree of nitridation of thick silicon castings. One concept was to blend a controlled amount of Si_3N_4 powder into silicon powder. The addition of Si_3N_4 powder was to vary the pore structure of the silicon compact and also to test the possible catalytic effect. A series of specimens are being made and one rotor was cast. Preliminary nitridation results were encouraging.

Several experimental rotors were cast and subsequently nitrided. The highest bulk density obtained was 2.52 g/cm^3. The density of the nitrided rotor did not vary significantly from the skin to the center of the rotor. An optical microscopic examination of one of the rotors showed only a very small amount of unreacted silicon (≈3 percent) exits in the interior of the rotor.

X-ray diffraction analysis of one of the nitrided rotors shows that the phase distribution is nearly identical across the hub section of the rotor. The percentages of the phases on x-ray peak intensities are: 56-percent αSi_3N_4, 36-percent β-Si_3N_4, 7-percent $Y_{20}N_4Si_{12}O_{18}$, and 1-percent Fe.

A preliminary sintering experiment showed that the density of a sintered SRN sample could be 3.16 g/cm^3 or higher. A series of experiments were conducted to determine the effect of Fe_2O_3 concentration on the nitridation behavior of SRN castings. The results show that the percent of weight gain increases with Fe_2O_3 content ranging from 1 to 5 percent (by weight), however the sintered density seems to be unaffected.

APPENDIX C

THE CARBORUNDUM COMPANY
(UNIQUE WORK)
ADVANCED GAS TURBINE (AGT)
POWERTRAIN SYSTEM DEVELOPMENT PROGRAM
NINTH AGT SEMIANNUAL
TECHNICAL PROGRESS REPORT

1. BACKGROUND

This report summarizes the work carried out by the Carborundum Company during the time period 1 January through 30 June 1984, for Garrett on the Advanced Gas Turbine Powertrain System Development Program.

Carborundum's objective is to optimize ceramic forming methods for sintered alpha silicon carbide (SASC) components and deliver SASC hardware for the AGT101 engine development program per the agreed schedule. Activities during this period continued to focus on 6 stationary ceramic parts: transition duct, combustor baffle, stator segments, turbine shroud, regenerator shield, and combustor liner. Four fabrication processes: injection molding, plastic forming, isopressing/green machining, and plastic extrusion were used to produce parts per the agreed work statement. These different processing methods were selected with respect to the complexity, size and shape of the individual component, and also to further the development of high volume, low cost SASC parts fabrication techniques.

Four of the 6 component configurations have already been subjected to various rig tests under a variety of conditions and have repeatedly performed well. The 4 configurations tested are: transition duct (isopressed/green machined), combustor baffle (slip cast), regenerator shield (isopressed/green machined), and stator segments (injection molded).

2. SUMMARY

Work continued on all projects and resulted in the delivery of 3 ground regenerator shields, 8 combustor liners, 1 combustor baffle, and 2 transition ducts. The latter incorporated additional stock in height, but no thermocouple tube holes (latest design iteration). Four of the shipped combustor liners were plastic extruded, the combustor baffle was slip cast and all other components sent during this reporting period were made by isopressing and green machining.

Plastic forming and injection molding were investigated for the fabrication of combustor baffles. Only small changes on the molding tool were required to make the dual forming approach feasible. The remaining 2 components stator segments and turbine shroud are injection molded. The main emphasis with respect to stator segments was put into optimization of mold design. In the case of turbine shrouds, work focused on obtaining sintering fixtures which minimize warpage of the locating tabs and aid in a uniform concentric shrinkage pattern on the turbine shroud/outer diffuser housing interface.

3. STATIC STRUCTURES

3.1 Turbine Stator

Individual SASC stator segments have been made using the injection molding process. A new steel mold which incorporates a new set of shrink factors was received. Initial molding runs indicated insufficient filet radii between

PRECEDING PAGE BLANK NOT FILMED

the airfoil and the sidewalls, a thin trailing edge, and a large parting line on the trailing edge. The mold was reworked and additional molding trails were conducted. Parts were fully processed and passed X-ray, fluorescent penetrant inspection (FPI) and visual inspection. Dimensional checks showed an undersized airfoil with respect to length and thickness. The mold cavity was increased accordingly and a new molding run is scheduled for early July 1984.

- Evaluation of the old molding tool in conjunction with a modified powder (Compound C) was continued.
- Two different moldings yielding 80 and 110 individual stator segments, respectively, were conducted. All parts were subjected to binder removal and in-process NDE. Fifty percent of the visually acceptable parts were sintered and inspected. The majority of parts had low densities and showed unacceptable dimensional vulnerability. Work on the old molding tool was discontinued.
- Molding trials with the new injection molding tool were scheduled early during this reporting period.
- Four hundred individual stator segments using standard mix (Compound B) were molded and baked. A total of 190 parts were cleaned and sintered in the new sintering fixtures.
- All parts had good densities and also showed good dimensional stability, but exhibited sharp filet radii and a thin trailing edge. Garrett received three as-sintered stator segments and verified the deviations.
- The molding tool was reworked and 400 parts were molded using Compound C.
- Parts were baked and cleaned. A total of 146 stator segments were sintered using standard conditions and submitted for inspection. Three as-molded plastic stator segments and 3 as-sintered SASC parts made with the reworked tool were sent to Garrett for evaluation.
- A 50-pound batch of Compound B was prepared and 300 stator segments were molded.
- All parts made from this Compound B completed bake-out, 88 were cleaned, and 38 of these were sintered and inspected. Similar results as for the recently molded Compound C stator segments were obtained. Parts had good densities and shape integrity but exhibited vane profiles which were too short and thin on the trailing edge. Consequently, the injection molding tool was sent out for rework in the trailing edge and an additional 50 pounds of Compound B was prepared.

3.2 Turbine Shroud

The turbine shroud, the largest injection molded SASC part fabricated by Carborundum, is made on a 1000-ton injection molding machine at a custom molding facility. Work on the redesigned turbine shroud continued. The old mold had been modified in areas with sufficient stock to accommodate the new shape. Additional green machining is required to minimize final grinding. Parts from the first molding trial, conducted at the end of the last reporting period, and parts from a second molding run were processed. Activities focused on sintering and the design of adequate sintering fixtures to reduce warpage and distortion.

- In-process nondestructive evaluation (NDE) on green machined turbine shrouds of Compounds B and D of the first molding trial revealed some plastic and metal contamination in the parts. Turbine shrouds that passed inspection, with the exception of those evidencing contamination, were used for fixturing trials during sintering.
- Nine green-machined turbine shrouds of Compound B and 2 of Compound D were processed through bake-out, cleaning and sintering. All turbine shrouds except the first one (Compound B) were sintered using specifically designed fixtures. The first part was sintered without any fixture to

allow observance of the undisturbed shrinkage behavior. Both parts made from Compound D exhibited very low density, therefore, no additional parts of this compound were processed.

- The sintering fixtures employed addressed mainly the warpage of the tabs, out-of-roundness on the large ID, and drag of the shrinking part on the setter surface.

- The second injection-molding trial yielded 23 parts made with Compound B and 22 parts made with Compound C.

- Twelve turbine shrouds from the second molding trial passed for in-process NDE, then were green machined and placed into bake-out. Three parts completed bake-out; one was cleaned and sintered.

- During this reporting period, 12 green-machined turbine shrouds were sintered, but all showed some distortion and insufficient stock for grinding on the large ID. Consequently, near the end of the reporting period, 6 unmachined turbine shrouds from the second molding run were submitted for bake-out. These parts should have sufficient stock to meet print dimensions on the large ID.

- Sintering of the first unmachined part is scheduled for late July 1984.

3.3 Combustor Baffle

Combustor baffles that were supplied and successfully tested, were made by using a slip casting method. To eliminate green machining of the inside contour an advanced plastic forming method was chosen to replace slip casting as a forming process. The steel mold was designed for easy conversion from a plastic forming tool to an injection molding tool. Both methods were used in sequence to produce combustor baffles during the current reporting period. The injection molding process yields parts closer to specification. Current work focuses on optimization of the injection-molded combustor baffles.

- Compound P2 was prepared and 35 combustor baffles were injection molded and submitted for in-process NDE. Three as-molded parts were sectioned and processed through sintering. Four injection-molded parts progressed through cleaning, presinter treatment, and sintering. These parts showed good surface finish, tab definition and adequate stock on the OD, but were oversized on the ID. The remaining parts will be used for sintering trials.

- The molding tool was reduced on the ID, an additional spacer was added to reduce the wall thickness from 0.25 to 0.20-inch and 14 baffles were molded. An incomplete filling pattern and some excessive overflow was attributed to flaws in the parting line of the tool and an insufficient radius on the ID.

- New molding trials with a reworked molding tool are scheduled for the middle of July 1984.

3.4 Transition Duct

The transition duct has been fabricated by using isopressed tube billets and green machining the height as well as inside and outside contours. Each part is sintered on a contoured mandrel and only minor grinding work is required to obtain a finished part.

This component has consistently performed satisfactorily in various rig and engine tests. Latest design optimizations resulted in the incorporation of integral thermocouple tube ports. This added feature represents a new development step with respect to assembly and sinter techniques.

- Three transition ducts with height added on the transition duct/turbine shroud interface were sintered. Two parts passed as-fired quality inspections. The parts were ground, inspected, annealed and shipped to Garrett with corresponding MOR test bars. One transition duct was rejected for linear FPI indications.

- Five billets for transition duct design PA3609649 resulted in 3 green-machined parts. One of these was used as a trial piece to test the selection method for tube insertion.

- Two sintering trials were conducted. The first consisted of a green tube section and sintered tube inserts, and the second of a green transition duct and green tube inserts. Both showed good integrity, -- the latter has been submitted for leak test and dimensional check.

- Three blanks for transition duct design PA3610213 were isopressed and pre-turned.

3.5 Combustor Liner

Previously supplied combustor liners were made by isopressing/green machining. Plastic extrusion has been chosen to replace isopressing/green machining of this configuration because of a potential for high volume production at low cost.

Developmental activities focused on the processing of large diameter plastic extruded tubing. Isopressing/green machining was used in a parallel approach to ensure a flow of parts to Garrett as extrusion development proceeded.

- Sintered and ground combustor liners from the third extrusion run showed internal and surface defects and exhibited warpage which resulted in only partial grinding of the OD and ID surfaces.

- Four isopressed/green-machined parts were sintered, inspected, cut to size, annealed and shipped to Garrett with corresponding MOR test bars.

- Work on extrusion continued and a fourth extrusion run yielded acceptable tube stock. Individual sections were checked for X-ray defects, baked, sintered, and inspected.

- Four extruded parts were OD/ID ground, cut to size, inspected, annealed, and shipped to Garrett with corresponding MOR test bars.

- An additional two isopressed/green-machined parts were sintered and submitted for inspection to complete delivery requirements.

3.6 Regenerator Shield

Previously supplied parts were made by isopressing/green machining and final grinding. Plastic extrusion has been investigated as an advanced forming process and developmental activities concentrated on the extrusion of a large diameter thick-walled tube and subsequent take-up and handling techniques. To meet delivery requirements, efforts on extruded as well as isopressed/green-machined parts were conducted.

- Parts from the second extrusion run were processed but did not yield deliverable quality parts. One sintered part was ground but showed surface flaws and insufficient stock on the OD. In-process NDE revealed internal flaws.

- Three isopressed/green-machined regenerator shields were ground inspected, annealed, and shipped to Garrett with corresponding MOR test bars.

- This completes 1984 delivery requirements for this component.

APPENDIX D

DISPERSION OF SILICON POWDER

by

M. D. Sacks
University of Florida
October 7, 1983

DISPERSION OF SILICON POWDER

I. INTRODUCTION

The objectives of this study were:

(1) to evaluate the effect of (a) pH and (b) dispersant additions on the state of dispersion of silicon suspensions and

(2) to determine the relationship between the suspension state of dispersion and the pore structure formed in cast green bodies.

The state of dispersion was evaluated using rheological, electrokinetic and particle sedimentation measurements. Porosity in the green bodies was evaluated by mercury porosimetry.

II. MATERIALS

The following materials were provided by AIResearch Casting Company:

(1) Ground Kemanord IV, 65-64, Silicon-3% Ferric Oxide

(2) Unground Kemanord IV Silicon

(3) Ground Kemanord IV Silicon

(4) Fisher Scientific Co. I-116 Ferric Oxide

Unless indicated otherwise, material (1) was used in all experiments. The as-received powder was "aged" in distilled water for 144 hours. Subsequently, the "aged" suspension was filtered, washed, and dried.

Suspensions were normally prepared using a Red Devil paint shaker for mixing. Ultrasonication was also used in some experiments (described in Section III). Unless indicated otherwise, pH adjustments were made using NaOH and HCl solutions.

PRECEDING PAGE BLANK NOT FILMED

III. RESULTS

A. Electrokinetic Behavior

Interparticle attractive and repulsive forces control the structural arrangements of particles in suspension (i.e. the state of dispersion). Good dispersion is achieved when repulsive forces are significantly greater than attractive forces, while flocculation occurs when attractive forces are dominant.

Electrokinetic measurements are used to give information about the magnitude of electrostatic repulsive forces in suspensions. In Fig. 1, the electrophoretic mobility (as determined by microelectrophoresis measurements) is plotted vs. suspension pH for aqueous Si - 3%Fe_2O_3 suspensions. (Measurements were carried out on at least two samples for each pH. At least 20 individual measurements were averaged for each sample.) High negative electrophoretic mobilities (indicative of high negative surface charge) were observed at high pH, while low or zero mobilities were obtained at low pH. This behavior is very similar to observations with aqueous silica suspensions, indicating that the Kemanord silicon surfaces are oxidized.

Zeta potentials (see Fig. 2) were calculated from the average electrophoretic mobility at each pH using the Helmholtz-Smoluchowski equation:

$$\zeta = \frac{\mu\eta}{\varepsilon\varepsilon_o} \qquad (1)$$

where

ζ = zeta potential in V

μ = electrophoretic mobility in $m^2 s^{-1} V^{-1}$

η = viscosity of the suspending liquid in Pa·s

ε = relative dielectric constant of the suspending liquid

ε_o = permittivity of vacuum (8.854×10^{-12} F/m)

The repulsive energy per unit area, V_R, as a function of separation, d, between two particles (flat plate approximation) can be approximated (for the case of symmetrical electrolytes) by:

$$V_R = \frac{64nkT}{\kappa} \left[\tanh \left(\frac{ze\psi_D}{4kT} \right) \right]^2 \exp(-\kappa d) \qquad (2)$$

where

$$\kappa = \left[\frac{e^2 N_A}{1000\, \varepsilon \varepsilon_o kT} \sum_i M_i z_i^2 \right]^{\frac{1}{2}} \qquad (3)$$

and

ψ_D = potential at the outer Helmholtz plane

e = elementary charge (1.602×10^{-19} C)

N_A = Avogadro constant (6.022×10^{23} mol^{-1})

k = Boltzmann constant (1.381×10^{-23} J/°K)

T = temperature in °K

z_i = valence number of ion species i

M_i = concentration of ion species i in mol L^{-1}

n = number of ions per cm^3

Since it is generally assumed that $\psi_D = \zeta$, the importance of zeta potential on electrostatic repulsive forces is readily seen.

B. Rheological Behavior

1. pH Effect

Fig. 3 shows the rheological flow behavior (i.e. shear stress vs. shear rate) at several pH values for suspensions containing 30 volume percentage (vol %) solids. The suspension at pH = 4.0 is characteristic of a highly flocculated suspension for two reasons: (1) a yield stress must be exceeded before flow occurs and (2) shear thinning behavior is observed, i.e. the viscosity decreases with increasing shear rate (see Fig. 5). In contrast, suspensions at pH = 9.0 and pH = 10.7 are relatively Newtonian, i.e. the shear stress is linearly proportional to the shear rate. In moderately concentrated suspensions, this behavior is characteristic of good dispersion. Low shear rate rheology measurements (Fig. 4) on the two high pH suspensions show that the suspension at pH = 10.7 is actually slightly shear thinning, indicating some flocculation occurs (at least at very low shear rates). This may seem somewhat surprising since the zeta potential (Fig. 2) is slightly higher at pH = 10.7 compared to pH = 9.0. However, the observed flocculation in the former suspension is readily explained by recognizing that interparticle electrostatic repulsive forces are strongly dependent upon the solution electrolyte concentration. (The inverse exponential dependence on κ, the Debye-Huckel parameter, is noted in equation (2). Equation (3) shows that κ is proportional to the solution ionic strength.) In order to achieve high suspension pH values, NaOH (i.e. an electrolyte) was added. The electrolyte

concentration at pH = 10.7 is apparently high enough to diminish repulsive forces and to cause some flocculation.

Figure 5 shows viscosity vs. shear rate plots for suspensions (with 30 vol % solids) of varying pH. Suspensions with low pH (and with low zeta potential, Fig. 2) are highly shear thinning, i.e. the viscosity decreases as the shear rate increases. Suspensions with intermediate pH (and with moderate to high zeta potentials, Fig. 2) are relatively Newtonian, i.e. the viscosity is independent of shear rate. As the suspension pH increases above 9.0 (and the electrolyte concentration becomes high), slightly shear thinning behavior is observed.

2. Solids Loading Effect

Figs. 6 and 7 show the effect of solids loading on suspensions with moderate repulsive forces (i.e. pH = 6.3, Fig. 6) and high repulsive forces (i.e. pH = 9.0, Fig. 7). In the former case (Fig. 6), suspension viscosities increase very rapidly as the solids loading increases. In addition, suspensions become highly shear thinning at the higher solids loadings. Viscosities are much lower for pH = 9.0 suspensions at higher solid loadings (i.e. 40, 50, and 56 vol% solids, Fig. 7) than corresponding pH = 6.3 suspensions. The pH=9.0 suspensions are also less shear thinning at low shear rates, and they show shear thickening behavior at high shear rates. This type behavior is often observed in suspension which have high solids loading and highly charged particles.

Fig. 8 shows the rheological flow behavior of a suspension received from AIResearch Casting Co. (reported to be 75 wt%, i.e. approximately 56 vol% solids). The suspension is similar to the pH = 9.0 (56 vol% solids)

suspension described above. Fig. 9 shows the low shear rate portion of the AiResearch suspension flow curve. It is evident that some structure builds up (i.e. particle-particle networks) at the very low shear rates.

3. Ultrasonication Effect

Figs. 10 and 11 show the effect of ultrasonication on the rheological behavior of suspensions (pH = 9.0 and pH = 7.8, respectively) containing 56 vol% solids. Sonication results in decreased viscosities, particularly at high shear rates. This can be attributed to more efficient breakdown of powder agglomerates. The effect of sonication tends to be less important at very low shear rates since some structure development appears to be unavoidable in high solids loading suspensions.

Fig. 12 compares the viscosity vs. shear rate for the: (1) as-received AiResearch suspension, (2) pH = 9.0, 56 vol% solids, 15 min. sonicated suspension, and (3) pH = 7.8, 56 vol% solids, 30 min sonicated suspension.

C. Porosity of Gravity Cast Samples

Several suspensions were cast in hollow cylinders on glass plates and allowed to settle under gravity. After sedimentation was complete, samples were dried, removed from the cylinders, and characterized by mercury porosimetry. Table I reports total porosity (volume percentage of pores) and the median pore radius (in nanometers) determined for these powder compacts. Samples prepared from flocculated suspensions form highly porous, large pore size powder compacts. For example, the 40 vol% solids, pH = 6.3 suspension resulted in a compact with ~44% porosity and ~250nm median pore radius. The

50 vol% solids, pH = 6.3 suspension resulted in a compact with ~42% porosity and ~260nm median pore radius. In contrast, samples formed using higher pH (i.e. 7.8, 9.0) suspensions (i.e. better dispersed) yielded lower total porosity and smaller median pore radius (see Table I). Samples formed with higher pH (i.e. 7.8, 9.0) sonicated suspensions (i.e. the conditions for best dispersion) had the lowest porosity and smallest median pore radius (see Table I).

Fig. 13 shows scanning electron micrographs of a compact formed from a 56 vol% solids, pH = 9.0, 45 min sonicated suspension. The dense particle packing (i.e. ~81% of the solid density) is evident. (Furthermore, fine particles have apparently coated larger particles. We know from X-ray sedimentation that ~10% of the particles are in the range ~9-15 microns, but these large particles are not evident in Fig. 13. The micrographs were taken of compact surfaces which had been in contact with the glass plate during casting). In contrast to Fig. 13, a considerably more porous microstructure was obtained with an unsonicated, 40 vol% solids, pH 6.3 suspension (see Fig. 14).

Fig. 15 shows that the median pore radius is related to the total porosity of the compact. The relationship appears to be linear, although a theoretical basis for this observation has not yet been fully established.

D. X-ray Sedimentation

Particle size distribution measurements, carried out with a Micromeritics X-ray Sedigraph, can give information on the suspension state of dispersion. Fully dipersed suspensions will give Sedigraph curves

characteristic of the primary particle size distribution. Sedigraph curves obtained on flocculated suspensions give qualitative information on "apparent" particle sizes (i.e. "apparent" floc sizes).

Suspensions of as-received ground Kemanord IV, 65-64, silicon-3% ferric oxide were prepared at two different pH values (5.8 and 9.0). Based on previously reported electrokinetic and rheological measurements, it was known that a suspension at pH = 9.0 would be well-dispersed while a suspension at pH = 5.8 would be partially flocculated. The Sedigraph curves for the two suspensions (Fig. 16) reflect these differences in the state of dispersion.

The particle size distribution was also determined (under good dispersion conditions) for the as-received, unground silicon powder (Fig. 16). Comparison of the unground and ground powders shows that the latter material has a much broader size distribution. This accounts for the ability to achieve a high solids loading (e.g. 56 vol%) in suspension, yet still maintain a relatively fluid (i.e. low viscosity) system.

The Sedigraph curve for the aged, ground material is also shown in Fig. 16. Within experimental error, it is identical to the as-received ground material.

X-ray sedimentation was also used as a method of quickly evaluating the effectiveness of several common defloculants. Table II gives a list of deflocculants which were effective at a concentration of 0.05 weight percentage (wt%) of the solids present in suspension. Within experimental error, sedigraph curves obtained at this concentration were identical to the curve shown in Fig. 16 for the ground, pH = 9.0 suspension.

Some caution should be exercised in applying the results of Table II

to concentrated suspensions, such as used in slip casting. Suspensions used in the X-ray Sedigraph are very dilute, i.e. ~3 wt% solids (~1.3 vol% solids). The optimum dispersant concentrations may not be the same for both dilute and concentrated suspensions. Nevertheless, the dispersants listed in Table II are expected to be effective at some concentration.

Several of the dispersants listed in Table II were found to be almost as effective at 0.01 wt% as they were at 0.05 wt%. These dispersants were: TSPP, FAC, AC, Tamol 731, Darvan C, and CDK8E-1A.

Table III gives a list of additives which were found to be ineffective as dispersants at concentrations of 0.25 wt%.

E. Powder Densities

Powder "true" densities were determined by helium gas pycnometry. Values are listed in Table IV.

F. Comparison of Porosity of Slip Cast and Gravity Cast Samples

Several suspensions were cast by two different methods: gravity casting (GC) and slip casting (SC). In the latter method, suspensions were cast into hollow cylinders on plaster blocks. Green bodies were characterized by mercury porosimetry. The total porosity (TP) and the median pore radius (MPR) are reported in Tables V-VIII.

The samples in Tables V-VIII are discussed separately from those reported in Table II because a different powder batch was used. (As before, the powder was "aged" 144h.) For some reason, as yet undetermined, this powder batch (no. 3) seems to have 'aged" differently from previous batches

(see section III.G.). Differences in "aging" behavior are suggested (and discussed in more detail below) because some of the cast samples prepared with powder batch no. 3 have total porosity (TP) several percent greater than expected (i.e. based on Table II results). This is also coupled with observations of entrapped bubbles (i.e. air pockets) in some cast bodies. This suggests the possibility that gas-forming reactions, e.g.

$$Si_{(s)} + H_2O_{(l)} \rightarrow SiO_{2(s)} + H_{2(g)}$$

occur during casting to a greater extent with powder batch no. 3.

Table V shows porosimetry results for one of the samples (prepared using powder batch no. 3) which <u>does</u> reproduce the results in Table II. Sample no. 1 was prepared from an unsonicated, pH=6.4 suspension containing 40 vol% solids. The TP (~44%) and MPR (~250 nm) are in good agreement with the first sample listed in Table II. Gas-forming reactions, as proposed above, may be less important in these suspensions because they are flocculated. (Green microstructural development is dominated by the presence of large floc networks in suspension.)

Table V also shows that the cast porosity is not dependent on the casting method in samples prepared from a flocculated suspension.

1. <u>Effect of FAC</u>

Table VI shows the porosimetry results on samples prepared using ferric ammonium citrate (FAC) as a dispersant. Sample nos. 3 and 4 were prepared from gravity casting (GC) and slip casting (SC), respectively, of unsonicated suspensions containing 40 vol% solids and 0.1 wt% FAC. Both casting methods give similar values of TP and MPR. (Two porosimeter runs are reported for each sample.) However, in each case the TP is several percent higher than expected (based on Table II results).

Sample nos. 5 and 6 are GC and SC bodies, respectively, prepared from sonicated (45 min) suspensions containing 56 vol% solids and 0.1 wt% FAC. Both casting methods again give similar TP and MPR values. TP values are again several percent higher than expected (based on Table II results). Sample nos. 7 and 8 are GC and SC bodies, respectively, prepared from sonicated (15 min), "aged" (~1 day) suspensions containing 56 vol% solids and 0.1 wt% FAC. GC and SC bodies again have similar TP and MPR values. Despite the shorter sonication time, these "aged" samples (nos. 7 and 8) have TP and MPR values comparable to "unaged" samples nos. 5 and 6.

2. pH Adjustment Using NH_4OH and NaOH

Table VII shows the porosimetry results for samples prepared using either NH_4OH or NaOH solutions to adjust the suspension pH. Sample nos. 9 and 10 are GC bodies prepared from sonicated (15 min), "unaged", 56 vol% solids suspensions in which the pH was adjusted to 8.0 ± 0.2 using NaOH and NH_4OH solutions, respectively. The TP and MPR are the same, within experimental error, for both samples. Rheological behavior (Fig. 17) is also similar for these suspensions. Samples nos. 11 and 12 are the SC bodies corresponding to nos. 9 and 10, respectively. As before, TP and MPR are essentially independent of the base (i.e. NaOH and NH_4OH) used to adjust the suspension pH. However, the SC bodies (nos. 11 and 12) have smaller MPR and several percent lower TP compared to the corresponding GC bodies (nos. 9 and 10). When considered as an isolated observation, this result is not necessarily surprising since the forming pressure is higher during slip casting (due to capillary forces). With large applied pressures, the observations of slightly denser packing arrangements are reasonable. However, denser packing was not

obtained for SC samples prepared from suspensions containing PAC (Table VI). At the present time, the reason for this different behavior is not known.

Sample nos. 13-16 correspond directly to samples nos. 9-12 except that suspensions used in preparing the former samples were "aged" (~2 days). There are three relevant observations:

(1) TP and MPR are again independent of the base used for pH adjustment.

(2) SC bodies again have slightly lower TP and MPR compared to GC bodies.

(3) Samples prepared from "aged" suspensions have lower TP.

The first two observations are consistent with the results obtained with sample nos. 9-12. The third observation is consistent with rheological measurements (Fig. 17) which show decreased viscosities for "aged" suspensions (i.e. compared to "unaged" suspensions).

3. Suspensions Prepared with Methanol

Table VIII shows porosimetry results on samples prepared using methanol (MEOH) as the suspension liquid. Sample no. 17 and 18 are GC and SC bodies, respectively, prepared using a sonicated (15 min) suspension containing 40 vol% solids and no dispersant. The porosimetry results were independent of casting method. TP and MPR values were both high, characteristic of samples prepared from a flocculated suspension. The rheological data (Fig. 18) confirms that the suspension was flocculated.

Sample nos. 19 and 20 are GC and SC bodies, respectively, prepared using a sonicated (15 min) suspension containing 40 vol% solids and 0.1 wt% PAC. These samples have smaller TP and MPR values (compared to samples nos. 17 and 18) and this correlates with improved suspension dispersion (Fig. 18).

It is interesting to note that sample no. 20 (SC) has a smaller MPR and several percent less TP compared to sample no. 19 (GC). This behavior was observed in casting aqueous suspensons dispersed by pH adjustments (section III.F.2., Table VII). However, it was not observed in samples prepared from flocculated suspensions (Table V and sample nos. 17 and 18 in Table VIII) or from casting aqueous suspensions containing PAC (section III.F.1., Table VI). In the case of flocculated suspensions, the additional forces (e.g. capillary) in slip casting are insufficient to breakdown floc networks (and to cause a denser packing). Thus, no differences in porosity are expected when comparing GC and SC samples prepared from flocculated suspensions.

Samples nos. 21 and 22 are GC and SC bodies, respectively, prepared from "aged" (~1 day), sonicated (15 min) suspensions containing 56 vol% solids and 0.1 wt% PAC. These "aged" suspensions yield samples with smaller TP and MPR compared to "unaged" samples nos. 19 and 20.

The TP and MPR values of samples nos. 21 and 22 suggest that the MEOH suspensions are not dispersed as well as comparable aqueous suspensions (e.g. compare the values to samples nos. 7 and 8 in Table VI). This is also supported by rheological measurements. First, the <u>relative</u> viscosity (i.e. the suspension viscosity divided by the liquid viscosity) is higher for the MEOH suspension (Fig. 19). Second, the MEOH suspensions shows rheopectic behavior. (The data shown in Fig. 19 is taken from shear stress vs shear rate curves, i.e. flow curves, obtained under conditions in which the shear rate was continuously increased from zero to 300 s^{-1}. For the aqueous suspension, the same results are obtained when the shear rate in continuously decreased from 300 to zero s^{-1}. This is not true for the MEOH suspensions. Higher

viscosities are obtained, at any given shear rate, from the flow curve in which the shear rate is continuously decreased, i.e. rheopectic flow behavior is obtained.

G. "Aging"

Table IX lists surface areas of (1) as-received materials and (2) ground Si - 3% Fe_2O_3 "aged" in distilled water under the conditions indicated.

The as-received Si - 3% Fe_2O_3 had a measured surface area of ~4.5 m^2/g. Increased surface areas were obtained in several samples after "aging". This effect may be related to oxidation of the silicon (e.g. by the suggested reaction in section III.F.). It is unclear why some samples listed in Table IX show increased surface area while others do not.

More recent surface area measurements, given in Table X, are also very puzzling. Surface areas of sample nos. 4 and 7, of Table IX, were recently remeasured (at least twice). Surface areas decreased in each case, but the magnitude of the charge varied considerably for different "aged" samples. In addition, the surface of "aged" batch no. 3 (prepared under the conditions used to "age" sample no. 4 of Table IX) did not increase relative to the as-received powder. At the present time, the observations in Tables IX and X cannot be explained. More detailed aging studies, carried out under highly controlled conditions (e.g. atmosphere control), are needed.

IV. SUMMARY AND RECOMMENDATIONS

A. Summary

The work carried out in this project is summarized below:

(1) Raw materials supplied by AIResearch Casting Co. were characterized. Density, surface area, and particle size distribution measurements were made.

(2) Electrokinetic behavior was determined as a function of pH.

(3) Rheological behavior was determined as a function of pH, solids loading, and sonication time.

(4) Total porosity and median pore radius of gravity cast and slip cast samples were deterined by mercury porosimetry. Samples were preparod using a variety of dispersion conditions. Variables investigated included suspension pH, type of base used for pH adjustment (NH_4OH and NaOH), sonication time, aging time, and the use of a dispersant.

(5) The effectiveness of a several deflocculants was evaluated using X-ray sedimentation.

(6) Preliminary experiments were carried out on the rheological and casting behavior of suspensions prepared using methanol as the liquid medium.

B. Recommendations

Further work is needed in the following areas:

(1) Controlled studies of "aging" phenomena should be carried out. "Aging" studies in aqueous suspensions would provide information necessary for improved process control. Similar studies in nonaqueous suspensions are also recommended, since it may be possible to avoid "aging" phenomena in some nonaqueous systems.

(2) Additional studies on the dispersion and casting behavior in nonaqueous suspensons should be carried out. The work described in this report is only preliminary. Considerably more effort would be required to determine the optimum dispersion conditions in several nonaqueous systems.

Figure 1

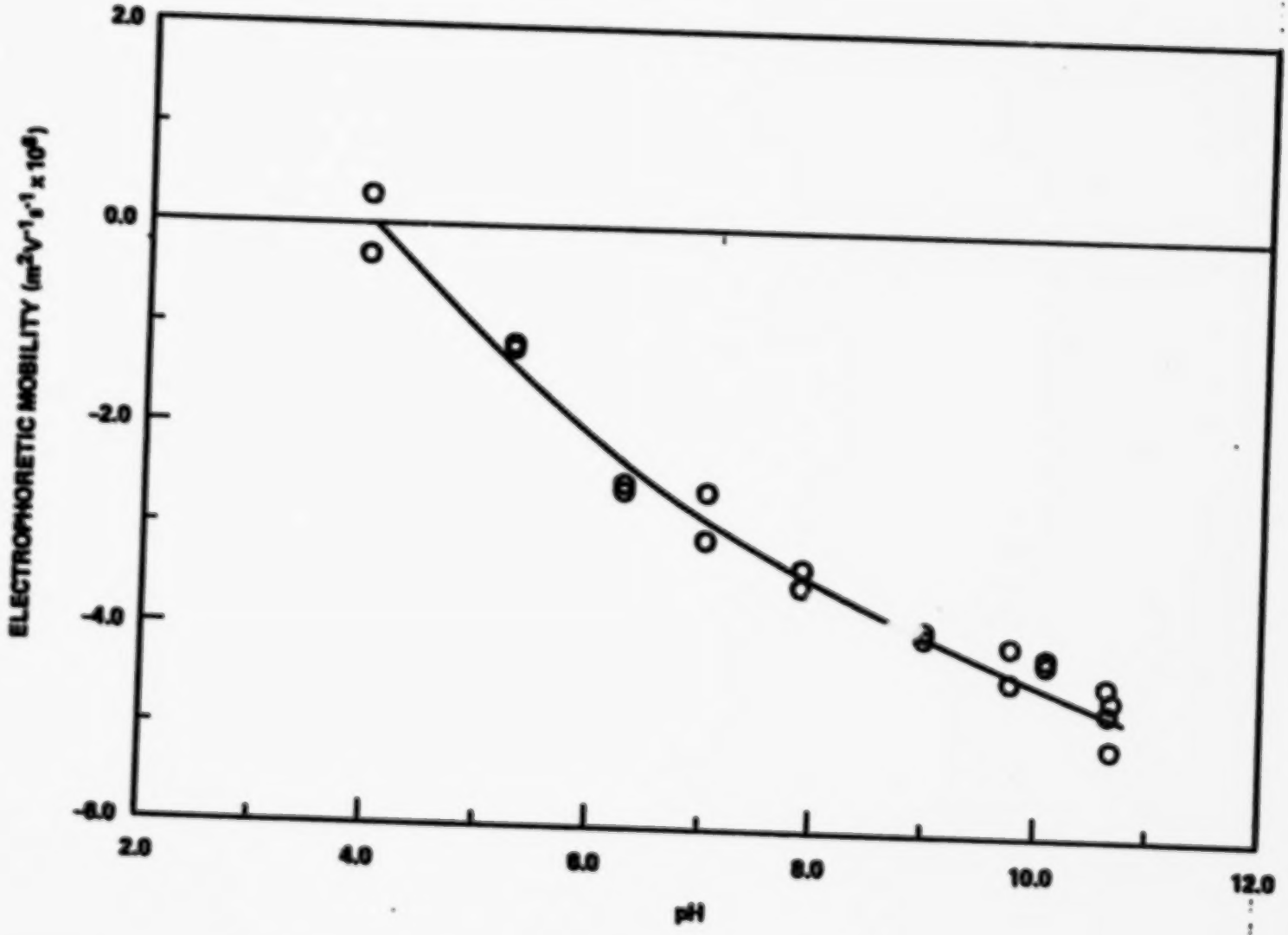
2.0
0.0
-2.0
-4.0
-6.0
ELECTROPHORETIC MOBILITY ($m^2V^{-1}s^{-1} \times 10^8$)
2.0
4.0
6.0
8.0
10.0
12.0
pH

Figure 2

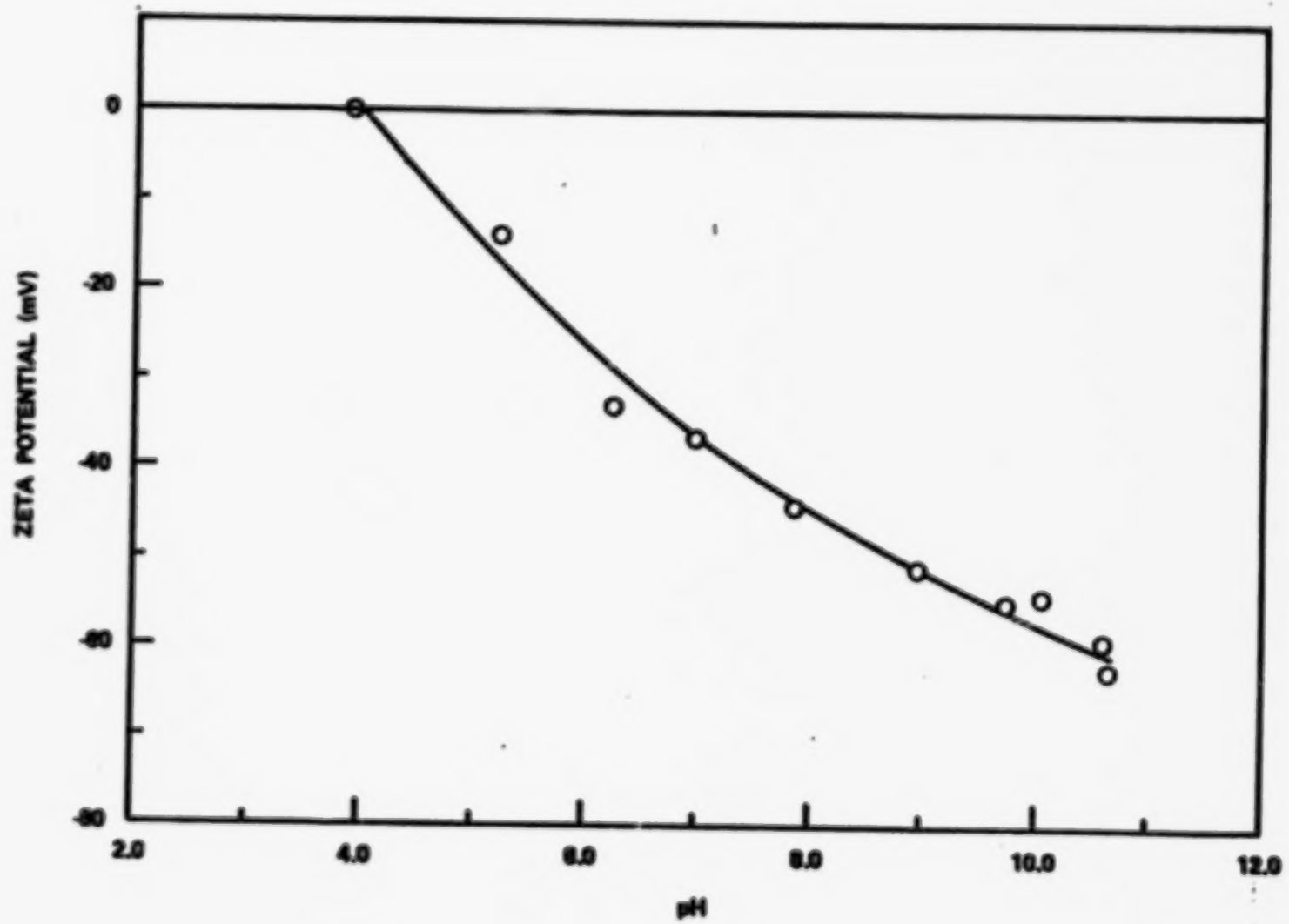

Figure 3

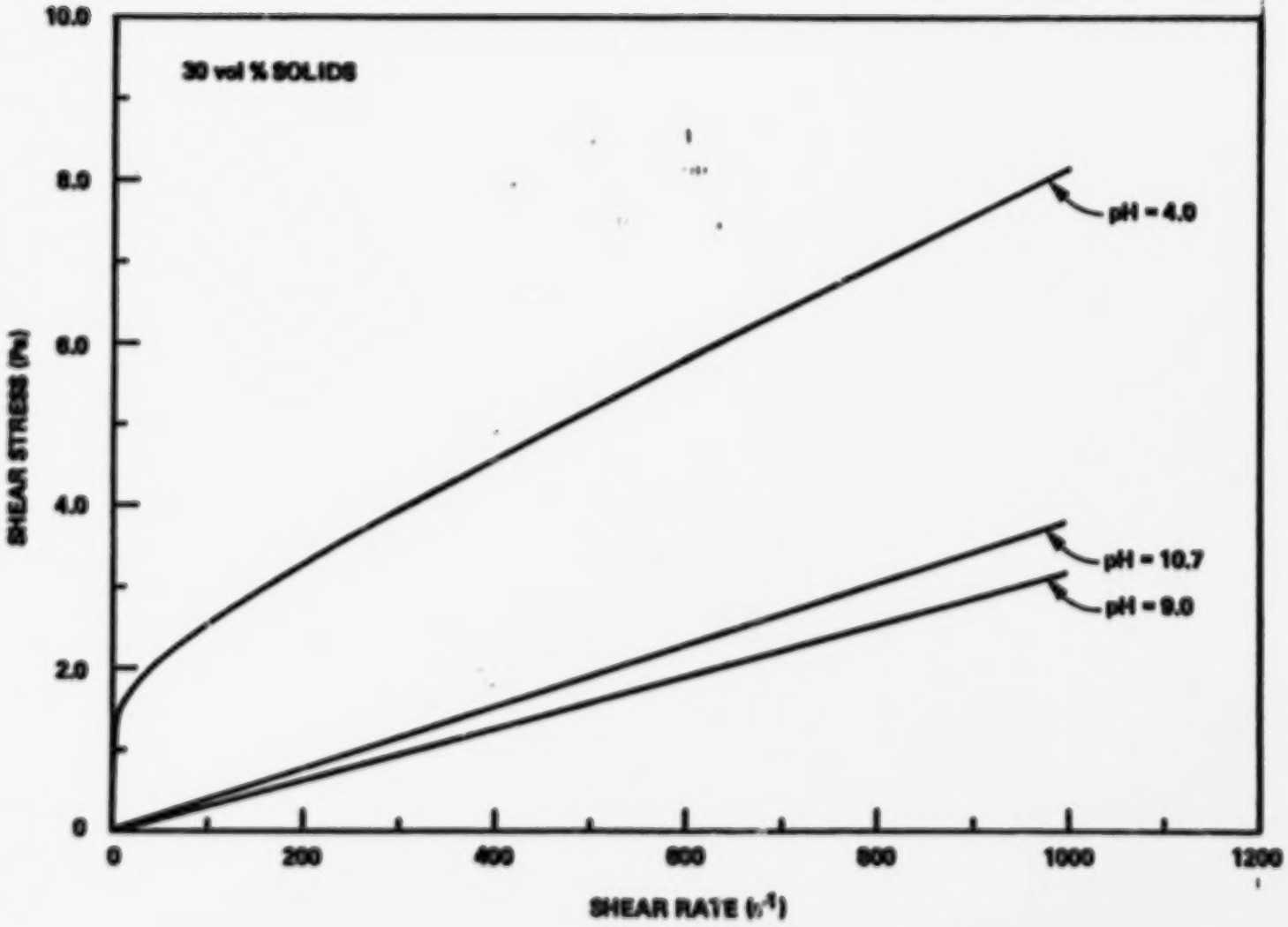
30 vol % SOLIDS
SHEAR STRESS (Pa)
SHEAR RATE (s⁻¹)
pH = 4.0
pH = 10.7
pH = 9.0
10.0
8.0
6.0
4.0
2.0
0
0
200
400
600
800
1000
1200

Figure 4

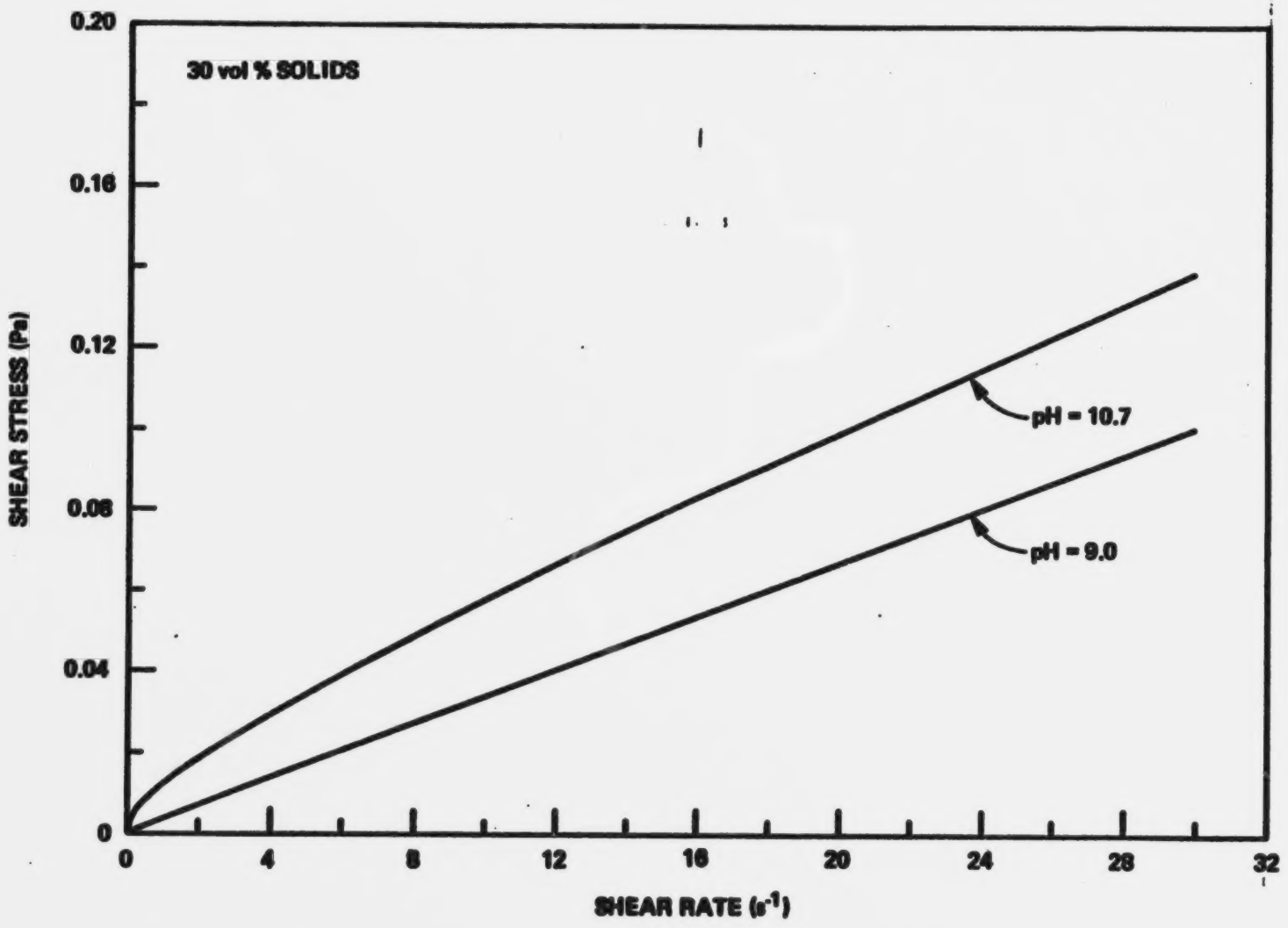
30 vol % SOLIDS
SHEAR STRESS (Pa)
0.20
0.16
0.12
0.08
0.04
0
pH = 10.7
pH = 9.0
0
4
8
12
16
20
24
28
32
SHEAR RATE (s⁻¹)

Figure 5

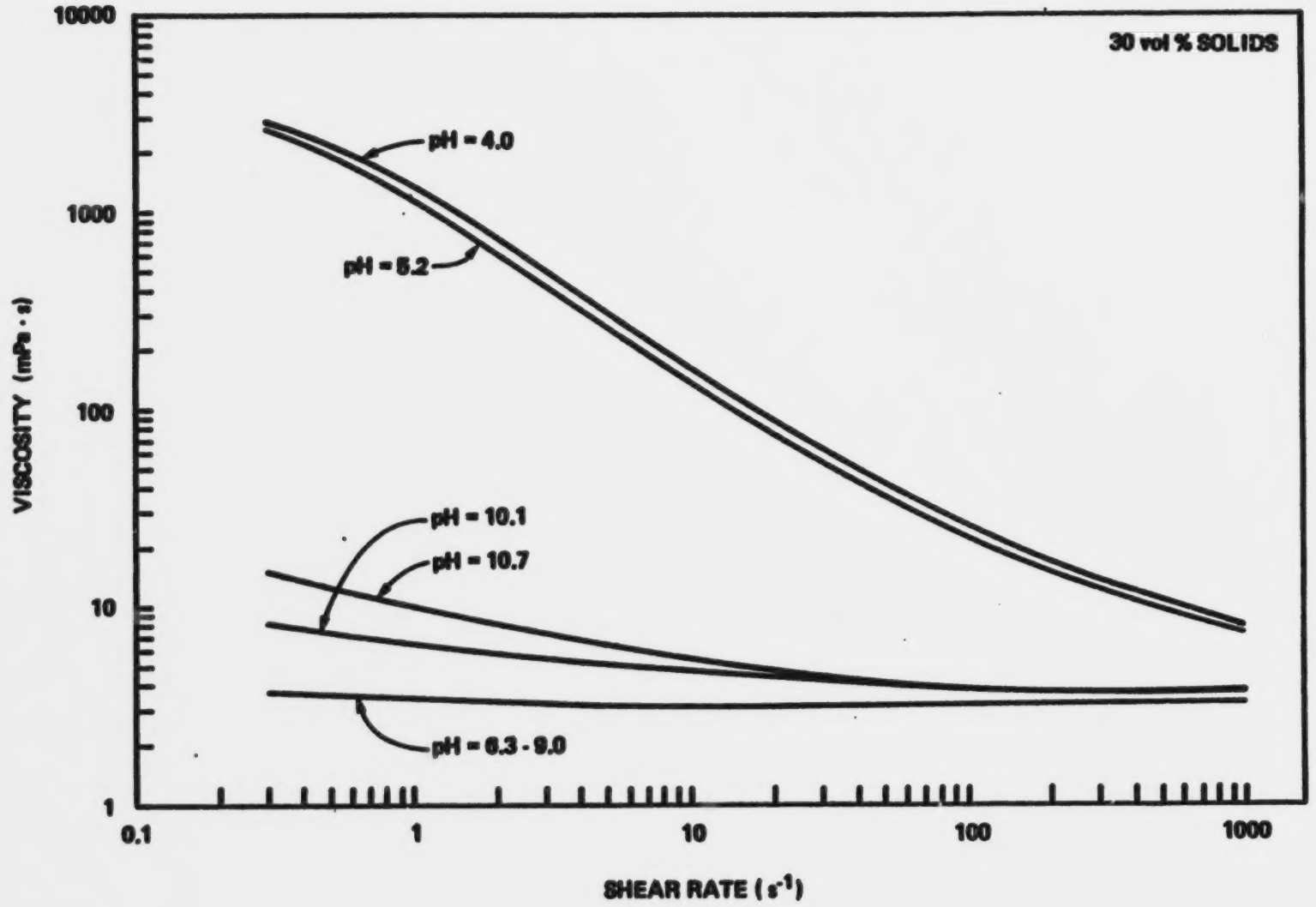
30 vol % SOLIDS
pH = 4.0
pH = 5.2
pH = 10.1
pH = 10.7
pH = 6.3 - 9.0
VISCOSITY (mPa · s)
10000
1000
100
10
1
0.1
1
10
100
1000
SHEAR RATE (s⁻¹)

Figure 6

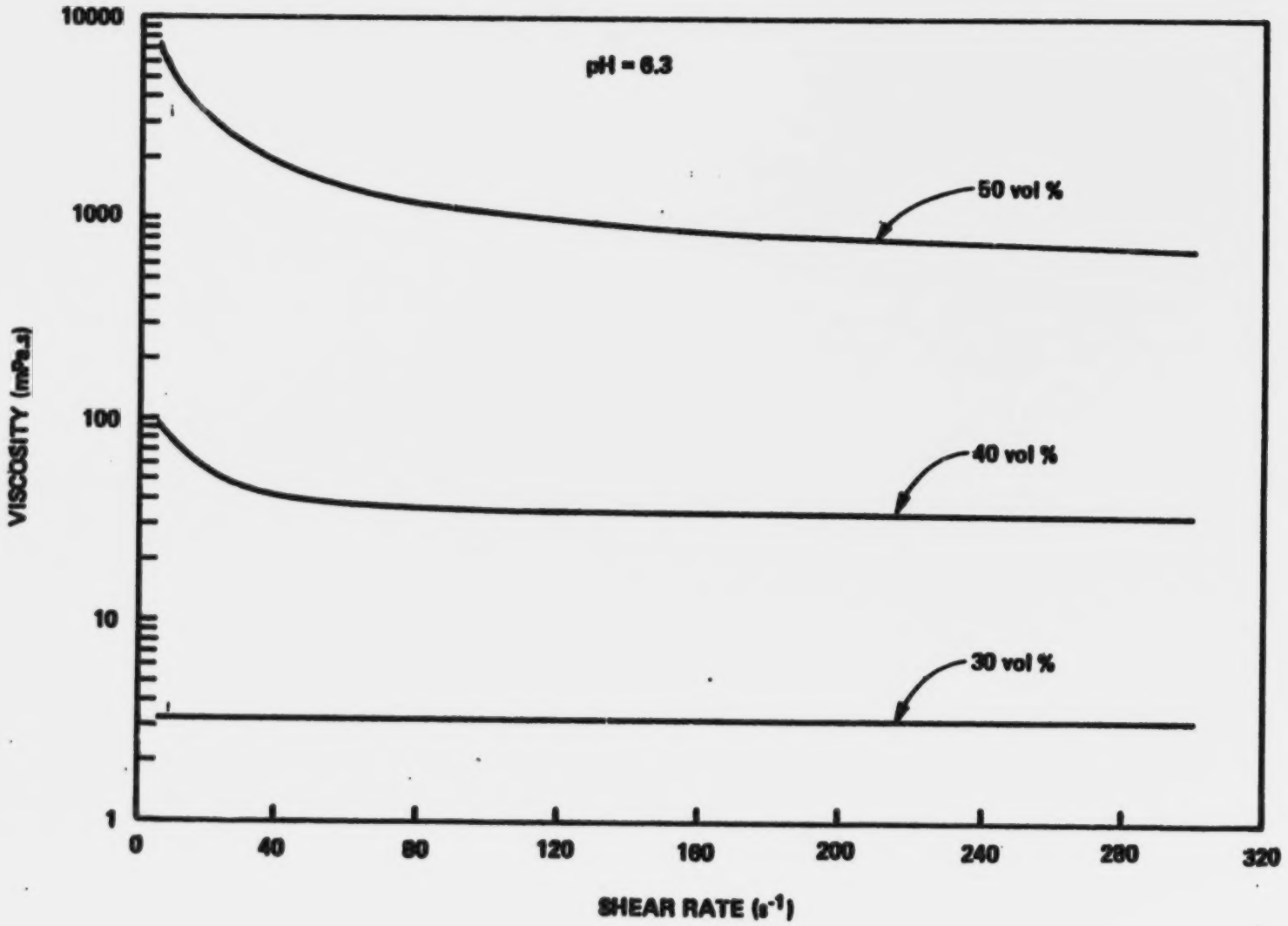
10000
1000
100
10
1
VISCOSITY (mPa.s)
pH = 6.3
50 vol %
40 vol %
30 vol %
0
40
80
120
160
200
240
280
320
SHEAR RATE (s-1)

Figure 7

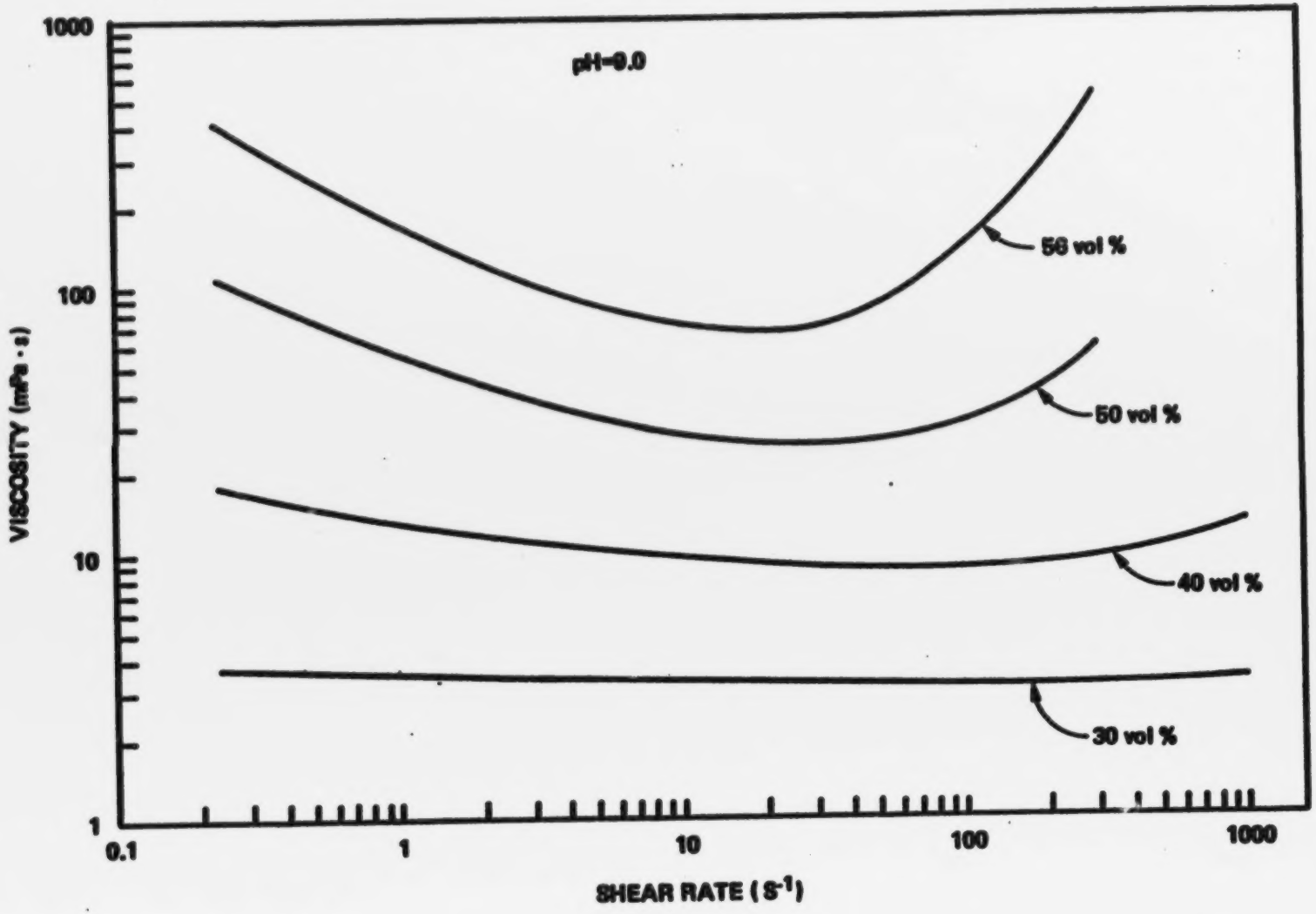
pH=9.0
56 vol %
50 vol %
40 vol %
30 vol %
VISCOSITY (mPa · s)
1000
100
10
1
0.1
1
10
100
1000
SHEAR RATE (S-1)

Figure 8

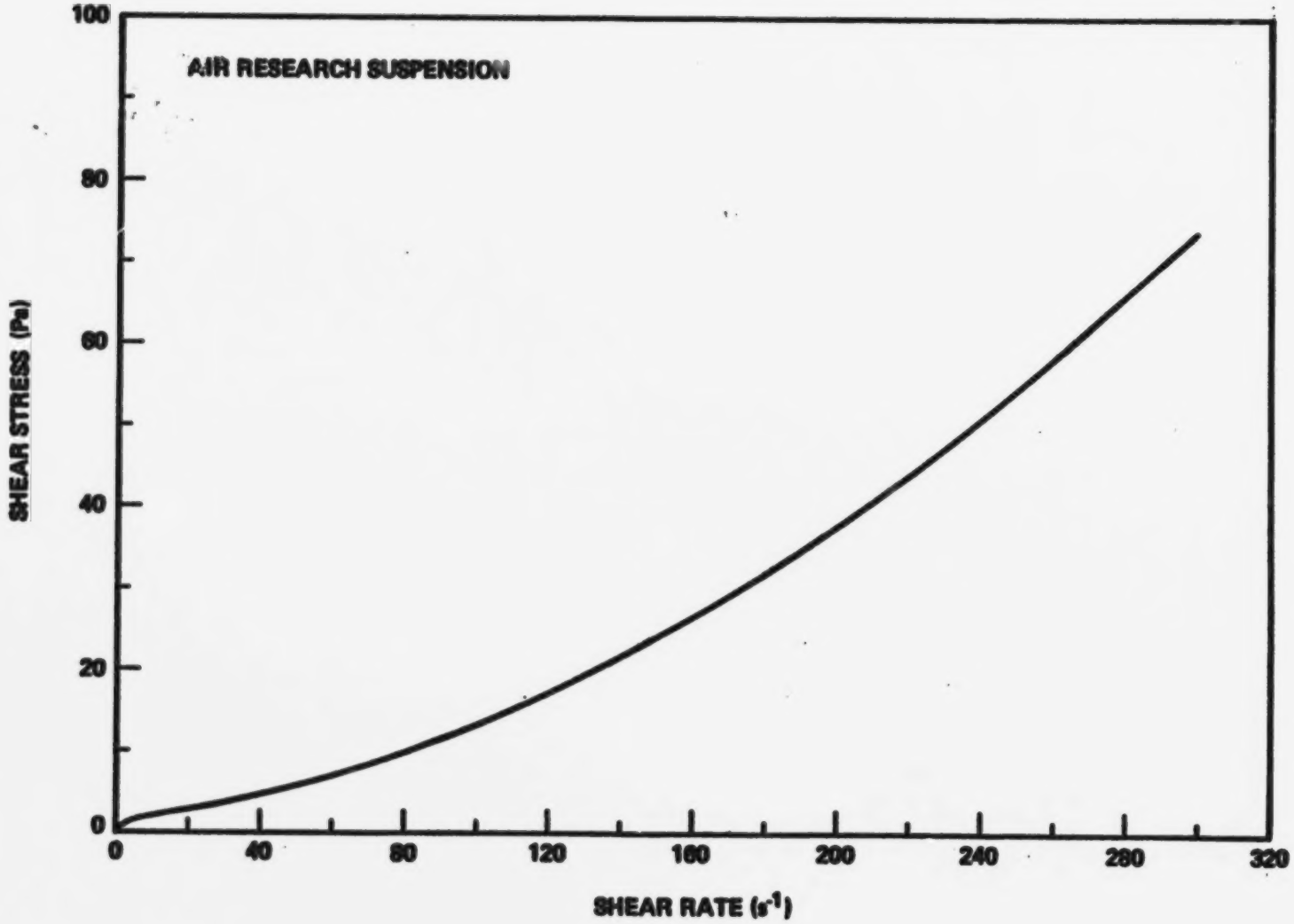
AIR RESEARCH SUSPENSION
SHEAR STRESS (Pa)
SHEAR RATE (s^{-1})
0
20
40
60
80
100
0
40
80
120
160
200
240
280
320

Figure 9

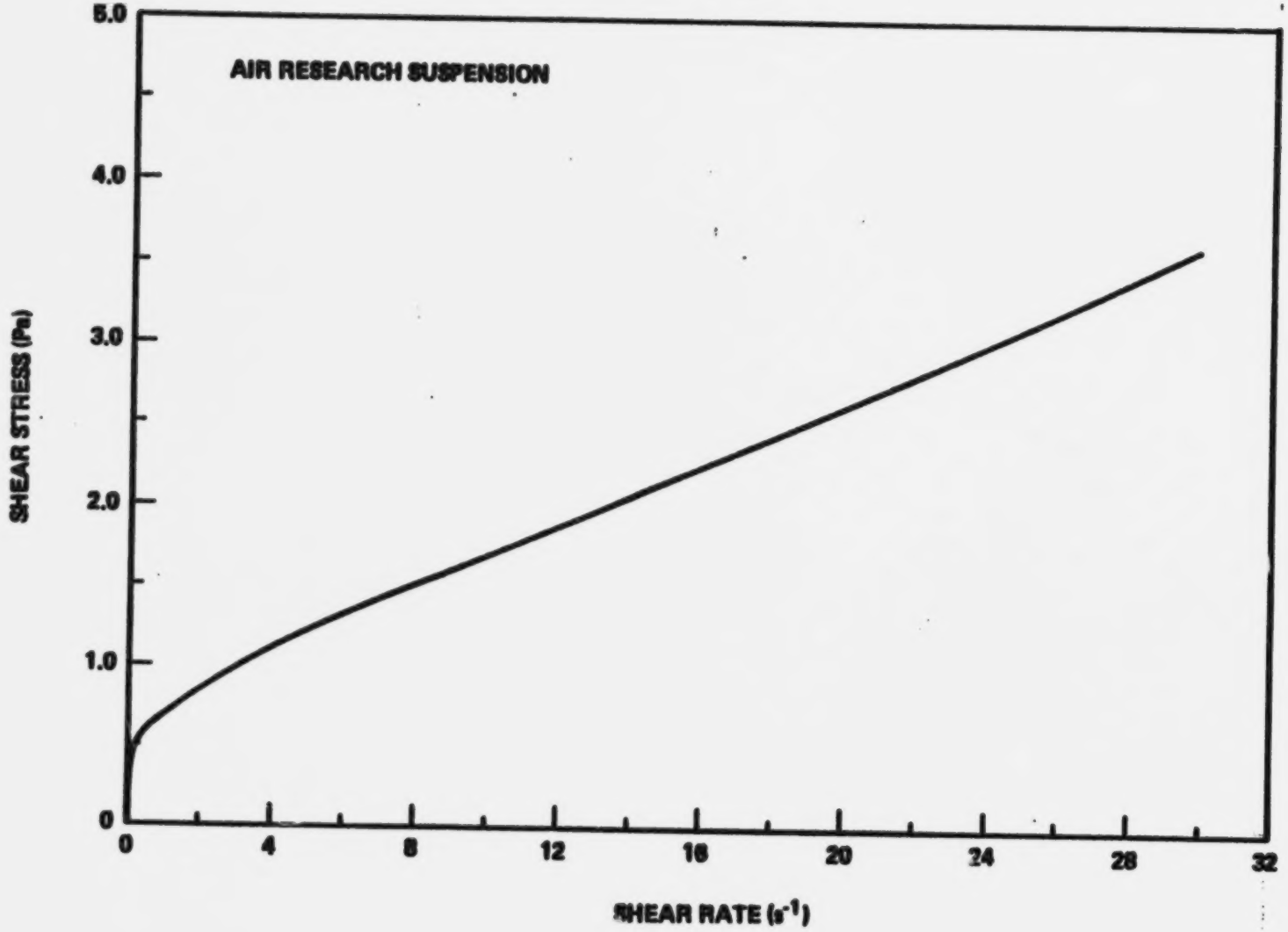
AIR RESEARCH SUSPENSION
SHEAR STRESS (Pa)
5.0
4.0
3.0
2.0
1.0
0
0
4
8
12
16
20
24
28
32
SHEAR RATE (s⁻¹)

Figure 10

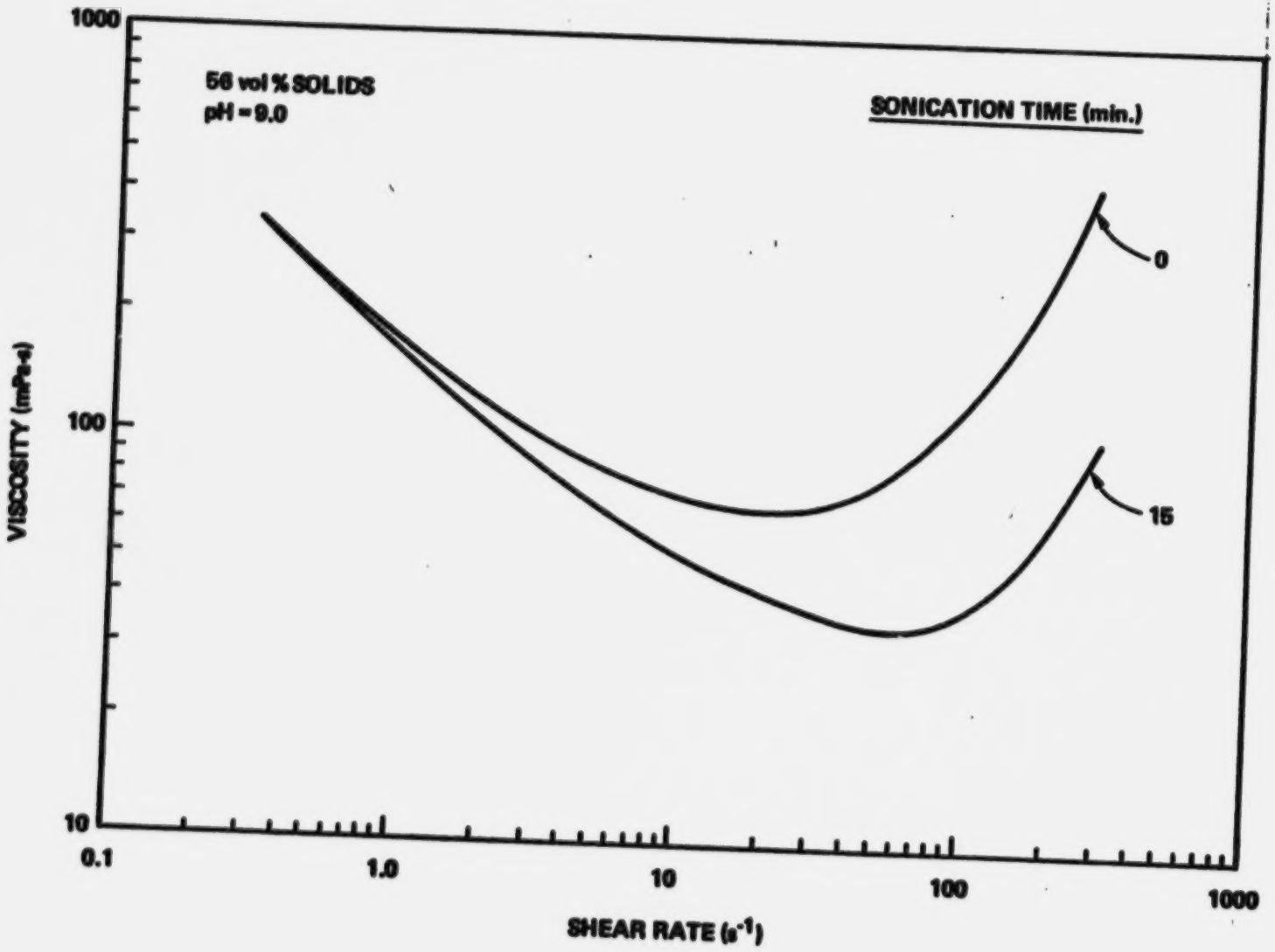
56 vol % SOLIDS
pH = 9.0
SONICATION TIME (min.)
0
15
1000
100
10
VISCOSITY (mPa-s)
0.1
1.0
10
100
1000
SHEAR RATE (s^{-1})

Figure 11

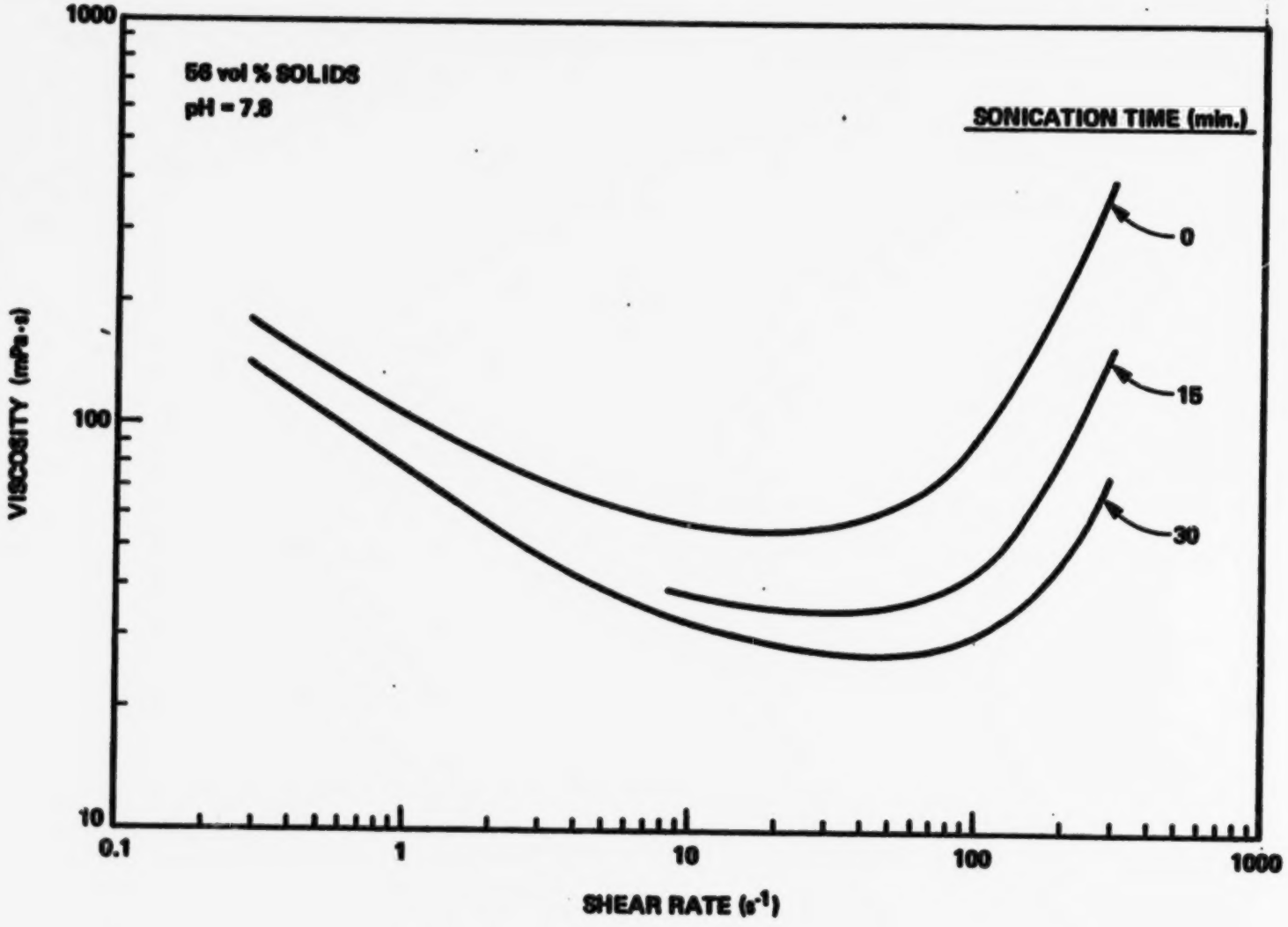
1000
100
10
56 vol % SOLIDS
pH = 7.8
SONICATION TIME (min.)
0
15
30
VISCOSITY (mPa·s)
0.1
1
10
100
1000
SHEAR RATE (s⁻¹)

Figure 12

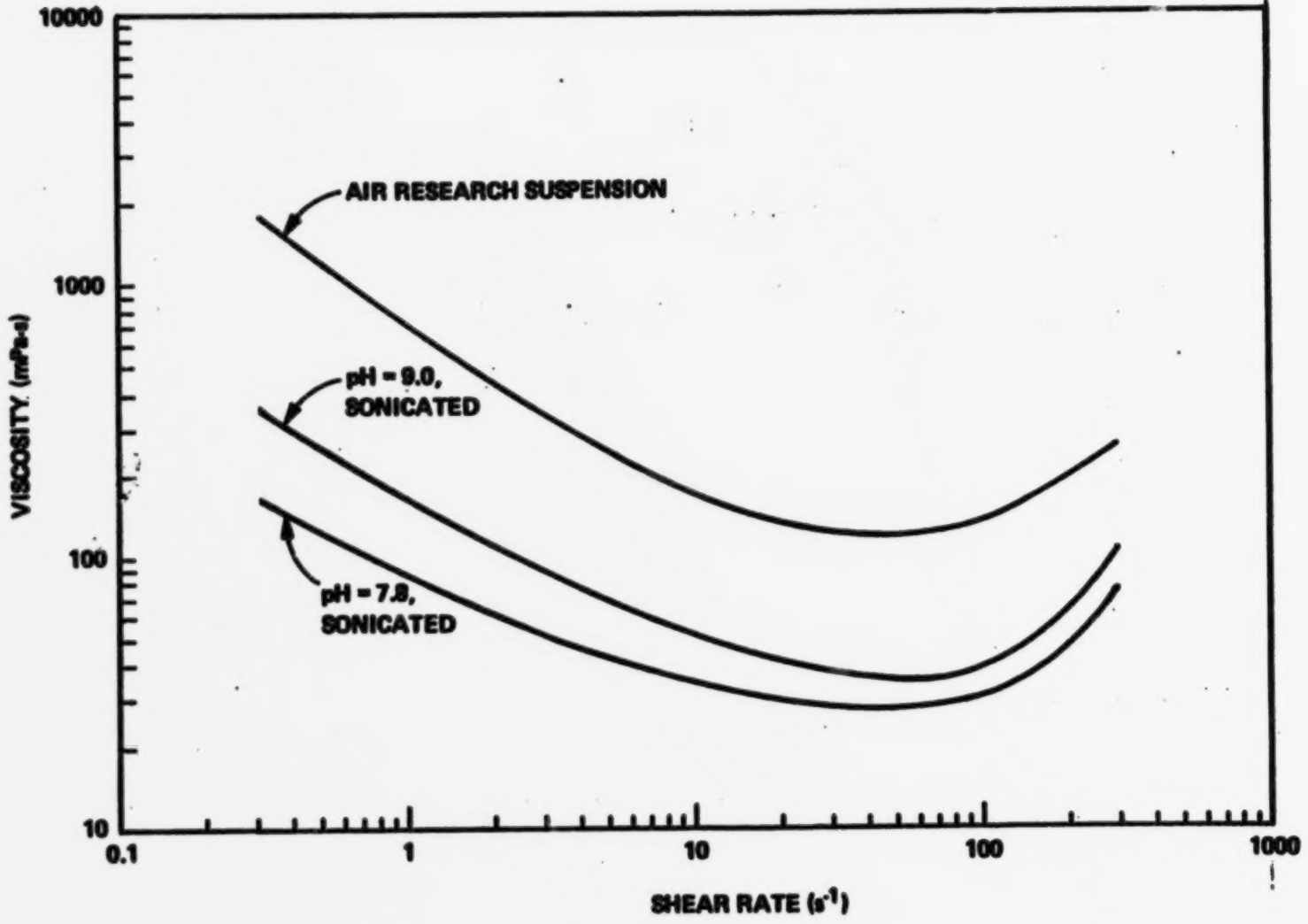
10000
1000
100
10
VISCOSITY (mPa-s)
AIR RESEARCH SUSPENSION
pH = 9.0,
SONICATED
pH = 7.8,
SONICATED
0.1
1
10
100
1000
SHEAR RATE (s-1)

ORIGINAL PAGE IS
OF POOR QUALITY

Figure 13

Magnification: 200X

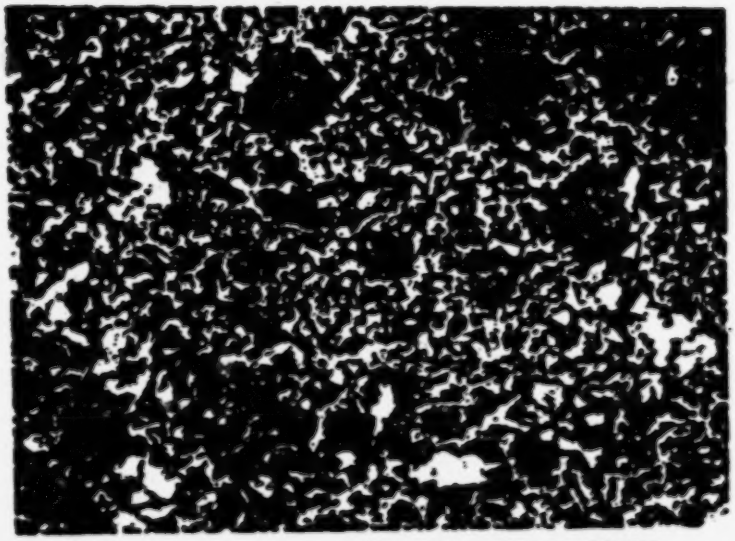

Magnification: 3000X

Magnification: 10000X

Figure 14

ORIGINAL PAGE IS
OF POOR QUALITY

Magnification: 1000X

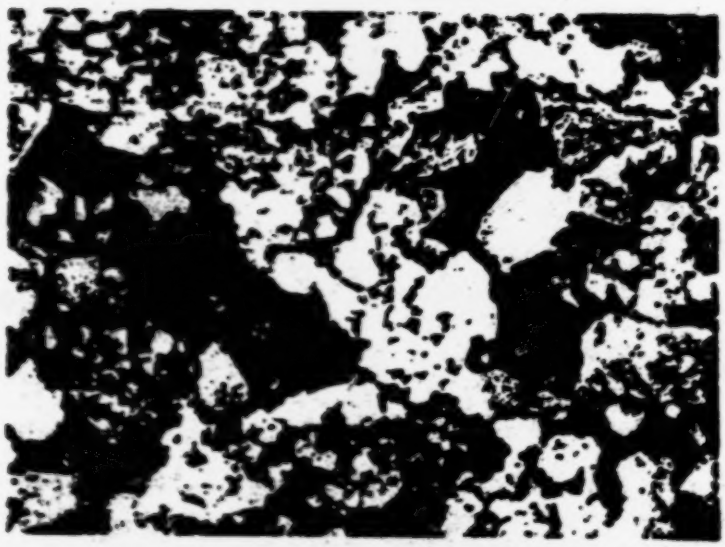

Magnification: 3000X

Figure 15

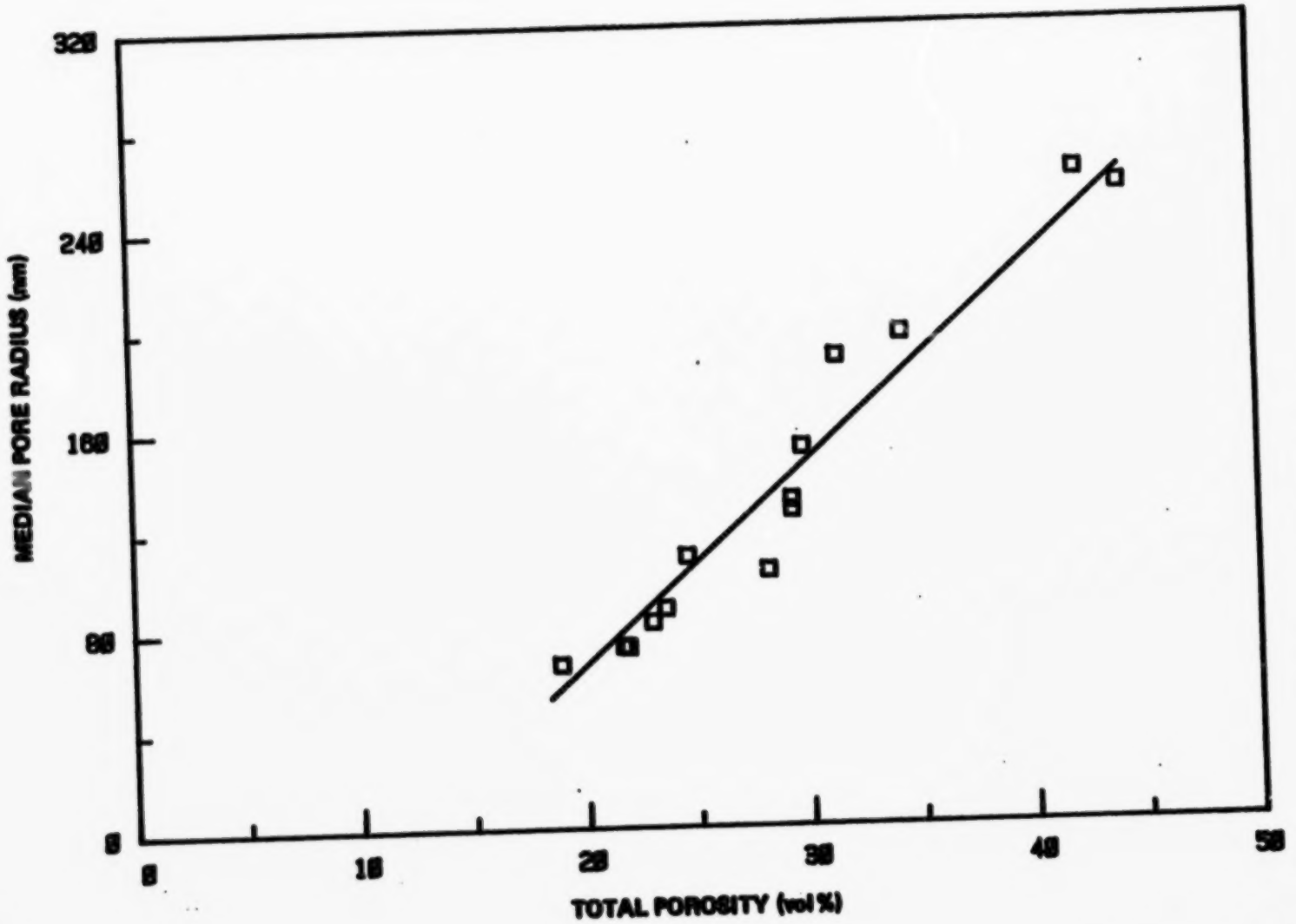
328
248
168
88
0
MEDIAN PORE RADIUS (nm)
0
10
20
30
40
50
TOTAL POROSITY (vol %)

Figure 16

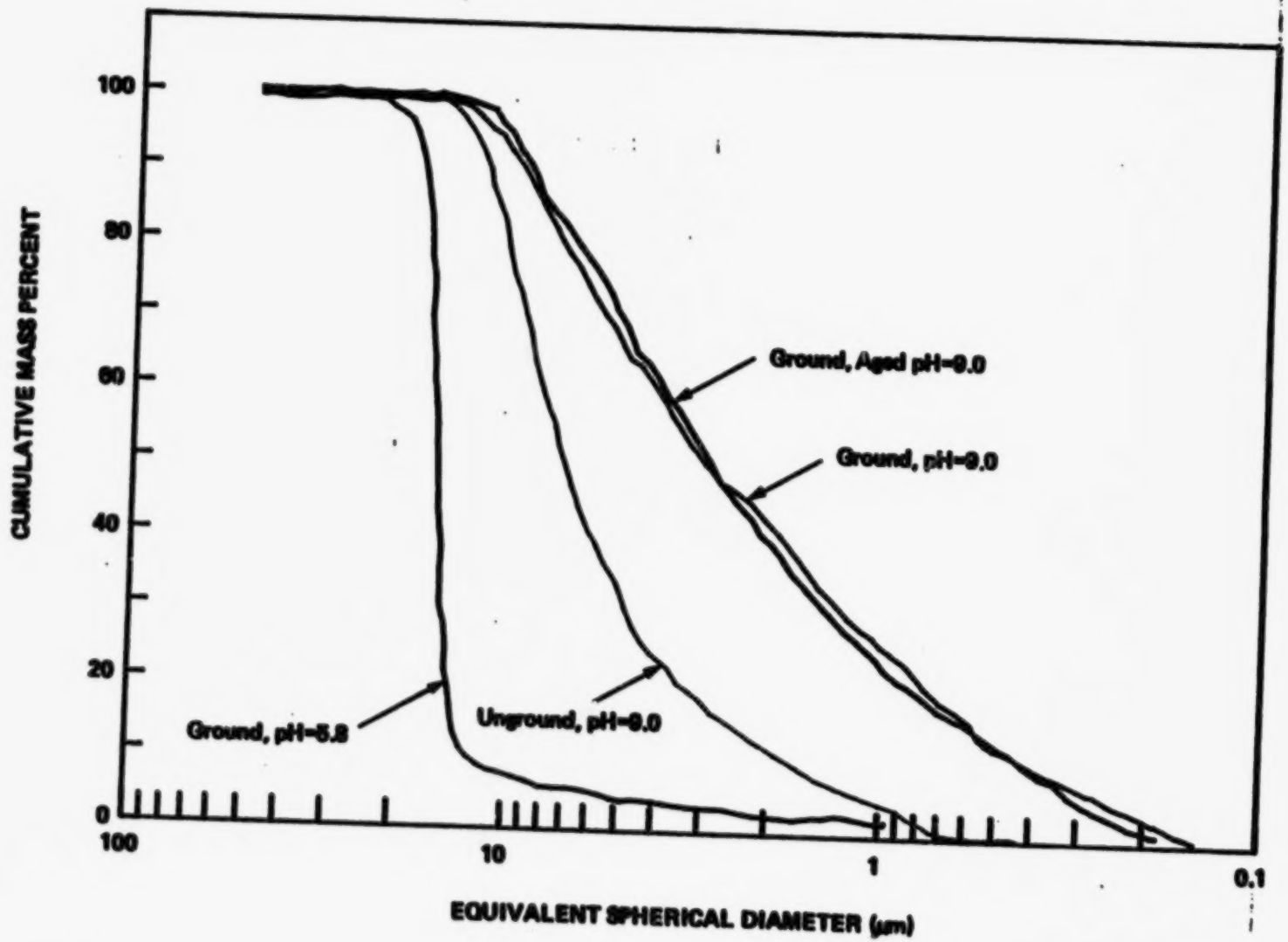
CUMULATIVE MASS PERCENT
100
80
60
40
20
0
100
10
1
0.1
EQUIVALENT SPHERICAL DIAMETER (μm)
Ground, Aged pH=9.0
Ground, pH=9.0
Unground, pH=9.0
Ground, pH=5.8

Figure 17

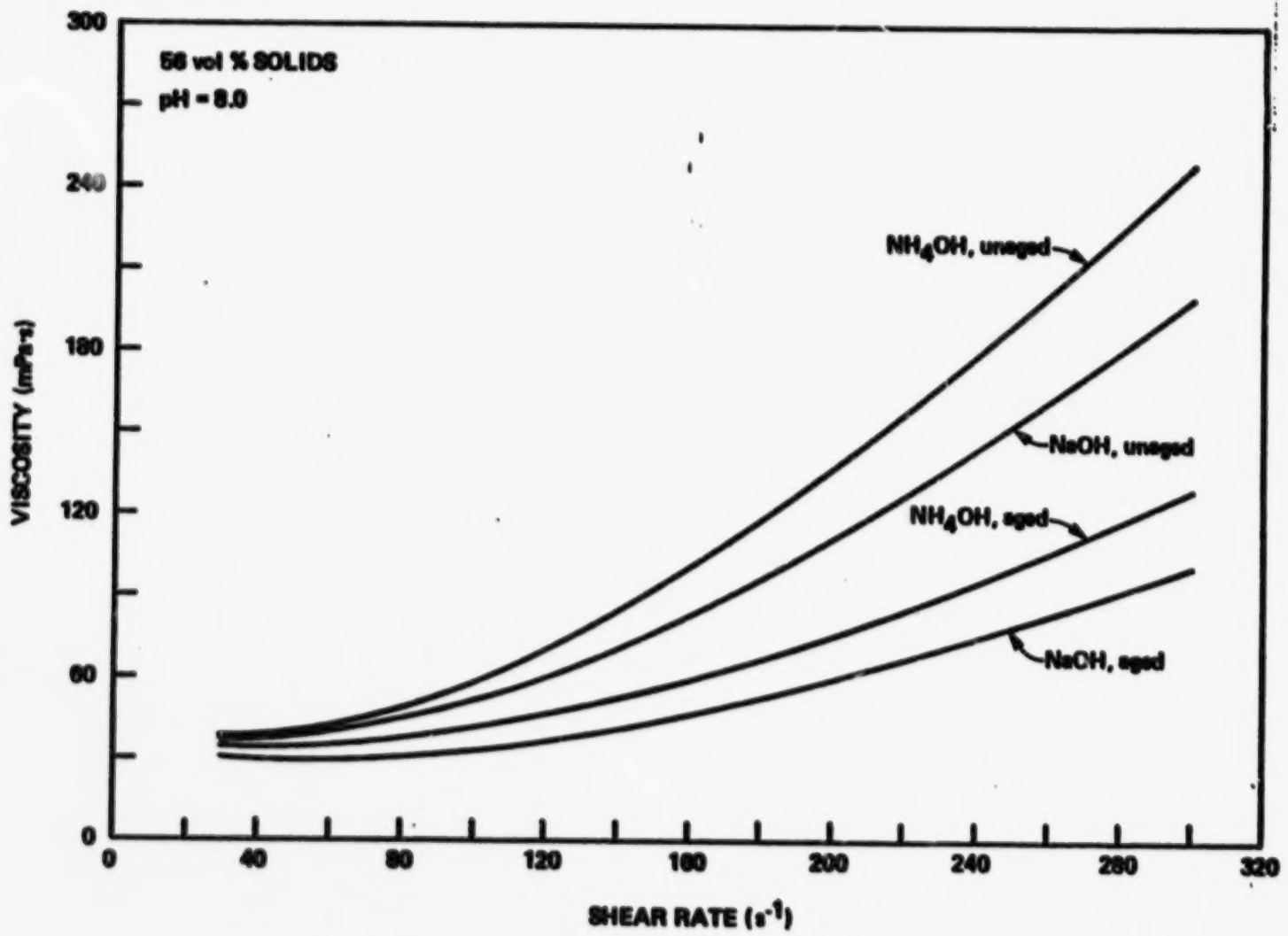
56 vol % SOLIDS
pH = 8.0
NH_4OH, unaged
NaOH, unaged
NH_4OH, aged
NaOH, aged
VISCOSITY (mPa·s)
SHEAR RATE (s^{-1})
0
60
120
180
240
300
0
40
80
120
160
200
240
280
320

Figure 18

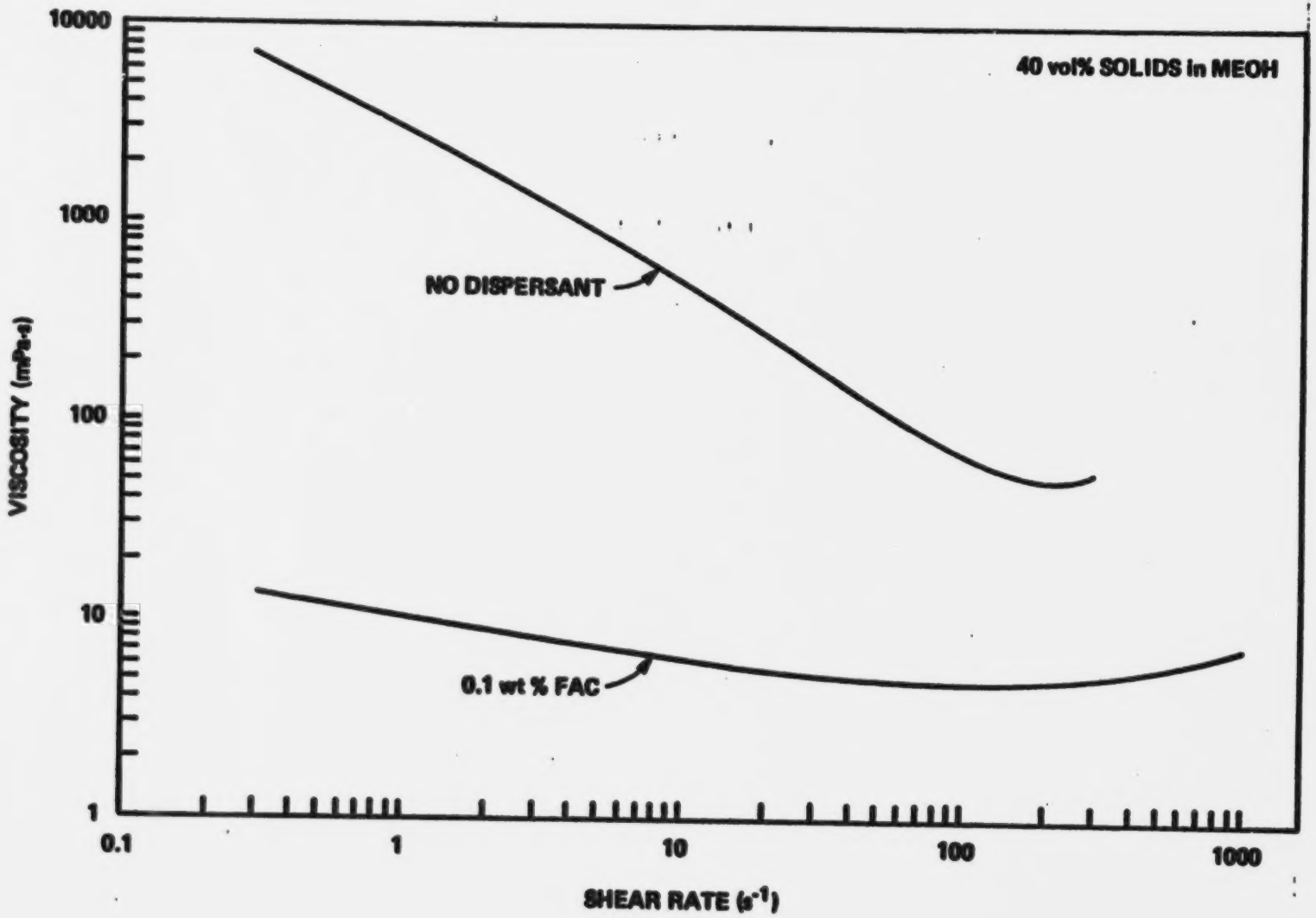
40 vol% SOLIDS in MEOH
NO DISPERSANT
0.1 wt % FAC
VISCOSITY (mPa-s)
SHEAR RATE (s-1)
10000
1000
100
10
1
0.1
1
10
100
1000

Figure 19

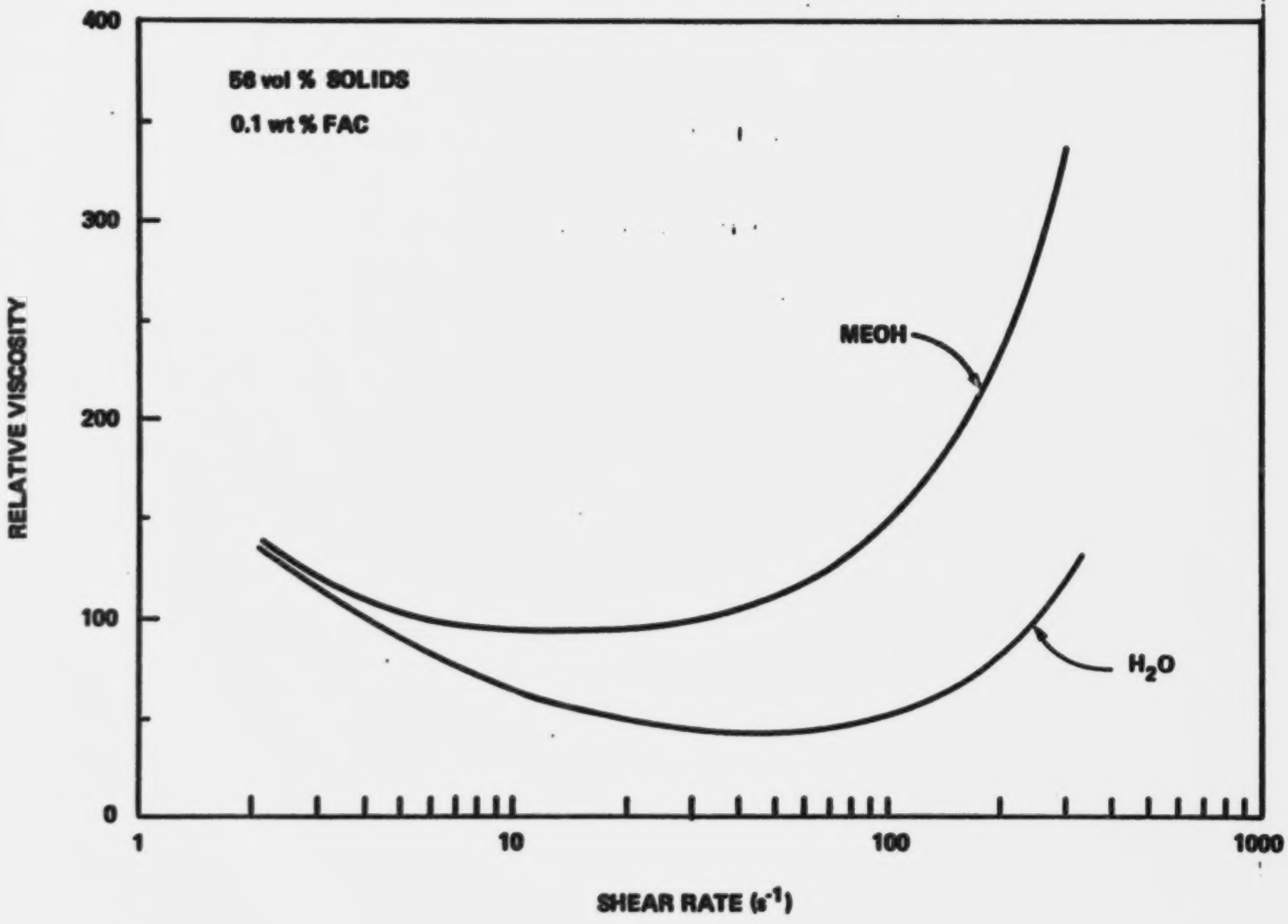
56 vol % SOLIDS
0.1 wt % FAC
MEOH
H_2O
RELATIVE VISCOSITY
SHEAR RATE (s^{-1})
400
300
200
100
0
1
10
100
1000

Table I. Porosity of Gravity Cast Samples

Solids Loading (Vol %)	pH	Sonication Time (min)	Total Porosity (Vol %)	Median Pore Radius (nm)
40	6.3	0	44.1	254
40	9.0	0	31.4	187
40	9.8	0	34.3	196
50	6.3	0	42.2	260
50	9.0	0	29.3	126
50	7.8	0	29.3	130
50	7.8	10	24.6	108
56	7.8	0	28.2	102
56	7.8	15	23.0, 23.6	82, 87
56	7.8	30	21.7, 21.9	73, 72
56	9.0	30	18.9	66
AIResearch Suspension			29.8	151

Table II. Effective Dispersants

Dispersants	Company	Available Chemical Information
CDXSS-1A	R.T. Vanderbilt Co.	ammonium polyacrylate
Darvan C	R.T. Vanderbilt Co.	ammonium polyelectrolyte
SMA-1440h	ARCO	styrene/maleic anhydride copolymer, ammoniated
TAMOL 731	Rohm & Haas Co.	sodium carboxylated polyelectrolyte
Victawet 85-X	Stauffer Chemical Co.	sodium alkyl phosphate
Gantrez S-95	GAF Corp.	polymethyl vinyl ether/maleic anhydride copolymer, prehydrolyzed
Tetrasodium Pyrophosphate (TSPP)	any major chemical supply co.	$Na_4P_2O_7$
Ammonium Citrate Dibasic	"	$(NH_4)_2HC_6H_5O_7$
Sodium Citrate Dihydrate	"	$Na_3C_6H_5O_7.2H_2O$
Ferric Ammonium Citrate (FAC)	"	$Fe_x(NH_4)_{3-x}C_6H_5O_7$

Table III. Ineffective Dispersants

Chemical	Company
Victawet 12	Stauffer Chemical Co.
Gantrez AN-119	GAF Corp.
EMA 1103	Monsanto Co.
PVP K-15	GAF Corp.
Pluronic L-92	BASF Wyandotte Corp.
Pluronic F-38	BASF Wyandotte Corp.
PA-18	Gulf Oil Chemicals Co.

Table IV. Pycnometer Density of Powders

Material	Density (g/cc)
Unground Kemanord IV, no Fe_2O_3	2.31 ± .02 g/cc
Ground Kemanord IV, no Fe_2O_3	2.33 ± 0.3 g/cc
Ground Kemanord IV, 65-64, w/Fe_2O_3	2.35 ± .02 g/cc
Fisher Scientific Co. I-116 Fe_2O_3	5.11 ± .05 g/cc

Table V. Porosity of Cast Bodies

Sample No.	(vol%)	pH	Base	Dispersant	Sonication Time (min)	Aging Time (days)	Casting Method	Total Porosity (vol%)	Median Pore Radius (nm)
1	40	6.4	NaOH	---	0	0	GC	43.8	277
2	40	6.4	NaOH	---	0	0	SC	43.4	254

Table VI. Porosity of Cast Bodies Formed Using Suspensions Containing FAC

Sample No.	(vol %)	pH	Base	Dispersant	Sonication Time (min)	Aging Time (days)	Casting Method	Total Porosity (vol %)	Median Pore Radius (nm)
3	40	--	--	FAC	0	0	GC	35.5, 35.2	157, 199
4	40	--	--	FAC	0	0	SC	36.2, 36.2	161, 162
5	56	--	--	FAC	45	0	GC	23.6, 23.4	86, 88
6	56	--	--	FAC	45	0	SC	24.4, 25.1	77, 83
7	56	--	--	FAC	15	1	GC	21.8, 22.3, 22.8	83, 76, 79
8	56	--	--	FAC	15	1	SC	21.9, 22.0	62, 66

Table VII. Porosity of Cast Bodies Formed Using Suspensions Containing NaOH or NH_4OH

Sample No.	(vol%)	pH	Base	Dispersant	Sonication Time (min)	Aging Time (days)	Casting Method	Total Porosity (vol%)	Median Pore Radius (nm)
9	56	8.0±0.2	NaOH	—	15	0	GC	28.2	107
10	56	8.0±0.2	NH_4OH	—	15	0	GC	27.7	101
11	56	8.0±0.2	NaOH	—	15	0	SC	24.6	67
12	56	8.0±0.2	NH_4OH	—	15	0	SC	25.2	68
13	56	8.0±0.2	NaOH	—	15	2	GC	23.8	94
14	56	8.0±0.2	NH_4OH	—	15	2	GC	23.9	95
15	56	8.0±0.2	NaOH	—	15	2	SC	21.9	72
16	56	8.0±0.2	NH_4OH	—	15	2	SC	22.1	62

Table VIII. Porosity of Cast Bodies Formed Using NEOH Suspensions

Sample No.	(vol%)	pH	Base	Dispersant	Sonication Time (min)	Aging Time (days)	Casting Method	Total Porosity (vol%)	Median Pore Radius (nm)
17	40	--	--	--	15	0	GC	40.8	243
18	40	--	--	--	15	0	SC	41.3	260
19	40	--	--	PAC	15	0	GC	32.3, 33.2	190, 211
20	40	--	--	PAC	15	0	SC	27.9, 28.1	119, 130
21	56	--	--	PAC	15	1	GC	26.4, 27.0	123, 137
22	56	--	--	PAC	15	1	SC	24.8, 26.1, 25.5	81, 113, 98

Table IX. Surface Areas of As-received and "Aged" Materials

Sample	Surface Area (m^2/g)
1. Unground Kemanord IV, as received	2.7
2. Ground Kemanord IV, w/ Fe_2O_3, as received	4.5, 4.6
3. I-116 Fe_2O_3, as received	11.3
4. Ground Kemanord IV, w/ Fe_2O_3, aged 144h (20 vol % aqueous suspension, occasionally vented container, mixed on roller mill)	
batch #1	6.9
batch #2	7.0
5. Ground Kemanord IV, w/ Fe_2O_3, aged 236h (30 vol % aqueous suspension, frequently vented container, mixed on roller mill)	4.8
6. Ground Kemanord IV, w/ Fe_2O_3, aged 430h (30 vol % aqueous suspension, frequently vented container, mixed on roller mill)	4.7
7. Ground Kemanord IV, w/ Fe_2O_3, aged 430h (30 vol % aqueous suspension, sealed container, mixed on roller mill)	8.7

Table X. Surface Areas of "Aged" Samples

Sample	Surface Area (m^2/g)	Date Measured
No. 4 from Table IX (Batch #1)	6.9	7-1-83
	6.6, 6.3, 6.4	9-28-83, 10-5-83
No. 4 from Table IX (Batch #2)	7.0	7-13-83
	4.3, 4.3	9-27-83, 10-2-83
Batch #3 ("aged" 144h)	4.7	8-30-83
	4.3	9-27-83
No. 7 from Table IX ("aged" 430h)	8.7	8-2-83
	6.9, 6.9	9-30-83, 10-3-83

APPENDIX E

DEVELOPMENT OF HOMOGENEITY IN Si_3N_4 CERAMICS BY COLLOIDAL FILTRATION

by

I. A. Aksay
University of Washington

C. A. Ambarian
University of California

September 15, 1983

PRECEDING PAGE BLANK NOT FILMED

Abstract

The methodology of developing microstructural uniformity in a polyphase Si_3N_4 (Al_2O_3, Y_2O_3) ceramic through a colloidal consolidation technique is outlined. The candidate Si_3N_4, Al_2O_3, and Y_2O_3 powders were first characterized according to ζ-potential behavior in aqueous suspensions, size distribution, and particle geometry. The chosen powders (in the as-received form) were then put into a dispersing-state aqueous suspension and ultrasonically dispersed. Particle and/or agglomerates larger than ~ 2.0 μm were removed through sedimentation. Suspensions containing only the remaining fine particles were used to consolidate a composite system with a composition of 92 w/o Si_3N_4 + 6 w/o Y_2O_3 + 2 w/o Al_2O_3 through colloidal filtration. The resultant sintered microstructures displayed uniformity in dimensions close to the primary particle size of the starting powders.

PRECEDING PAGE BLANK NOT FILMED

1.0 INTRODUCTION

Powder consolidation and sintering is the most widely used route to process engineering ceramics. Compared to other routes, e.g. melt/solidification and vapor deposition, powder techniques have the potential for achieving the general goal of fine-grained (or fine-porosity) structures for an almost unlimited range of single phase and polyphase chemistries. The key problem associated with powder consolidation routes, however, is that powders (especially in the submicrometer range) always have a tendency to agglomerate due to van der Waals forces. These agglomerated powders give rise to both poor mixing and packing density variations in the consolidated compact. In such instances, if the materials processor cannot control particle-particle interactions, the potential for homogeneous consolidation is lost. As a result strength degrading flaws are generated and retained in the final product due to inhomogeneities introduced into the system during consolidation.

In the case of Si_3N_4 based ceramics, which are also processed by powder consolidation and sintering techniques, inhomogeneities introduced into a powder system play a detrimental role on the mechanical properties not only at low temperatures but at elevated temperatures as well. At low temperatures, flaws caused mainly by the inhomogeneities result in low strength values.[1] At elevated temperatures, strength is degraded due to the presence of a glassy phase.[2,3] Components that result in the formation of this glassy phase are purposely introduced into the system as liquid phase sintering aids. Studies have shown that high temperature failure rates are enhanced as the amount of this glassy

PRECEDING PAGE BLANK NOT FILMED

phase increases.[4] Thus, it is clear that if the amount of this glassy phase can be reduced, with improved homogeneity and phase distribution, a reduction in high temperature deformation rates would be achieved.

Recent studies have shown that colloidal suspensions provide an opportunity to control particle-particle interactions and thus homogeneity in powder-processed systems.[5,6] First, particulates in a colloidal suspension can be dispersed through particle-particle repulsive forces resulting from electrostatic interaction or steric hindrance, or from a combination of both.[7] This particle-particle repulsion helps assure both the break up of the soft agglomerates held together by van der Waals forces and the formation of well dispersed suspensions, even in multiphase systems. Second, during removal of the suspending medium, consolidation behavior of the particles can be controlled.

In this report we summarize the results of a study on the colloidal consolidation of a polyphase Si_3N_4 ceramic. The main objective of this study was to establish the methodology of obtaining uniformity in dimensions close to the primary particle size of the raw materials. The work was performed in the Department of Materials Science and Engineering of UCLA during the period of June 15, 1983 to September 15, 1983 and was sponsored by the Garrett Turbine Engine Company under P.O. #1804333.

2.0 EXPERIMENTAL

In the following sections we outline the experimental procedure followed in order to achieve uniformity in the consolidated powder compacts. All the experimental work was based on a system composition of 92 w/o Si_3N_4 + 6 w/o Y_2O_3 + 2 w/o Al_2O_3 as specified by the Garrett Turbine Engine Co. Commercially available powders were evaluated and a selection was made for use in our consolidation studies through colloidal filtration.

The powders which were evaluated in this study were:

- Si_3N_4
  1. GTE SN-502*
  2. UBE Si_3N_4 (Lot #A-15)†
  3. UBE Si_3N_4*

- Y_2O_3
  1. Ames Lab. Y_2O_3(A/B)§
  2. Molycorp Regular SA (Lot #808-639)*
  3. Molycorp Regular SA (Lot #1345)*
  4. Molycorp High SA (Lot #1264/94)*
  5. Molycorp Higher SA (Lot #B108)*
  6. UBE Y_2O_3† (Lot #5725, Shinetsu Chemical)

---

* Obtained from Garrett/AiResearch Casting Co., Torrance, CA 90509
† UBE Industries, Ltd., (Rep. Office), New York, NY 10019
§ Ames Laboratory, Iowa State University, Ames Iowa 50011

- Al_2O_3
  1. A-16 SG¶
  2. Sumitomo AKP-30†

2.1 ζ-Potential Behavior of the Powders in Aqueous Suspensions

In our dispersion studies, an electrostatic route (vs. steric stabilization) was followed. All the work was done with aqueous systems.

It was necessary to determine the ζ-potential vs. pH behavior for each of the candidate powders, because in order to achieve particulate-level homogeneity, it is necessary to disperse all particles. This dispersion can only be achieved when the particles have a ζ-potential (effective surface charge) higher than 30 to 40 mV.

The determination of ζ-potential behavior vs. pH, then, tell us two things: first, it indicates whether the particulates can indeed be dispersed, and second, it tells us what pH this dispersion occurs.

ζ-potential vs. pH curves were determined for each of the candidate powders using a conventional microelectrophoresis apparatus.* This process basically involved the application of an electric field to a suspension of the given powder, and microscopic observation of the resultant particle velocities at any given fluid pH. This gives us directly the mobility of the suspended particles. As the suspending fluid's pH value is changed (by addition of either an acid or a base, in this case

¶ Aluminum Company of America, Bauxite, AR 72011
† Sumitomo Chemical Co., Ltd., Osaka, Japan
* Mark II Electrophoresis Unit, Rank Brothers, Cambridge, England.

HCl and either NH_4OH or NaOH), the surface charge (and thus the mobility) of the particles is changed.

Experimentally, ten measurements of particle velocity at each pH were made, with the mean values taken in order to minimize error. From these velocities and the applied-field values, the mobilities were calculated. Since there is almost a linear relation between mobility and ζ-potential, a standard multiplier was used to further compute the ζ-potentials from observed mobilities.

2.2 Characterization of Particle Size Distribution

In order to limit the flaw size to dimensions < 10 μm, it was necessary to characterize the powders to determine their size-suitability for our purpose. To this end, size distributions of the candidate powders were obtained using a sedimentation/x-ray absorption technique.† Size-distribution plots were made using scales of cumulative mass-percent (or "percent-finer than") vs. equivalent spherical diameter (based on Stokes' law sedimentation). [The details of suspension preparations prior to characterization are outlined in the figure captions of the next section.]

Further, scanning-electron micrographs were taken for each of the powders in the as-received form.

2.3 Reduction of Particle-Agglomeration by Ultrasonic Rupture

Even though the powders were chosen on the basis of fine particle size, the best-available powders were still heavily agglomerated. It

† Sedigraph 5000E, Micromeritics Inst. Co., Norcross, GA

was possible to eliminate much of this agglomeration through ultrasonic rupture* in the suspension stage, with the suspensions prepared at a pH giving optimal dispersion. The effectiveness of ultrasonication was continuously monitored through particle size distribution measurements. In most cases, ultrasonication was continued for 5 minutes. However, it should be pointed out that the duration of ultrasonication was not nearly so important as the energy-per-unit-volume of vibration used.

2.4 Elimination of Unwanted Particle Units by Sedimentation

Although the ultrasonication procedure outlined above was quite effective in dispersing a major portion of the agglomerates, it was still necessary to remove any remaining agglomerates and particles larger than a desired (~ 2-3 μm) size.

Stokes' Law for the sedimentation of a particle under the influence of gravity through a viscous fluid is given as

$$r^2 = \frac{9\eta v}{2(\rho_{solid} - \rho_{fluid})\, g} \qquad (1)$$

or, rearranging,

$$v = \frac{(\rho_{solid} - \rho_{fluid})\, g\, d^2}{18\eta} \qquad (2)$$

where r = radius of particle (spherical equivalent),

d = diameter of particle,

v = velocity of particle through fluid,

ρ_{solid} = density of particle,

* Model 300 Sonic-Dismembrator, Artek Systems Co., Farmingdale, NY

ρ_{fluid} = density of fluid,

η = viscosity of fluid,

g = acceleration due to gravity.

Thus, for any given solid particle of size d, we can calculate its velocity through a fluid of viscosity η.

Given this information, it is possible to calculate the amount of time required for all particles of a given size to settle out of suspension. Using this approach, almost all particles larger than 2 micrometers in diameter were removed from the as-received Si_3N_4 and Y_2O_3 powders.

The fine particles (still in suspension) were siphoned off, and then dried in a conventional oven overnight at 150°C. The dried powders, which were now free of hard agglomerates and large particles but were in weakly agglomerated form due to drying, were then dry-milled with an agate mortar and pestle.

2.5 Composite Suspensions

For reasons that will be discussed in the next section, a mutual pH range where Si_3N_4, Y_2O_3, and Al_2O_3 could be dispersed was found to be above pH = 9.9. Composite suspensions containing these three phases, at a composition of 92 w/o Si_3N_4 +6 w/o Y_2O_3 + 2 w/o Al_2O_3, were prepared by adding the powders prepared by the techniques described above into a predescribed amount of deionized water. Powders were first added quickly, but more slowly as the viscosity of the suspension increased. pH was monitored and adjusted with NH_4OH as the solids were added.

The optimum concentration of solids in the suspension was decided through viscosity measurements.* In order to retain a highly fluid state, the addition of the solids was stopped when the viscosity of the suspensions reached ~ 200 cP.

2.6 Consolidation by Filtration and Sintering

Consolidation of the composite systems was initially done on plaster of Paris molds prepared with a 100:75 plaster/water ratio by weight. Vacuum filtration using both a running-water aspirator-type vacuum pump and a mechanical pump was also tried.

Some of our initial samples were sent to AiResearch Casting Co., Torrance, CA for sintering experiments which were performed at 1600°C (16.7 psi nitrogen pressure in Run HPST-268), 1750°C (104.7 psi nitrogen pressure in Run Q-271), and 1850°C (104.7 psi nitrogen pressure in Run Q-269).

* Brookfield Model RVTD, Digital Viscometer, Brookfield Engineering Laboratories, Inc., Stoughton, MA 02072.

.3.0 RESULTS AND DISCUSSION

In the following sections we will first present the results on the powder characteristics and outline the reasoning that led us to the selection of the powders used in the preparation of the composite suspension. Next, we will present the data on the microstructural evolution of the colloidally filtered systems during sintering.

3.1 Powder Characteristics and Selection

3.1.1 Si_3N_4 Powders

The ζ-potential vs. pH curves for the two types of Si_3N_4 powders evaluated are shown in Fig. 1. The isoelectric point (pH value where ζ=0) of GTE SN-502 was determined to be ~ 4.7 whereas the isoelectric point of both the UBE powders was around 6.5. It is important to note that if these powder surfaces were similar to that of SiO_2, due to an expected oxidation product, the isoelectric points should have been much lower since our studies on SiO_2 powders always indicated values around pH=2. In fact, in this respect GTE SN-502 powders showed a behavior closer to that of SiO_2. This low isoelectric point for the GTE SN-502 powder also resulted in low ζ-potential values in the acidic range, thus making it useful only in the basic (~ > pH=6.5) range. In contrast, the UBE powders displayed considerably higher ζ-potential values both in the acidic and the basic ranges.

The UBE Si_3N_4 powder supplied to us by Garrett/ACC (Lot #A-15) was shown to be highly agglomerated, as evidenced by the SEM micrographs

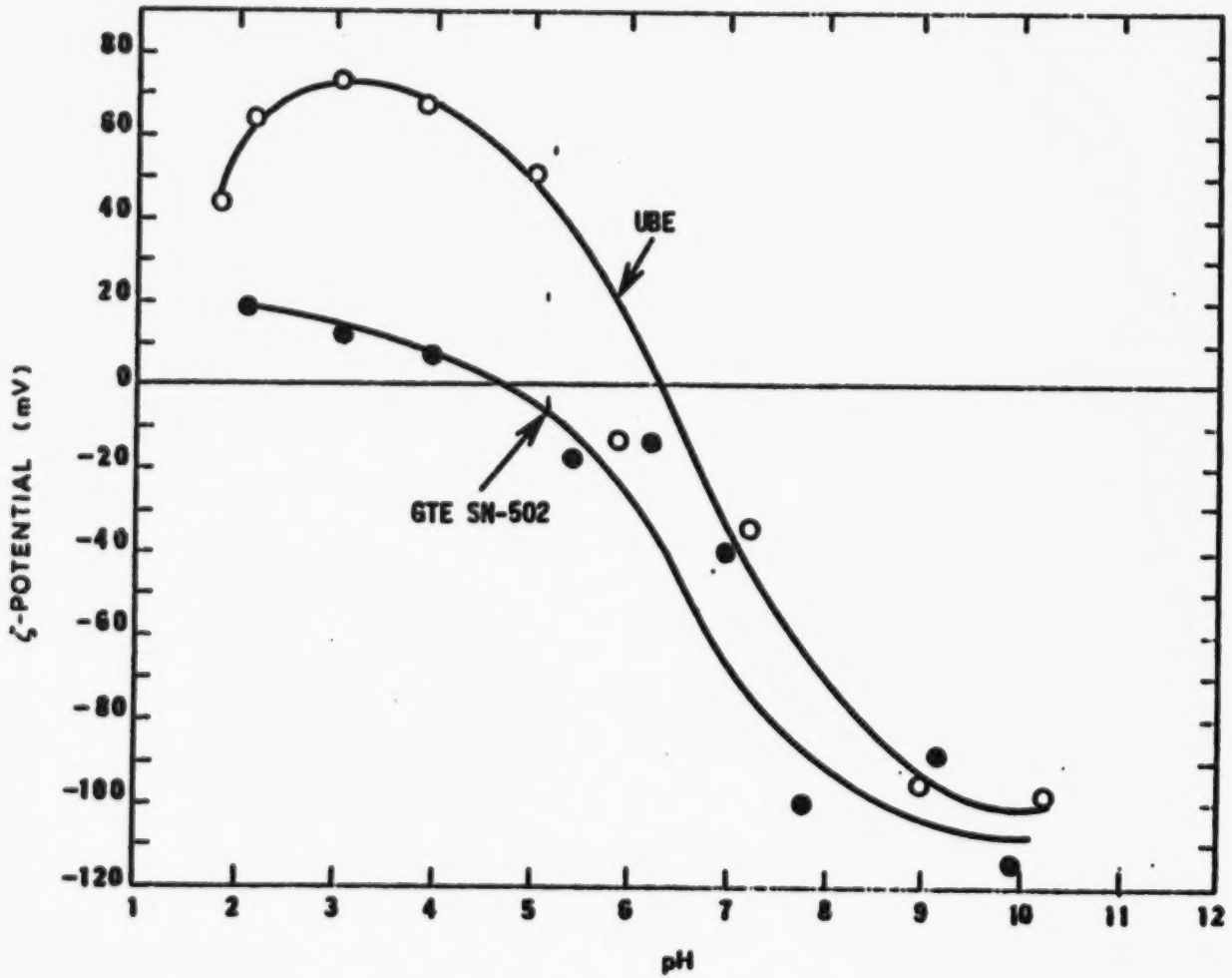

Fig. 1 ζ-potential vs. pH relationship of GTE SN-502 and UBE Si_3N_4 powders.

(Fig. 2) and the size-distribution plots (Fig. 3). Although the primary particles are indeed small, they are locked into hard agglomerates, most of which are in excess of 20 μm in diameter. These hard agglomerates could not be completely dispersed with ultrasonication (Fig. 3).

Another batch of UBE powder, which was sent to us directly from UBE in Japan, was much less agglomerated (Figs. 4 to 6). These agglomerates were easily dispersed through ultrasonication within less than 5 minutes.

Two distinctly different forms were visible in the GTE SN-502 powder, apparently as α- and β-Si_3N_4 (Fig. 7). Notice the micrometer sized spheroidal particles and the elongated particles which "link" the agglomerated spheroids. Most of these agglomerates, however, could be dispersed with ultrasonication to yield a fine-sized alternative comparable to the direct shipment of UBE.

The direct shipment from UBE was chosen as the powder to be used in our studies mainly due to the fact it was more uniform not only in physical (particle size and shape) characteristic but also with respect to ζ-potential behavior in the acidic and basic ranges.

3.1.2 Al_2O_3 Powders

ζ-potential vs. pH behavior of Sumitomo's AKP-30 is shown in Fig. 8. The isoelectric point of ~ 7.5 measured for this powder was lower than the 9.8 value obtained for Alcoa's A-16 SG. Both powders displayed high ζ-potential values in the acidic as well as the basic ranges. However, compared to A-16 SG, Sumitomo's AKP-30 was found to be not only highly

ORIGINAL PAGE IS
OF POOR QUALITY

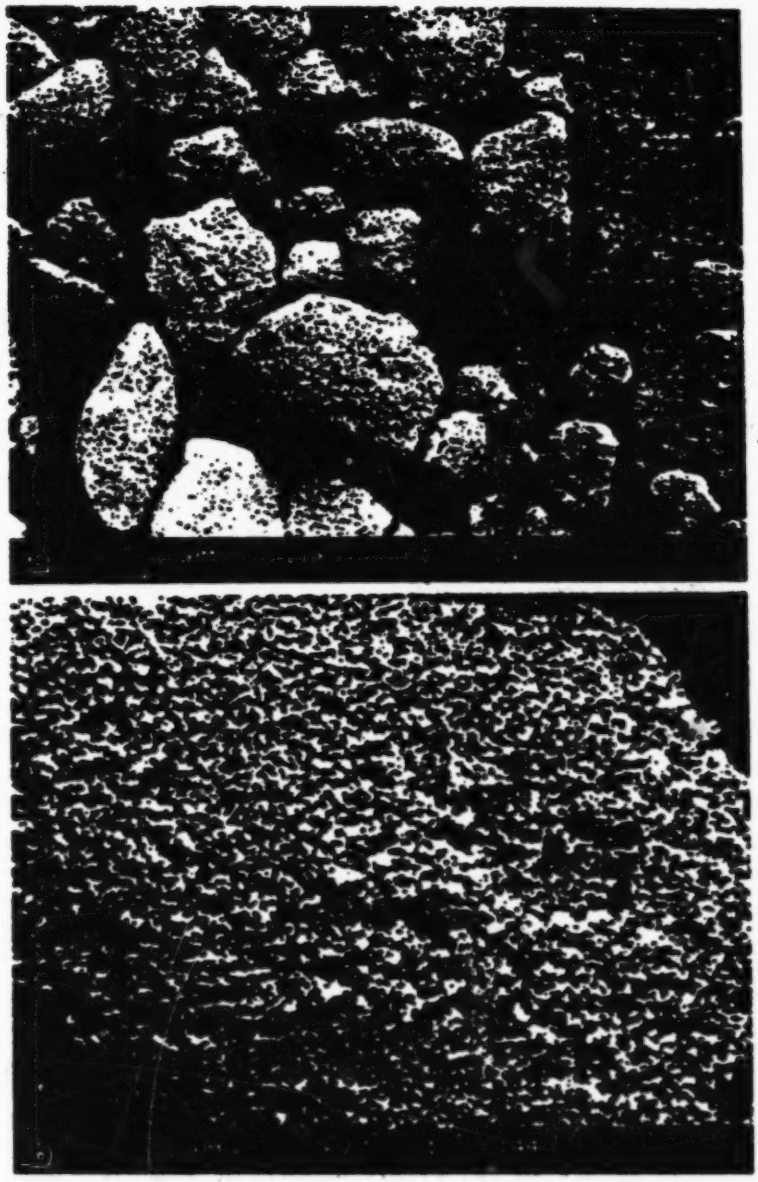

Fig. 2 SEM micrographs of UBE Si_3N_4 obtained from Garrett/ACC.

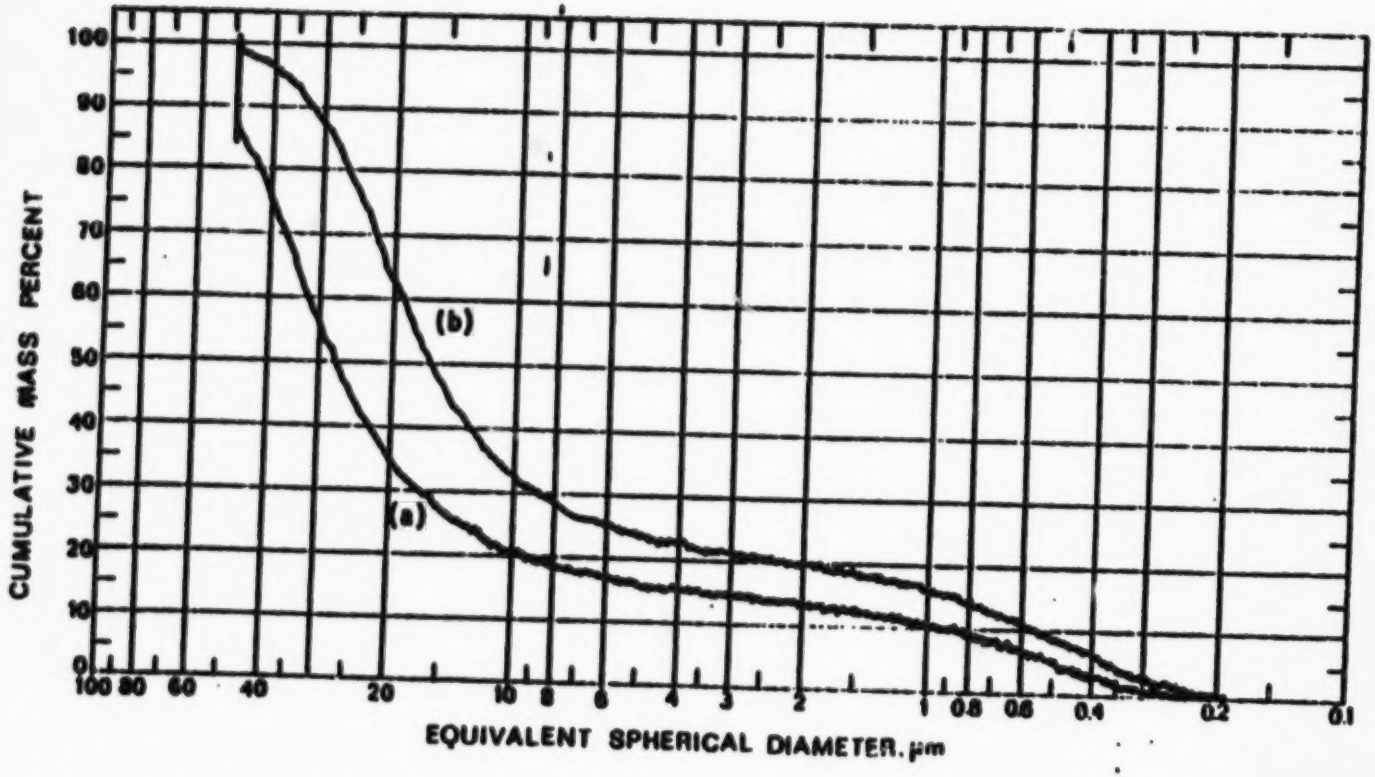

Fig. 3 Particle (agglomerate) size distribution of UBE Si_3N_4 powder obtained from Garrett/ACC at (a) pH = 10 and (b) pH = 3, after ultrasonication in both cases.

ORIGINAL PAGE IS
OF POOR QUALITY

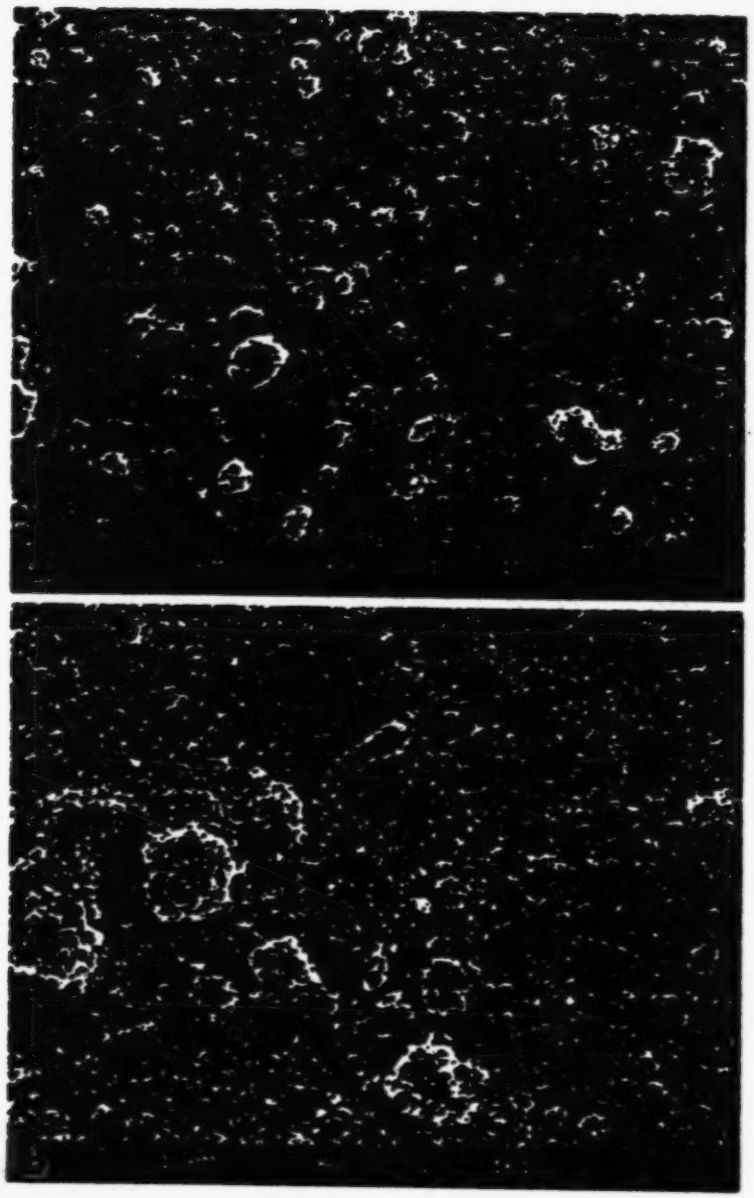

Fig. 4 SEM micrographs of UBE Si_3N_4 powder (Lot #A-15).

ORIGINAL PAGE IS
OF POOR QUALITY

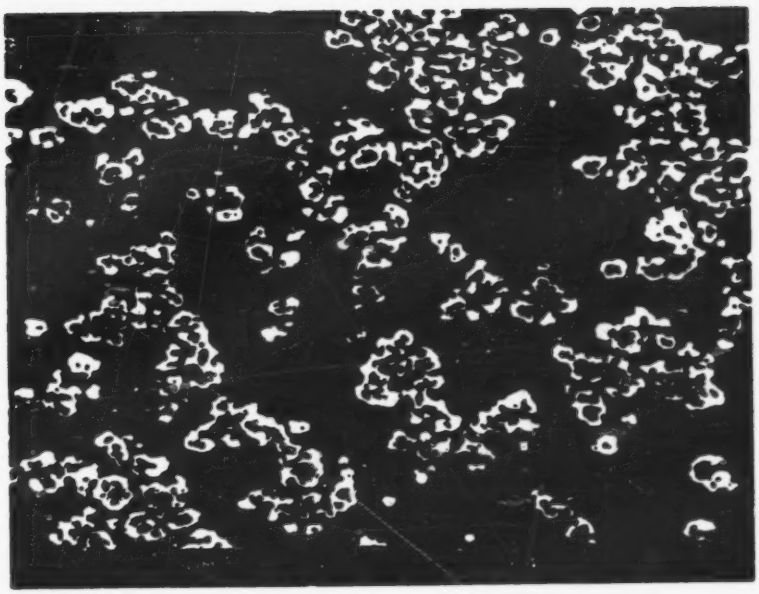

Fig. 5 SEM micrograph of UBE Si_3N_4 powder (Lot #A-15).

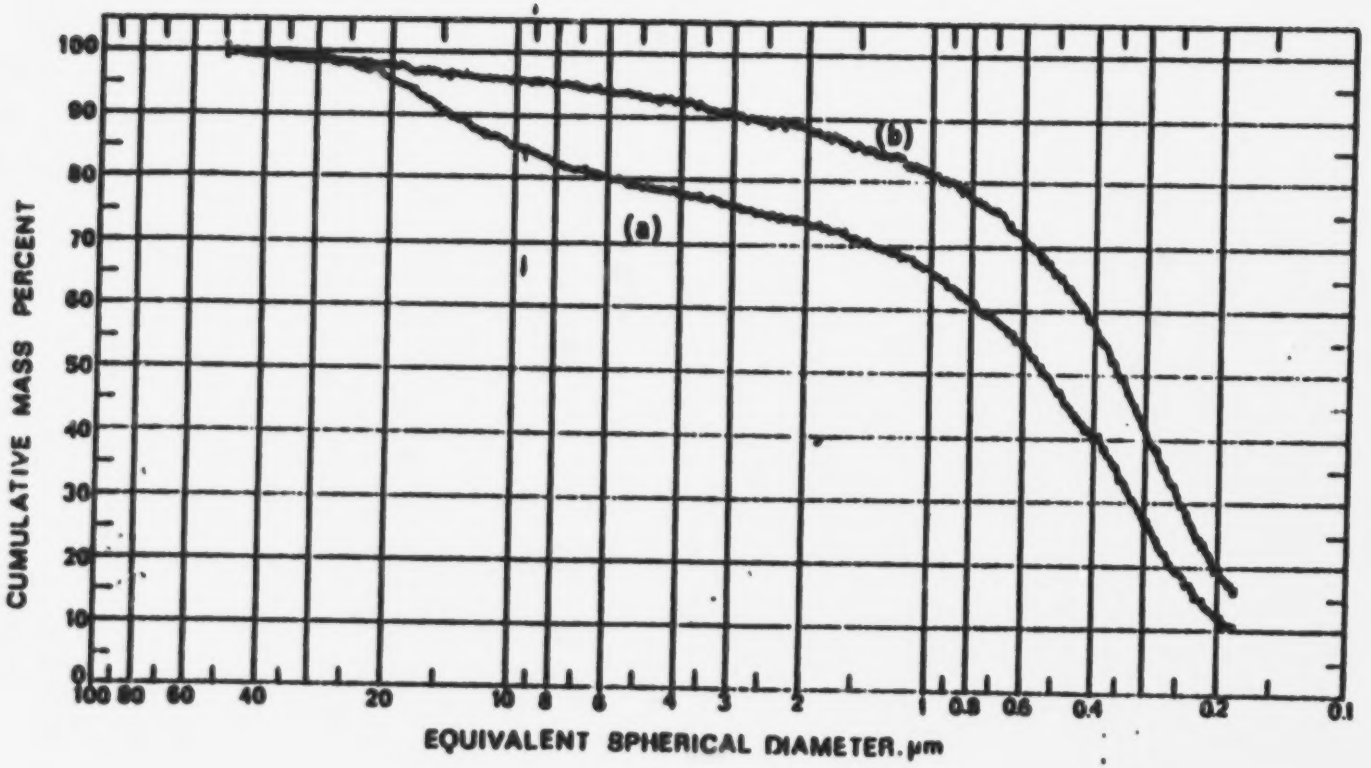

Fig. 6 Particle (agglomerate) size distribution of UBE Si_3N_4 powder (Lot #A-15) at pH = 9.8 (a) before and (b) after ultrasonication.

ORIGINAL PAGE IS
OF POOR QUALITY

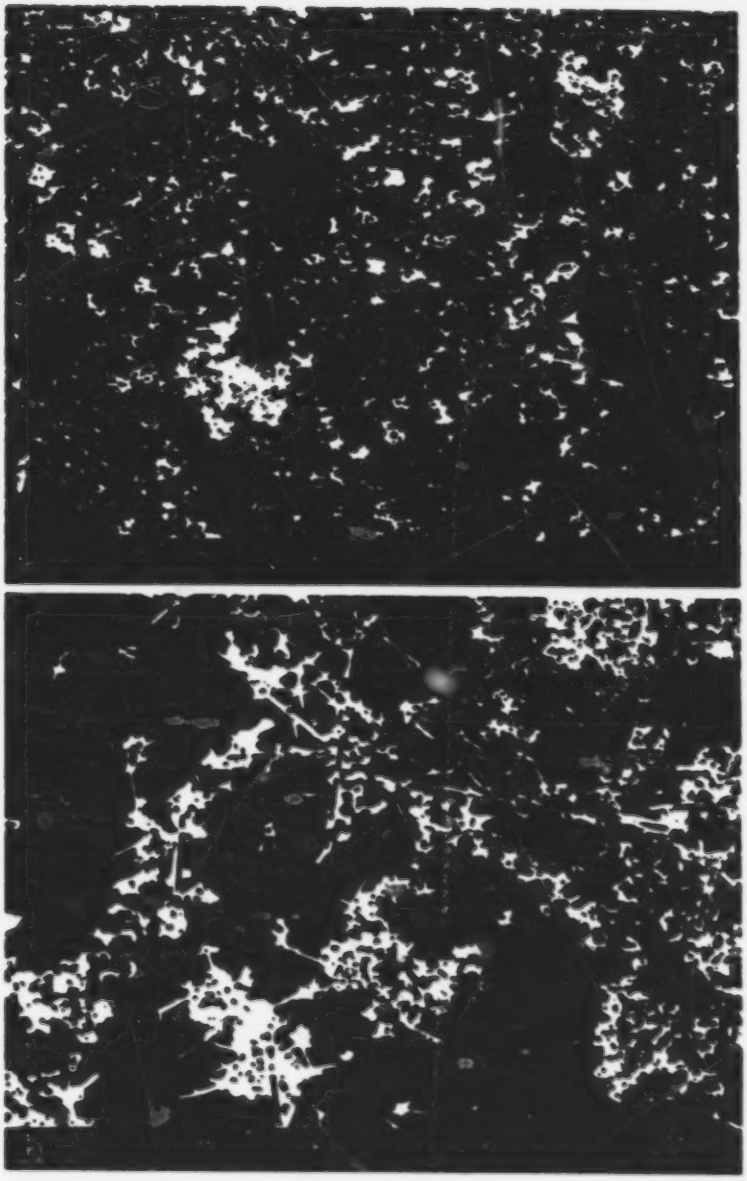

Fig. 7 SEM micrographs of GTE SN-502 Si_3N_4 powder.

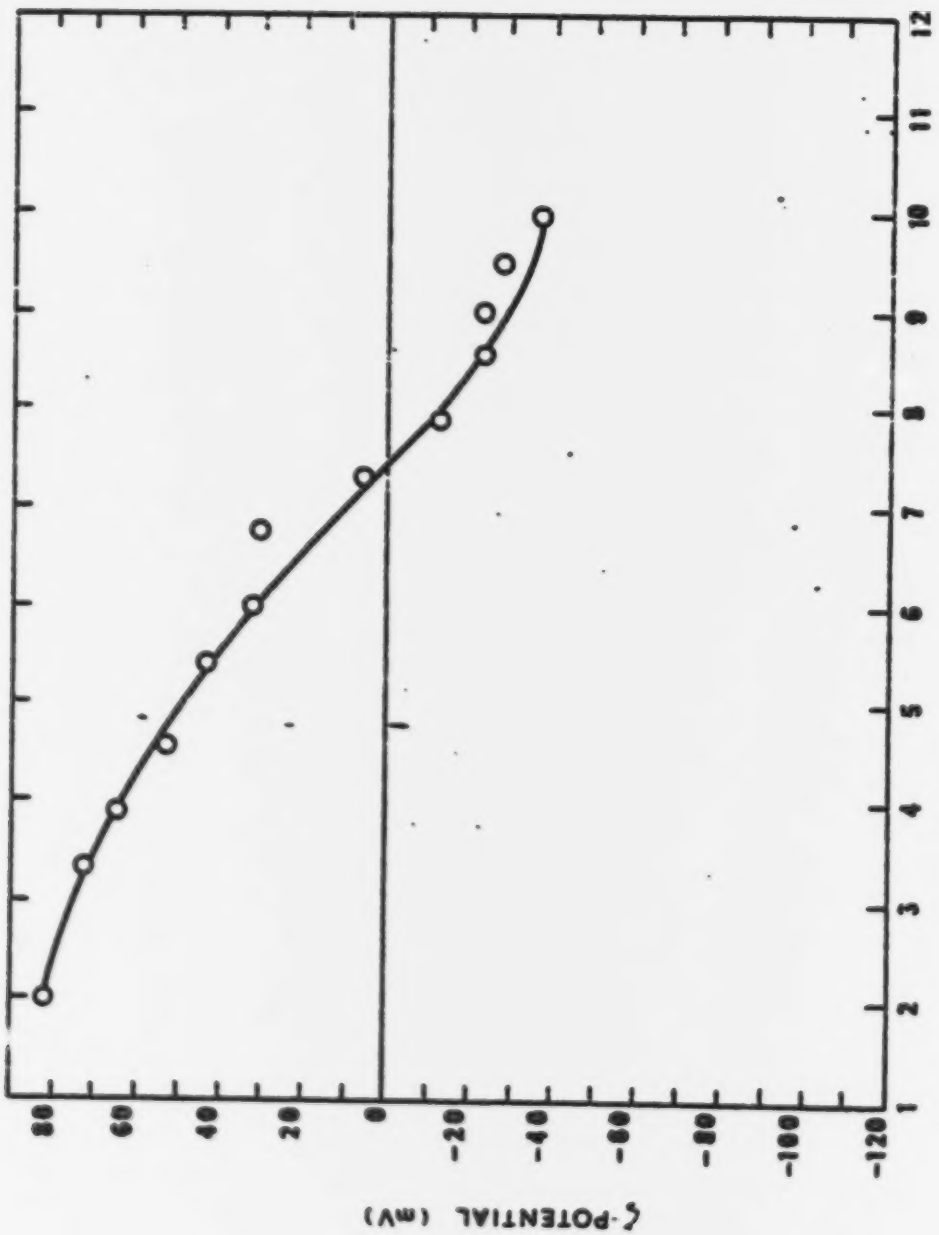

Fig. 8 ζ-potential vs. pH relationship of Sumitomo Al_2O_3 (AKP-30).

uniform in particle size (Fig. 9) but also practically free of agglomerates or particles larger than 2 μm (Figs. 9 and 10). Therefore, our choice was the Sumitomo's AKP-30.

3.1.3 Y_2O_3 Powders

The ζ-potential behavior of Y_2O_3 powders was highly irregular, exhibiting fluctuations especially in the pH range of 6 to 9 (Fig. 11). This behavior could not be confirmed by previous literature data. In the only reported work on the ζ-potential behavior of Y_2O_3 in aqueous suspensions by Persson, et al.[8], this phenomenon was not observed. We provide no explanation for this observation at this time. Further experimental work will be necessary in order to provide a full explanation. ζ-potential behavior of all the Molycorp powders were similar (Fig. 11). Ames Lab. Y_2O_3 displayed low ζ-potential almost across the entire pH range; and, thus, on this basis alone it was unacceptable for our use. Since the UBE Y_2O_3 was received late in the program, it was not evaluated with respect to its ζ-potential characteristics.

Y_2O_3 powder prepared by the Ames Laboratory was found to be highly agglomerated (Fig. 12). These agglomerates were very strong and could not be dispersed through ultrasonication. Therefore, in addition to its unacceptable ζ-potential behavior, this powder was unacceptable on the basis of its physical characteristics as well.

Among the Molycorp Y_2O_3 powders, the one designated as "Higher Surface Area" by Garrett/ACC was the most acceptable one (Fig. 13) although the ones designated as "Regular Surface Area" did not significantly

ORIGINAL PAGE IS
OF POOR QUALITY

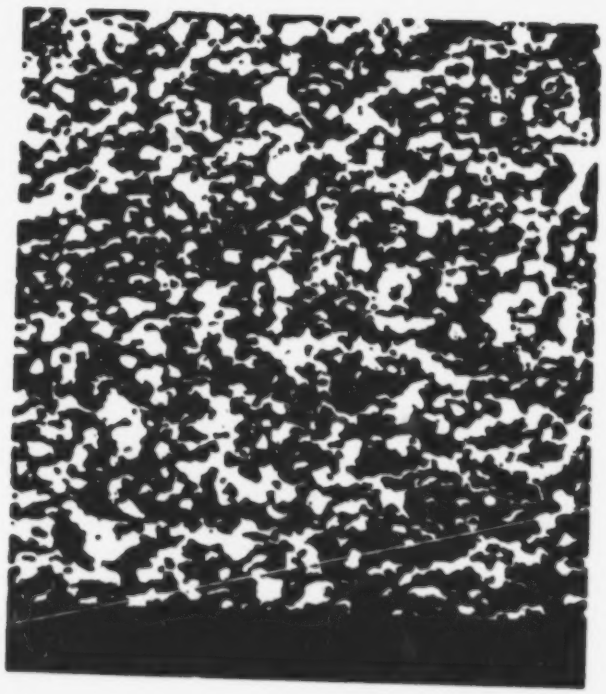

Fig. 9 SEM micrograph of Sumitomo Al_2O_3 (AKP-30).

ORIGINAL PAGE IS
OF POOR QUALITY

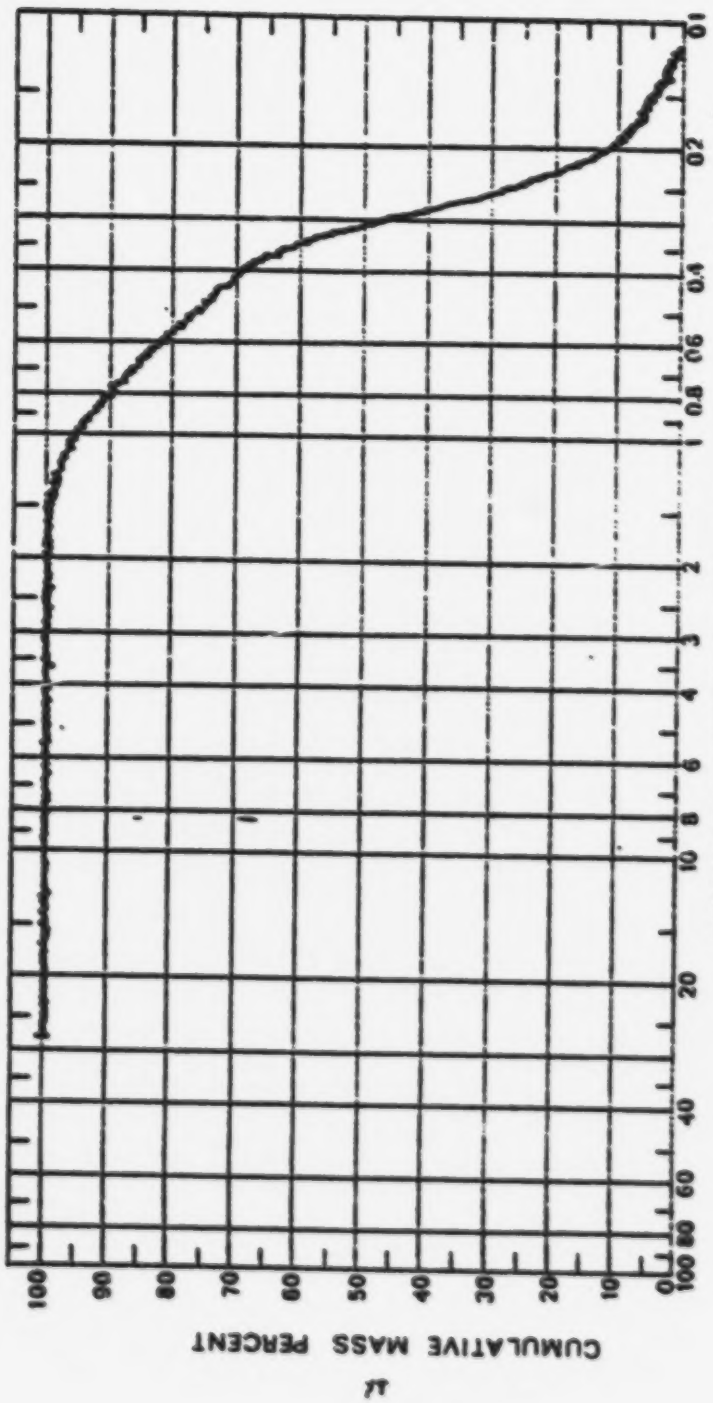

Fig. 10 Particle (agglomerate) size distribution of Sumitomo Al_2O_3 (AKP-30) at pH = 2.0 after ultrasonication.

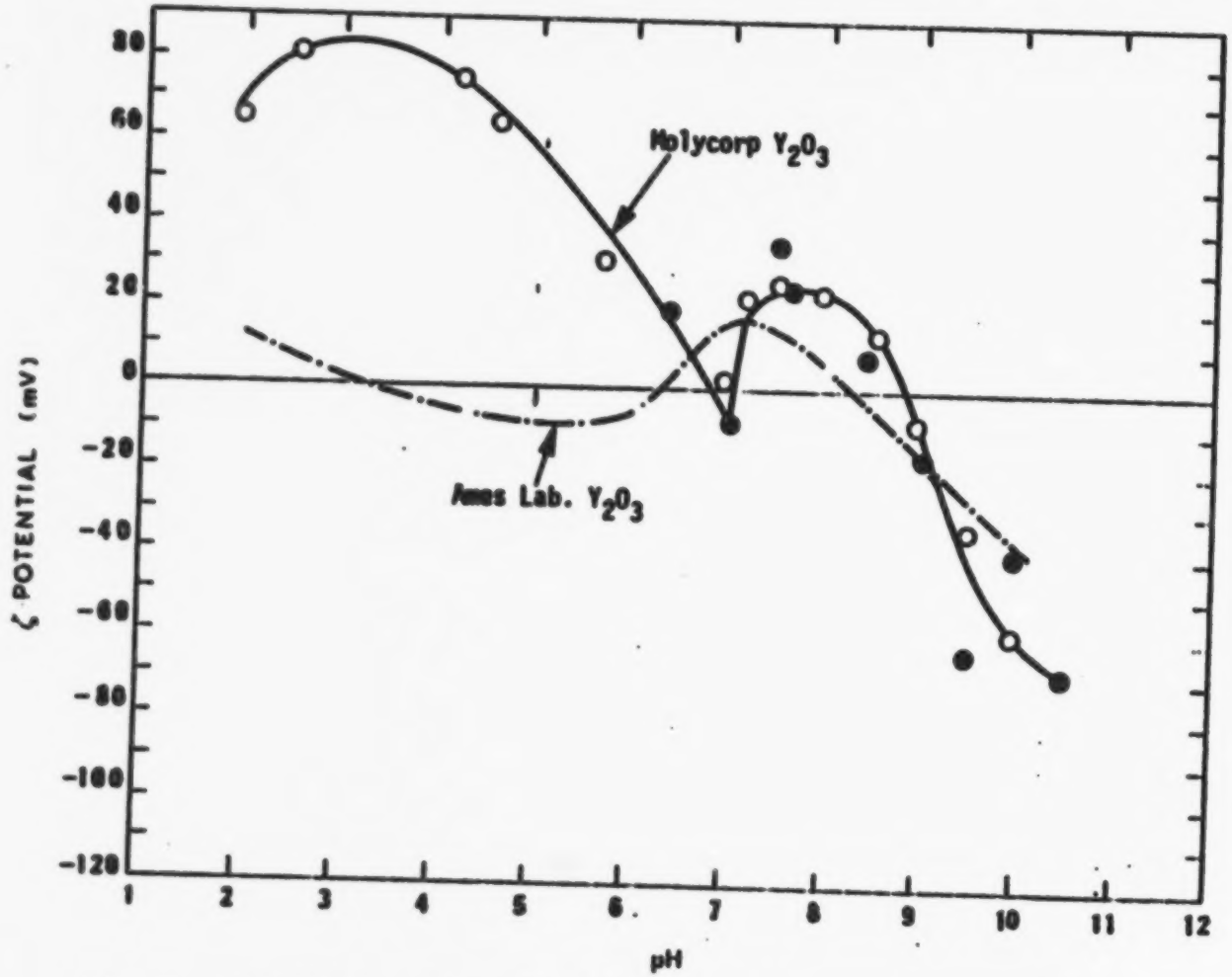

Fig. 11 ζ-potential vs. pH relationship of Ames Lab. and Molycorp Y_2O_3 powders.

ORIGINAL PAGE 13
OF. POOR QUALITY

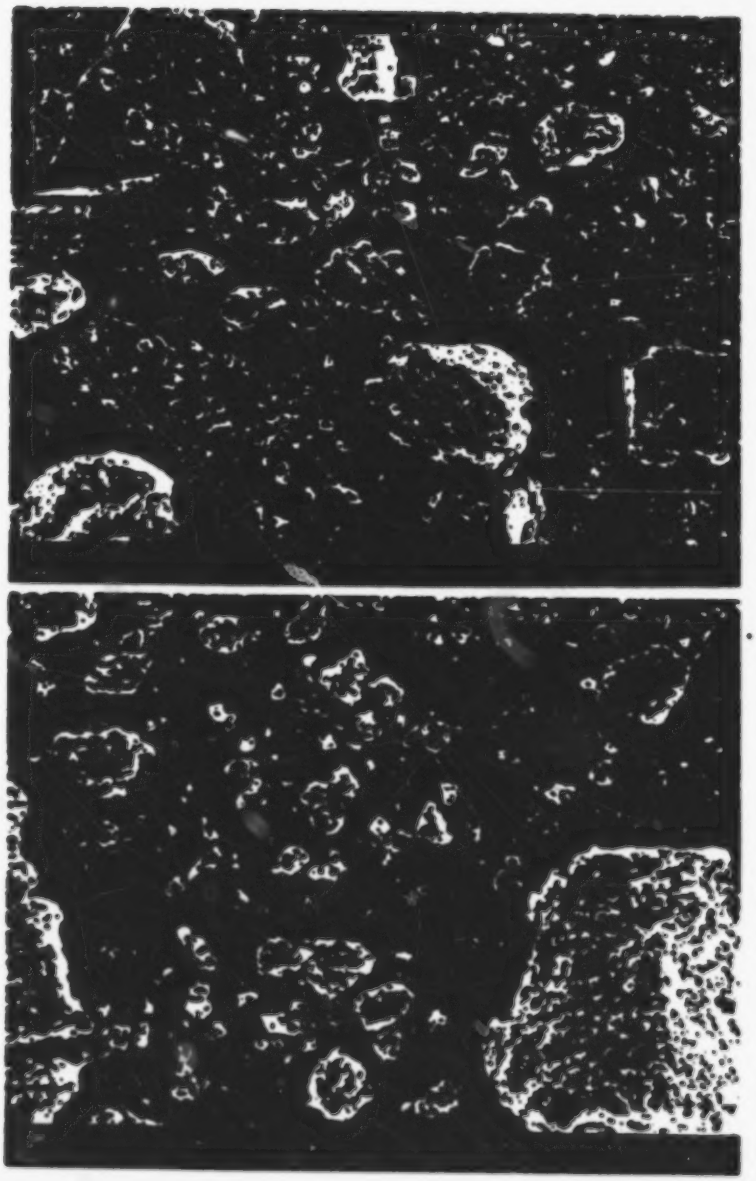

Fig. 12 SEM micrographs of Ames Lab. Y_2O_3 powder.

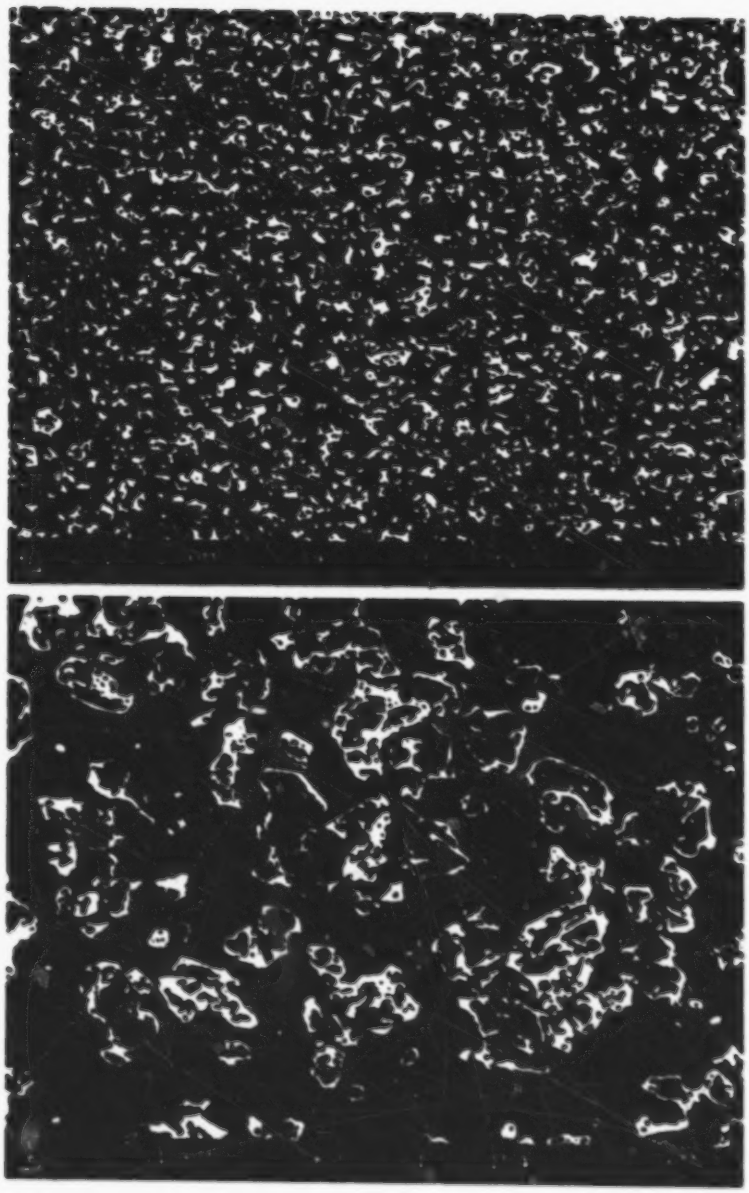

Fig. 13 SEM micrographs of Molycorp Y_2O_3 powder (higher surface area).

differ in appearance (Fig. 14). These powders also showed agglomeration and ultrasonication was again necessary in order to reduce the agglomerate size (Fig. 15).

The Y_2O_3 powder supplied by UBE was nearly identical to the Molycorp Higher Surface Area powder (Figs. 16 and 17), but Molycorp's was chosen to avoid total dependence upon a single manufacturer.

One major problem encountered with Y_2O_3 was that of dispersability in the acidic range. Although initial ζ-potential measurements displayed high values, apparently due to chemical reactions, Y_2O_3 powders could not be dispersed in the acidic range. Therefore, the basic range (pH > 9.0) was the only logical choice.

3.2 Composite Suspensions and Consolidation by Filtration

The first step in this phase of the study was the determination of the optimal consolidation conditions for filtration that would retain the homogeneity of the colloidal state.

Our first move in that direction was to select a mutual pH range where all the powders displayed high (> 30-40 mV) ζ-potential values. As shown in Fig. 18, for the three powders selected, this region had to be either below pH = 5.6 or above pH = 9.3. Since the acidic region was out of the question (due to the apparent chemical instability of Y_2O_3), the basic region was our only choice.

The point of maximum dispersion generally corresponds to the viscosity minimum for a suspension of some given solids content. As a test

ORIGINAL PAGE IS
OF POOR QUALITY

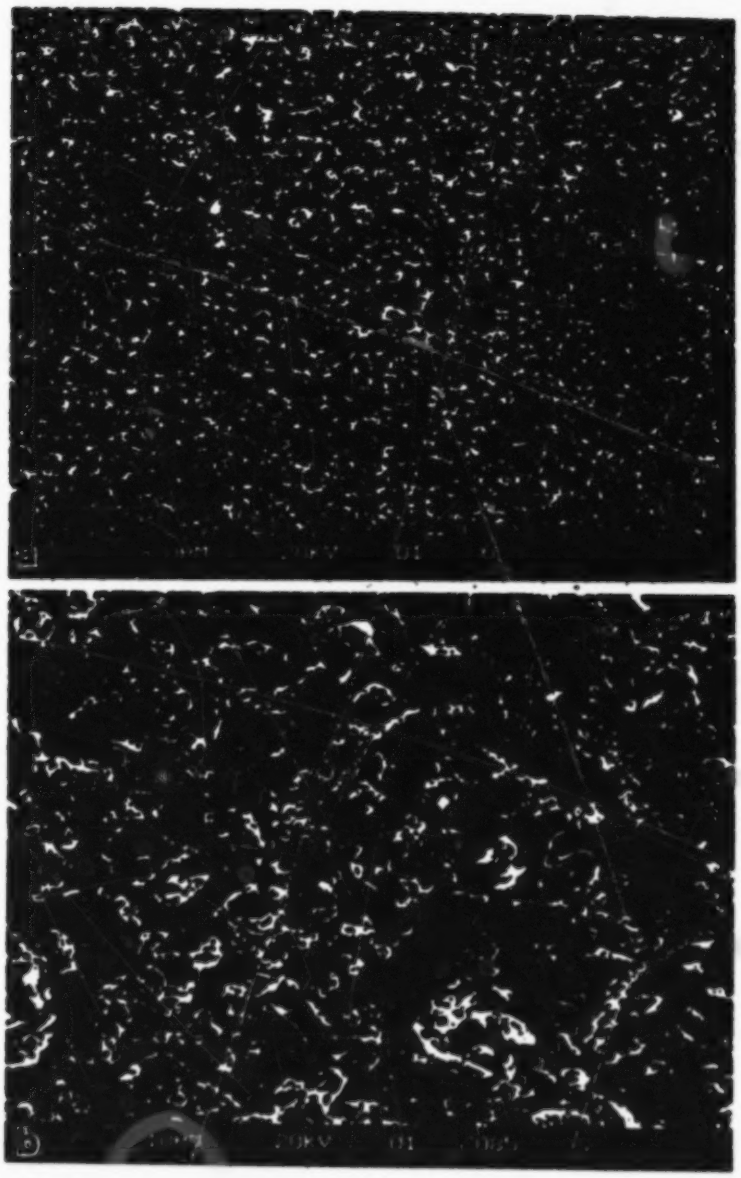

Fig. 14 SEM micrographs of Molycorp Y_2O_3 powder (regular surface area).

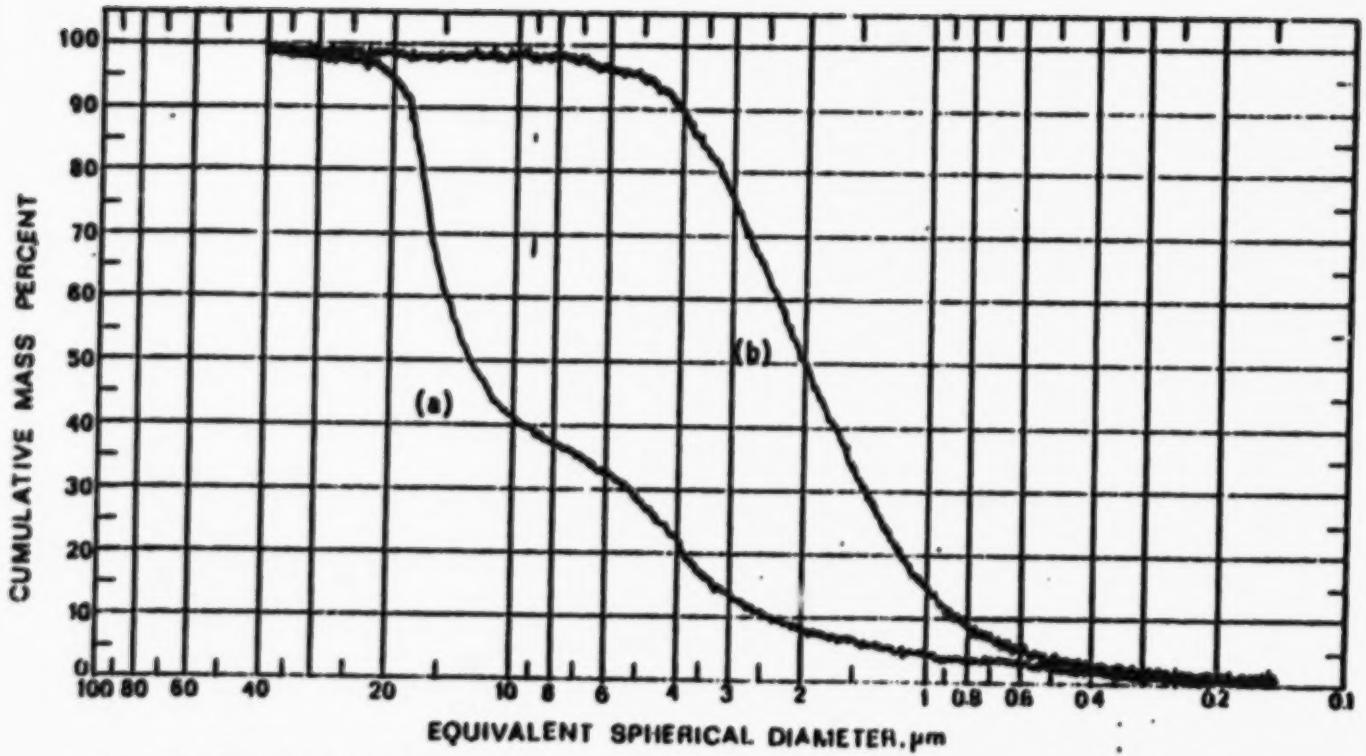

Fig. 15 Particle (agglomerate) size distribution of Molycorp Y_2O_3 (higher surface area) at pH = 10 (a) before and (b) after ultrasonication.

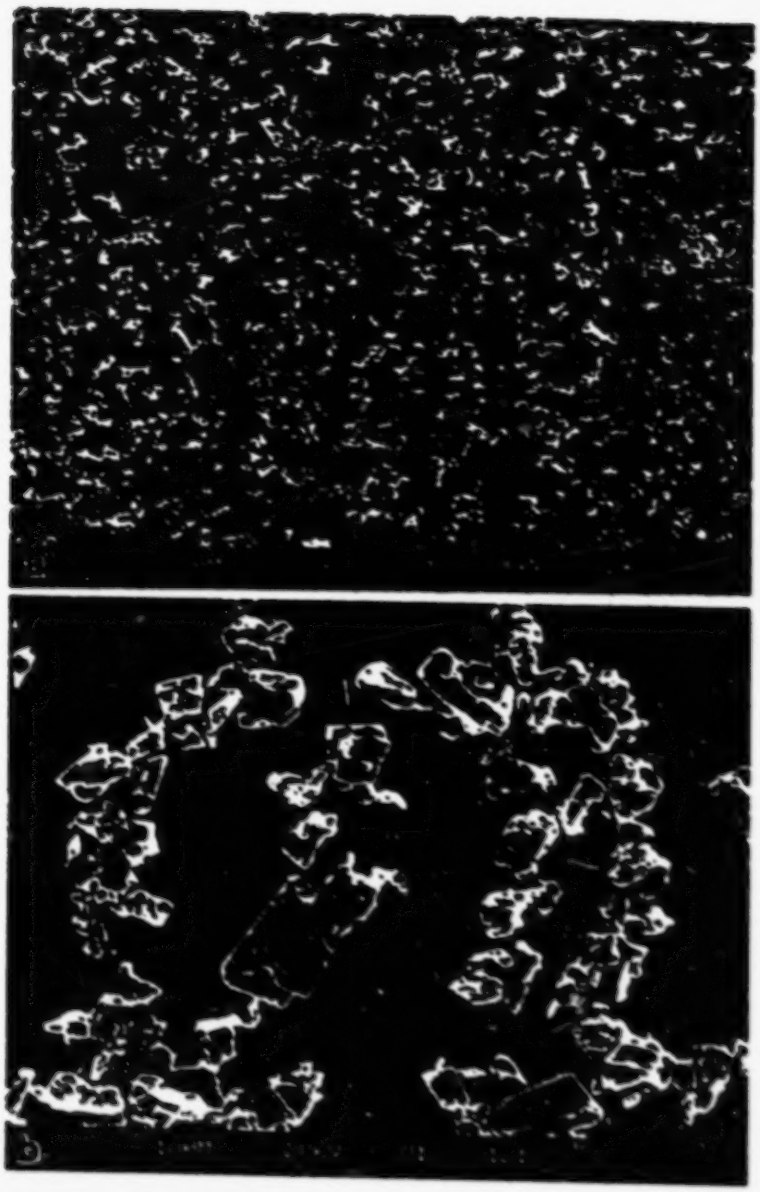

Fig. 16 SEM micrographs of UBE Y_2O_3 powder (Lot #5725).

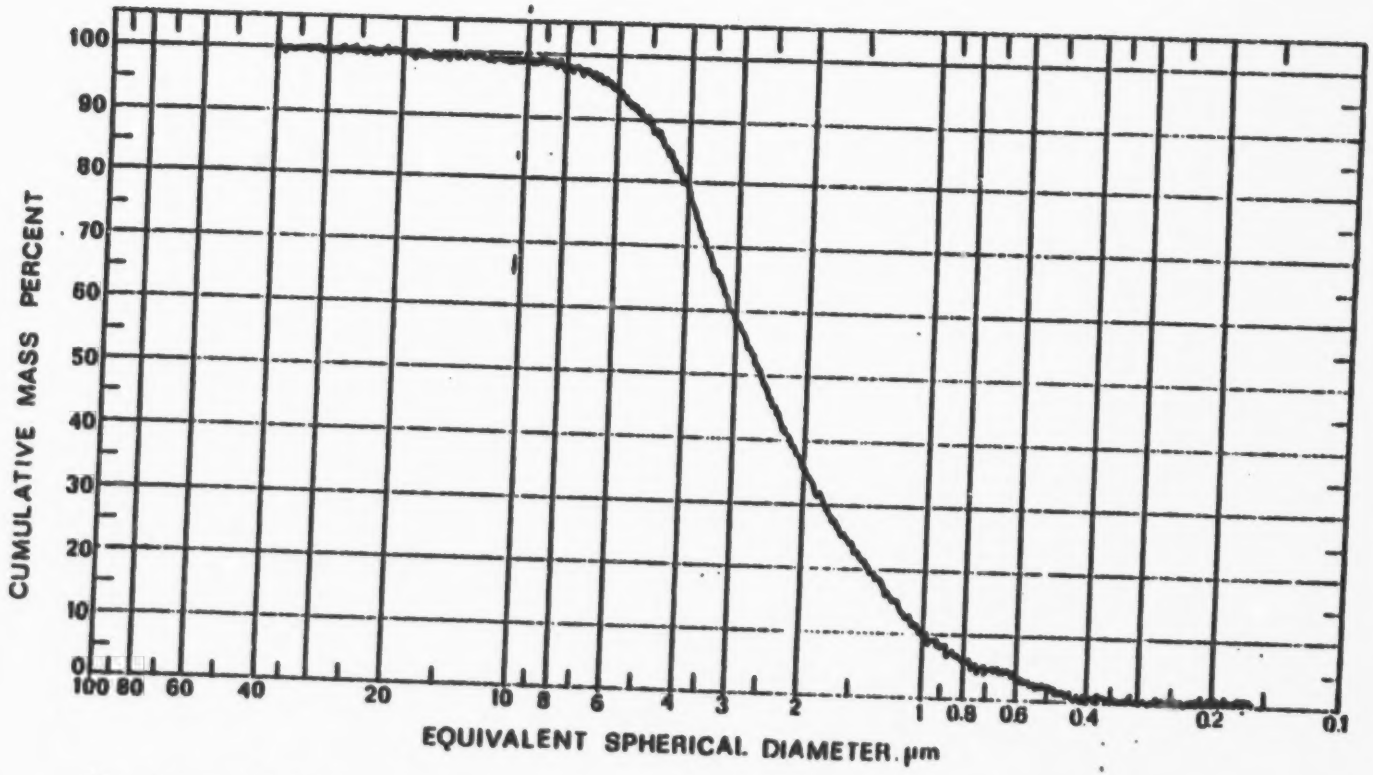

Fig. 17 Particle (agglomerate) size distribution of UBE Y_2O_3 powder at pH = 10 after ultrasonication.

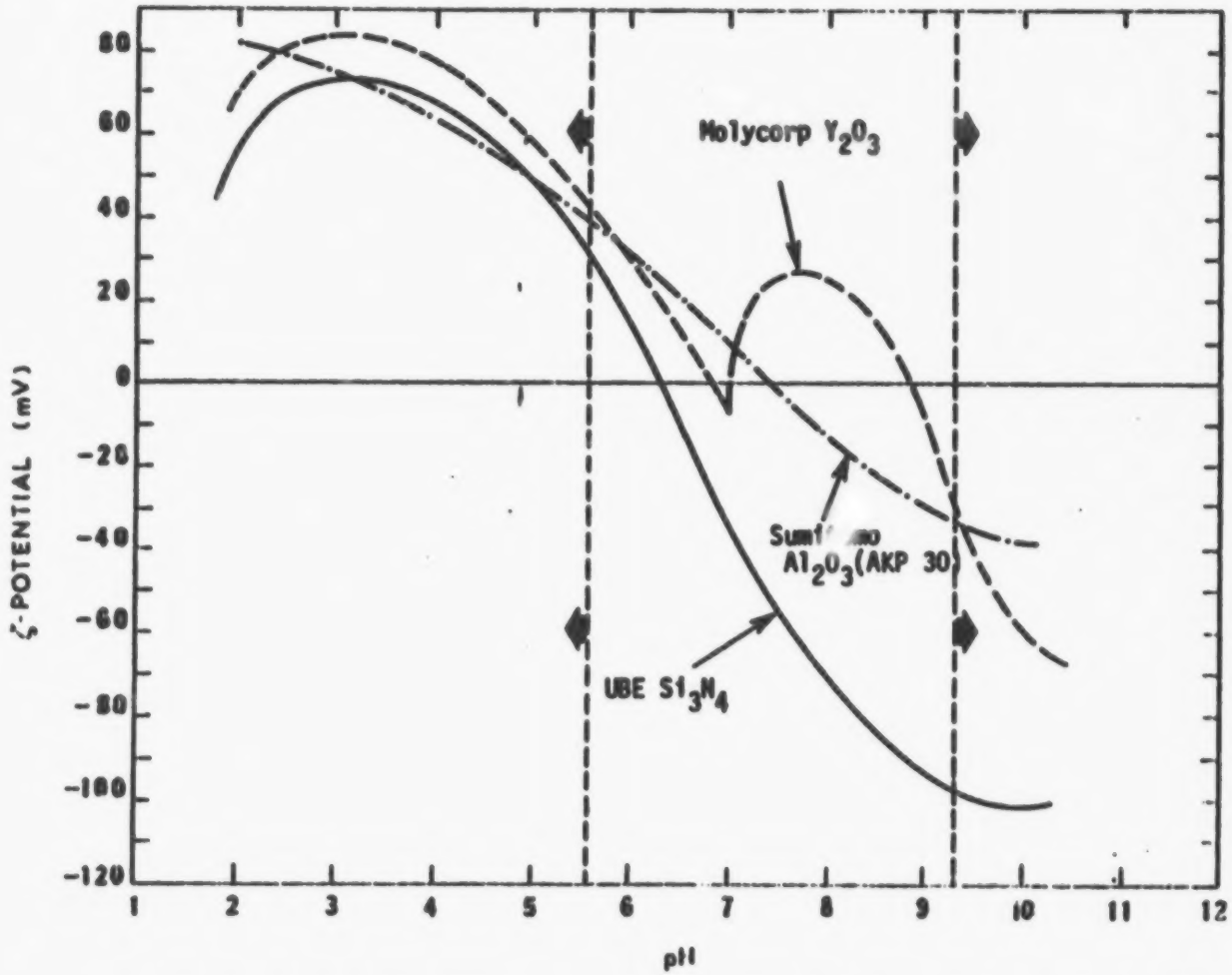

Fig. 18 Composite ζ-potential vs. pH relationships of Si_3N_4, Al_2O_3, and Y_2O_3 powders used in this study. Region between the arrows is the heterogeneous regime.

of the validity of our concepts, viscosity was measured as a function of pH for the Garrett/ACC-specified 92 w/o Si_3N_4 + 6 w/o Y_2O_3 + 2 w/o Al_2O_3 - composition suspension prepared with the as-received powders at 35 v/o solids (=65.6 w/o). Indeed, the suspension exhibited "flocculated" viscosity behavior up to pH = 9.9, but above 10.1 the suspension (which was prepared using the powders in their as-received forms; i.e, including large particles) lowered in viscosity and exhibited stable, disperse behavior. Measured viscosities at this point were around 50 cP.

As with other sub-micron-sized ceramic powders, the size-distribution plots and the SEM micrographs we have generated show that the as-received dry-state powders are highly agglomerated; indeed, even though individual particle sizes may be small, many of these particles are rendered useless to us by being locked into hard agglomerates which are "unbreakable". The elimination of these agglomerates is one of the more necessary steps if, in the end product, complete intimate mixing of the different components is desired.

In order to avoid impurity pick-up problems associated with milling techniques, our attempt was to use ultrasonication to rupture soft- to medium-hard agglomerates; however, some agglomerates (as well as large particles) still remained in the Si_3N_4 and Y_2O_3 systems and these were removed through sedimentation. Particle size distributions after this sedimentation treatment are shown in Figs. 19 and 20.

In subsequent experiments using only the fine powders, however, a workable suspension was much more difficult to achieve than with the

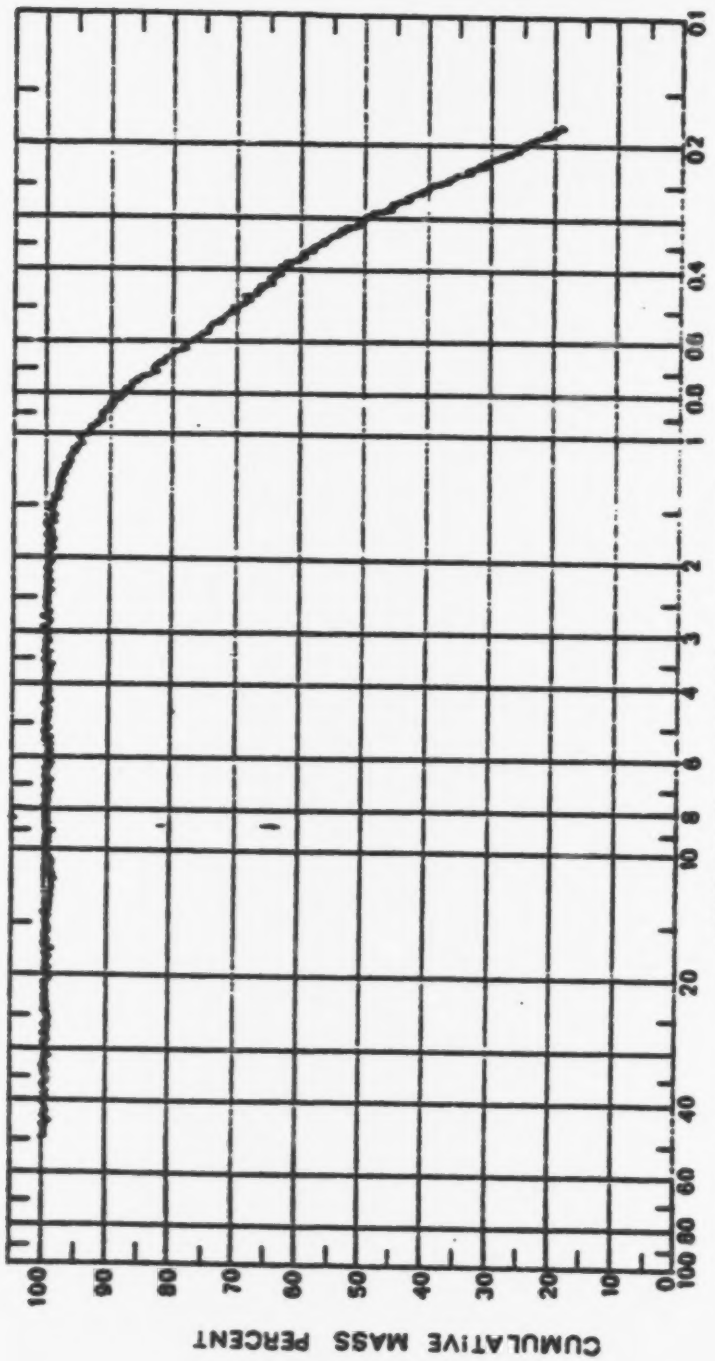

Fig. 19 Particle size distribution of UBE Si_3N_4 (Lot #A-15) after sedimentation treatment.

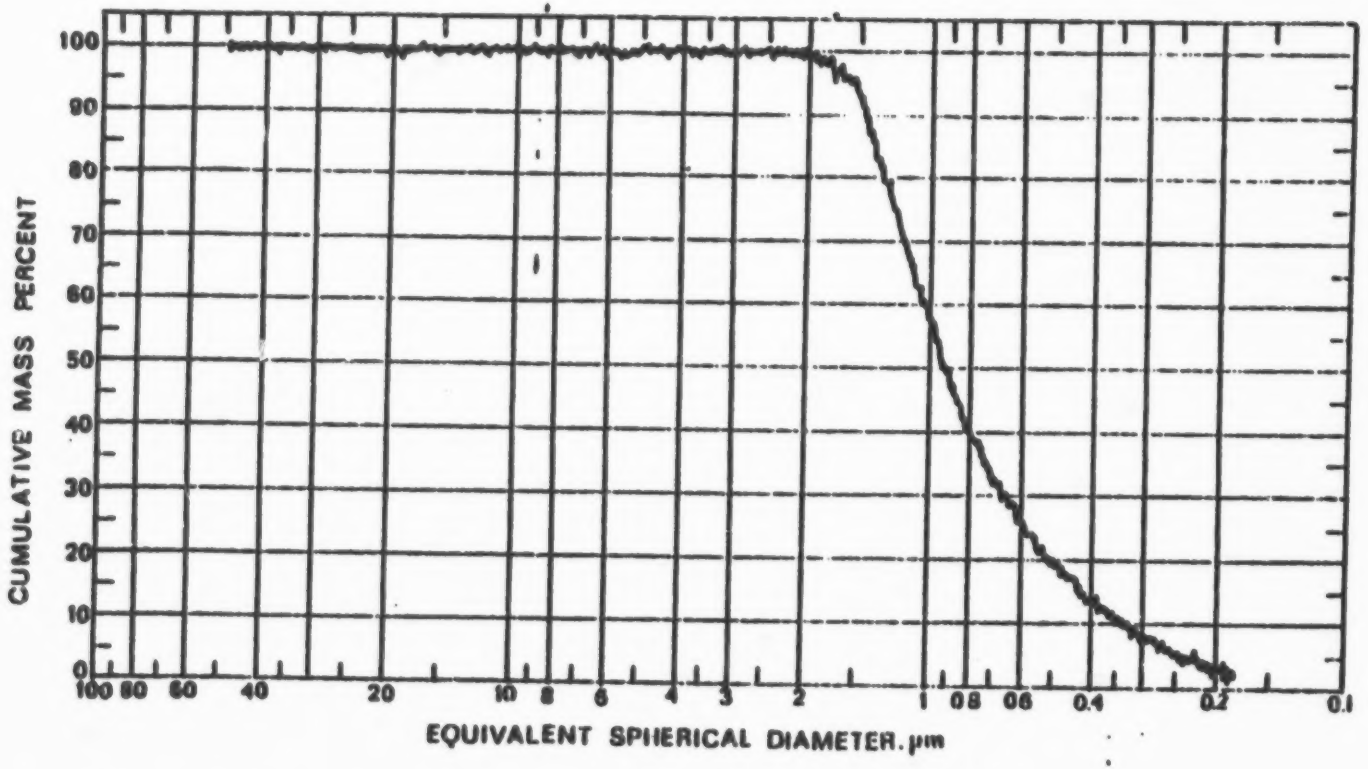

Fig. 20 Particle size distribution of Molycorp Y_2O_3 (higher SA) after sedimentation treatment.

previous coarse (as-received) particles viscosity experiments. The viscosity differences between coarse and fine particle suspensions were then measured, and they were considerably different. For the large-particle system, viscosities in the pH = 9 to pH = 10.5 range were about 200 to 400 cP. However, the smaller particle suspensions displayed more viscous behavior, registering around 1700 cP at pH = 10 to 10.5.

Another observation made was that the behavior of suspensions prepared with the fine Si_3N_4 powder was strongly time-dependent. Suspensions we prepared one day were fluid and manageable up to 40 v/o (70 w/o) solids concentration; however, aging overnight resulted in a stiff, dry-appearing, non-viscous mass although there was no observable pH shift (pH = 10.35). On the other hand, some decrease in the ζ-potential of both GTE SN-502 and UBE Si_3N_4 powders was observed with increasing aging time, suggesting a possible explanation for the time dependent behavior of these suspensions.

Initial casting experiments done on plaster of Paris molds with the fine-particle-size-suspensions indicated to us that casting times would be considerably longer (up to a week) than the casting times presently experienced at Garrett/ACC to cast a 5 inch thick layer. As explained in Appendix I, this is mainly due to the higher hydraulic specific resistance of the fine particulate systems.

3.3 Microstructural Evolution During Sintering

Typical SEM micrographs* of the composite specimens sintered at 1600°, 1750°, and 1850°C are shown in Figs. 21 to 23. The average

*Characterization of the sintered microstructures was done at Garrett Turbine Engine Co., Phoenix, AZ 85010.

ORIGINAL PAGE IS
OF POOR QUALITY

Fig. 21 Microstructure of 92 w/o Si_3N_4 + 6 w/o Y_2O_3 + 2 w/o Al_2O_3 after sintering at 1600°C.

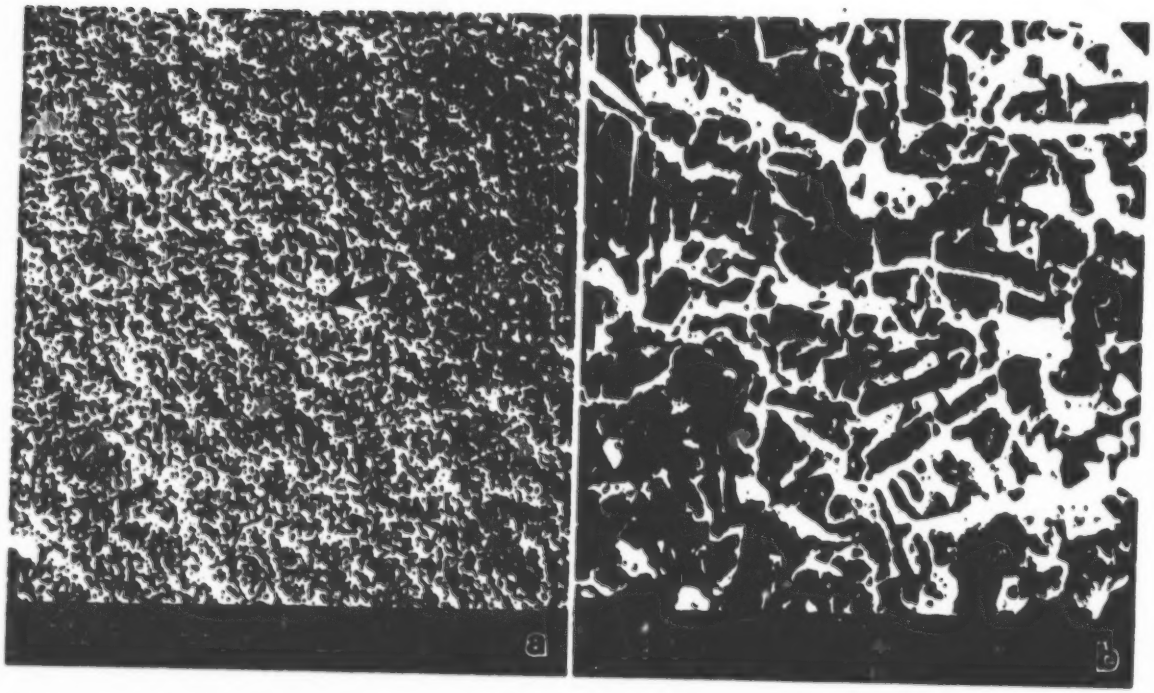

Fig. 22 Microstructure of 92 w/o Si_3N_4 + 6 w/o Y_2O_3 + 2 w/o Al_2O_3 after sintering at 1750°C.

ORIGINAL PAGE IS
OF POOR QUALITY

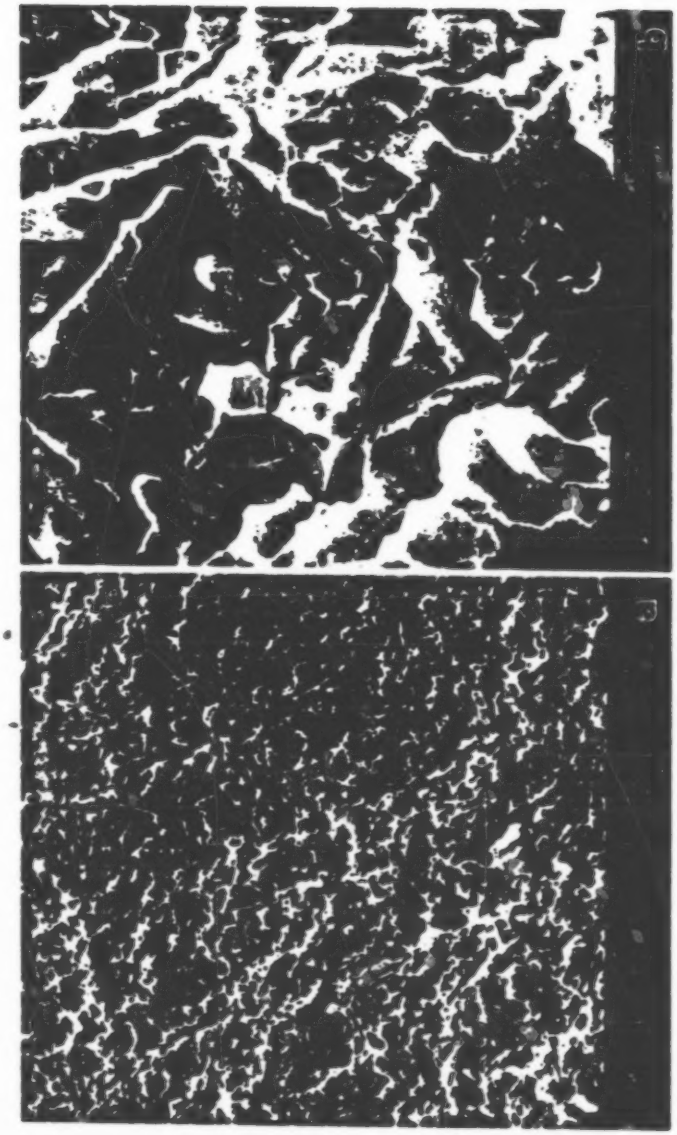

Fig. 23 Microstructure of 92 w/o Si_3N_4 + 6 w/o Y_2O_3 + 2 w/o Al_2O_3 after sintering at 1850°C.

densities of these specimens were 2.84, 3.29, and 3.22 gm/cc at 1600°, 1750°, and 1850°C, respectively. As indicated in Appendix II, at 1750°C and 1850°C specimens were totally converted to β-Si_3N_4; however, at 1600°C, α to β Si_3N_4 ratio was 50/50.

From an examination of these micrographs and data presented in Appendix II, it is clear that for the proper sintering of the composite microstructures prepared by the techniques outlined in the previous sections, temperatures higher than 1750°C will not be needed. The specimens sintered at 1600°C show fully dense particle domain regions separated from each other by porous channels. These channels are created during the initial consolidation stage as filtration channels. At temperatures higher than 1600°C, the porosity remaining at these filtration channels is eliminated as a result of some grain growth in the fully dense domains.[9] Thus, some grain growth at elevated temperatures appears to be necessary in order to densify the filtration channels. On the other hand, densification could have been completed at 1600°C without grain growth if ways of eliminating these filtration channels were developed in the pre-sintering stages.

4.0 SUMMARY AND CONCLUSIONS

Our main objective in this study was to establish the methodology of obtaining uniformity in polyphase Si_3N_4 ceramics in dimensions close to the primary particle size of the raw materials. This goal was achieved as evidenced by the sintered microstructures presented in the previous section. However, as in any research problem, deviations from the established technqiues resulted in new disadvantages along with the advantages they introduced. Below, we list the advantages and the disadvantages of the techniques used in this study.

The main advantage of the colloidal suspension and consolidation techniques used in this study is the uniformity achieved in the consolidated state not only with respect to phase distribution but also the density variations (i.e., pore distribution). This was made possible (1) by outlining the co-dispersion regions of Si_3N_4, Al_2O_3, and Y_2O_3 powders in electrostatically stabilized aqueous suspensions, (2) by eliminating all the particles or particle clusters (agglomerates) larger than ~ 2 μm through ultrasonication and removal by sedimentation techniques, and (3) by retaining the uniformity of a colloidally mixed system (to a certain extent) during consolidation by filtration.

The main disadvantages can be identified as: (1) slow filtration rates due to the increased hydraulic resistance of submicron size particulate systems, (2) chemical instability problems associated with the electrostatically stabilized colloidal suspension (i.e., instability of Y_2O_3 in the acidic ranges and changes in ζ-potential during aging),

(3) introduction of filtration channels into the consolidated structures which actually constitute the main hindrance to densification during sintering.

Nevertheless, in view of the fact that the colloidal consolidation routes can indeed result in uniform microstructures in a finished product with flaw sizes drastically reduced in comparison to other consolidation techniques, the disadvantages listed above should only be taken as problem areas that should be eliminated with future research.

REFERENCES

1. F. F. Lange, "Fabrication and Properties of Dense Polyphase Silicon Nitride," Am. Ceram. Soc. Bull., 62 [12] 1369-74 (1983).

2. D. R. Clarke, "Densification of Silicon Nitride: Effect of Chlorine Impurities," J. Am. Ceram. Soc., 65, C-21 (1982).

3. D. R. Clarke, F. F. Lange, and G. D. Schmittgrurd, "Strengthening of a Sintered Silicon Nitride by a Post-Fabrication Heat Treatment," J. Am. Ceram. Sco., 65, C-51 (1982).

4. D. R. Clarke, "Review: The Microstrucure of Nitrogen Ceramics," in Progress in Nitrogen Ceramics, Proceedings of Advanced Study Institute of Nitrogen Ceramics, Brighton, 1981.

5. I. A. Aksay, F. F. Lange, and B. I. Davis, "Uniformity of Al_2O_3-ZrO_2 Composites by Colloidal Filtration," J. Am. Ceram. Soc., 66 [10] C-190-2 (1983).

6. I. A. Aksay, "Microstructure Control through Colloidal Consolidation," in Forming of Ceramics, Advances in Ceramics, Vol. 9 (Mangels, J. A., Ed.) The Am. Ceram. Soc., Inc., Columbus, OH, 1984.

7. J. Th. G. Overbeek, "Recent Developments in the Understanding of Colloid Stability," J. Coll. Int. Sci., 58 [2] 408-422 (1977).

8. M. Persson, L. Hermansson, and R. Carlsson, "Some Aspects of Slip Casting of Silicon Nitride and Silicon Carbide," in the Proceedings of the 5th International Meeting on Modern Ceramics Technologies, Ceramic Powders: Preparation-Consolidation-Sintering, Elsevier Scientific Publ. Co., Amsterdam, 1983.

9. F. F. Lange, "Sinterability of Agglomerated Powders," J. Am. Ceram. Soc., 67 [27] 83-89 (1984).

APPENDIX I

THE MECHANICS OF COLLOIDAL FILTRATION

I.A. AKSAY

Department of Materials Science and Engineering
College of Engineering
University of Washington, Seattle, WA 98195

C.H. Schilling

Department of Materials Science and Engineering
School of Engineering and Applied Science
University of California, Los Angeles, CA 90024

ABSTRACT

A model is presented for the filtration of a colloidal suspension on the surface of a semi-infinite porous medium. The kinetics of the consolidation process are described by an equation which also includes the contribution of the mold resistance. Conditions that lead to rapid filtration and thus particle consolidation rates are outlined.

December 1983

1.0 INTRODUCTION

The potential of colloidal filtration* has long been recognized in clay-based technologies as a technique to fabricate complex geometries. Recent applications of this technique to the processing of nonclay systems have illustrated that a more important advantage of this approach to the shaping of ceramics is in the potential of controlling particle dispersion and consolidation to achieve homogeneous microstructures with single phase and polyphase chemistries.[1-3]

A colloidal suspension is composed of two phases: (1) solid particles, and (2) fluid matrix. In a filtration process, the consolidation of the solid particles at a filter front is accomplished when part of the fluid matrix moves through the filter medium under a pressure gradient. As the consolidation of the particles proceeds, the consolidated layer itself behaves as an additional filtering medium and thus the effective thickness of the filter increases continuously throughout the filtration process.

---

*This technique is more popularly known as slip casting. The terminology "slip casting" is purposely avoided here for the reasons that (1) the word "slip" does not adequately describe the "colloidal" nature of a particulate-fluid system that one must be dealing with in order to fully exploit the advantages of this technique, and (2) while slip casting was originally intended to imply casting by filtration, the mode of casting from a colloidal suspension in present-day applications may be other than filtration, i.e. evaporation as in the case of tape casting or particle motion under an applied force field as in the case of electrophoresis. Therefore, it becomes necessary to describe the process with such a title that adequately defines not only the state of the particle-fluid system (i.e. colloidal) but also the mode of the consolidation (i.e. filtration).

The pressure gradient can be due to the application of an external pressure or, as in the case of colloidal filtration, it may result from the capillary suction pressure of a porous mold. In the latter case, as the filtrate front moves into the porous mold, the continuously increasing thickness of the mold/filtrate medium also adds onto the effective thickness of the filtering medium.

It is clear that studies on colloidal filtration must address two main issues: (1) the mechanics of the filtration process itself, and (2) the nature of the colloidal suspension and its role on the microstructure development when suspension to consolidated layer transition occurs. The purpose of this paper is to deal only with the first issue and establish a fundamental understanding of the filtration mechanism itself. Our treatment will particularly consider the case of filtration under the capillary suction pressure of a porous mold, i.e. slip casting.

Some of the earlier studies dealing with the mechanics of colloidal consolidation incorrectly treated the case as a diffusional process.[4,5] In 1957, Adcock and McDowall [6] were first to properly treat the process as viscous flow of the filtrate through the porous medium of the consolidated layer. Their model, however, did not consider the hydraulic resistance of the mold. In 1958, Dal and Deen [7] also proposed a model which, in addition to the consolidated layer, considered the hydraulic resistance of the mold. Dal and Deen model, although more general than the Adcock and McDowall treatment, has not received proper recognition in the literature, perhaps due to its lack of rigorous

derivation of the proposed equation. Our treatment will show that the equation proposed by Dal and Deen for the kinetics of colloidal filtration is correct for the most general case. When the hydraulic resistance of the mold can be ignored, Dal and Deen equation will reduce to the one introduced by Adcock and McDowall.

2.0 MODEL

The model presented below will deal with particle consolidation on the surface of a semi-infinite porous mold as shown in Figure 1. In the absence of an external pressure, the motion of the fluid into the dry porous mold is mainly due to the capillary suction pressure resulting from the formation of menisci in the channels of the mold. In addition to this capillary pressure, the formation of a hydration film over the dry particle surfaces may also contribute to the suction pressure.[8] The reported values of the capillary suction pressure of molds made with gypsum powder range between 0.1 to 0.2 MPa.[6,9,10] In the following treatment it will be assumed that this suction pressure applies uniformly at a sharp "wetting front". The motion of this "wetting front" will be first related to the motion of the other interfaces between (1) suspension and air, and (2) suspension and consolidated layer through the conservation of matter equations. The filtration rate will then be expressed by the use of Darcy's law.[11]

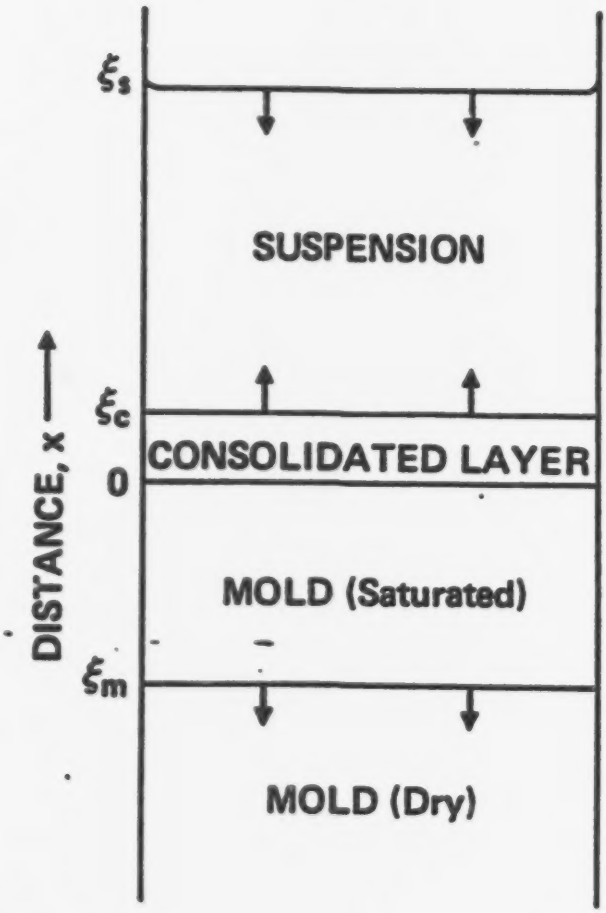

Figure 1. The schematic cross-sectional view of the filtration system.

2.1 CONSERVATION OF MATTER

In our initial treatment, mass separation due to gravitational potential will be neglected. Filtration will be the only cause of solid/liquid separation. Furthermore, it will be assumed that during filtration all the solid particles will accumulate at the consolidated layer; whereas, the fluid matrix will be partitioned into two portions as the filtrate that moves into the mold and as the fluid that is retained in the consolidated layer. When the original mold-suspension interface is taken as the reference plane, the motion of the other interfaces can be related to each other through the conservation of volume equations.

Conservation of the fluid volume requires:

$$\int_{\xi_m}^{0} \varepsilon_m A dx + \int_{0}^{\xi_c} \varepsilon_c A dx + \int_{\xi_c}^{\xi_s} (1-x_p) A dx = \int_{0}^{\xi_s^o} (1-x_p) A dx \quad , \quad (1)$$

where, as illustrated in Figure 1,

A = cross sectional area,

x_p = volume fraction of particles in the suspension,

ε_c = volume fraction of voids in the consolidated layer,

ε_m = volume fraction of voids in the mold,

ξ_s^o = location of the suspension-air interface at t=0,

ξ_s = location of the suspension-air interface during filtration,

ξ_c = location of the suspension-consolidated layer interface, and

ξ_m = location of the filtrate-air interface in the mold.

Similarly, the conservation of the particle volume (assuming that all the particles are stopped at the consolidated layer)

requires:

$$\int_0^{\xi_c}(1-\varepsilon_c)A\,dx + \int_{\xi_c}^{\xi_s} x_p A\,dx = \int_0^{\xi_s^0} x_p A\,dx \quad . \tag{2}$$

When the cross-sectional area and the volume fraction quantities are independent of x, Eqs. (1) and (2) result in:

$$\varepsilon_m\xi_m + (1-x_p-\varepsilon_c)\xi_c + (1-x_p)(\xi_s^0-\xi_s) = 0 \quad , \text{and} \tag{3}$$

$$(1-x_p-\varepsilon_c)\xi_c - x_p(\xi_s^0-\xi_s) = 0 \quad . \tag{4}$$

Eqs. (3) and (4) establish the relations between the positions of the three interfaces as:

$$\xi_s^0 - \xi_s = n\xi_c = -\varepsilon_m\xi_m \quad , \tag{5}$$

where,

$$n = \frac{1-x_p-\varepsilon_c}{x_p} \tag{6}$$

is defined as a system parameter. As it will be shown in the following sections, this parameter is a key factor to be considered in the control of filtration kinetics.

2.2 FILTRATION RATE

Linear flux of the filtrate is defined as:

$$J_f = \frac{1}{A}\cdot\frac{dV_f}{dt} \quad , \tag{7}$$

where dV_f is the incremental volume of the filtrate advancing into the dry portion of the mold during the time period of dt.

The relation between dV_f and the motion of the interfaces indicated above is:

$$dV_f = -Ad(\xi_s^o - \xi_s) = -And\xi_c = A\varepsilon_m d\xi_m \quad \text{, and} \tag{8}$$

thus:

$$J_f = \frac{d\xi s}{dt} = -n\frac{d\xi c}{dt} = \varepsilon_m \frac{d\xi m}{dt} \tag{9}$$

The implication of Eq. (9) is that an experimentalist can determine the filtration rate by monitoring the motion of any one of the three interfaces.

The relations as expressed in Eq. (9) outline the continuity condition which should be combined with Darcy's law in order to establish the relation between interfacial motion and the parameters of the filtration system. According to Darcy's law [11] the linear flux of a fluid through a porous medium, in a one-dimensional case, can be expressed as:

$$J_f = -\frac{1}{\eta\alpha} \cdot \frac{dp}{dx}, \tag{10}$$

where η is the viscosity of the filtrate, α is the specific porous medium resistance, and dp/dx is the hydraulic pressure gradient. In the geometry of Figure 1, the flow is taking place through two different types of porous media in series, and the linear flux for this case may be expressed as:

$$J_f = \frac{1}{\eta\alpha_c} \cdot \frac{dp}{d\xi_c} = -\frac{1}{\eta\alpha_m} \cdot \frac{dp}{d\xi_m} \quad , \tag{11}$$

where α_c and α_m are the specific porous medium resistances of the consolidated layer and the mold, respectively. Combining Eq.

(11) with Eq. (9), we get:

$$\frac{d}{d\xi_c}\left(\frac{dp}{d\xi_c}\right) = -\frac{d(n\alpha_c n)}{dt} \quad \text{, and} \tag{12}$$

$$\frac{d}{d\xi_m}\left(\frac{dp}{d\xi_m}\right) = -\frac{d(n\alpha_m \varepsilon_m)}{dt} \quad . \tag{13}$$

In systems where n, α_c, α_m, n, and ε_m do not change with time, Eqs. (12) and (13) reduce to:

$$\frac{d^2p}{d\xi_c^2} = \frac{d^2p}{d\xi_m^2} = 0. \tag{14}$$

Thus, for the conditions outlined, the pressure profiles across the consolidated layer and the mold become linear as illustrated in Figure 2, where p_t, p_i, and p_o correspond to the hydraulic pressures at the indicated interfaces. In this case, Eq. (11) can be expressed as:

$$-\dot{\vartheta}_f = \frac{1}{n\alpha_c} \cdot \frac{p_i - p_t}{\xi_c} = -\frac{1}{n\alpha_m} \cdot \frac{p_o - p_i}{\xi_m} \quad ; \text{ and} \tag{15}$$

substitution of Eq. (5) into Eq. (15) results:

$$\frac{p_t - p_i}{p_i - p_o} = \frac{\alpha_c}{\alpha_m} \cdot \frac{\varepsilon_m}{n} \quad . \tag{16}$$

Since in our treatment, the parameters on the RHS of Eq. (16) are assumed to be constant, for a given p_t, and p_o, the hydraulic pressure, p_i at the mold-consolidated layer interface also becomes constant throughout the filtration process. In the Adcock and McDowall treatment of "slip casting", p_i is assumed to be

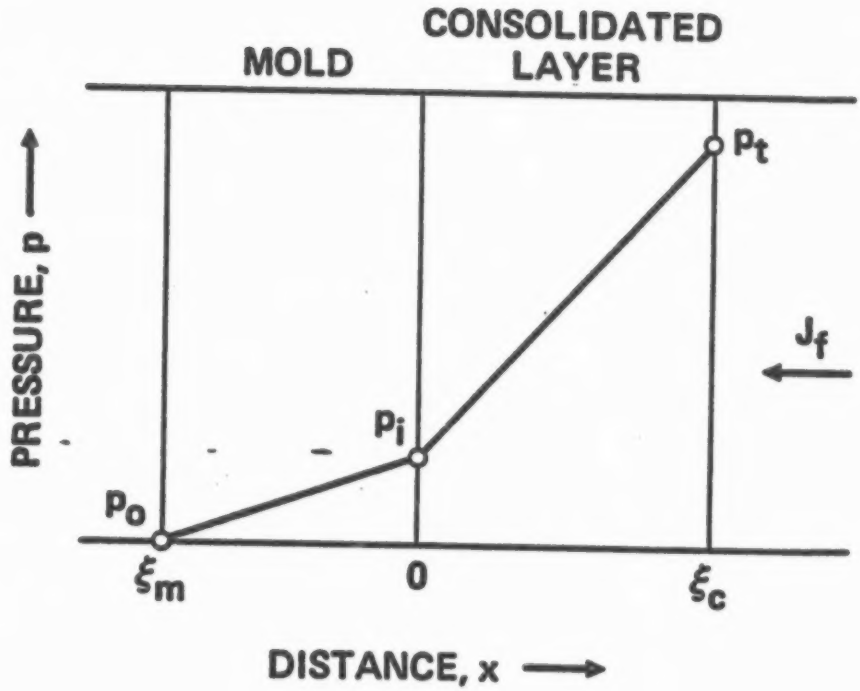

Figure 2. Hydraulic pressure profiles across the consolidated layer and the mold.

identical to p_0 . As it will be shown in the following section, this assumption will only be valid under certain conditions.

Now, Eqs. (9) and (15) can be combined to obtain:

$$(p_i - p_t)dt = -\eta n \alpha_c \xi_c d\xi_c \quad , \text{ and} \tag{17}$$

$$(p_0 - p_i)dt = -\eta \varepsilon_m \alpha_m \xi_m d\xi_m \quad . \tag{18}$$

Upon integration between the corresponding limits at t=0 and t, Eqs. (17) and (18) result:

$$p_t - p_i = \frac{\xi_c^2}{t} \cdot \frac{\eta n \alpha_c}{2} \quad , \text{ and} \tag{19}$$

$$p_i - p_0 = \frac{\xi_m^2}{t} \cdot \frac{\eta \varepsilon_m \alpha_m}{2} \quad . \tag{20}$$

The total pressure drop $p_t - p_0$ may be expressed by summing Eqs. (19) and (20) and by substituting $\xi_m = -(n/\varepsilon_m)\,\xi_c$ from Eq. (5):

$$p_t - p_0 = \frac{\xi_c^2}{t}\left(\frac{\eta n \alpha_c}{2} + \frac{\eta n^2 \alpha_m}{2\varepsilon_m}\right) \quad . \tag{21}$$

Eq. (21) is in a form similar to the one proposed by Dal and Deen [7] and properly expresses the total pressure drop across the consolidated layer and the mold for the conditions outlined above. When the hydraulic resistance of the mold can be ignored, Eq. (21) reduces to Eq. (19) and becomes identical to the one proposed by Adcock and McDowall.[11] It is worth noting that in either case, the consolidation or filtration process is expected to follow a parabolic rate behavior. A plot of ξ_c^2 vs t should yield a linear line, the slope of which is related to the pres-

sure head and the system parameters indicated in Eq. (21).

3.0 IMPLICATIONS OF THE MODEL

From a practical point of view, it is desirable to outline the conditions that lead to rapid filtration and thus consolidation rates. As outlined in Eqs. (19) and (21), in order to achieve rapid consolidation rates (i.e. high ξ_c^2 /t values), while we are maintaining a high pressure gradient across the consolidated layer, we must also minimize the hydraulic resistances associated with both the consolidated layer itself and the mold. In the following sections, we outline the methods of achieving this goal.

3.1 SPECIFIC RESISTANCE OF THE CONSOLIDATED LAYER

One effective way of increasing the filtration rate is to work with systems where the specific resistance (or the reciprocal permeability) of the consolidated layer is low. As indicated in Eq. (19), for a given pressure drop, $p_t - p_l$, and a system parameter, n, the lowering of α_c simply results in an increase in the filtration rate. Therefore, we must first outline the parameters that affect the specific resistance of a porous medium.

Various models have been proposed to describe the specific resistance of a porous medium to flow. However, as discussed by Scheidegger [11] and Dullien [12], all the models fail to provide a rigorous description of the flow channel morphology and thus must be interpreted cautiously. Among these, the Kozeny-Carman model [13] is used in our discussion simply due to the fact that

it outlines the key parameters just as effectively as the other models.

The Kozeny-Carman model is based on the assumption of uniform flow throughout all of the available void space, where the porous medium is assumed to be equivalent to a bundle of conduits with complex shapes but constant cross-sectional areas. The specific porous medium resistance is expressed as:

$$\alpha = \frac{B(1-\varepsilon)^2 S^2}{\varepsilon^2} \quad , \qquad (22)$$

where B is the ratio of the shape factor to the the tortuosity constant and S is the specific surface area, which is usually taken as the ratio of the total solids surface area to the apparent volume of the consolidated system. According to Carman, a value of B = 5.0 fits most experimental data.

Figure 3 shows the dependence of the specific resistance of a porous medium, based on Eq. (22), on the particle size and the void ratio, in a system where all the particles are assumed to be spherical and monosize. It is clear that in order to reduce the specific resistance, one should either increase the particle size or the void ratio of the consolidated layer. The control of the consolidation rate by varying the void ratio may prove to be quite effective in certain cases.[14] As illustrated in the next article [15], the void ratio of a consolidated layer can be changed by simply varying the particle interaction forces in the colloidal suspension. On the other hand, the control of consolidation rate by varying the particle size may not be a desirable

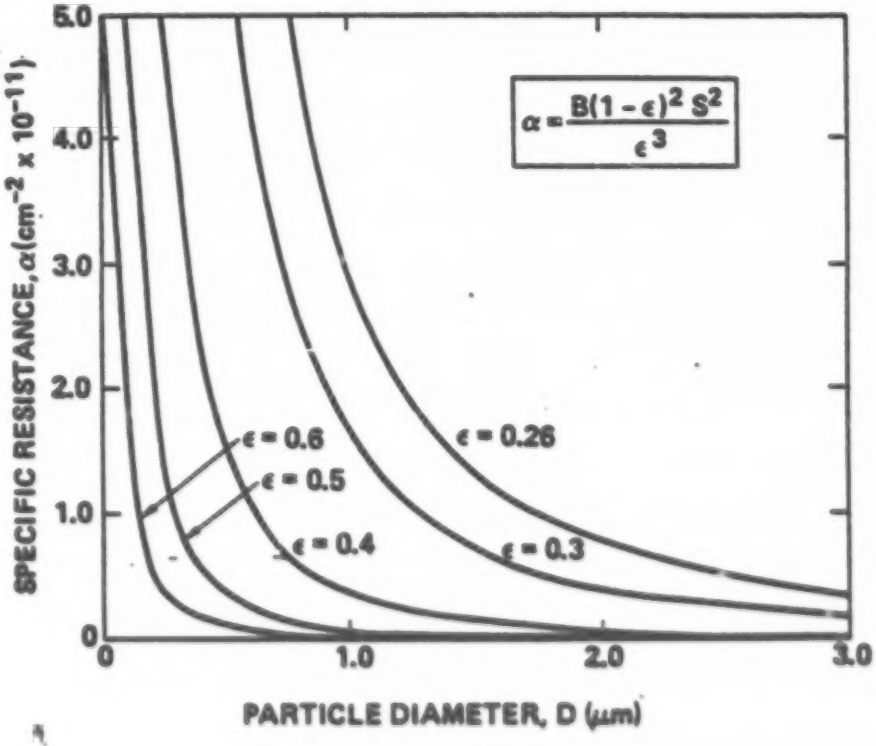

Figure 3. The specific resistance of a porous medium, at varying void ratios (ε), formed by packing monosize spherical particles.

method especially when our goal is to work with submicron size systems. It should also be pointed out that in systems where the particle size is < 0.1 μm, the filtration route to consolidation would not be a suitable forming technique due to the drastic increases in the specific resistance in this particle size range.

3.2 MOLD RESISTANCE

A second effective way of increasing the consolidation rate is by minimizing the contribution of the mold resistance. The ratio of the mold resistance to the resistance of the consolidated layer is:

$$\frac{R_m}{R_c} = -\frac{\alpha_m \xi_m}{\alpha_c \xi_c} = \frac{\alpha_m n}{\alpha_c \epsilon_m} = \frac{P_i - P_o}{P_t - P_i} \quad , \qquad (23)$$

where Eq. (5) was used to relate ξ_m to ξ_c. A common industrial practice is to use plaster of Paris molds as the suction medium. Typically, the specific resistance values of these molds are considerably lower than those of the consolidated layers [14]; and thus, as in the Adcock and McDowall treatment, there is a tendency to ignore the contribution of the mold resistance in consolidation rate studies. However, as illustrated in Figure 4, the contribution of the mold resistance to the consolidation rate can be considerably higher than that of the consolidated layer itself, especially in systems where the particle size is > 1.0 μm and/or the particle concentration (ϵ_p) of the colloidal suspension is low. Thus, in order to minimize the contribution of the mold resistance, it is necessary to work with suspensions where not only the particle concentration is high (ϵ_p > 0.35) but also

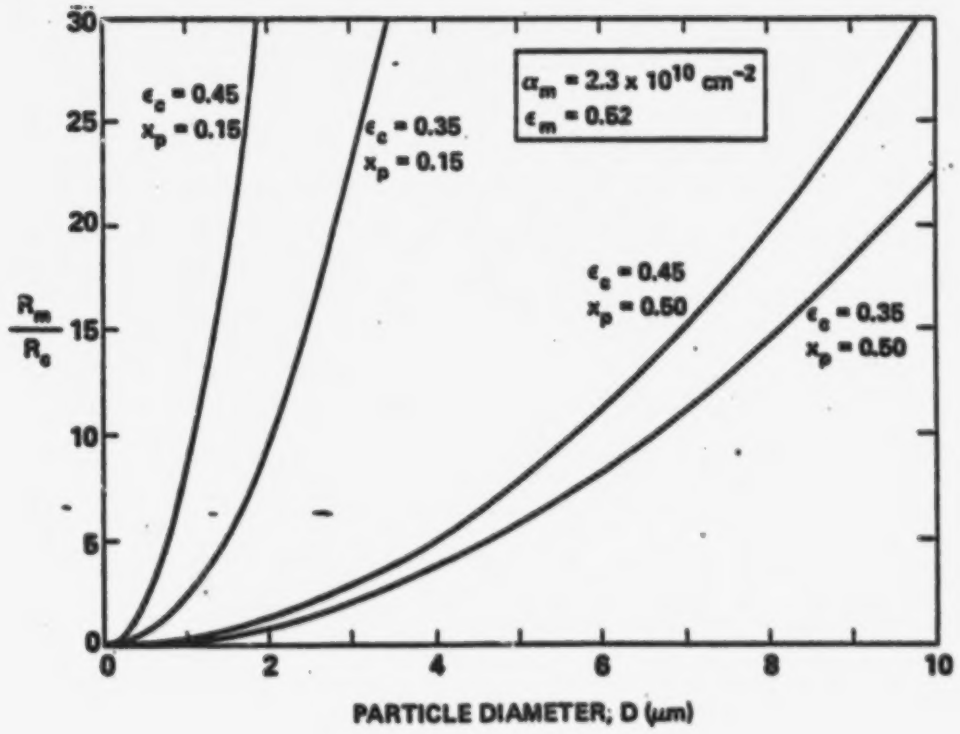

Figure 4. The ratio of the resistance of the mold to that of the consolidated layer at two different consolidated layer void ratios and suspension particle concentrations. The calculations were done at the indicated α_m and ϵ_m values.

C-3

the particle size is in the submicron range. Only under these conditions, p_1 approaches p_0, and thus the Adcock and McDowall treatment becomes a valid one for this special case.

3.3 SYSTEM PARAMETER

Finally, the most obvious way of attaining a high consolidation rate is to work with a system where the system parameter, n, is minimized (Eqs. (6) and (19)). However, it should also be noted that when working with highly concentrated suspensions and thus low values of the system parameter, our initial assumption of ignoring the gravitational settling effects becomes more justifiable due to hindered sedimentation effects.[16]

4.0 SUMMARY

The colloidal filtration model outlined in this work was developed for the case of particle consolidation on the surface of a semi-infinite porous mold. Our equation describing the parabolic nature of the filtration process for this case is similar to the one proposed by Dal and Deen.[7] Only when the hydraulic resistance of the mold can be ignored, the equation reduces to the one derived by Adcock and McDowall.[11]

For a given total pressure drop, the conditions resulting in high consolidation rates are outlined in terms of the hydraulic resistance contributions of the consolidated layer and the mold. High consolidation rates can be achieved when the resistance of the consolidated layer is lowered by using large particle size systems and/or by increasing the void ratio of the conso-

lidated layer. Both of these approaches may not necessarily be desirable when the nature of microstructure evolution in the subsequent sintering stage is considered. Alternatively, a more effective way of increasing the consolidation rate is to work with suspensions where the particle concentration is maximized.

ACKNOWLEDGMENT

Discussions with A. Davutoglu are gratefully acknowledged. This work was supported by the Office of Naval Research under Contract No. N00014-82-K-0336.

REFERENCES

1. P.H. Rieth, J.S. Reed, and A.W. Naumann, "Fabrication and Flexural Strength of Ultrafine-Grained Yttria-Stabilized Zirconia," Am. Ceram. Soc. Bull., 55 [8] 717-27 (1976).

2. I.A. Aksay, F.F. Lange, B.I. Davis, "Uniformity of A1203-Zr02 Composites by Colloidal Filtration," J. Am. Ceram. Soc., 66 [10] C190-92 (1983).

3. A.E. Pasto, J.T. Neil, and C.L. Quackenbush, "Microstructural Effects Influencing Strength of Sintered Silicon Nitride," Ultrastructure Processing of Ceramics, Glasses, and Composites, L.L. Hench and D.R. Ulrich (Eds.), John Wiley and Sons, New York, 1983.

4. E. Deeg, "Die Scherbenbildung beim Schlicker-Giessprozess als Diffusionproblem," Ber. deut. keram. Ges., 32 [6] 129-38 (1953).

5. A. Dietzel and H. Mostetzky, "Vorgange beim Wasserentzug aus einem keramischen Schlicker durch die Gipsform: I, Experimentelle Untersuchungen zur Diffusionstheorie des Schlickergiessprozess," Ber. deut. keram. Ges., 33 [1] 7-18 (1956).

6. D.S. Adcock and I.C. McDowall, "The Mechanism of Filter Pressing and Slip Casting," J. Am. Ceram. Soc., 40 [10] 353-62 (1957).

7. P.H. Dal and W. Deen, "Die Scherbenbildung beim Keramischen Giessverfahren," Sixth International Ceramic Congress, Wiesbaden, Deut. Keram. Gesell., 1958, pp.219-42. (Part of the information

provided in this references may also be found in reference 10.)

8. D. Hillel, Soil and Water: Physical Principles and Processes, Academic Press, New York, 1971, pp.56-58.

9. M.A. Sogut, "Mechanism and Kinetics of Slip Casting," M.Sc. Thesis, Middle East Technical University, Ankara, Turkey, 1980.

10. P.H. Dal and W.J.H. Berden, "The Capillary Action of Plaster Moulds," Science of Ceramics, Vol. 4, G.H. Stewart (Ed.), The Brit. Ceram. Soc., 1968, pp.113-31.

11. A.E. Scheidegger, The Physics of Flow Through Porous Media, Univ. of Toronto Press, Third Edition, Toronto, 1974, pp.73-98.

12. F.A.L. Dullien, Porous Media: Fluid Transport and Pore Structure, Academic Press, New York, 1979, pp.157-90.

13. P.C. Carman, Flow of Gases Through Porous Media, Butterworths, London, 1956.

14. C.H. Schilling, "Microstructure Development by Colloidal Filtration," M.Sc. Thesis, University of California, Los Angeles, CA 1983.

15. I.A. Aksay, "Microstructure Control Through Colloidal Consolidation," in this volume.

16. N. Ise, T. Okubo, H. Kitano, M. Sugimura and S. Date, "Ordering of Charged Particles in Solution," Naturwissenschaften 69 S.544 (1982).

APPENDIX II

Garrett Turbine Engine Company
A Division of The Garrett Corporation
111 S. 34 ST.
P.O. BOX 5217
PHOENIX
ARIZONA 85010
Tel: (602) 267-3011
Telex: 667337 GARRETT PHX

December 21, 1983

RECEIVED
[illegible]
ILHAN AKSAY

Dr. Ilhan Aksay
Dept. of Materials Science
and Engineering
Roberts Hall FB-10
University of Washington
Seattle, WA 98195

Dear Ilhan:

Enclosed are SEM photomicrographs of the specimens cast by you with the Ube powder and sintered at ACC at 1600, 1750 and 1850°C. These show an excellent sequence of the development of the microstructure. One item that is missing is documentation of the morphology and size of the starting powder. Do you have a sample left for SEM study?

The following are my observations regarding the microstructures. I am interested in your comments and additional observations.

1600°C Microstructure

- Appears to have a domain structure rather than a close-packed structure, i.e., regions of dense packing of roughly equiaxed grains (which are probably very similar to the starting powder) surrounded or interspersed with pore channels.
- Appear to be elongated grains extending into pores. Have they grown into the pores preferentially, or are they uniformly distributed and just more visible in porous regions?
- X-ray diffraction shows a 50/50 ratio between α and β Si_3N_4* plus $Y_{20}N_4Si_{12}O_{18}$. α → β transformation has begun at 1600°C but is not completed.
- Sintering was conducted at 16.7 psi nitrogen pressure in Run HPST-268. Densities** of two samples were 2.87 and 2.80 g/cm^3.

*Ratio determined using the technique of Z. Mencik and M.A. Short, "Quantitative Phase Analysis of Synthetic Si_3N_4 by x-ray diffraction: An Improved Procedure", Ford Motor Company Scientific Research Staff Technical Report #SR-72-98.

**Density measured according to ASTM C373.

APPENDIX F

LIST OF SYMBOLS, ABBREVIATIONS AND ACRONYMS

Acronym	Definition
ACC	AiResearch Casting Company
AE	acoustic emissions
AGT	advanced gas turbine
AGT101	AGT model being developed by Garrett/Ford
Al_2O_3	aluminum oxide
ASEA	ASEA Pressure Systems, Inc. Los Angeles
ATS	air turbine starter
CBO	Carborundum Company, Niagara Falls, NY
CFDC	Combined Federal Driving Cycle
dB	decibel
DF	diffusion flame (relates to combustor/nozzle)
DF-2	diesel fuel grade 2
DOE	Department of Energy
ECU	electronic control unit
EPA	Environmental Protection Agency
F	Fahrenheit (degrees of)
FC	film-cooled (relates to fuel nozzle)
Ford	Ford Motor Company
FPI	fluorescent-penetrant inspection
Fuller's earth	fine, dust-like material for detecting flow paths
Garrett	Garrett Turbine Engine Company, Division of The Garrett Corporation
GE - Cordierite	coating material made by General Electric
g	gravity, 1-g = force equal to one gravity
g/cm^3	grams per cubic centimeter
HIP	hot isostatic pressing
HPSN	hot pressed silicon nitride
HTP	high temperature protection insulation made by Lockheed Corporation
Hz	Hertz, cycles per second
ID	inner diameter
IGV	inlet guide vane
inch	U.S. customary linear unit~centimeters
in-lb	inch-pounds (work)
I-85	copper base coating material (regenerator seals)
I-151	zinc oxide base coating material (regenerator seals)
JP-4	kerosene base aviation jet fuel
ksi	one-thousand pounds per square inch
Kyocera	Kyocera International, Inc, Kyoto, Japan
LAS	lithium alumina silicate ceramic material
LBO	*lean blowout* (combustor fuel-air mixture)
lb-in	pound-inch (torque)
lb/hr	pounds per hour (flow)
lb/min	pounds per minute (flow)
mil	one-thousandth of one inch

PRECEDING PAGE BLANK NOT FILMED

APPENDIX F (Contd)

LIST OF SYMBOLS, ABBREVIATIONS AND ACRONYMS

Acronym	Definition
MOR	modulus of rupture
NASA	National Aeronautics and Space Administration
NDE	nondestructive evaluation
NGK	NGK - Locke, Inc
NO_x	nitric oxides
OD	outer diameter
pH	relative acidity to alkalinity balance
psid, ΔP	differential pressure, pounds per square inch
pound, lb	U.S customary weight measure~0.373 kilograms
p-p	peak-to-peak
P_{rig}	rig pressure psi
PSD	particle size distribution
RBSN	reaction bonded silicon nitride
RCG	reaction cured glass, Lockheed Corp.
Rene 41	high temperature heat resistant superalloy
RM-1	Ford rotor material, first generation
RM-2	Ford rotor material, second generation
RM-3	Ford rotor material, third generation
rpm	revolutions per minute
SASC	sintered alpha silicon carbide ceramic material
SC201	silicon carbide ceramic material
SIMCAB	simplex cone air blast fuel nozzle
Si_3N_4	silicon nitride
S/N	serial number
SNN	sintered silicon nitride ceramic material
shp	shaft horsepower
TBC	thermal barrier coating
TF	tensile face
Ti	titanium
TIT	turbine inlet temperature
T_{max}	maximum temperature
TSF	temperature spread factor
$T_{3.5}$	rating point - combustor inlet temperature
$T_{4.1}$	rating point - turbine inlet temperature
UCLA	University of California at Los Angeles
VIGV	variable inlet guide vane
Wayne-Kerr	rotor dynamic measuring devices
watt	electrical power - one volt x one ampere
Waspalloy	heat resistant, high temperature superalloy
Y_2O_3	yttrium oxide
μ	micron, one millionth meter
2-D	two-dimensional
3-D	three-dimensional

REFERENCES

1) Garrett Turbine Engine Company, "Advanced Gas Turbine (AGT) Powertrain System Development for Automotive Applications," Semiannual Progress Report Number 1 (October 1979 through June 1980), NASA Report CR-165175, November 1980, Contract DEN3-167.

2) Garrett Turbine Engine Company, "Advanced Gas Turbine (AGT) Powertrain System Development for Automotive Applications," Semiannual Progress Report Number 2 (July 1980 through December 1980), NASA Report CR-165329, June 1981, Contract DEN3-167.

3) Garrett Turbine Engine Company, "Advanced Gas Turbine (AGT) Powertrain System Development for Automotive Applications," Semiannual Progress Report Number 3 (January 1981 through June 1981), NASA Report CR-167901, December 1981, Contract DEN3-167.

4) Garrett Turbine Engine Company, "Advanced Gas Turbine (AGT) Powertrain System Development for Automotive Applications," Semiannual Progress Report Number 4 (July 1981 through December (1981), NASA Report CR-167983, June 1982, Contract DEN3-167.

5) Garrett Turbine Engine Company, "Advanced Gas Turbine (AGT) Powertrain System Development for Automotive Applications," Semiannual Progress Report Number 5 (January 1982 through June 1982), NASA Report CR-168104, December 1982, Contract DEN3-167.

6) Garrett Turbine Engine Company, "Advanced Gas Turbine (AGT) Powertrain System Development for Automotive Applications," Semiannual Progress Report Number 6 (July 1982 through December 1982), NASA Report CR-168246, June 1983, Contract DEN3-167.

7) Garrett Turbine Engine Company, "Advanced Gas Turbine (AGT) Powertrain System Development for Automotive Applications," Semiannual Progress Report Number 7 (January 1983 through June 1983), NASA Report CR-174694, December 1983, Contract DEN3-167.

8) Garrett Turbine Engine Company, "Advanced Gas Turbine (AGT) Powertrain System for Automotive Applications," Semiannual Progress Report 8 (July 1983 through December 1983), NASA Report CR-174809, June 1984, Contract DEN3-167.

9) F. Elrich, D. Childs, "Self-Excited Vibration in High-Performance Turbomachinery," Mechanical Engineering, (May 1984), pp 66-79.

1. Report No.	2. Government Accession No.	3. Recipient's Catalog No.
NASA CR-174886		

4. Title and Subtitle	5. Report Date
Advanced Gas Turbine (AGT) Powertrain System Development for Automotive Applications Ninth Semi-Annual Progress Report (January-June 1984)	December 1984
	6. Performing Organization Code
7. Author(s) Engineering Staff of Garrett Turbine Engine Company A Division of The Garrett Corporation	8. Performing Organization Report No. 31-3725(9)
	10. Work Unit No.
9. Performing Organization Name and Address Garrett Turbine Engine Company Division of Garrett Corporation P.O. Box 5217 Phoenix, Arizona 85010	11. Contract or Grant No. DEN3-167
	13. Type of Report and Period Covered Interim, January - June 1984
12. Sponsoring Agency Name and Address Department of Energy Division of Transportation Energy Conservation Washington, D.C. 20545	14. Sponsoring Agency Code DOE/NASA/0167-9

15. Supplementary Notes

Interim Progress Report under Interagency Agreement
Project Mananger T.N. Strom, Transportation Propulsion Division,
NASA-Lewis Research Center, Cleveland, Ohio 44135

16. Abstract

This report is the ninth in a series of Semi-Annual Technical Summary reports for the Advanced Gas Turbine (AGT) Powertrain System Development Project, authorized under NASA Contract DEN3-167, and sponsored by the Department of Energy (DOE). This report has been prepared by Garrett Turbine Engine Company, A Division of the Garrett Corporation, and includes information provided by Ford Motor Company, the Carborundum Company, and AiResearch Casting Company. The Project is administered by Mr. Thomas N. Strom, Project Manager, NASA-Lewis Research Center, Cleveland, Ohio. This report presents plans and progress for the period January through June 1984.

17. Key Words (Suggested by Author(s))	18. Distribution Statement
Advanced Gas Turbine Single Shaft Engine Ceramic Turbine Turbine Transmission	Unclassified - Unlimited Star Category 85 DOE Category UC-96

19. Security Classif. (of this report)	20. Security Classif. (of this page)	21. No. of Pages	22. Price*
Unclassified	Unclassified	204	

* For sale by the National Technical Information Service, Springfield, Virginia 22161